The Intermediate Detector and Neutrino Phenomenology of the Hyper-Kamiokande Experiment

Nicholas William Prouse

29th September 2018

Submitted in partial fulfilment of the requirements of the Degree of Doctor of Philosophy

Queen Mary University of London
Particle Physics Research Centre, School of Physics and Astronomy
Faculty of Science and Engineering

and

University of Southampton
School of Physics and Astronomy
Faculty of Physical Sciences and Engineering

I, Nicholas William Prouse, confirm that the research included within this thesis is my own work or that where it has been carried out in collaboration with or supported by others, that this is duly acknowledged below and my contribution indicated. Previously published material is also acknowledged below.

I attest that I have exercised reasonable care to ensure that the work is original, and does not to the best of my knowledge break any UK law, infringe any third party's copyright or other Intellectual Property Right, or contain any confidential material.

I accept that the College has the right to use plagiarism detection software to check the electronic version of the thesis.

I confirm that this thesis has not been previously submitted for the award of a degree by this or any other university.

Signature:

Date:

Details of collaboration and publications:

Due to the highly collaborative nature of all parts of the work of this thesis, a full account of the individual contributions is given here:

Chapters 1 and 2 provide an overview of background work, which does not constitute original research of this thesis.

The work of Chapters 3 and 4 was completed as part of the Hyper-Kamiokande, TITUS and E61 collaborations.

In Chapter 3, the high-energy reconstruction software was developed by the author, with some input also into the low-energy reconstruction that was mainly developed by TITUS collaborator W. Ma. The selections described were also developed by the author, which were then provided to TITUS collaborator R. Shah to perform the analysis on their effect on oscillation sensitivities. The remaining software described in the chapter was developed by other members of the TITUS, Hyper-Kamiokande and T2K collaborations.

The simulation and reconstruction software used in Chapter 4 was mainly developed by other members of the E61, Hyper-Kamiokande, Super-Kamiokande and T2K collaborations, except for the addition of Gadolinium support to the simulation software, which was by the author. The primary event selection was developed by other members of the E61 and νPRISM collaborations. The remaining steps of the analysis: the neutron selections, background separation, efficiency and background correction and the production of the final results were performed by the author.

The work of Chapters 5 and 6 were performed in collaboration with S.F. King of the University of Southampton and P. Ballett, S. Pascoli and T. Wang of the University of Durham, as published in [1, 2]. The simulations of Hyper-Kamiokande in both of these chapters were developed by the author, while the simulations of DUNE were developed by T. Wang.

The simulations of Chapter 5 use the existing GLoBES library, with the additional code to perform the simulations produced by the author, except for the simulations of Section 5.4 which were produced by T. Wang.

The results for new sum-rules presented in Chapter 6 and Appendix D were found by the author, with the rest of the theoretical and phenomenological development of the model by S.F. King. The fits to existing data in this chapter were performed by the author. The simulations of future experiments were performed using GLoBES, with modifications by the author to allow fitting to the oscillation models being tested, and with the additional code to perform the simulations also developed by the author.

Abstract

In this thesis, a number of aspects of neutrino oscillation physics are investigated, focusing on the design and phenomenology of next generation neutrino beam experiments.

In working to optimise the sensitivity of the Hyper-Kamiokande experiment, new reconstruction software has been developed to meet the goal of fast, flexible reconstruction of particle positions, directions, energies and species. This is demonstrated for the TITUS intermediate detector, producing samples of neutrino interactions to constrain systematic uncertainties of oscillation analyses. Inclusion of these samples achieves a reduction of over 50 % of systematic errors in measurements of θ_{23} and δ and increases the parameter space for CP violation discovery after 10 years at $5\,\sigma$ from 51 % to 74 %.

A full analysis is presented of a potential neutron measurement at the E61 detector, including full simulations of all major backgrounds, a likelihood method of background removal, and a procedure for correcting for efficiency and backgrounds. Large, pure samples are produced, with the ability to accurately reproduce true distributions of neutron capture multiplicity, distance and angle relative to neutrino interactions, with true and reconstructed distributions agreeing within ~ 2 %.

The sensitivities of Hyper-Kamiokande, including with a possible second tank in Korea, in combination with the DUNE experiment, have been thoroughly investigated. Several areas of strong synergy are identified, with the optimal combination of experiments possessing the ability to definitively resolve all remaining unknowns of 3-neutrino oscillations: determining both the octant of θ_{23} and the mass-ordering in under 2 years and discovering CP violation at $5\,\sigma$ for 50 % of parameter space after 5 years.

The highly predictive Littlest Seesaw flavour models of neutrino masses and mixing are tested against current oscillation data, finding no tension even at $1\,\sigma$. The ability of the next-generation experiments' oscillation measurements to probe these models is investigated, with all strands of the programme, including long baseline beam experiments and short and medium baseline reactor experiments, found to show high potential to exclude the models both individually and in combination.

Acknowledgements

Firstly, I would like to give enormous thanks to both my supervisors, Jeanne Wilson and Steve King. Your knowledge, guidance, support and encouragement throughout this PhD have been invaluable and I feel immensely fortunate to have had not one but two supervisors who always found the time for discussions and advice whenever I needed it. I can't imagine any better people to have led me through this journey.

I am also indebted to the many friends and collaborators who I have worked with on the various projects: In particular to Ryan, Matthew and Wing for guiding me through my first PhD project in Chapter 3, to Peter, Silvia and TseChun, for their insights into the world of phenomenology through our collaboration in my second year in Chapters 5 and 6, to Mark S, Mark H and Ben, for their help throughout my final projects in Chapter 4, to Susana for her help discussing the theory of Chapter 1, to the staff at Whipps Cross for their help with my appendix, to Alex for his computing help and getting the thesis to actually print, and to Teppei and Francesca who have given help and guidance at various times throughout. Special thanks should go to Soph and Pierre, who were there from beginning to end, and Paul and Stephane, who were there at the beginning and at the end, all always there to help with the physics, computing, making the most of our trips to Japan and academic life in general.

Thank you to the many others who have helped me along the way, joining me for countless lectures, conferences, workshops, meetings, lunches, films, football matches, pizza parties, drinks in the pub, and travels around London, the UK, Europe, Asia and Mesoamerica. Starting from my undergrad, I would not be where I am today without the friends who joined though the years, especially to Jon, continuing to wander round London with me throughout both our PhDs and beyond, and to Guy, Richard, and Tom. To Tom, and the rest of Team Penetrate, thank you for helping me stay sane while we've adventured through insanity. In my final undergrad year I was sent down this path by working with the Imperial T2K group; thanks especially to Yoshi and Morgan who made me into a neutrino physicist for life, despite my experiment at not being one. That was at Betgenius, where I must thank Pob, Kieron, Alex and all the others there; my experience working with you – and meeting up at the pub, cinema and the DCPs since – certainly helped make this PhD possible. You also helped see me through my postgrad course, where I met incredible physicists in Alejandro, Pete, Zoe, Giulia, Tom, Cian, Simon, Marcos, Andrew and all the rest, who are still great friends even if not all still physicists. Our shared QFFF experience has led me directly to this PhD. Thank you in particular to Alejandro who has never failed to be there whether I've been in a good place, bad place or the normal place. This PhD itself has also allowed me to meet many great people; I already mentioned some, but thank you as well to Tom S, Andres, Billy, Shivesh, Rodrigo, Eddie, Tom C, Jesal and everyone else who made so much time spent in the SCR so enjoyable. And thank you to all those others around the world who have made collaboration meetings and conferences something to look forward to regardless of the inevitable last minute late nights preparing talks.

Finally, I would like to give the biggest thanks to my family, who have been supporting me my entire life, in every way. Thank you to all my (n^{th}) cousins, uncles, aunts, brothers, sister and brother-in-law, step-parents and, most of all, my parents, without whom I would not have been able to exist, let alone complete this PhD.

Contents

List of Figures

List of Tables

Introduction

In the two decades since the observation of neutrino oscillations gave the first measurements directly contradicting the Standard Model of particle physics [3] – less time than it took to first observe the neutrino [4] after its proposal [5] – experiments have provided information on all six independent neutrino oscillation parameters [6]: Precision measurements of the size of every mixing angle and mass-squared difference have been made, with some angles of the CP-violating Dirac phase also now starting to be excluded, leaving only the sign of the larger mass splitting, the octant of the atmospheric mixing angle and the precise value of the Dirac phase left undetermined. This has been achieved through a diverse array of experiments observing solar neutrinos from nuclear fusion reactions in the Sun [7–9], atmospheric neutrinos from interactions of cosmic rays with nuclei in the upper atmosphere [3], reactor neutrinos from fission reactions at nuclear power stations [10] and accelerator neutrino beams from decaying muons produced in collisions of protons accelerated to high energies [11, 12].

Oscillations involving all three neutrino flavours have now been observed: solar and reactor electron neutrino disappearance, atmospheric and accelerator muon neutrino disappearance and appearance into electron neutrinos [13, 14] and tau neutrinos [15], for neutrinos having travelled distances spanning eight orders of magnitude: reactor neutrinos oscillating in a couple of kilometres [13] to solar neutrinos travelling 150 million kilometers to Earth, with energies spanning four orders of magnitude: MeV scale solar neutrinos up to several GeV accelerator neutrinos (or ten orders of magnitude when including PeV scale cosmic neutrinos [16]).

In the three neutrino oscillation picture that has emerged, the few remaining missing pieces are expected to be resolved with the next-generation accelerator neutrino projects [17, 18]. In particular, for a precision measurement of the Dirac phase they provide the only opportunity to improve on the hints to its value coming from the current neutrino beam experiments. In order to achieve this, an unprecedented quantity of neutrino oscillation data will be needed to reduce statistical errors, through new detectors with larger mass and higher power beams than are available today, as well as a corresponding reduction in systematic errors from improved detector capabilities and additional measurements to constrain model uncertainties.

This thesis will investigate several aspects of the goals of the next-generation programme of neutrino oscillation experiments, starting from the design of the Hyper-Kamiokande experiment and how its performance can be optimised through an intermediate water Cherenkov detector, then studying its performance in the context of running alongside the DUNE experiment, and investigating the ability of these and other future exper-

iments to probe theoretical models of flavour introduced to explain the addition of neutrino mass and mixing to the Standard Model.

The first two chapters provide a review of background material relevant to the remaining chapters: Chapter 1 gives an overview of neutrino physics covering the theoretical grounding, current state and future prospects of neutrino masses and mixing, as well as the physics of the detection of neutrinos. Chapter 2 then details the design, physics goals and sensitivities of the Hyper-Kamiokande project. The following two chapters then focus on two intermediate detector designs; Chapter 3 describes the development of the reconstruction software for the TITUS detector and its use in selecting event samples to constrain systematic errors and Chapter 4 demonstrates a potential neutron measurement at the E61 detector. Chapter 5 then provides a thorough analysis of the sensitivities of Hyper-Kamiokande and DUNE and the complementarity of their measurements. The ability of these and other experiments to potentially exclude the Littlest Seesaw class of neutrino mass models is then investigated in Chapter 6. The thesis then closes with some final concluding remarks and comments on future work and prospects.

Chapter 1

Neutrino Physics

Introduction

The history of the neutrino begins with Pauli's proposal [5] of an uncharged spin-$\frac{1}{2}$ particle to allow the continuous β-decay spectrum to be explained in a way which conserves energy and spin. While Pauli originally conceived of this particle as being a massive particle contained within the nucleus, Chadwick's discovery [19] of the neutron two years later suggested a mass much heavier than Pauli's requirement of "not larger than 0.01 proton masses". However, Fermi included Pauli's much lighter neutral particle as an essential component of his theory of the weak interaction [20, 21], predecessor to our current understanding of the weak interaction, also originally developed to describe β-decay; he named this particle the neutrino.

The first direct detection of neutrinos came more than two decades after Fermi's theory, with the Cowan-Reines experiment [4] detecting the inverse β-decay interactions predicted to occur when a neutrino interacts with a proton, producing a neutron and positron. The particles detected in this experiment (and produced in beta decay) turned out not to be simply neutrinos, but to be electron anti-neutrinos: With further understanding of the weak force, the development of electroweak unification as part of the Standard Model, the neutrino lost its mass but gained *flavour* and *chirality* [22, 23]; the model now contained three distinct neutrino fields (ν_e, ν_μ, ν_τ) all with left-handed (LH) chirality, along with three corresponding right-handed (RH) anti-neutrino fields ($\overline{\nu}_e$, $\overline{\nu}_\mu$, $\overline{\nu}_\tau$), associated with the three flavours of charged leptons, electron (e^-), muon (μ^-) and tau(τ^-), and their antiparticles (e^+, μ^+, τ^+).

In the Standard Model, the weak force interacts only with the LH chiral component of particles, and the RH component of anti-particles. The (anti)neutrinos are massless particles with LH (RH) chirality and no electric or colour charge, interacting only with the weak force and gravity. They are partners of the massive, charged (anti)leptons, which together form three LH electroweak doublets. The RH components of the charged leptons (and LH components of the charged antileptons) do not interact with the weak force and form electroweak singlets, with no RH components of the neutrinos or LH components of the antineutrinos.

The Standard Model, with massless neutrinos, has no need to include RH neutrinos or LH antineutrinos; all massive Dirac fermions must have both RH and LH components, but this is not true of massless fermions. If RH neutrinos were to be included, they would be required to form electroweak singlets (like the RH charged leptons) so would not interact with the weak force, and being neutral would be unable to interact with the other fundamental forces (except gravity), thus making it effectively impossible for them to be directly detected.

The next section describes how this picture fails to account for observations of the non-conservation of neutrino flavour, and details some attempts to extend the Standard Model to explain this phenomenon. Section 1.2 then describes the physics of the detection of neutrinos as applied to the detector designs described in the next chapter and used in the work of this thesis.

1.1 Neutrinos beyond the Standard Model

The Homestake experiment provided the first indication [24] that the Standard Model neutrino did not have the properties of the neutrinos we observe; the experiment measured a flux of electron neutrinos, originating from the sun, that was significantly lower than expected. The possibility of electron neutrinos changing into other flavours, in an analogous way to the oscillations of neutral mesons, had already been suggested [25, 26] and could explain the reduction of the observed flux due to the experiments inability to detect neutrino flavours other than ν_e.

However, this solution was not confirmed until further observations – the directional measurement of the atmospheric ν_μ flux at Super-Kamiokande (Super-K) [3], and measurements of ν_e-only and total (all flavours) ^{8}B solar neutrino fluxes at Super-K [7] and the Sudbury Neutrino Observatory (SNO) [8, 9] – conclusively confirmed that neutrinos were changing flavour: Super-K found that the atmospheric ν_μ flux coming from above was about twice that of the flux coming from below (where the neutrinos have had to travel a much greater distance). SNO compared their observed solar neutrino flux seen in charged-current ν_e interactions to the total solar neutrino flux observed through the detection of interactions of all three neutrino flavours; a comparison was first made to elastic scattering interactions measured at Super-K (and later also at SNO), sensitive mostly to ν_e but also with some sensitivity to other flavours, and the conclusive comparison was then made to neutral-current interactions on deuteron in SNO itself, sensitive equally to all neutrino flavours. They found that the total flux matched the predicted solar neutrino flux, without the deficit observed in measurements of the ν_e flux alone.

These observations suggested that both the atmospheric ν_μ and solar ν_e were changing in flavour as they propagated from their source to the detector. However, the mechanism for this change in flavour, through flavour oscillations, requires that the neutrino has more than one mass state. Since the Standard Model neutrino does not – and cannot – have any non-zero mass (the reasons for which will be detailed in Section 1.1.3) this meant that the observation of neutrino oscillations provided the first (and currently only) clear and direct measurement of particle physics beyond the Standard Model.

1.1.1 Neutrino mixing and flavour oscillations

For three massive neutrino flavours, the flavour eigenstates need not coincide with the mass eigenstates of the neutrino fields. In general, the three neutrino fields in the flavour basis ν_α, $\alpha \in \{e, \mu, \tau\}$, form linear combinations of the three fields in the mass basis, ν_i with masses m_i, $i \in \{1, 2, 3\}$, related by the 3×3 unitary matrix $U_{\alpha i}$, known as the PMNS matrix after Pontecorvo introduced neutrino oscillations [25] and Maki, Nakagawa and Sakata introduced the 3×3 mixing matrix [26]:

$$\nu_\alpha = \sum_{i=1}^{3} U_{\alpha i} \nu_i \tag{1.1.1}$$

Equivalently, this relationship can be applied to the flavour and mass eigenstates as vectors of the fields:

$$|\nu_\alpha\rangle = \sum_{i=1}^{3} U^*_{\alpha i} |\nu_i\rangle \tag{1.1.2}$$

This matrix was originally introduced as a 2×2 matrix with two states; however we have now observed three states, requiring a 3×3 matrix. Of the nine independent real parameters describing an arbitrary 3×3 unitary matrix, for the PMNS matrix three of those can be absorbed as phases into the definition of the fermion fields, leaving six physical parameters.

The matrix can then be parametrised in the standard factorisation [27] as

$$\begin{aligned} U &= \begin{pmatrix} c_{12}c_{13} & s_{12}c_{13} & s_{13}e^{-i\delta} \\ -s_{12}c_{23} - c_{12}s_{23}s_{13}e^{i\delta} & c_{12}c_{23} - s_{12}s_{23}s_{13}e^{i\delta}e^{i\frac{\alpha_{21}}{2}} & s_{23}c_{13} \\ s_{12}s_{23} - c_{12}c_{23}s_{13}e^{i\delta} & -c_{12}s_{23} - s_{12}c_{23}s_{13}e^{i\delta} & c_{23}c_{13}e^{i\frac{\alpha_{31}}{2}} \end{pmatrix} \\ &= \begin{pmatrix} 1 & 0 & 0 \\ 0 & c_{23} & s_{23} \\ 0 & -s_{23} & c_{23} \end{pmatrix} \begin{pmatrix} c_{13} & 0 & s_{13}e^{-i\delta} \\ 0 & 1 & 0 \\ -s_{13}e^{-i\delta} & 0 & c_{13} \end{pmatrix} \begin{pmatrix} c_{12} & s_{12} & 0 \\ -s_{12} & c_{12} & 0 \\ 0 & 0 & 1 \end{pmatrix} \begin{pmatrix} 1 & 0 & 0 \\ 0 & e^{i\frac{\alpha_{21}}{2}} & 0 \\ 0 & 0 & e^{i\frac{\alpha_{31}}{2}} \end{pmatrix}, \end{aligned} \tag{1.1.3}$$

where $s_{ij} \equiv \sin\theta_{ij}$ and $c_{ij} \equiv \cos\theta_{ij}$, θ_{ij} are the three mixing angles, δ is the Dirac CP phase [28] and α_{21} and α_{31} are the Majorana phases, which are physical only if the neutrinos have a Majorana mass [29].

The evolution in time of a neutrino state vector $|\nu(t)\rangle$ from time $t = 0$ to time t is (in natural units)

$$|\nu(t)\rangle = e^{-iHt}\,|\nu(0)\rangle\,. \tag{1.1.4}$$

The three mass eigenstates are eigenstates of the Hamiltonian, H, with eigenvalues $E_i = \sqrt{p^2 + m_i^2}$, where p is the neutrino momentum.

Then taking the plane wave solution and assuming the neutrino is ultrarelativistic so that[1] $E_i \approx p + \frac{m_i^2}{2p} \approx p + \frac{m_i^2}{2E_\nu}$, where E_ν is the total energy of the neutrino, gives

$$|\nu_i(t)\rangle = e^{-i(E_i t - p\cdot x)}\,|\nu_i(0)\rangle\,, \tag{1.1.5}$$

$$|\nu_i(L)\rangle = e^{-i\frac{m_i^2 L}{2E_\nu}}\,|\nu_i(0)\rangle\,, \tag{1.1.6}$$

where $L \approx ct$ is the distance travelled by the neutrino. Then, for a neutrino of a specific flavour eigenstate $|\nu_\alpha(t)\rangle$, Equations (1.1.1) and (1.1.6) combine to give

$$|\nu_\alpha(L)\rangle = \sum_{i=1}^{3} U_{\alpha i}^* e^{-i\frac{Lm_i^2}{2E_\nu}}\,|\nu_i(0)\rangle \tag{1.1.7}$$

[1] It should be noted here that while this standard derivation provides a demonstration of how the oscillation formula can be obtained, the approximations made are not entirely mathematically or physically consistent; the correct formula is eventually reached only through some rather fortuitous cancellation of effects that this derivation overlooks but are seen in more rigorous treatments. More details on this issue and its resolution using more complete derivations with wavepackets and/or a full field theoretical approach can be found in [30, 31].

The probability of observing a neutrino of a given flavour β at a distance L from where it was created as flavour α is then

$$P_{\alpha\to\beta}(L) = |\langle\nu_\beta(L)|\nu_\alpha(0)\rangle|^2 \tag{1.1.8}$$

$$= \left|\sum_{i=1}^{3} \langle\nu_i(L)|\, U_{\beta i} e^{-i\frac{Lm_i^2}{2E_\nu}} \sum_{j=1}^{3} U^*_{\alpha j} e^{-i\frac{0m_j^2}{2E_\nu}} |\nu_j(0)\rangle\right|^2 \tag{1.1.9}$$

$$= \left|\sum_{i=1}^{3} U^*_{\alpha i} U_{\beta i} e^{-i\frac{Lm_i^2}{2E_\nu}}\right|^2 \tag{1.1.10}$$

$$= \delta_{\alpha\beta} - 4\sum_{i>j} \mathrm{Re}(U^*_{\alpha i} U_{\beta i} U_{\alpha j} U^*_{\beta j}) \sin^2 \frac{L\Delta m^2_{ij}}{4E_\nu} + 2\sum_{i>j} \mathrm{Im}(U^*_{\alpha i} U_{\beta i} U_{\alpha j} U^*_{\beta j}) \sin \frac{L\Delta m^2_{ij}}{2E_\nu}, \tag{1.1.11}$$

using $\langle\nu_i|\nu_j\rangle = \delta_{ij}$ and where $\Delta m^2_{ij} \equiv m_i^2 - m_j^2$ and m_i, $i \in \{1, 2, 3\}$ are the three mass states. For neutrino oscillations to occur, it is therefore required that there is at least one non-zero mass squared difference Δm^2_{ij} in addition to non-zero mixing angles.

The Majorana phases appear only on the diagonal elements of the mixing matrix, which in Equation (1.1.11) are always multiplied by their complex conjugate, and so they cancel and are not observable in oscillation experiments. The Dirac phase δ, however, remains when $\alpha \neq \beta$. The probability for antineutrinos is identical to that of neutrinos given in Equation (1.1.11), except that the replacement $U \to U^*$ must me made, which is equivalent to replacing $\delta \to -\delta$ as can be seen from Equation (1.1.3). This makes clear how a non-zero Dirac phase violates CP symmetry by altering the oscillation probability for RH antineutrinos compared to LH neutrinos, which must be identical if CP is to be conserved.

This gives a total of six independent free parameters describing the oscillations between three neutrino (and anti-neutrino) flavours; three mixing angles θ_{12}, θ_{23} and θ_{13}, two independent mass squared differences, usually Δm^2_{21}, and either Δm^2_{31} or Δm^2_{32}, and the CP violating Dirac phase δ. Table 1.1 gives a summary of the experimentally determined values of these parameters from a recent fit to global data [6].

The mixing angles θ_{12}, θ_{13} and θ_{23} are often referred to as the solar, reactor and atmospheric mixing angles respectively; all of these angles are now known to be non-zero [6]. The parameter which has been constrained the least is δ, which has only recently had any angles excluded by combined fits of experimental data at the $3\,\sigma$ level [32]. The possibility of discovering CP violation in the lepton sector through a non-zero value of $\sin\delta$ was opened up after the discovery of a large θ_{13}, the last of the three angles to be measured, first hinted at by the T2K experiment [33] and then confirmed by the Daya Bay experiment [34].

The prospect of CP violations in neutrinos is of particular interest due to the possibility of it having a role in leptogenesis and the origin of the matter-antimatter asymmetry of the universe [35, 36]. Leptonic CP violation can arise through the three neutrino

	Normal Ordering		Inverted Ordering	
Parameter	best fit $\pm 1\,\sigma$	$3\,\sigma$ range	best fit $\pm 1\,\sigma$	$3\,\sigma$ range
$\sin^2\theta_{12}$	$0.307^{+0.013}_{-0.012}$	$0.272 \to 0.346$	$0.307^{+0.013}_{-0.012}$	$0.272 \to 0.346$
$\sin^2\theta_{23}$	$0.538^{+0.033}_{-0.069}$	$0.418 \to 0.613$	$0.554^{+0.023}_{-0.033}$	$0.435 \to 0.616$
$\sin^2\theta_{13}$ $[10^{-2}]$	$2.206^{+0.075}_{-0.075}$	$1.981 \to 2.436$	$2.227^{+0.074}_{-0.074}$	$2.006 \to 2.452$
Δm^2_{21} $[10^{-5}\,\mathrm{eV}^2]$	$7.40^{+0.21}_{-0.20}$	$6.80 \to 8.02$	$7.40^{+0.21}_{-0.20}$	$6.80 \to 8.02$
Δm^2_{3l} $[10^{-3}\,\mathrm{eV}^2]$	$2.494^{+0.033}_{-0.031}$	$2.399 \to 2.593$	$-2.465^{+0.032}_{-0.031}$	$-2.562 \to -2.639$
δ [°]	234^{+43}_{-31}	$144 \to 374$	278^{+26}_{-29}	$192 \to 354$

Table 1.1: Three neutrino flavour oscillation parameter values determined from a recent fit to global data [6]. The large mass-squared difference, Δm^2_{3l}, refers to Δm^2_{31} for normal ordering or Δm^2_{32} for inverted ordering.

mixing phases δ, α_{21} and α_{31}; CP violating effects in neutrino oscillations, however, are only dependant on δ due to the Majorana phases appearing only on the diagonal of the mixing matrix. A large value of θ_{13} is also required for leptonic CP violation to be seen in oscillations as δ always appears in U with $\sin\theta_{13}$. In fact all three oscillation angles are required to be non-zero to allow CP violating effects of δ.

The CP violating term, which appears in the probability of oscillation from ν_α to ν_β for $\alpha \neq \beta$, comes from the third term in Equation (1.1.11). Its effect on the difference between oscillation probabilities for neutrinos and anti-neutrinos can be written in full as

$$P(\nu_\alpha \to \nu_\beta) - P(\overline{\nu}_\alpha \to \overline{\nu}_\beta) = 16\,\mathrm{Im}(U_{\alpha1}U^*_{\alpha2}U^*_{\beta1}U_{\beta2}) \sin\frac{\Delta m^2_{21}L}{2E_\nu} \sin\frac{\Delta m^2_{32}L}{2E_\nu} \sin\frac{\Delta m^2_{31}L}{2E_\nu} \tag{1.1.12}$$

$$= \pm\, 16J \sin\frac{\Delta m^2_{21}L}{2E_\nu} \sin\frac{\Delta m^2_{32}L}{2E_\nu} \sin\frac{\Delta m^2_{31}L}{2E_\nu}, \tag{1.1.13}$$

where the positive (negative) sign is taken for (anti-)cyclic permutations of e, μ and τ in α and β. J is the Jarlskog invariant [37], the invariant measure of CP violation given by

$$\pm J = \mathrm{Im}(U_{\alpha1}U^*_{\alpha2}U^*_{\beta1}U_{\beta2}) \tag{1.1.14}$$

$$= \sin\theta_{12}\cos\theta_{12}\sin\theta_{23}\cos\theta_{23}\sin\theta_{13}\cos^2\theta_{13}\sin\delta. \tag{1.1.15}$$

This invariant is proportional to the sine of each of the three mixing angles, clearly demonstrating that they must all be non-zero for CP violation to be possible through neutrino oscillations. With the current best-fit values, $J \simeq 0.035\sin\delta$, allowing for significant CP violation effects to be seen in oscillations; the size of these effects is given by

$$|P(\nu_\alpha \to \nu_\beta) - P(\overline{\nu}_\alpha \to \overline{\nu}_\beta)| \simeq 0.56\sin\delta \sin\frac{\Delta m^2_{21}L}{2E_\nu} \sin\frac{\Delta m^2_{32}L}{2E_\nu} \sin\frac{\Delta m^2_{31}L}{2E_\nu}. \tag{1.1.16}$$

The ordering of the sizes of the mass eigenstates is another aspect of neutrinos which is not yet fully determined. Although the oscillation probability does not depend on the sign of the mass squared differences, experiments can still probe the ordering of the masses through the identity $\Delta m^2_{21} + \Delta m^2_{32} = \Delta m^2_{31}$. The effects of neutrino oscillations in matter detailed below also give oscillation experiments sensitivity to the sign of these mass splittings, potentially providing a more experimentally accessible way to determine the signs of the mass-squared differences. While the sign of Δm^2_{21} is known, the sign of Δm^2_{31} is still currently unknown; experimental data is consistent with both *normal ordering* where $m_1 < m_2 < m_3$ and *inverted ordering* where $m_3 < m_1 < m_2$. Determining which of these is the case is another major goal of current and future neutrino oscillation experiments.

Whether the value of the mixing angle θ_{23} is greater or less than 45°, known as the *octant* of θ_{23}, is also considered a important question for experimental neutrino physics to answer. The reason for this is that the octant, along with the value of δ and the mass ordering, has implications for investigations into understanding the origin of neutrino masses [38], which may in turn guide experimental and theoretical advances in particle physics beyond the Standard Model.

Further details on the phenomenological aspects of neutrino oscillations will be covered in Chapters 5 and 6.

1.1.2 Neutrino oscillations in matter

The discussion above assumed the neutrinos propagate through a vacuum, however the situation is more complex for neutrinos passing through matter due to matter effects introduced by Mikheyev, Smirnov and Wolfenstein [39, 40], also known as the MSW effect. In fact, this effect is required to correctly explain the flavour changes seen in solar neutrinos at different energies [41].

The effect arises as electron neutrinos have different interaction cross-sections to muon or tau neutrinos when travelling through matter containing electrons. The dominant contribution to the effect comes from elastic forward scattering $\nu_e + e \to \nu_e + e$ which creates a difference in potentials for ν_e compared to ν_μ or ν_τ, given by [39]

$$V_e = \pm\sqrt{2} G_F n_e, \tag{1.1.17}$$

where G_F is the Fermi constant, n_e is the electron density in the matter, and the positive sign is taken for ν_e or negative sign for $\overline{\nu}_e$. This potential modifies the Hamiltonian from that of the vacuum, and therefore modifies how the neutrinos propagate in time, leading to a modification of the oscillation formula of Equation (1.1.11). In the vacuum, Equation (1.1.4) can be rewritten as

$$i\frac{d}{dt}\left|\nu_i\right\rangle = H_m \left|\nu_i\right\rangle = E_i \left|\nu_i\right\rangle, \tag{1.1.18}$$

$$i\frac{d}{dt}\left|\nu_\alpha\right\rangle = H_f \left|\nu_\alpha\right\rangle = U H_m U^\dagger \left|\nu_\alpha\right\rangle, \tag{1.1.19}$$

where H_m and H_f are the Hamiltonian in the mass and flavour bases respectively. For particles propagating through matter, the Hamiltonian is modified as $H_0 \to H' =$

$H_0 + H^{\text{int}}$, where H^{int} accounts for neutrino-matter interactions and H_0 is the vacuum Hamiltonian. This leads to the new time-evolution of neutrino flavour states in matter

$$i\frac{d}{dt}\left|\nu_\alpha\right\rangle = H'_f\left|\nu_\alpha\right\rangle = \left(UH_mU^\dagger + H_f^{\text{int}}\right)\left|\nu_\alpha\right\rangle, \tag{1.1.20}$$

where H_f^{int} is the modification to the Hamiltonian in the flavour basis and can simply be given by

$$H_f^{\text{int}} = \text{diag}\left(V_e, V_\mu, V_\tau\right) = \text{diag}\left(\sqrt{2}G_F n_e, 0, 0\right), \tag{1.1.21}$$

after removing the effect of neutral current interactions that all neutrino flavours undergo and so do not affect oscillations.

This new form of the Hamiltonian will have different eigenvalues and eigenstates to the vacuum and so the propagating neutrino states no longer match either the flavour states or the mass states, so determining the new oscillation probabilities requires solving the flavour evolution equation given in Equation (1.1.20). The full three-flavour solution is complicated and so approximations are usually used in practice, but in the two neutrino case the oscillation formula in matter matches the two neutrino vacuum oscillation formula with modified parameters [40]:

$$P(\nu_e \to \nu_\tau) = \sin^2 2\theta_m \sin^2\left(\frac{\Delta m_m^2 L}{4E_\nu}\right), \tag{1.1.22}$$

where

$$\sin^2 2\theta_m = \frac{\sin^2 2\theta}{\left(\cos 2\theta - A\right)^2 + \sin^2 2\theta}, \tag{1.1.23}$$

$$\Delta m_m^2 = \Delta m^2\sqrt{\left(\cos 2\theta - A\right)^2 + \sin^2 2\theta}, \tag{1.1.24}$$

$$A = \frac{2\sqrt{2}E_\nu G_F n_e}{\Delta m^2}, \tag{1.1.25}$$

and in the case of antineutrinos in matter $A \to -A$.

It can now be seen that a positive value of A, which is proportional to the electron density of the medium through which the neutrinos propagate, has two effects; both the oscillation amplitude and oscillation length are increased, by increasing $\sin^2 2\theta$ and decreasing Δm^2. The oscillation amplitude is also seen to become equal to 1, even for arbitrarily small vacuum oscillation angles, when the resonance condition $A = \cos 2\theta$ is met. For antineutrinos (or for a negative value of A), the effect is reversed, decreasing the oscillation amplitude and oscillation length.

The only difference between the oscillation probabilities of neutrinos and antineutrinos, other than from this matter effect, comes from CP violating terms involving the Dirac phase δ. This means that when attempting to determine δ through measurements of oscillations of neutrinos and antineutrinos, the matter effect can make this more difficult by mimicking the CP-violating difference in oscillation probabilities. Note that the matter effect does not violate CP symmetry; the difference comes from the fact that everyday matter contains electrons and not positrons[2].

[2]However, the fact that everyday matter contains electrons and not positrons is itself also evidence of CP-violation: that of the baryon asymmetry of the universe, which to be explained requires CP-violation, which may well itself be largely due to the CP-violating effects of δ!

Since the sign of A depends on the sign of Δm^2, the matter effect also provides sensitivity to the ordering of the neutrino masses. This is particularly apparent in the case of resonant matter effects; the resonance condition can only be met for neutrinos when Δm^2 is positive or for anti-neutrinos when Δm^2 is negative. This fact, with the observation of solar neutrino oscillations, requires that the sign of Δm^2_{21} is positive [39, 40], and will contribute to the sensitivity of future experiments to determine the mass ordering through measuring the sign of Δm^2_{32}, which will be covered in Chapter 5.

1.1.3 The origin of neutrino mass

While the phenomenological model of neutrino oscillations presented above has been highly successful in describing the observed flavour changes of neutrinos over a wide variety of sources, energies and distances, it leaves the open question of where the neutrino mass originates. As mentioned previously, the Standard Model forbids neutrino masses. Understanding the reasons for this will help identify the possible extensions of the Standard Model to allow for neutrino masses.

The simplest attempt to include a neutrino mass could be to add a Dirac mass term to the Standard Model Lagrangian,

$$\mathcal{L} = \cdots - m_D \overline{\nu_L} \nu_R + \text{h.c.}, \tag{1.1.26}$$

where m_D gives the neutrino mass and h.c. refers to the Hermitian Conjugate term. As with the other fermions, adding such terms breaks electroweak gauge invariance unless generated through Yukawa interactions with the Higgs,

$$\mathcal{L} = \cdots + y_D \overline{L} H \nu_R + \text{h.c.}, \tag{1.1.27}$$

where y_D is the Yukawa coupling constant, L the LH lepton doublet and H the Standard Model Higgs doublet. The presence of the RH neutrino singlet ν_R in Equations (1.1.26) and (1.1.27) clearly demonstrates that this mass term requires the RH neutrino's existence, which is explicitly not included in the Standard Model.

As mentioned previously, these right-handed or *sterile* neutrinos, do not interact with the weak force (since they are right-handed) or the strong or electromagnetic forces (since they are uncharged). While there is no *a priori* reason why such particles cannot simply be introduced to the Standard Model to allow Dirac mass terms for the neutrinos, this option is not usually considered satisfactory. The first reason for this is that it provides no insight into why the neutrino masses (or, more fundamentally, their unitless Yukawa coupling constants to the Higgs, y_D) must be so drastically small; it might be expected that they be of similar orders of magnitude to the other fermions whose masses are generated through the same mechanism. A second reason comes from the fact that there is an alternative type of mass available only to neutral particles: the Majorana mass term.

A Majorana fermion is an alternative type of massive particle to the Dirac fermions of the standard model, constructed such that they are their own antiparticle. This can only be the case for a neutral particle, since particles and antiparticles have charges of opposite signs; for a particle and its antiparticle to be the same, those charges must therefore be zero. Since neutrinos are the only neutral fermions of the Standard Model, they provide the only observed candidate for Majorana particles.

A mass term of a LH Majorana neutrino can be generated using only the LH neutrino field, through a mass term of the form[3]

$$\mathcal{L} = \cdots - \frac{1}{2} m_L \overline{\nu_L} \nu_L^C + \text{h.c.}, \tag{1.1.28}$$

where m_L now gives the neutrino mass and $\nu_L^C = C\overline{\nu}_L^T$ is the charge conjugated LH neutrino. Again this mass term, like the Dirac mass terms, breaks electroweak gauge symmetry and so will need to be generated after symmetry breaking. However, this time it is not possible to generate such a term using the Standard Model Higgs doublet: Attempting to add a term like $y_M \overline{\nu_L} H \nu_L$ fails to conserve weak isospin and hypercharge, while using a product of Higgs doublets as in $y_W \overline{L} H H L$ (the 5-dimensional Weinberg operator [42]) introduces a non-renormalisable coupling y_W. Only by introducing a new Higgs triplet could a renormalisable Higgs interaction term be added to generate the LH neutrino's Majorana mass term.

On the other hand, returning to the above approach of introducing a RH neutrino field to allow a Dirac mass, its second potential issue can now be seen more clearly; the RH neutrinos, being electroweak singlets, could also have a Majorana mass term,

$$\mathcal{L} = \cdots - \frac{1}{2} M_R \overline{\nu_R^C} \nu_R + \text{h.c.}, \tag{1.1.29}$$

where M_R is the Majorana mass of the RH neutrino. With no symmetry or invariance preventing such a term, it could be considered an extreme case of fine-tuning to set it to zero.

So far, to generate the neutrino masses, the options available include introducing RH neutrinos to generate a Dirac mass through Yukawa interaction with the Higgs, or generating a Majorana mass either by using the non-renormalisable Weinberg operator, by extending the Higgs sector of the Standard Model, or by finding some other mechanism. The seesaw mechanism combines the first and last of these options to generate neutrino masses in a way which resolves both of the issues of the Dirac mass approach described above. While there are many other approaches to generating neutrino masses and several versions of the seesaw mechanism itself (for a recent review, see [43]), here only the type I seesaw mechanism will be considered.

If a RH neutrino is introduced, as in the Dirac neutrino case, but both the RH and LH neutrinos are considered Majorana particles, then there are three potential mass terms which could be generated: the two Majorana mass terms in Equations (1.1.28) and (1.1.29) and the Dirac mass term in Equation (1.1.26) (plus its Hermitian conjugate). As explained previously, while there is nothing preventing the addition of the RH neutrino's Majorana mass term and the Dirac mass term can be generated after electroweak symmetry breaking through the Higgs Yukawa interactions, the LH neutrino's mass term is forbidden by electroweak gauge invariance and cannot be generated using renormalisable interactions with the Standard Model Higgs. Instead, an effective Majorana mass of the LH neutrino can be generated in a different way, combining the two other mass terms, while also providing a natural explanation for the small size of the LH neutrino mass.

[3] the factor of $\frac{1}{2}$ here is required for the Majorana field $\nu = \nu_L + \nu_L^C$ to satisfy the Dirac equation when using the conventional Majorana neutrino kinetic term $i\overline{\nu_L}\gamma^\mu \partial_\mu \nu_L = \frac{1}{2} i \overline{\nu} \gamma^\mu \partial_\mu \nu$.

The neutrino mass sector of the Lagrangian, including Hermitian conjugates, then looks like

$$\begin{aligned}\mathcal{L} &= \cdots - M_R \overline{\nu_R^C} \nu_R - m_D \overline{\nu_L} \nu_R - m_D \overline{\nu_R^C} \nu_L^C + \text{h.c.} \\ &= - \begin{pmatrix} \overline{\nu_L} & \overline{\nu_R^C} \end{pmatrix} \begin{pmatrix} 0 & m_D \\ m_D & M_R \end{pmatrix} \begin{pmatrix} \nu_L^C \\ \nu_R \end{pmatrix} + \text{h.c.},\end{aligned} \tag{1.1.30}$$

where on the second line the terms have been collected into matrix form for convenience and the zero in the upper left element of the matrix corresponds to the lack of Majorana mass term for the LH neutrino.

The Dirac mass, m_D, being generated after symmetry breaking from interactions with the Higgs, is expected to be of similar size to the other fermions of the Standard Model. The Majorana mass, M_R, however, is not restricted to being generated only at the electroweak symmetry breaking scale and so could be reasonably expected to be much larger. For example, it could generated through some mechanism that occurs at a higher GUT scale, suggesting a higher value then the Dirac masses generated at the electroweak unification scale.

Since Equation (1.1.30) contains terms in the off-diagonal elements of the mass matrix, this implies that the basis of the chiral fields used up to now do not have a definite mass, but are superpositions of mass states. To obtain these mass states – the physical particles we can observe – the chiral basis is changed to the mass basis by diagonalising the mass matrix. The physical particles will then be given by superpositions of the chiral fields, with masses given by the eigenvalues of the mass matrix,

$$\lambda_\pm = \frac{M_R \pm \sqrt{M_R^2 + 4m_D^2}}{2}. \tag{1.1.31}$$

With the assumption that $M_R \gg m_D$, based on the arguments given above, the mass states found correspond to a heavy mostly right-handed particle with effective Majorana mass $\lambda_+ \approx M_R$, and a much lighter mostly left-handed particle with effective Majorana mass $\lambda_- \approx -m_D^2/M_R$. The lighter mass state can of course be identified with the masses of the nearly massless LH neutrinos that have been observed, while the heavy mass state would be some new as yet unobserved particle.

The above derivation of the type I seesaw mechanism was completed for just a single LH neutrino and single RH neutrino, however this could be applied using three RH neutrinos to provide a mass to each of the LH neutrinos[4]. In this case, the neutrino mass terms of the Lagrangian become

$$\mathcal{L} = \cdots - \begin{pmatrix} \overline{\nu_L} & \overline{\nu_R^C} \end{pmatrix} \begin{pmatrix} 0 & m_D \\ m_D^T & M_R \end{pmatrix} \begin{pmatrix} \nu_L^C \\ \nu_R \end{pmatrix} + \text{h.c.}, \tag{1.1.32}$$

which differs from Equation (1.1.30) as each ν_L and ν_R (or $\overline{\nu_L}$ and $\overline{\nu_R}$) term now corresponds to a column (or row) vector of chiral neutrino fields, and each element of the

[4]Using just two RH neutrinos results in one massless and two massive neutrinos, which is possible given that the absolute neutrino mass scale has not been measured, and using more than three RH neutrinos is also possible.

matrix corresponds to a matrix itself with the element in the lower left now the transpose of the element in the upper right.

In the approximation used above, $M_R \gg m_D$ (which now applies to the relative sizes of the elements of M_R compared to those of m_D), the 3×3 mass matrix of the three LH light effective Majorana neutrinos, m_ν, after applying the seesaw mechanism, is given by $m^\nu = -m_D M_R^{-1} m_D^T$. Furthermore, since the diagonalisation of the full mass matrix in Equation (1.1.32) links the chiral states to the mass states, the matrix used to diagonalise m^ν can be identified as (approximately) the PMNS matrix introduced in Section 1.1.1.

By introducing RH Majorana neutrinos to the existing LH neutrinos (now also specified to be Majorana particles) the type I seesaw mechanism has provided a possible origin of the neutrino masses, with a natural explanation of their much smaller size compared other fermion masses, as well as a link to the neutrino oscillations and the misalignment of the (chiral) flavour and mass eigenstates.

1.1.4 Family symmetry models

All fermions of the Standard Model have been found to come in families each containing three flavours – three copies of varying mass but otherwise identical properties – but the theoretical framework provides no explanation as to the hierarchical nature of their masses, either between the different families of fermions or between the different flavours within each family, nor an explanation of the mixing patterns that occur between the flavours, nor even a reason for the number of flavours of each fermion always being three.

Elsewhere throughout the Standard Model, its structure – the eight gluons and three colours of QCD, the pattern of mesons and baryons formed of quarks, the three W bosons and the B boson of the electroweak interaction and their relation to the photon, $W^\pm$ and Z^0 bosons, and the pattern of weak isospins, weak hypercharges and electric charges of the fermions – is governed by the local gauge symmetries and the representations of their corresponding symmetry groups.

The introduction of a flavour symmetry (or family symmetry) aims to extend this framework, building upon the existing symmetries of the Standard Model in an attempt to solve the mystery of its flavour structure. This is depicted in Figure 1.1, showing a minimal extension of the Standard Model to include three RH neutrinos and a flavour symmetry. While the formal details of the theoretical framework are beyond the scope of this thesis[5], a basic overview of the technique, as applied to the models investigated in Chapter 6, is presented here. This overview is based largely on the more detailed presentation given in [45].

The family symmetry group G_F added to the Standard Model acts on the generations of fermions, with each family transforming as a triplet, restricting the choice of group G_F to one which admits triplet representations. Having the fermions transform as a triplet of the family symmetry by construction enforces the number of generations to be three. The more ambitious goal than simply determining the number of generations, however, is to explain the pattern of masses and mixing of these generations.

[5] See *e.g.* [38, 44] for reviews.

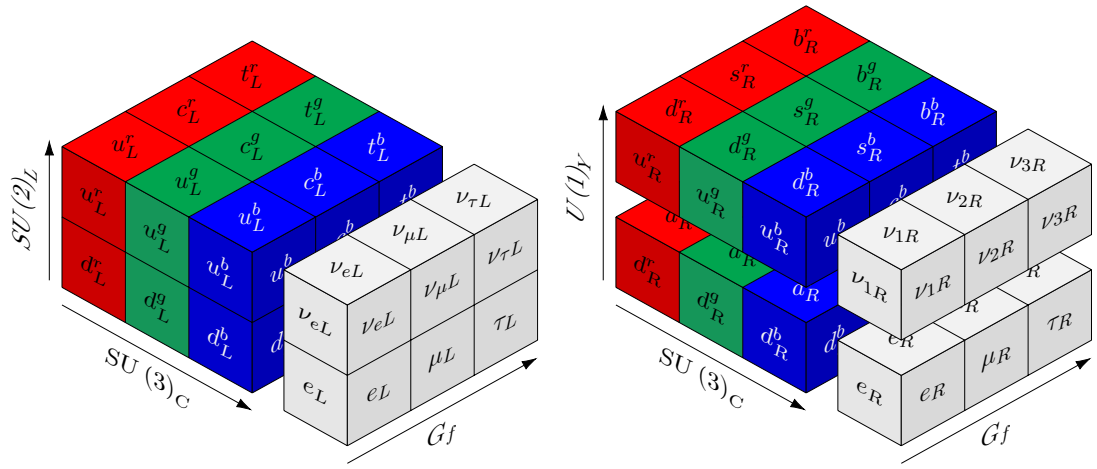

Figure 1.1: An example of how a family symmetry can extend the symmetry structure of the LH and RH fermions of the Standard Model, here including three RH neutrinos. Particles are represented by blocks, which are connected along a direction when those particles form multiplets of the group indicated to represent that axis: Each family of quarks and leptons forms a triplet of the family symmetry group G_f, the left-handed quarks and leptons all form doublets of the gauge symmetry group $SU(2)_L$, and both the LH and RH quarks all form triplets of the gauge symmetry group $SU(3)_C$. For the $U(1)_Y$ gauge symmetry, each set of connected blocks has a different weak hypercharge (and particles within these sets have the same weak hypercharge).

Since a family symmetry is not actually observed – we observe generations with different masses and mixing and so they are not invariant under the family symmetry – we know that the symmetry must be broken. This can be done in an analogous way to the spontaneous symmetry breaking of the Higgs mechanism, using new Higgs-like particles known as *flavons*, whose vacuum expectation values will end up determining the fermion mass matrices after family symmetry breaking, and hence their masses and mixing parameters.

The gauge fields do not interact with the flavons, ensuring that the part of the family symmetry that we do observe is retained: the gauge (strong, weak, electromagnetic) interactions remain identical for each generation.

Consider now the case relevant to this thesis – lepton mixing: The various flavon fields can be arranged, through careful selection of the charges associated with the symmetries of the model assigned to each particle, such that one set of flavon fields appear only in Lagrangian terms responsible for the charged lepton masses, with others appearing in the only terms for the neutrino masses. The vacuum expectation values (VEVs) of these flavon fields are generally 3-dimensional vectors, since the flavons also form triplets of G_f, and are therefore known as vacuum alignments.

In the *direct* approach, the group G_f splits into subgroups corresponding to the symmetry of the charged lepton and neutrino sectors: The VEVs of the flavons associated with generating the charged lepton masses are those that preserve the generators of the subgroup whose symmetry determines the form of the charged lepton mass mat-

rix. Similarly the VEVs of the flavons associated with the neutrino masses preserve the generators of the subgroup determining the form of the neutrino mass matrix.

For example, the discrete symmetry group S_4 has generators S, U and T; if the flavons with VEVs that preserve T appear with the charged lepton mass terms in the Lagrangian, while those of S and U appear with the neutrino mass terms, then this results in a diagonal charged lepton mass matrix, enforced by the symmetry group generated by T, and tri-bimaximal mixing [46] is found for the neutrinos, enforced by the symmetry group generated by S and U. The patterns of mixing predicted by this approach, while often fairly similar to the observed mixing pattern, have now mostly been experimentally excluded by precision measurements such as the value of θ_{13} [38].

In the *semi-direct* approach, the residual symmetry of G_f includes some, but not all, of its generators. This allows for models which lead only partially to the patterns found in the direct approach.

In the *indirect* approach, none of the generators of G_f remain unbroken in the residual symmetry. In this case, the VEVs of the flavons still determine the form of the resulting charged lepton and neutrino mass matrices, but must themselves be determined through some alternative mechanism.

Both the indirect and semi-direct approaches have been used in separate models to produce versions of the Littlest Seesaw forms of the neutrino mass matrix [47, 48], the phenomenology of which will be investigated in Chapter 6.

1.2 Detection of neutrino interactions

In order to better understand the properties of the neutrinos, to try to guide the building of models extending the Standard Model to account for their mass and explain their flavour structure, a number of experimental measurements can be made. While attempts are already underway to measure the neutrino masses directly [49] and to search for neutrinoless double β-decay [50], aiming to provide information directly on the nature of neutrino masses, our current knowledge of neutrino properties comes almost exclusively from measurements of the oscillation parameters [51]. This thesis will focus on these measurements and in particular on the future measurements of the Hyper-Kamiokande (Hyper-K) experiment, whose main goals are to perform the first precision measurement of the Dirac phase, δ, and provide improved measurements of the mixing angles and mass-squared differences.

To measure the neutrino oscillation parameters, experiments aim to detect neutrinos coming from a known source, where they are created with a known energy distribution in a specific flavour state; most commonly these are electron neutrinos produced in the sun, electron anti-neutrinos produced in nuclear reactors, muon neutrinos produced in the atmosphere, and muon neutrinos or anti-neutrinos produced by accelerators. By measuring the rates of neutrino interactions of each flavour at some distance from the source, the oscillation probabilities can be determined and the values of the oscillation parameters can be constrained.

The neutrinos themselves are detected via the products of their interactions with matter in the detectors. The systematic errors on the neutrino fluxes, determined either from

theoretical calculation or measured interaction rates, will depend heavily on our understanding of these interactions and their cross sections. To make precision measurements of oscillation parameters it is therefore important to understand these interactions as thoroughly as possible. As seen in Section 1.1.2, when neutrinos pass through matter additional terms to the oscillation probability are introduced by the MSW mechanism, so understanding these interactions is also important to understand this effect. Since the sign of the additional terms is different for neutrinos and for anti-neutrinos, the effect could mimic the CP-violating consequence of a non-zero $\sin\delta$. The sign of the additional terms also depends on the mass ordering, and so sensitivity to δ will also be improved if the mass ordering is known.

1.2.1 Neutrino interactions with matter

The weak interactions between neutrinos and matter have very small cross-sections and so occur very rarely, as compared to those of the strong nuclear force and the electromagnetic force. Neutrino interactions seen in detectors generally occur between a neutrino and either an electron or a nucleus of the target material. Lower energy solar neutrinos are often seen through the former, through elastic scattering (ES) of neutrinos on electrons via exchange of either a Z^0 boson in neutral current (NC) interactions or a $W^\pm$ Boson in charged current (CC) interactions. NC ES interactions occur for all neutrino flavours, however the flavours of the interacting neutrinos are experimentally indistinguishable as only the outgoing electron is visible. These interactions are shown in Figure 1.2. CC scattering off an electron can also occur for all flavours, so long as the energy is high enough to produce the charged appropriate charged lepton. At the higher energies, of atmospheric or beam neutrinos, interactions on nuclei dominate, separated again into CC interactions via exchange of a $W^\pm$ boson, with an outgoing charge lepton, or NC interactions via a Z^0 boson, which have no outgoing charged lepton, making them more challenging to detect.

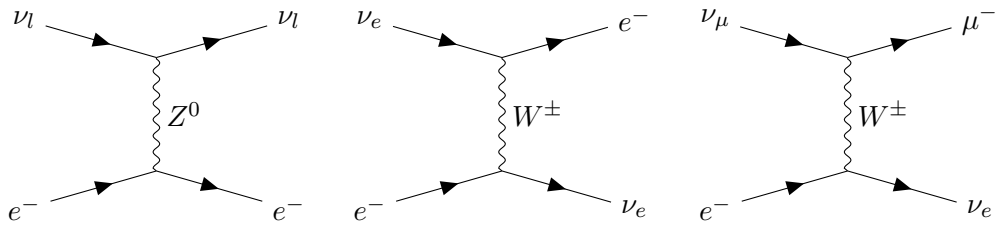

Figure 1.2: Feynman diagrams for neutrino-electron scattering. Neutral current elastic scattering (left) can occur for all neutrino flavours, with the flavour of the incoming neutrino experimentally indistinguishable. Charged current elastic scattering for ν_e (middle) and inverse muon decay for ν_μ (right) produce electrons and muons respectively, which can be distinguished in experiment. Similar interactions occur for antineutrinos, with the negatively charged leptons in the CC case being replaced with positively charged antileptons. S-channel diagrams with $W^\pm$ propagator are also allowed for electron scattering of $\overline{\nu}_e$, however at low neutrino energies this is suppressed by the mass of the $W^\pm$.

Accelerator neutrino beam experiments most commonly use the CC quasielastic (CCQE) channel, as shown in Figure 1.3, $\nu_l + n \to l^- + p$ for neutrinos and $\overline{\nu}_l + p \to l^+ + n$

for antineutrinos, which is the interaction mode with the highest cross section below 1 GeV. These CCQE interactions are the dominant neutrino interactions of interest for the long-baseline accelerator neutrino experiments covered throughout this thesis. This interaction mode is useful as the neutrino energy can be reconstructed from the kinematics of the observed outgoing lepton:

$$E_{\text{rec}} = \frac{m_N E_l - m_l^2/2}{m_N - E_l + p_l \cos\theta} \tag{1.2.1}$$

where m_N is the mass of the hit nucleon, E_l, m_l and p_l are the energy, the mass and the magnitude of the momentum of the charged lepton, and θ is the angle between the incoming neutrino beam and the outgoing charged lepton. An important consideration of these interactions is that due to the chiral nature of the weak force, when calculating the cross-sections for $\nu + n \rightarrow l^- + p$ and for $\overline{\nu} + p \rightarrow l^+ + n$, the cross-section for neutrinos is three times larger than that of antineutrinos, at first order [52].

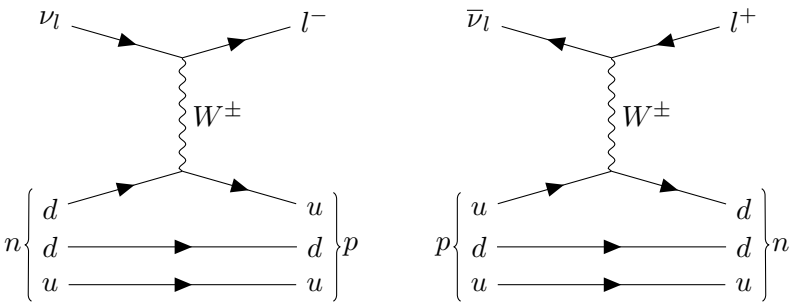

Figure 1.3: Feynman diagrams for CCQE neutrino-nucleus and antineutrino-nucleus scattering. Neutrinos interact with a neutron in the nucleus converting it into a proton (left), while antineutrinos convert a proton in the nucleus into a neutron (right).

Close to the peak energy for CCQE interactions, inelastic resonance production starts to become significant. These interactions are where the hit nucleon is excited into a resonance which then decays, for example a Δ resonance may be produced which then decays into a neutron or proton and a pion. These may be difficult to distinguish from CCQE interactions if, for example, the outgoing pion is not observed. At higher energies deep inelastic scattering (DIS) dominates, where the neutrino scatters with a quark within a nucleon, fragmenting the nucleon into any of a wide range of possible final states.

While the neutrino energy reconstruction method of Equation (1.2.1) gives a reasonable approximation in the region dominated by CCQE interactions, there is the implicit assumption that the hit nucleon is initially at rest, which is generally not the case. Furthermore, non-CCQE interactions, such as resonance production described above, or interactions involving a pair of correlated nucleons rather than a single nucleon within the target nucleus, can appear as CCQE interactions, especially when only the outgoing lepton is detected. Since the oscillation probability is dependent on the neutrino energy, accurately reconstructing this quantity is essential and so these nuclear effects need to be understood. If a detector can identify outgoing nucleons in addition to the charged lepton then this could provide useful information to help understand the hadronic system and the cross-sections of the different interaction modes.

1.2.2 Water Cherenkov detectors

One of the most successful methods of detecting neutrino interactions is from the Cherenkov light emitted by the charged lepton produced in CC interactions (or scattered in ES interactions). By using target material such as water, which is cheap, transparent, and has a high enough refractive index for the Cherenkov effect (*i.e.* charged particles at the energy produced by the neutrino interactions of interest meet the Cherenkov threshold energy determined by this refractive index), the water Cherenkov technique is well suited to the large detector sizes required to see a significant number of neutrino events.

The Cherenkov effect [53] occurs when a charged particle travelling through a dielectric material is moving faster than the speed of light in that material [54]. This light is emitted at the Cherenkov angle, θ_C, given by

$$\cos\theta_C = \frac{1}{\beta n(\epsilon)} \tag{1.2.2}$$

where βc is the particle's velocity and n is the material's refractive index which is a function of the emitted photon's energy ϵ.

In a dispersive material such as water, the refractive index increases with photon energy, and beyond a certain energy these photons will be reabsorbed into the material, giving a maximum angle at which the light is emitted which depends on the particle velocity [55]. This results in a cone of light that propagates through the water, emanating from the particle track, with the opening angle of the cone decreasing as the particle loses energy. Below the threshold of $\beta = 1/n$ the particle will not emit Cherenkov light. A particle of charge $\pm 1e$ will produce N photons along its track x at a rate given by [51]

$$\frac{d^2N}{d\epsilon dx} = \frac{\alpha}{\hbar c}\sin^2\theta_C = \frac{\alpha}{\hbar c}\left(1 - \frac{1}{\beta^2 n^2(\epsilon)}\right), \tag{1.2.3}$$

where α is the fine structure constant.

A water Cherenkov detector consists of a large tank of water, surrounded by photomultiplier tubes (PMTs) which detect the Cherenkov radiation. A ring of hits on the PMTs indicates a cone of Cherenkov light, where the pattern, timing and total number of photoelectrons observed in the PMTs, as a result of photons emitted as Cherenkov radiation, is used to determine the particle's position, direction and energy.

The type of particle can also be determined, often with very high accuracy dependent on the particle's energy, by the type of ring produced: A muon will produce a sharp cone of Cherenkov light, with an opening angle which closes as the muon travels through the detector and loses energy. The muon will also usually decay producing an electron with a second ring at a later time. An electron, however, will continually interact in the water, producing an electromagnetic shower containing electrons with slightly differing directions. These electrons will each produce cones, but due to their directional variation they will not entirely overlap, and so the ring seen by the detector will be distinctly less sharp than that produced by a muon.

1.2.3 Neutron capture and Gadolinium doping

While water Cherenkov detectors' performance in identifying charged leptons is excellent, they are unable to distinguish the charge and often do not have the ability to detect the nucleons in the final state. This results in a complete inability to distinguish neutrino and antineutrino events, as well as limited capability in separating out some non-CCQE interactions. The detection of neutrons through the few-MeV γs released after the neutron captures on a nucleus provides an additional signal for water Cherenkov detectors beyond just the outgoing lepton. Such measurements could potentially provide a number of benefits:

- The statistical separation of neutrino and anti-neutrino events which are otherwise indistinguishable in a water Cherenkov detector.
- A significantly enhanced ability to detect inverse β decay interactions from low energy $\overline{\nu}$ interactions such as those from the diffuse supernova neutrino background (supernova relic neutrinos).
- Additional information to distinguish the interaction modes of higher energy neutrino interactions.
- Additional information to help improve the neutrino energy reconstruction.
- Observations of the number, energies and directions of neutrons produced in these interactions to help improve models for the neutrino interaction cross-sections and subsequent final state interactions within the nucleus.

The use of the Gadolinium added to the water target through a Gadolinium salt allows high efficiency tagging of neutrons produced in neutrino interaction events. Neutrons produced from neutrino interactions have in the past been detected from their capture on Hydrogen, however a neutron tagging efficiency of only 18 % has been achieved [56] due to the relatively small amount of visible energy produced, 2.2 MeV, and long capture time of around 200 µs. Neutron capture on Gd has much higher cross-section of around 48 000 b (compared to 0.33 b on H) [57], leading to more observable neutron captures within the detector, with a shorter capture time of around 20 µs, with a cascade of photons produced with total energy of about 8 MeV, providing 4 MeV to 5 MeV of visible energy that can be detected with much greater efficiency [58]. Figure 1.4 compares the capture time distributions on Hydrogen and on Gadolinium, as well as the energy released after a capture on Gadolinium.

For an oscillation analysis this can provide purer samples of CCQE interaction events for when a neutrino is interacting (initially producing no neutrons) or when an anti-neutrino is interacting (initially producing 1 neutron). The number of neutrons that would actually be observed then depends on interactions of these initial neutrons (and also protons) within the nucleus, as well as the possibility of nucleons scattering with other nuclei after exiting the initial nucleus, potentially causing additional neutrons to escape. This neutron tagging also enhances the purity of samples with respect to the interaction mode, due to the different neutron multiplicities for non-CCQE interactions, allowing for measurements of cross-sections for interactions as a function of the numbers neutrons in the final state.

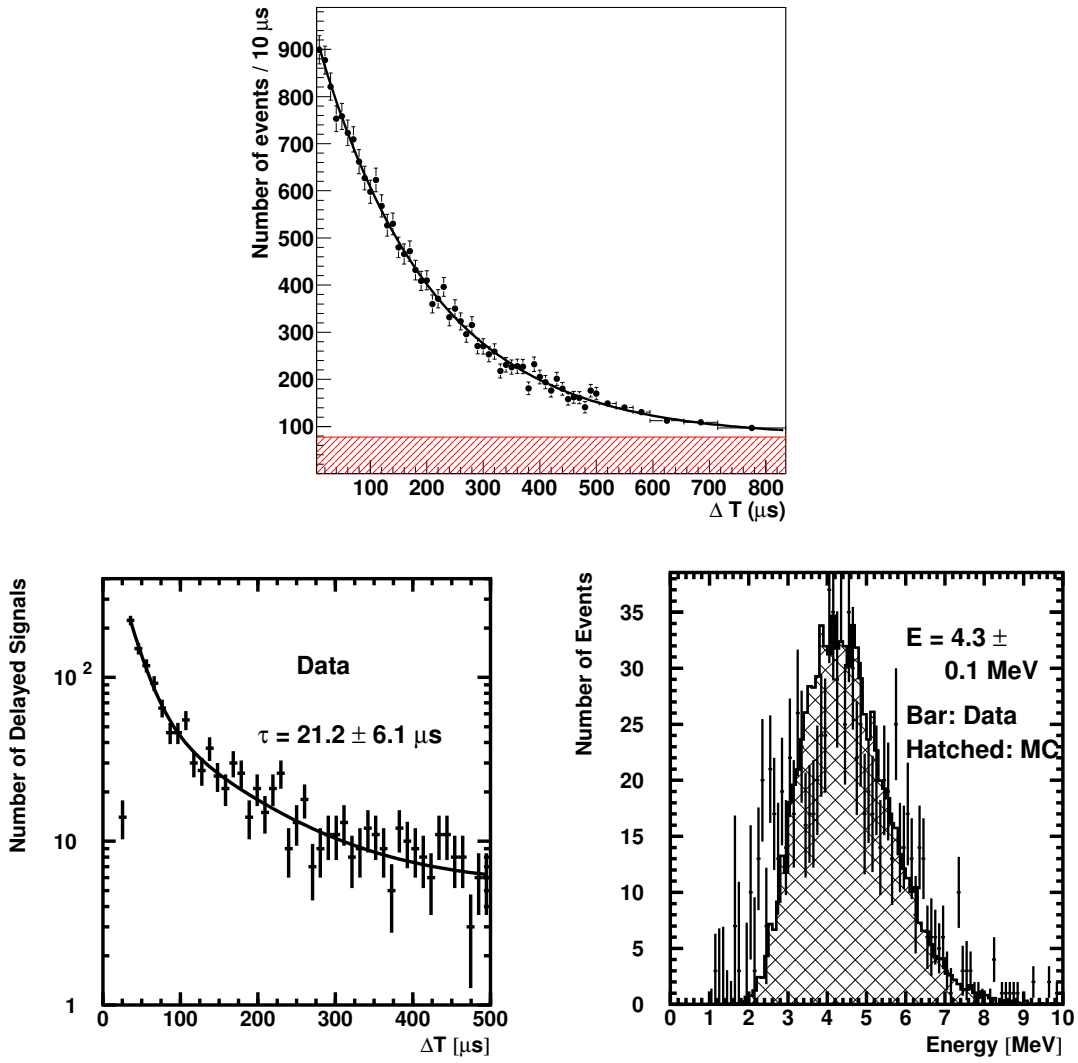

Figure 1.4: Time for delayed thermal neutron capture signal on Hydrogen (top, data in black with expected background rate in red) is around 200 µs while on Gadolinium (bottom left) is around 20 µs. The capture signal on Gadolinium consists of an 8 MeV gamma cascade, with 4 MeV to 5 MeV visible energy (bottom right), compared to the barely detectable single 2.2 MeV gamma for capture on Hydrogen.

R&D to monitor the feasibility and response of the detector when the water is doped with Gadolinium has been ongoing through the EGADS project [59, 60], with Super-K now undergoing refurbishment work in preparation for being filled with Gd-doped water for the SK-Gd project [61, 62].

Chapter 2

The Hyper-Kamiokande Experiment

Introduction

The Hyper-Kamiokande (Hyper-K) project [17] is a proposed next generation long baseline neutrino oscillation experiment consisting of the Hyper-Kamiokande detector – a new megatonne-scale water Cherenkov detector to be constructed near the existing Super-K detector in Kamioka – together with the megawatt neutrino beam, produced at the J-PARC synchrotron 295 km away in Tokai and directed 2.5° off-axis to the Hyper-K detector. In addition to the far detector, a suite of near detectors (ND), located 280 m from the beam source, and an intermediate water Cherenkov detector (IWCD), 1 km to 2 km from the beam source, will be used to constrain the neutrino beam and interaction cross-section systematics.

The primary aim of the experiment is to study CP violation in the lepton sector by measuring the oscillation probabilities for neutrinos and antineutrinos to determine the oscillation phase δ. Additional physics at Hyper-K will include increasing the precision on measurements of other neutrino oscillation parameters, probing the proton life-time at an order of magnitude beyond the current limit [63, 64], and studying atmospheric neutrinos and neutrinos from astrophysical sources in addition to those produced in the J-PARC beam.

This chapter provides an overview of these physics goals, as well as the detector design of Hyper-K. Sections 2.1 to 2.4 detail the experiment's technical design, with the neutrino beam covered in Section 2.1, the far detector in Section 2.2, near detectors in Section 2.3, and intermediate detector in Section 2.4. Section 2.5 then discusses in more detail the physics goals and projected sensitivities of the experiment and how these will be achieved.

2.1 The J-PARC neutrino beam

The neutrino beam produced at J-PARC (Japan Proton Accelerator Research Complex) has been in use for the current T2K neutrino oscillation experiment [65] and is expected to continue operation for use with Hyper-K. The facility consists of a linear accelerator which accelerates protons to 400 MeV before they are injected into a rapid cycling synchrotron. Here the protons are accelerated to 3 GeV, after which they enter the main ring synchrotron where they are further accelerated up to 30 GeV. They are then fed through to the target station, shown in Figure 2.1 where they collide with a graphite target producing pions, amongst other hadrons. The charged pions are then focused using three magnetic horns and enter a decay volume where the neutrino beam is formed from the neutrinos produced as the pions decay.

The magnetic horns focusing the pions are capable of running with a *forward horn current* to focus positively charged pions that decay producing neutrinos, or *reverse horn current* to focus negatively charged pions that decay producing antineutrinos. This allows the production of a beam consisting mostly of either neutrinos or antineutrinos, so that the oscillation probabilities for neutrinos and antineutrinos can be separately measured for the determination of δ. A small contamination (less than 1 % of the neutrino flux) of ν_e or $\overline{\nu}_e$ in the beam and $\overline{\nu}_\mu$ (ν_μ) in the ν_μ ($\overline{\nu}_\mu$) beam result from the decays of kaons produced and focused alongside the numerous pions; these more massive

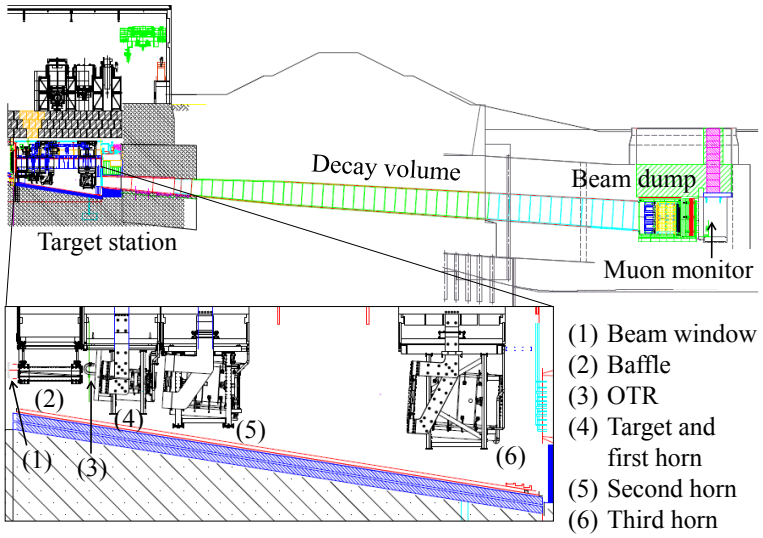

Figure 2.1: Target station at J-PARC [65].

kaons have larger branching ratios to decay modes that include undesired neutrino flavours. These neutrino flavours can also enter the beam from the decay of the μ^+ (μ^-) produced in the pion decay, however the majority of these $\mu^\pm$ are stopped after reaching the end of the decay volume before decaying, minimising this background component of the beam. The antineutrino beam in particular has a larger background contamination (and smaller signal flux) than the neutrino beam, due to the (positively charged) proton beam naturally producing more positively charged pions than negatively charged pions.

The beam power has recently been upgraded from 240 kW to 480 kW, in the process of reaching the design power of 750 kW, with the potential for further upgrades to 1.3 MW planned [66, 67].

The neutrino energy spectrum of the beam is dependant on the angle from the centre of the beam axis to the point where the neutrino is observed; at larger angles, the energy distribution has a narrower peak, with the peak located at lower energies. For water Cherenkov detectors, it is desirable to have fewer higher energy neutrinos where deep inelastic scattering becomes more common, as opposed to the lower energy CCQE interactions which give a cleaner signal in the detector, making it easier to reconstruct the incoming neutrino energy. At 2.5°, the distribution is peaked around 600 MeV, close to where CCQE interactions are most dominant. This is leveraged by the T2K experiment, directing the beam such that Super-Kamiokande, the far detector, is located 2.5° off-axis at the distance that coincides with the first oscillation maximum at this energy, and the same technique will be used for Hyper-K. Figure 2.2 demonstrates this technique as used in the T2K experiment. The final energy spectra of the fluxes of each neutrino flavour in both the neutrino and antineutrino enhanced beams at Hyper-K are shown in Figure 2.3.

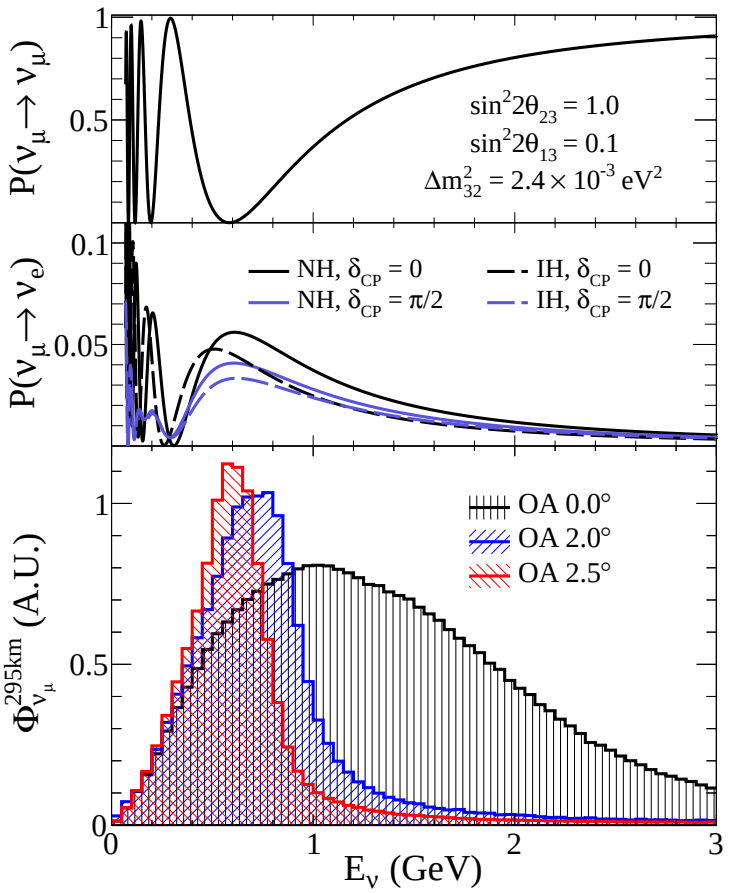

Figure 2.2: The muon neutrino (top) and electron neutrino (middle) survival probabilities with the unoscillated neutrino flux at different off-axis angles (bottom) for the T2K experiment [68].

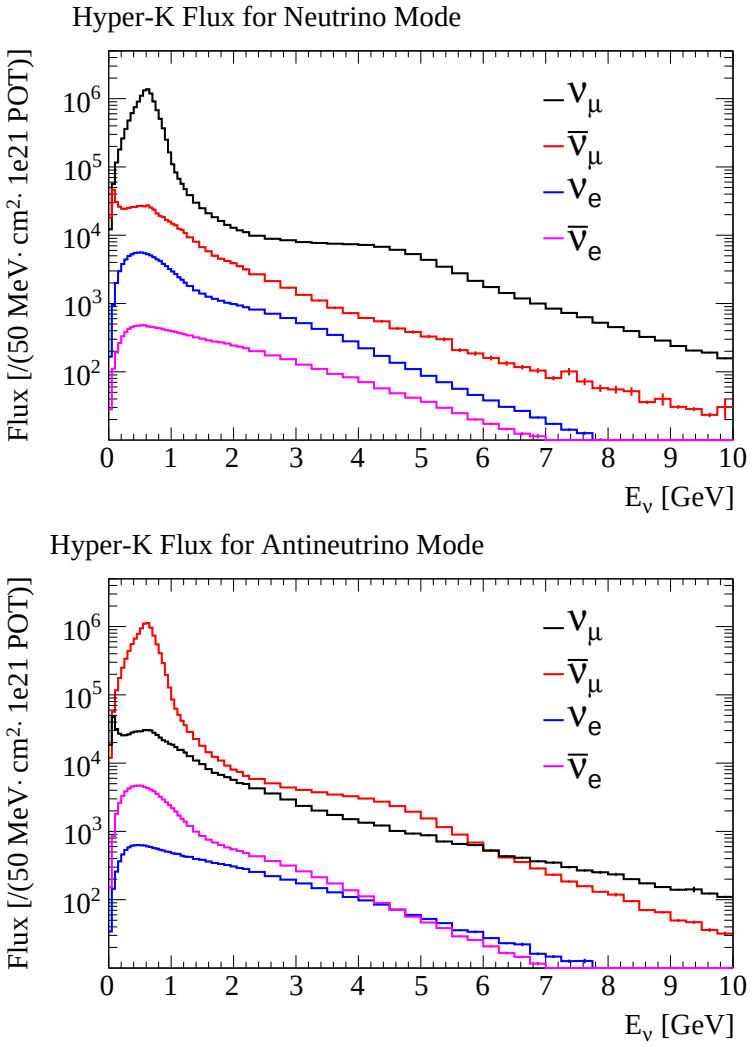

Figure 2.3: The (anti)neutrino flux energy spectra for the neutrino enhanced beam (top) and antineutrino enhanced beam (bottom) at Hyper-K [17].

2.2 The Hyper-Kamiokande far detectors

The Hyper-K detector itself is a water Cherenkov detector planned to be constructed in the Mozumi mine at a depth of 650 m, near to the existing Super-Kamiokande detector in Kamioka, 295 km west of the J-PARC accelerator complex. The baseline design for the detector consists of two separate cylindrical tanks 60 m tall and 74 m diameter, with one tank planned for the initial phase and the second tank planned to start taking data six years after the first.

Each tank will be filled with pure water, circulated through a purification system keeping Radon concentration below 1 mBq m^{-3} in order to minimise low-energy background from radioactive decays. The tanks will be divided into two optically separated regions; the inner detector (ID) and outer detector (OD). The ID of each tank will comprise all but the outermost 1 m of the tank around the barrel and 2 m at the top and bottom, giving a total volume of 258 kt of water, and will be surrounded by 40 000 PMTs each of 50 cm diameter, resulting in a photocoverage (proportion of the surface covered by PMTs) of 40 %. The fiducial volume of each tank – the volume in which signal events are selected (a cylinder 2 m inside of the PMTs on all sides of the ID) – contains 187 kt of water. While the development of the PMTs to be used is still under development, the design goal is for each PMT to have a single photon detection efficiency of 24 % and timing resolution of 1 ns. The OD region contains 6700 20 cm outward facing PMTs and its purpose is mainly to reject the incoming background from cosmic-ray muons. The possibility of adding Gadolinium to the detector for the neutron capture signal discussed in Section 1.2.3 is also being considered.

Another possibility being investigated is placing the second tank in Korea [69], with just one tank built in Mozumi. At the baselines of 1000 km to 1300 km being considered, this would place the tank close to the second oscillation maximum, making it the first long-baseline experiment to have a detector at this physically interesting point. Doing so is expected to increase sensitivity in a number of areas; in particular, the increased baseline would result in an increased matter effect, which would allow for improved sensitivity to the mass ordering as well as to the measurement of δ. The phenomenology of this and a detailed analysis of the effect on various sensitivities is presented in Chapter 5.

2.3 Near detectors for Hyper-K

A suite of detectors, shown in Figure 2.4 located 280 m downstream of the J-PARC neutrino beam target have been and continue to be used by the T2K experiment [65] and it is expected that Hyper-K will continue to use these in an upgraded form. The detectors consist of an on-axis detector, INGRID, and 2.5° off-axis detector, ND280. INGRID consists of 16 modules, arranged in a cross pattern centred on the beam axis, to measure the neutrino interaction rate at each module's location with the primary purpose of precisely constraining the beam direction. ND280 is a magnetised detector consisting of a π^0 detector, three time-projection chambers and two fine grain scintillator detectors, surrounded by electromagnetic calorimeters and a side muon range detector built within the coils of the magnet. Together, these are capable of measuring the charge and momentum of the leptons produced in CC interactions and the protons and pions

produced in both CC and NC interactions, with the primary purpose of constraining the neutrino flux, neutrino interaction cross-sections, and beam contamination of neutrinos of the wrong sign and wrong flavour. The ND280 detector is expected to be upgraded for future runs of the T2K experiment [70] and this upgraded version will be used with Hyper-K, with possible further upgrades made if required [17].

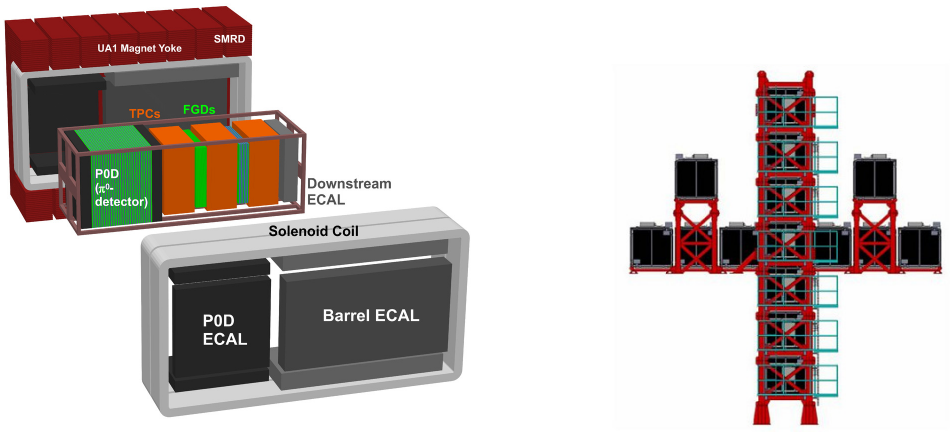

Figure 2.4: The ND280 off-axis near detectors (left) and INGRID on-axis near detector (right) of the T2K experiment [65].

2.4 Intermediate Water Cherenkov Detector

In order to reach the low level of systematic uncertainties required for Hyper-K's measurements, the addition of an intermediate water Cherenkov detector is planned [17]. While the near detectors of ND280 are able to accurately distinguish neutrino and antineutrinos through the outgoing lepton's charge, as well as detect particles below Cherenkov threshold, the intermediate detector's 4π acceptance, water target, and water Cherenkov detection method better match the far detector. This makes the IWCD's measurements directly applicable in constraining uncertainties at Hyper-K in a way that would be far more challenging if only using the existing near detectors.

The key measurements for the IWCD are the (mostly unoscillated) flux $\times$ cross-section for both ν_e and ν_μ (as well as $\overline{\nu}_e$ and $\overline{\nu}_\mu$), since these dominate the uncertainties on oscillation measurements at Hyper-K. In order to achieve this, the detector's size needs to be large enough to contain the majority of muons so that their momentum can be determined, with its location then needing to be far enough from the beam source that the flux is low enough that pile-up is kept minimal.

An additional feature of the IWCD design is to dope the tank's water with Gadolinium, to allow high-efficiency detection of neutron capture as detailed in Section 1.2.3. This would allow possible outgoing neutrons in both CC and NC interactions to be detected when captured on the Gadolinium, allowing a large, high-efficiency and high-purity sample of neutron captures to be observed. Such a measurement can then be used to better understand the neutron capture signal in the far detector, providing the benefits described in Section 1.2.3, both for its uses in beam neutrinos as well as atmospheric neutrinos. The potential for such a measurement will be analysed in detail in Chapter 4.

The IWCD can also be used for other physics purposes including detection of supernovae neutrinos, sterile neutrino studies and understanding the background for proton decay searches.

The design of the IWCD has taken several forms over the past few years; two of these – TITUS and E61 – have been studied in the work of this thesis.

2.4.1 The TITUS detector

TITUS (Tokai Intermediate Tank for the Unoscillated Spectrum) [71] was a proposed design for the intermediate water Cherenkov detector, which has now merged with the alternative νPRISM [72] design to form the E61 detector design discussed in the next subsection. The detector's location is approximately 2 km from the J-PARC neutrino beam, at the same 2.5° angle off axis from the beam as the far detector. TITUS is a cylindrical water Cherenkov detector, containing approximately 2 kt of water doped with a 0.2 % concentration of Gadolinium salt, leading to a 0.1 % concentration of Gadolinium. The detector is also partially surrounded with a magnetised iron muon range detector (MRD) located at the downstream part of the tank, to detect muons exiting that region of the tank.

Figure 2.5 shows the ratio of the flux at different baselines for TITUS and the flux at Hyper-K, where it can be seen that the flux at $\sim$ 2 km is very similar to that at Hyper-K. Due to being located much closer to the beam source, where the beam is not well approximated as a point source like it is at the distance of Hyper-K and TITUS, the ND280 detectors do not measure a flux as similar to that expected at Hyper-K. Additionally, the water target of TITUS will help reduce systematic errors that are difficult to constrain using ND280 due to the differing nuclei of neutrino interaction targets at ND280 compared to Hyper-K.

The design of TITUS has been under continual development, with the baseline design, shown in Figure 2.6 used for the work of this thesis: The 23 m long, 13 m diameter cylindrical tank, aligned with the axis of the beam, consists of a 22 m by 11 m inner detector surrounded by a 1 m outer detector on all but the downstream end of the tank. The downstream end is instead adjacent to the 2 m thick MRD, which covers this entire end of the tank with the additional possibility of a 7 m by 4 m side-MRD covering a portion of the barrel of the tank. The ID is surrounded by a 30 % photocoverage of 12″ PMTs. An alternative possibility is the use of multi-PMT (mPMT) modules, similar to those used by KM3NeT [73], allowing for finer granularity and additional directional information to aid in reconstruction.

Due to the size of TITUS, around 18 % of the muons coming from beam neutrino interactions escape the tank. These muons come from neutrinos in the higher end of the spectrum. It is therefore important to quantify their energy after they ranged out of the detector to help in understanding the high energy background. A Magnetised Muon Range Detector (MRD) with magnetic field of 1.5 T can provide energy and charge reconstruction. Figure 2.7 shows the charge reconstruction efficiency dependent on neutrino energy. Combined with the neutron tagging this could give very high purity samples as well as providing a method for validating and calibrating the neutron tagging.

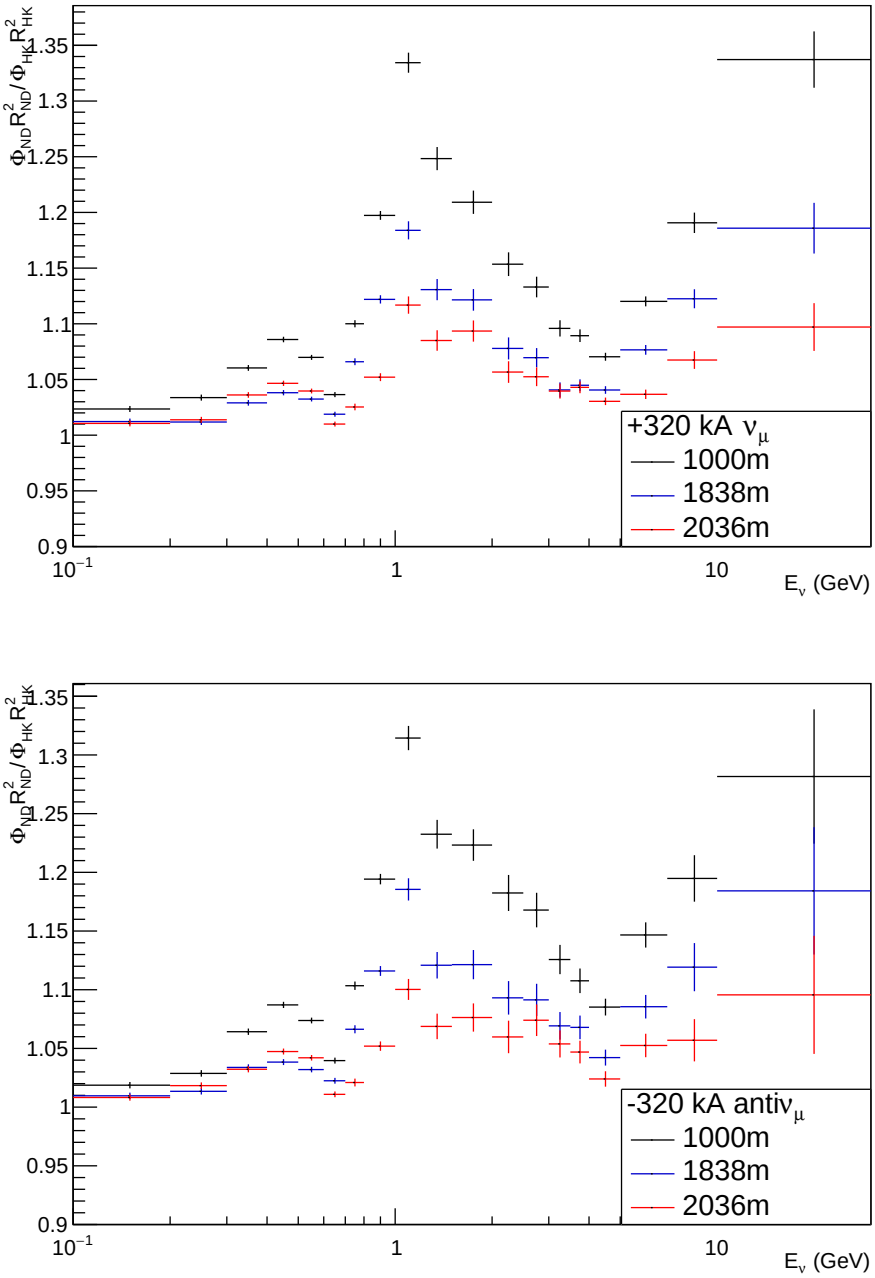

Figure 2.5: Unoscillated flux ratios (Near Detector / Nominal Hyper-K) at baselines of 1000 m, 1828 m, and 2036 m, for ν_μ with neutrino enhanced beam (top) and $\bar{\nu}_\mu$ with antineutrino enhanced beam (bottom) [71].

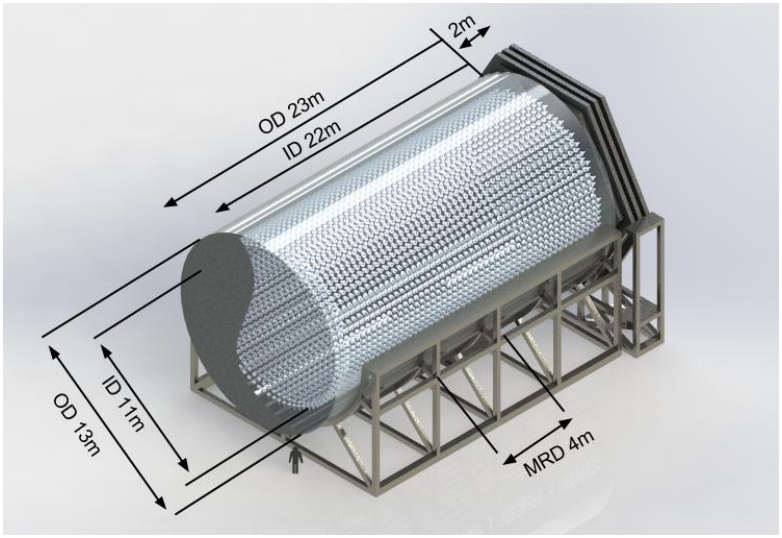

Figure 2.6: The TITUS detector [71].

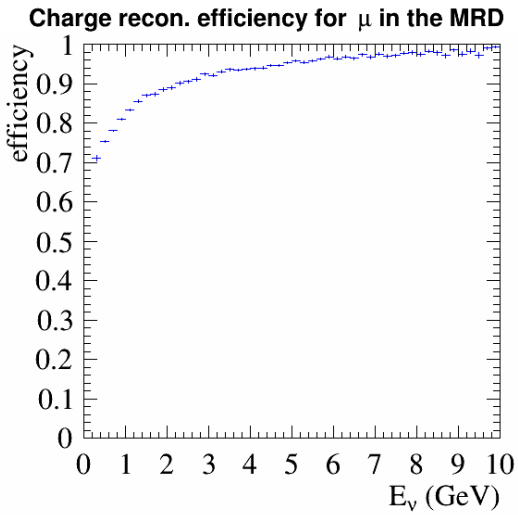

Figure 2.7: MRD charge reconstruction efficiency for muons coming from the interaction of the neutrinos within the tank [71].

Chapter 3 covers the development of the reconstruction software used for this detector and the results of its use in producing neutron-tagged measurements of the unoscillated flux for Hyper-K.

2.4.2 The E61 detector

The E61 experiment [17] is the result of the merging of the TITUS and νPRISM [72] collaborations, combining features of both previous detector designs into a unified approach to the IWCD of Hyper-K.

Like the TITUS detector design, the E61 design is planned to have Gadolinium doping for the detection of neutrons through neutron capture. However, sensitivity studies with the IWCD designs found that the ν_e cross section was the key measurement, being more crucial to measurements at Hyper-K than the ν_μ cross-sections. For this reason, the E61 detector does not include the muon range detector, instead focusing on features of the νPRISM detector designed to optimise the ν_e cross-section measurements.

The novel feature of the νPRISM detector, included also in the E61 detector, is to span a range of off-axis angles, allowing measurements of beam neutrinos over a range of energy spectra. A linear combination of measurements at different off-axis angles can then be combined to effectively produce measurements for a desired energy spectrum, such as the expected flux observed at the far detector, or a gaussian shaped flux centred around some energy of interest. The ability to detect interactions with a tuneable flux also provides additional information to use in developing cross-section models. Additionally, at higher off-axis angles, the ν_e proportion of the flux relative to ν_μ increases, allowing for a more precise measurement of the ratio of ν_e to ν_μ cross-sections – a significant source of uncertainty for $\nu_\mu \rightarrow \nu_e$ appearance measurements.

The current design for phase-1 of the detector, used in the work in Chapter 4, is for a cylindrical tank, vertically oriented, with the ability to be raised and lowered using an elevator in order to cover a range of off-axis angles spanning 1° to 4°, located 1 km from the beam source. The detector itself consists of an inner detector of height 10.42 m and radius 3.71 m, surrounded by 832 multi-PMT modules, each containing 19 inward facing 3″ PMTs, and an outer detector surrounding the ID by 1 m on all sides. This tank would be situated at various depths in a pit, with the volume beneath the OD filled with pure water and the volume between the top of the OD up to the surface also filled with up to 6 m of water (and any remaining volume above this water filled with air). The total depth of the pit below the surface is 57 m, with the seven vertical positions specified as being centered at the off-axis angles of 1.24°, 1.66°, 2.08°, 2.5°, 2.92°, 3.34° and 3.76°. These positions are shown in Figure 2.8.

2.5 Physics potential

In this section the physics programme of Hyper-K is detailed along with the projected sensitivities of the planned measurements. While the focus is on the neutrino beam programme of Hyper-K, a brief overview is also given for two of the other significant physics goals; the atmospheric neutrino oscillation analysis and nucleon decay search. The vastly increased volume of the Hyper-K detector also allows for a wide range of

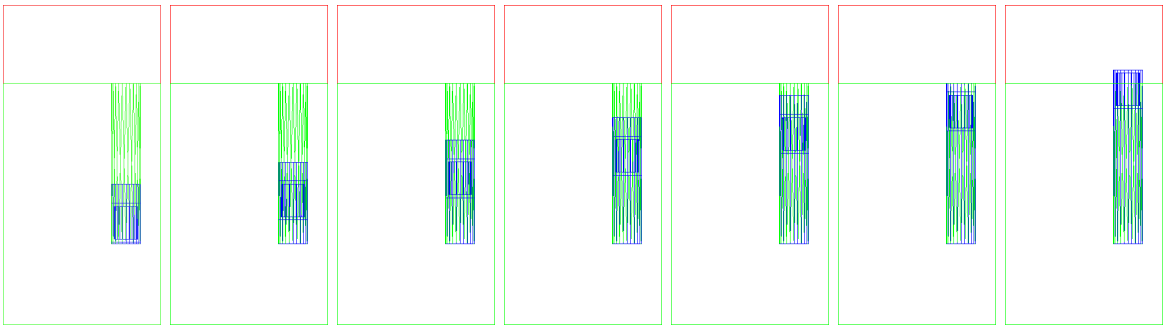

Figure 2.8: The seven off-axis positions of the E61 detector, centered about 1.24°, 1.66°, 2.08°, 2.5°, 2.92°, 3.34° and 3.76°, shown from left to right. Volumes filled with water (ID, OD and any water above or below the OD) are shown in blue.

new or improved measurements in other areas of neutrino physics not covered here [17], including observations of solar, supernova and other astrophysical neutrinos, indirect dark matter searches, and neutrino geophysics.

2.5.1 Neutrino oscillation physics

In the past two decades, all three neutrino mixing angles and the magnitude of both mass-squared differences (and the sign of one of them) have been successfully measured [51]. The last remaining parameter is the CP violating phase δ, which up until recently was entirely unknown and has still had no value excluded above around the $4\,\sigma$ level, even in global fits combining data from all neutrino oscillation experiments [74]. The key goal of the neutrino beam programme of Hyper-K is to perform the first precision measurement of this parameter, allowing the potential for discovery of CP-violation in the lepton sector. The combination with observations of atmospheric neutrino oscillations will make possible measurements of the atmospheric mixing parameters – θ_{23}, including its octant, and Δm^2_{32}, including its sign – and improved measurements of the solar mixing parameters will be possible through observations of the ^{8}B solar neutrinos.

2.5.1.1 Beam neutrinos

The measurement of δ will be achieved through studying the oscillation of muon neutrinos, produced using the J-PARC accelerator, into electron neutrinos detected at Hyper-K. This is known as the $\nu_\mu \rightarrow \nu_e$ appearance channel. After including the matter effect,

the oscillation probability is given by [75]

$$
\begin{aligned}
P(\nu_\mu \to \nu_e) =& 4c_{13}^2 s_{13}^2 s_{23}^2 \left(1 + \frac{2a}{\Delta m_{31}^2}(1 - 2s_{13}^2)\right) \sin^2 \frac{\Delta m_{31}^2 L}{4E_\nu} \\
&+ 8c_{13}^2 s_{12} s_{13} s_{23} (c_{12} c_{23} \cos\delta - s_{12} s_{13} s_{23}) \cos \frac{\Delta m_{32}^2 L}{4E_\nu} \sin \frac{\Delta m_{31}^2 L}{4E_\nu} \sin \frac{\Delta m_{21}^2 L}{4E_\nu} \\
&- 8c_{13}^2 s_{13}^2 s_{23}^2 \frac{aL}{4E}(1 - 2s_{13}^2) \cos \frac{\Delta m_{32}^2 L}{4E_\nu} \sin \frac{\Delta m_{31}^2 L}{4E_\nu} \\
&+ 4s_{12}^2 c_{13}^2 (c_{12}^2 c_{23}^2 + s_{12}^2 s_{23}^2 s_{13}^2 - 2c_{12} c_{23} s_{12} s_{23} s_{13} \cos\delta) \sin^2 \frac{\Delta m_{21}^2 L}{4E_\nu} \\
&- 8c_{13}^2 c_{12} c_{23} s_{12} s_{13} s_{23} \sin\delta \sin \frac{\Delta m_{32}^2 L}{4E_\nu} \sin \frac{\Delta m_{31}^2 L}{4E_\nu} \sin \frac{\Delta m_{21}^2 L}{4E_\nu},
\end{aligned}
\tag{2.5.1}
$$

with the replacements $\delta \to -\delta$ and $a \to -a$ for the probability for antineutrinos.

The location of the far detector and peak of the neutrino energy spectrum are chosen such that the value of L/E_ν corresponds to the first maximum of this oscillation probability. Maximising the oscillation probability in this way optimises the sensitivity to the parameters in Equation (2.5.1).

The final term in Equation (2.5.1) contains $\sin\delta$ and so is sensitive to the sign of δ, which modifies the probability for neutrinos and antineutrinos. This will allow Hyper-K to determine the value of δ by combining measurements of the electron neutrino appearance rates when the unoscillated beam is formed mostly of muon neutrinos and when it is mostly muon antineutrinos. As in the two neutrino mixing case described in Section 1.1.2, the sign of the terms containing $a = 2\sqrt{2} G_F n_e E_\nu$ will also differ for neutrinos and antineutrinos, creating an asymmetry between neutrinos and antineutrinos that is not directly CP violating and not related to δ. The sign of these terms is also changed depending on the mass ordering, which is the effect that enables the mass ordering to be determined through observations of atmospheric neutrino oscillations.

By measuring accurately the unoscillated neutrino flux at near detectors and the oscillated flux at the far detector, then the value of δ is determined by fitting to Equation (2.5.1).

Additional information is available from the $\nu_\mu \to \nu_\mu$ disappearance channel, governed by the survival probability

$$
P(\nu_\mu \to \nu_\mu) \simeq 1 - 4c_{13}^2 s_{23}^2 [1 - c_{13}^2 s_{23}^2] \sin^2 \frac{\Delta m_{32}^2 L}{4E\nu}. \tag{2.5.2}
$$

With the approximation of $c_{13}^2 = 1$, this becomes

$$
P(\nu_\mu \to \nu_\mu) \simeq 1 - 4\cos^2 2\theta_{23} \sin^2 \frac{\Delta m_{32}^2 L}{4E\nu}, \tag{2.5.3}
$$

which has a degeneracy in θ_{23} (the octant degeneracy) either side of the maximal mixing value of $\theta_{23} = 45°$. This means that while the measurement of $\nu_\mu \to \nu_\mu$ disappearance provides information on the value of θ_{23}, using this information alone it is difficult to

determine the octant. However, the appearance measurement above is also sensitive to $\sin^2 2\theta_{13}s^2_{23}$ and short-baseline reactor experiments have provided very precise measurements of $\sin^2 2\theta_{13}$. The combination of these measurement can therefore provide sensitivity on the octant of θ_{23}.

Sensitivity to the mass ordering in long-baseline neutrino beam experiments can come from two complementary places. The first is due to the matter effect, as described above and in Section 1.1.2, however at Hyper-K this effect is expected to be relatively small. The second is through comparison between reactor neutrino experiments' measurements of

$$\Delta m^2_{ee} = c^2_{12}\Delta m^2_{31} + s^2_{12}\Delta m^2_{32} \tag{2.5.4}$$

with a ν_μ disappearance measurement of [76, 77]

$$\Delta m^2_{\mu\mu} = s^2_{12}\Delta m^2_{31} + c^2_{12}\Delta m^2_{32} + \cos\delta s_{13}\sin 2\theta_{12}\tan\theta_{23}\Delta m^2_{21}. \tag{2.5.5}$$

Determining the mass ordering through this comparison is challenging, requiring very low uncertainties on both measurements.

In order to perform these measurements, samples are produced of CCQE-like events with either e-like or μ-like rings for the appearance and disappearance samples observed in the far detector. The reconstructed neutrino energy can be calculated assuming the events are CCQE interactions, using a version of Equation (1.2.1) which includes corrections for the average nucleon binding energy V, given for neutrino interactions on neutrons by

$$E^{\text{rec}}_\nu = \frac{2(m_n - V)E_l + m^2_p - (m_n - V)^2 - m^2_l}{2(m_n - V - E_l + p_l\cos\theta)}. \tag{2.5.6}$$

These samples, together with measurements at the near detector to determine the unoscillated flux and interaction cross-sections, can then be fitted to the oscillation formulae to determine the oscillation parameters.

The expected signal and background rates and reconstructed neutrino energy spectra for the appearance channel are given in Table 2.1 and Figure 2.9, with those for the disappearance channel given in Table 2.2 and Figure 2.10. Figure 2.11 shows the different appearance rates as the value of δ changes, showing how this measurement will allow the determination of the value of δ.

The main systematic errors for these measurements come from uncertainties on the incoming neutrino flux estimate, neutrino interaction cross-sections, and far detector efficiency and reconstruction. The first two of these are constrained directly through measurements at the near and intermediate detectors. The far detector uncertainties are constrained mainly through the use of atmospheric neutrino control samples and the calibration systems of the detector. Table 2.3 summarises the expected systematic uncertainties in observed event rate.

		Signal		Background						
		$\nu_\mu \to \nu_e$	$\overline{\nu}_\mu \to \overline{\nu}_e$	ν_μCC	$\overline{\nu}_\mu$CC	ν_eCC	$\overline{\nu}_e$CC	NC	Total	Total
ν mode	Events	1643	15	7	0	248	11	134	400	2058
	Eff. (%)	63.6	47.3	0.1	0.0	24.5	12.6	2.4	1.6	—
$\overline{\nu}$ mode	Events	206	1183	2	2	101	216	196	517	1906
	Eff. (%)	45.0	70.8	0.03	0.02	13.5	30.8	1.6	1.6	—

Table 2.1: Expected number of event candidates selected in the $\nu_\mu \to \nu_e$ and $\overline{\nu}_\mu \to \overline{\nu}_e$ appearance channels at Hyper-K [17]. Rates are for 13×10^7 MW s, corresponding to 2.7×10^{22} POT from the 30 GeV proton beam, assuming normal mass hierarchy, $\sin^2 2\theta_{13} = 0.1$, $\sin^2 \theta_{23} = 0.5$ and $\delta = 0$.

		ν_μCCQE	ν_μCC non-QE	$\overline{\nu}_\mu$CCQE	$\overline{\nu}_\mu$CC non-QE	$\nu_e + \overline{\nu}_e$ CC	NC	$\nu_\mu \to \nu_e$	Total
ν mode	Events	6043	2981	348	194	6	480	29	10080
	Eff. (%)	91.0	20.7	95.6	53.5	0.5	8.8	1.1	—
$\overline{\nu}$ mode	Events	2699	2354	6099	1961	7	603	4	13726
	Eff. (%)	88.0	20.1	95.4	54.8	0.4	8.8	0.7	—

Table 2.2: Expected number of event candidates selected in the $\nu_\mu \to \nu_\mu$ and $\overline{\nu}_\mu \to \overline{\nu}_\mu$ disappearance channels at Hyper-K [17], under the same assumptions as for Table 2.1.

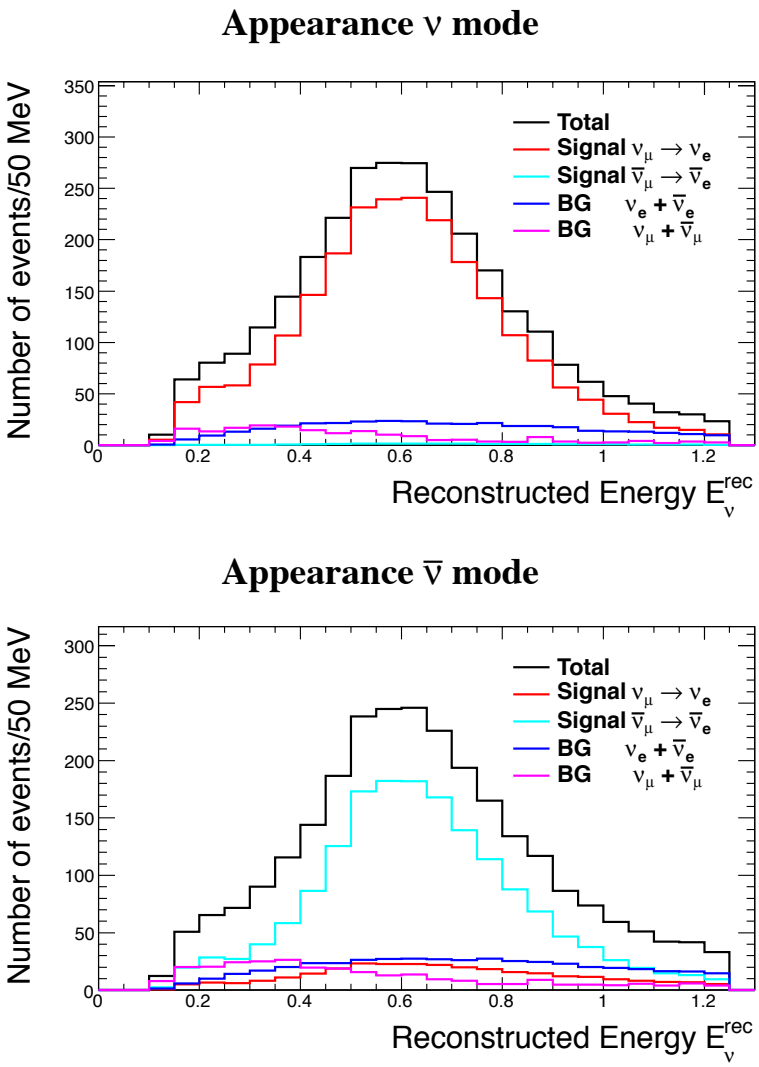

Figure 2.9: Reconstructed neutrino energy spectra for the $\nu_\mu \to \nu_e$ (top) and $\overline{\nu}_\mu \to \overline{\nu}_e$ (bottom) appearance channels at Hyper-K [17].

For Hyper-K running for a total of 1×10^8 s with a beam power of 1.3 MW, the value of δ is expected to be determined with a precision of 7.2° at $\delta = 0°$ or 180° and a precision of 23° at $\delta = \pm 90°$, under the assumption that the mass ordering has been determined. This will allow the observation of CP violation for 76 % of possible values of δ at $3\,\sigma$ and 57 % of values at $5\,\sigma$. Measurements of the other oscillation parameters will include determining $\sin^2\theta_{23}$ with a precision of 0.017 at $\sin^2\theta_{23} = 0.5$ or of 0.006 at $\sin^2\theta_{23} = 0.45$, and determining $|\Delta m^2_{32}|$ with an uncertainty of less than 1 %. These sensitivities of the beam programme of Hyper-K will be explored in detail in Chapter 5.

2.5.1.2 Atmospheric neutrinos

Atmospheric neutrinos provide a flux of ν_μ (before oscillations) covering a wide range of energies from 100 MeV to 10 GeV, having travelled a distance varying with zenith angle. Unlike the $\nu_\mu \to \nu_e$ appearance from beam neutrinos, the longer distance for

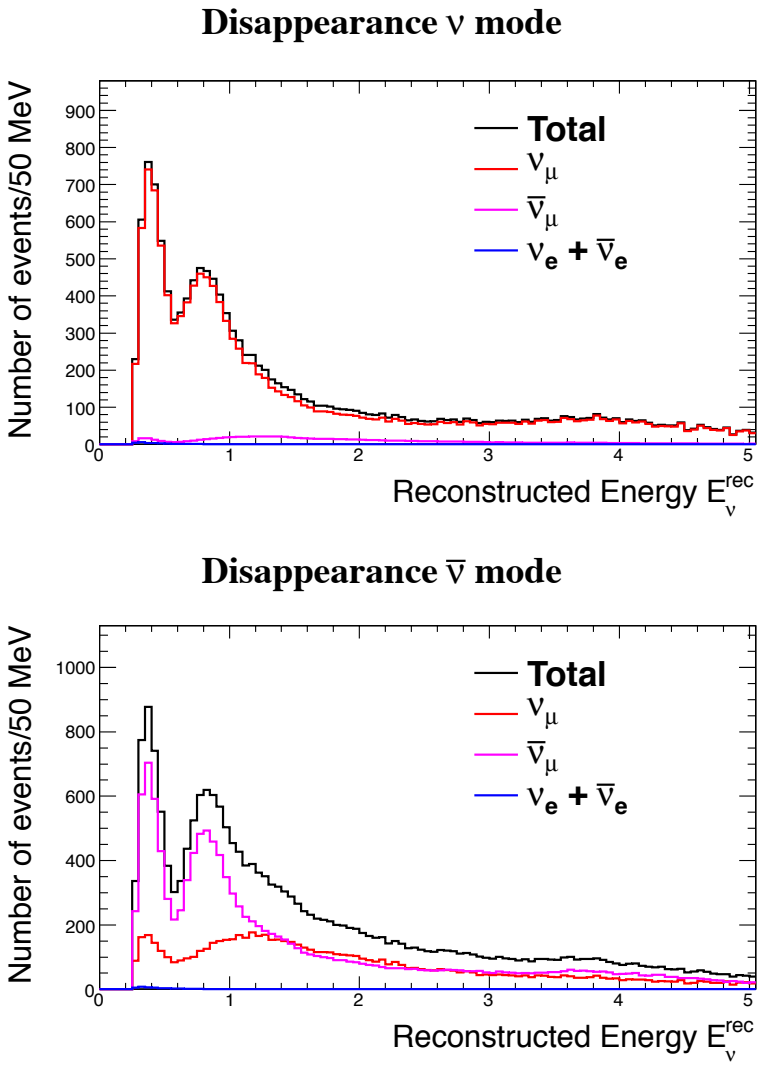

Figure 2.10: Reconstructed neutrino energy spectra for the $\nu_\mu \to \nu_\mu$ (top) and $\overline{\nu}_\mu \to \overline{\nu}_\mu$ (bottom) disappearance channels at Hyper-K [17].

	ν mode		$\overline{\nu}$ mode	
	Appearance	Disappearance	Appearance	Disappearance
Flux & ND-constrained cross-section	3.0 %	3.3 %	3.2 %	3.3 %
Flux ND independent cross-section	0.5 %	0.9 %	1.5 %	0.9 %
Far detector	0.7 %	1.0 %	1.5 %	1.1 %
Total	3.2 %	3.6 %	3.9 %	3.6 %

Table 2.3: Systematic errors on the expected number of events at Hyper-K [17].

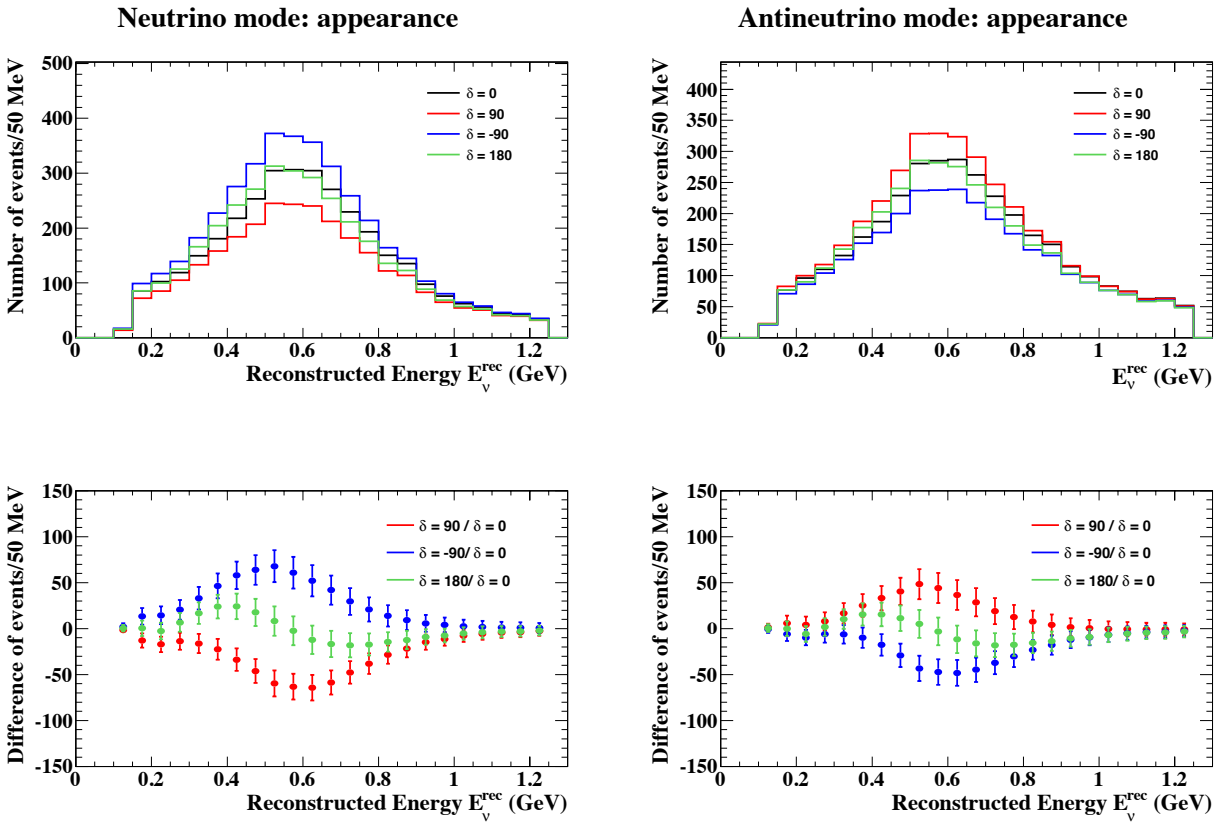

Figure 2.11: Reconstructed neutrino energy spectra for the $\nu_\mu \to \nu_\mu$ (top) and $\overline{\nu}_\mu \to \overline{\nu}_\mu$ (bottom) appearance channels at Hyper-K, with differing values of δ [17]. The top plots show the rates for the four values $\delta \in \{0°, \pm 90°, 180°\}$ while the bottom two plots show the difference from the $\delta = 0°$ case with error bars representing the statistical errors.

the atmospheric neutrinos which travel through the earth is significantly affected by the matter effect. In addition to characterising the atmospheric neutrino background of other measurements, the key goals of the atmospheric neutrino programme at Hyper-K are measurements of the octant of the atmospheric mixing angle θ_{23} and determining the mass ordering. These measurements are particularly powerful when combined into a joint analysis including the observations of beam neutrinos described above.

While both the atmospheric and beam neutrino observations are of the same types of oscillations, $\nu_\mu \to \nu_e$ appearance, these two measurements are highly complementary. The beam neutrinos have the benefit of having a relatively narrow energy spectrum and a well known baseline; with a well understood L/E_ν this results in the ability to measure θ_{23} with high precision. However, the approximate degeneracy in the octant of θ_{23} described above, and the approximate degeneracy between the octant and the mass ordering, mean that these two properties of the oscillations are difficult to determine through beam neutrino observations alone. Atmospheric neutrinos, on the other hand, have a wide range of energies and direction dependent baseline, as well as significant contributions from the matter effect. This range of energies and baselines, providing additional data points in measurements of the oscillations, and the matter effect giving sensitivity to the mass ordering, allow the degeneracy to be broken. By performing a combined fit to the atmospheric neutrino data with the beam neutrino data described above, sensitivity to the mass ordering and octant can be dramatically improved over that of atmospheric or beam neutrinos alone. Figure 2.12 shows the projected sensitivities of the combined analysis to reject the wrong θ_{23} octant and to reject the wrong mass ordering, as a function of experimental run time, and Table 2.4 gives the expected sensitivities comparing the atmospheric only analysis to the combined beam and atmospheric analysis.

	Octant		Mass ordering	
True value of $\sin^2\theta_{23}$	0.45	0.55	0.40	0.60
Atmospheric analysis	$2.2\,\sigma$	$1.6\,\sigma$	$2.2\,\sigma$	$4.9\,\sigma$
Combined analysis	$6.2\,\sigma$	$3.6\,\sigma$	$3.8\,\sigma$	$6.2\,\sigma$

Table 2.4: Expected sensitivities of the atmospheric neutrino only analysis and of a combined beam and atmospheric neutrino analysis for rejecting the wrong octant of θ_{23} and wrong mass-ordering after 10 years [17].

2.5.2 Nucleon decay

Another of the main physics goals of Hyper-K is the search for currently unobserved nucleon decays. Proton decay is predicted by many theories beyond the Standard Model [78], but has so far remained undiscovered with the best limits in many channels coming from Super-K [51]. With the number of protons within the Hyper-K tank an order of magnitude more than Super-K, Hyper-K is expected to be able to probe the lifetime of the proton to an order of magnitude larger than Super-K has.

The main channels for the proton decay search at Hyper-K are $p \to e^+\pi^0$ and $p \to \overline{\nu}K^+$, although the experiment will also be sensitive to a large number of other modes. For

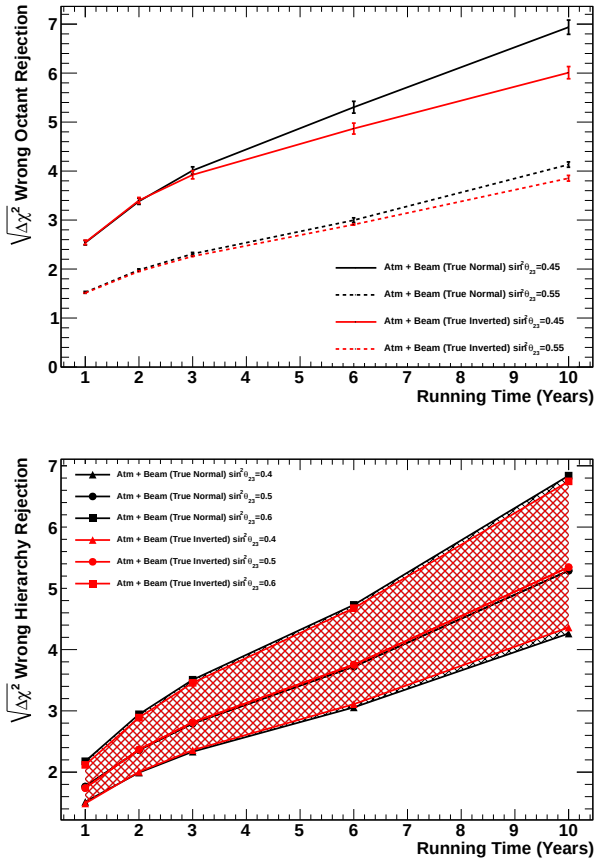

Figure 2.12: Projected sensitivities of a combined beam and atmospheric neutrino analysis for rejecting the wrong octant of θ_{23} (top) and wrong mass-ordering (bottom), as a function of experimental run-time, for different true values of $\sin^2\theta_{23}$ [17]. Blue lines correspond to the true normal ordering case and red lines to true inverted ordering.

both of these decay modes, as well as many others, the main background is dominated by atmospheric neutrino interactions. For example, for $p \to e^+\pi^0$, neutrino interactions can produce the exact same final state or other final states with the same event topology: one Cherenkov ring for the e^+ and two (which may overlap into one) for the π^0. The main method for reducing this background is to reconstruct the proton's invariant mass from the kinematics of the observed outgoing particles, however further reduction can be achieved through neutron tagging; neutrino interactions are significantly more likely than proton decays to include a neutron in the final state.

The sensitivity for various nucleon decay modes are given in Table 2.5, along with the current limits from Super-K.

	Partial lifetime [10^{34} years]	
Mode	Sensitivity (90 % CL)	Current limit
$p \to e^+\pi^0$	7.8	1.6
$p \to \overline{\nu}K^+$	3.2	0.7
$p \to \mu^+\pi^0$	7.7	0.77
$p \to e^+\eta^0$	4.3	1.0
$p \to \mu^+\eta^0$	4.9	0.47
$p \to e^+\rho^0$	0.63	0.07
$p \to \mu^+\rho^0$	0.22	0.06
$p \to e^+\omega^0$	0.86	0.16
$p \to \mu^+\omega^0$	1.3	0.28
$n \to e^+\pi^-$	2.0	0.53
$n \to \mu^+\pi^-$	1.8	0.35

Table 2.5: Sensitivity of Hyper-K to various nucleon decay modes for 1.9 Mt · year exposure [17] and the current limits from Super-K [79–81].

Chapter 3

Intermediate detector event simulation, reconstruction and selection

Introduction

The neutrino interaction event generation, detector simulation and event reconstruction for the detectors of Hyper-K are an essential part of the software used for any physics analysis. For a neutrino oscillation analysis, the energy and type of the incoming neutrino must be determined in order to measure the values of the oscillation parameters, due to the oscillation probabilities' dependence on all of these inputs. The interaction position, timing and direction are also required to identify neutrinos originating from the beam and separate these from interactions from other sources. For experiments in the design and development stage, such as Hyper-K, the simulation and reconstruction software is required to determine its potential physics sensitivity and guide decisions on the experiment's design.

This chapter details the development of simulation and reconstruction software for the TITUS intermediate detector, and its use in determining the detector's capabilities. Existing event generators can be used for events in both the near and far detectors of Hyper-K, however at the time of this analysis the existing detector simulation and reconstruction software used for the Hyper-K detector itself was not suitable for TITUS. The simulation package, WCSim, did not have a working implementation of the Gadolinium doped water for neutron capture, and the reconstruction package, fiTQun, requires a significant amount of hand-tuning to a particular detector configuration which has not been completed for the TITUS detector. For the development of the detector design, the software described and used in this chapter had the additional requirements of being fast and simple to run for different tank designs, photodetector types and coverages, while these properties had not been fully determined.

The detector simulation software WChSandBox, developed for the ANNIE Gadolinium-doped water Cherenkov detector [60], was used for the simulation of events in TITUS. Since no existing suitable reconstruction software was available, a new reconstruction package was been developed as part of this work, for use with the WChSandBox simulation package. The simulation and reconstruction for the MRD were both unavailable, and so this part of the detector has not been included in this analysis.

The neutrino event generation and simulation software used for this analysis are described in Section 3.1, followed by the low-energy and high-energy event reconstruction software described in Section 3.2 and Section 3.3, respectively. Section 3.4 then presents the results of event selections developed to optimise the performance of the reconstruction and sample efficiency and purity.

3.1 Monte-Carlo event generation and detector simulation

The neutrino flux used for event generation was produced by the FLUKA target simulation and JNUBEAM beamline simulation used for the T2K neutrino flux [82]. This is then used for both the GENIE [83] and NEUT [84] Monte-Carlo event generators, however all results shown here have used events generated using NEUT version 5.3.3.

The interaction models used by NEUT are the CCQE model of Benhar [85], the model of Rein and Seghal for coherent pion production [86, 87] and resonance production [88],

with form factors of Graczyk and Sobczyk for resonance decaying to a nucleon and pion [89], and the GRV98 parton distribution function [90] with corrections by Bodek and Yang [91] for DIS. The nuclear model used is the relativistic Fermi gas model.

The detector simulation package WChSandBox uses the GEANT4 framework [92], version 4.9.6, to simulate all particles and processes within the water tank. The simulation starts with the outgoing particles of the initial neutrino interaction, after final state interactions in the nucleus, provided by NEUT. These are then tracked through the detector as they interact, where elastic and inelastic electromagnetic and hadronic scattering and decays, as well as neutron captures the subsequent gamma cascades, are all simulated according to the models of GEANT4. Any charged particles will produce Cherenkov radiation, as discussed in Section 1.2.2, when their speed is above the Cherenkov threshold. The optical photons produced are themselves tracked through the detector, allowing for scattering and reabsorption, until they reach the detector wall. Once the event has been fully simulated, the photons arriving at the detector wall are discarded unless stopped at a position covered by a PMT. The remaining photons have the possibility (according to the PMT's wavelength-dependant quantum efficiency) of being recorded as producing a photoelectron at the PMT's position at a time which is smeared by the PMT's timing resolution. Randomised dark noise can then be added to each PMT, although in these studies dark noise was not included. These final steps, which are dependant on the PMTs' properties and positioning, are completed separately from the rest of the simulation to allow for a single set of simulation results to be used with a number of different configurations of PMT types and coverages.

3.2 Low-energy event reconstruction

All events are initially reconstructed using reconstruction software [93] that has been developed for low-energy events simulated in WChSandBox.

For these events, a basic estimate of the energy of the event is calculated as a simple function of the number of hit PMTs registering at least one photoelectron, where only the photoelectrons occurring within a timing window of 50 ns are included, to ensure that only the hits from the particle of interest are counted.

In order to find this time window, a hit clustering algorithm is first used. The algorithm is the same as that of MiniBooNE [94]: Initially any cluster of at least 10 PMT hits is found, with consecutive hits separated by no more than 10 ns. This cluster is then extended to include as many later hits as possible while requiring that no consecutive two hits are separated by more than 20 ns and that there are not more than two pairs of consecutive hits separated by 10 ns to 20 ns.

The interaction vertex (position and time) of the event is determined using an algorithm similar to that used in SNO [95], where all photons hitting a PMT are assumed to have come from a point source. This assumption combined with the speed of light in water allows the four unknowns of the vertex to be constrained with the time and position of each hit, based on the time of flight from the vertex to the PMT. Four PMT hits are chosen at random and using their positions and times the system of four equations can be solved to find a single candidate vertex. This is repeated for a large number of quadruplets of hits, with the best candidate vertex chosen by taking the solution with

the highest goodness,

$$G = \sum_{i=1,2,3,4} \exp\left(-\frac{(t_i' - t_0)^2}{2\sigma^2}\right), \tag{3.2.1}$$

where σ is the detector timing resolution, t_0 is the reconstructed interaction time and t_i' is the hit timing residual, given by

$$t_i' = t_i - \frac{x_i - x_{\text{reco}}}{c/n_{\text{ref}}} \tag{3.2.2}$$

where t_i is the hit time, $x_i - x_{\text{reco}}$ is the distance from the reconstructed vertex position to the hit PMT, and c/n_{ref} is the speed of light in water. Note that the form of this goodness expression looks similar to a likelihood, but the sum rather than product helps to reduce the impact of outliers, which could occur due to dark noise, for example. Alternative methods of choosing the best vertex, using a likelihood function or the geometric centre of the ensemble of candidate vertices, were also investigated, but found to give poorer performance.

To determine the particle's direction, the unit vectors pointing from the reconstructed vertex to each hit PMT are summed, and the direction of the result is taken as the direction of the particle. Since Cherenkov light is emitted as a cone around the particle's direction, this average direction from the vertex to the point where the light is observed should point to the centre of the ring and give a good approximation of the particle's direction.

The Cherenkov ring's opening angle, determined by Equation (1.2.2), is also reconstructed as this can give information on particle type; the angle of electrons travelling close to c in water will be around 42°, whereas muons will have a smaller angle due to their higher mass. In a similar process to the vertex reconstruction, the angle is reconstructed by choosing three hits at random and solving the system of three equations which describe the opening angle. Repeating this for many triplets of hits gives a distribution of opening angles, which is fitted with a Gaussian whose mean is taken as the reconstructed angle.

3.3 High-energy event reconstruction

A new set of tools has been developed to provide the reconstruction of events where the visible energy is above a threshold of 60 MeV, chosen to exclude the majority of secondary sub-events such as Michel electrons and neutron capture signals. After an event has been reconstructed with the low-energy reconstruction tools described in Section 3.2, if the energy estimate is above 60 MeV, then it is passed to these high-energy reconstruction tools with the results of the low-energy reconstruction used as the seed for the interaction vertex position, direction and energy. In practice this energy threshold simply corresponds to a given number of photoelectrons in the event, since the reconstructed energy from the previous step is a simple function of the number of photoelectrons seen in a window of 50 ns. However, the number of photoelectrons corresponding to the reconstructed energy threshold will vary according to the configuration of PMTs in the detector.

While low energy particles can be approximated as a point source, for high energy particles the non-zero track length must be taken into account, along with the possibility of multiple particles producing Cherenkov rings, to give an accurate reconstruction. The high energy reconstruction consists of first searching for rings in the pattern of PMT hits and identifying which observed photoelectrons (PE) belong to each found ring. Then the timing information of each photoelectron hitting a PMT is used to improve the reconstructed vertex position and direction. The final part of the reconstruction is completed for both a muon and electron hypothesis, using a lookup-based method to determine the energy and a likelihood-based method of particle identification (PID) to determine whether the ring is electron-like or muon-like.

3.3.1 Ring searching

A Hough transform, similar to that used in Super-K [96], is used to search for rings. The algorithm, depicted in Figure 3.1 converts rings imaged on the detector wall into peaks in Hough space by first mapping the PMTs onto a spherical surface and then producing a circle centred around each hit PMT. The center of the ring will be the point where these circles coincide. By filling bins that fall on circles around the hit PMTs, peaks will form corresponding to the centres of any rings.

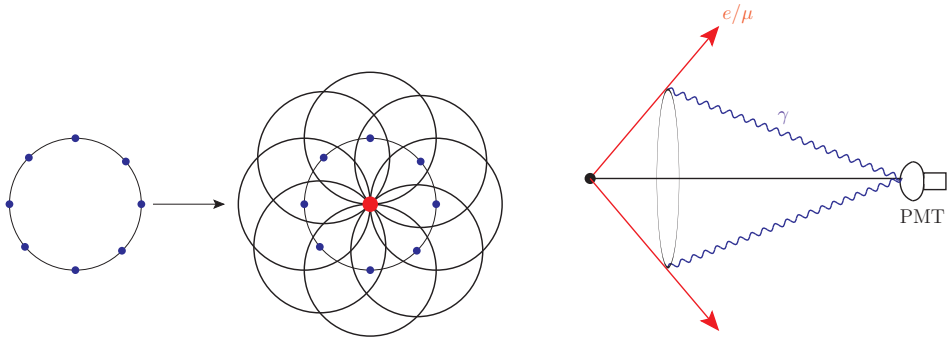

Figure 3.1: Left: Hough transform finds the centre of a ring-shaped pattern of PMT hits by identifying the intersection (red point) of rings drawn around each hit PMT (blue points). Right: Multiple possible track directions can produce a photon arriving at a PMT at a given time and location; the circle drawn around each hit PMT corresponds to the cone formed by these possible tracks.

To implement the Hough transform, the sphere of possible directions of the track must be partitioned into bins. Using regular bins as a histogram in the zenith angle θ and azimuthal angle ϕ results in bins which do not cover an equal solid angle. Correcting for this either by weighting bin contents by the solid angle covered by each bin, or by binning in $\cos\theta$ instead of θ, still leaves the bins unevenly distributed leading to poor performance of the Hough transform. Instead, the sphere is partitioned into bins based on the method of evenly distributing points on a sphere along a spiral [97]. Figure 3.2 shows how this binning provides bins of equal area that are distributed more evenly than other methods. Each bin centre is spaced along the spiral with a fixed change in the z-coordinate between consecutive bins and the rate that the spiral descends along the sphere is chosen so that the number of complete revolutions is equal to the number

of bins around the sphere's equator, to ensure they are evenly distributed and all cover an equal area. The bin in which any given direction (as a pair of θ and ϕ coordinates) is contained is then determined simply by calculating how far along the spiral strip the point falls. This gives this binning scheme the additional advantage of having a single array of bins with a fast and simple filling mechanism, which is not the case for some other regular binning schemes.

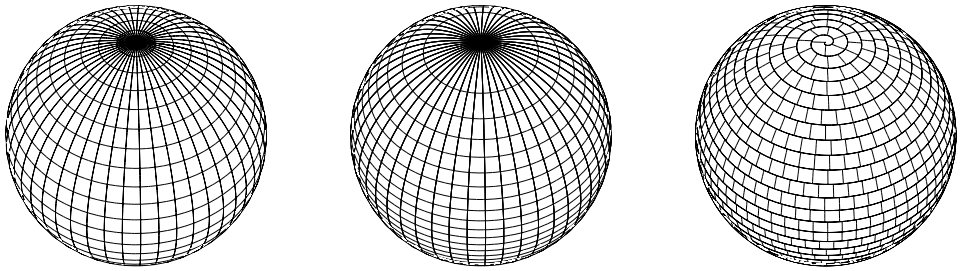

Figure 3.2: Possible ways of partitioning the unit sphere into bins for the spherical Hough transform. Left: Regular binning in the zenith angle θ and azimuthal angle ϕ suffers from unequal sized bins, with a smaller solid angle covered by bins closer to the poles of the sphere. Centre: Correcting for the unequal area by using regular binning in $\cos\theta$ rather than θ ensures all bins cover the same solid angle, but are still unevenly distributed with long and narrow bins at the poles. Right: Using a spiral to distribute points on the sphere and constructing the bins along this spiral gives evenly equal-area bins that are evenly distributed.

Given this binning of the possible directions, the Hough transform proceeds by creating a circle, for each photoelectron, of the possible particle directions that could result in a photon arriving at the PMT at the observed time. The circles are then mapped onto the sphere of possible directions, and the corresponding bins are filled. The radius of these circles is dependant on the angle between the direction of the particle's track and the direction from the interaction vertex and the hit PMT, shown in Figure 3.3. This angle, α, is determined as the solution for the expression for the expected time-of-flight (TOF) t, using the distance d between reconstructed interaction vertex and hit PMT, and the Cherenkov angle θ_C (which is approximated by that of a charged particle travelling through water at c):

$$t = \frac{s_1}{c} + \frac{n_{\text{ref}} s_2}{c} = \frac{d\sin(\theta_C - \alpha)}{c\sin\theta_C} + \frac{n_{\text{ref}} d\sin\alpha}{c\sin\theta_C}, \tag{3.3.1}$$

where n_{ref} is the refractive index. The solution for the angle α is

$$\begin{aligned} \tan\alpha &= \frac{A - B\sqrt{A^2 - B^2 + 1}}{B^2 - A^2}, \\ A &= \frac{n_{\text{ref}} - \cos\theta_C}{\sin\theta_C}, \quad B = \frac{ct}{d}. \end{aligned} \tag{3.3.2}$$

By performing this for a large number of photoelectrons, the bins at the centre of the Cherenkov rings, where the circles of the Hough transform coincide, will have the highest value. The direction of the first Cherenkov ring is therefore taken to be the centre of the highest value bin.

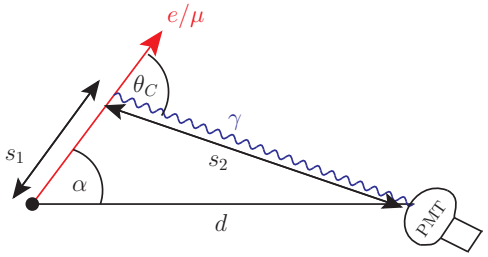

Figure 3.3: The Hough transform and track fit use time-of-flight based on the lepton travelling a distance s_1 before emitting a photon at angle θ_C, which travels distance s_2 before arriving at a PMT located distance d from the interaction vertex at an angle α to the lepton track.

To search for additional rings, photoelectrons are first removed if they are observed at a time consistent with having hit a PMT after being emitted by the particle travelling in the direction of any previously identified ring centres (within twice the PMT's timing resolution). The direction for the next ring is then taken as the bin with highest value after the removal of the photoelectrons from the previously found rings. If the ring is found with at least 9 % as many observed photoelectrons as the first ring then it is considered genuine, if there are fewer than 9 % as many photoelectrons then the ring is discarded and the ring searching process ends. While this simple method of determining which secondary rings to keep and which to discard, using the threshold of 9 %, was found to give acceptable results in these early studies, a more refined approach could be developed by examining the improvement in quality of a fit of all hits to the found rings as each additional ring is added. The remainder of the reconstruction is applied to individual rings, using only the photoelectrons that were identified as belonging to that ring.

3.3.2 Track fit

To improve the reconstructed vertex, the PMT hit timing information is used in a fit taking into account the track length of the particle. The algorithm used is based on that used by Super-K [96] using the goodness test value given by

$$G = \sum_{i \in \mathrm{PE}} \exp\left(-\frac{(t_i' - t_0)^2}{2\sigma^2}\right). \tag{3.3.3}$$

This is the same as Equation (3.2.1) used for the low-energy reconstruction, except that the sum is now over all observed photoelectrons, and $t_i' = t_i - \tilde{t}_i$ is the timing residual determined by the expected total TOF ($\tilde{t}_i$) and PMT hit time (t_i) of the ith observed photoelectron, and t_0 is determined by taking the mean value of the t_i'. Given a candidate vertex, direction and Cherenkov emission angle, the expected TOF for each hit is calculated according to Equation (3.3.1), assuming the lepton travels a distance s_1 at speed c along its track before emitting a photon at the Cherenkov angle θ_C that travels distance s_2 to the centre of the PMT, as shown in Figure 3.3. Maximising G has the effect of making the distribution of timing residuals more sharply peaked when the fitted vertex position and direction are close to the true values. The maximisation

is performed using the MIGRAD algorithm of MINUIT2 [98]. Taking the seed vertex position from the low energy reconstruction and the seed direction from the centre of the bin at the peak of the Hough transform, first the direction is allowed to vary with the position fixed, followed by varying the position with the direction fixed. These steps are iterated twice, with the interaction time and Cherenkov angle allowed to vary throughout.

3.3.3 Energy reconstruction

The energy estimate from the low energy reconstruction becomes less accurate at higher energies and so an improved estimate is required. For this, a simple lookup table is used based on the total number of photoelectrons observed in the PMTs and the reconstructed distance from the interaction vertex to the wall of the tank. For a higher energy particle, the number of photons emitted will increase as per Equation (1.2.3), and the distance to the wall will affect how many of these photons are detected. The energies for a similar number of photoelectrons and distance to the wall will also be different depending on the particle type due to the higher mass of a muon giving a higher Cherenkov threshold than that of an electron. The lookup tables are generated from a Monte-Carlo simulation of CCQE beam events in TITUS. These events are binned according to the number of observed photoelectrons and distance to the wall, taking the mean true charged lepton energy of these events for the given bin, separately for muons and electrons. The reconstructed energy is taken from these tables, linearly interpolated, using the observed number of photoelectrons and reconstructed vertex. An improved energy reconstruction should be possible by including the energy as a free parameter in the likelihood fit described in the next section. An alternative improved energy reconstruction has also been developed, after this study had been completed, using a machine-learning based multivariate analysis [99].

3.3.4 Likelihood fit

To perform the particle identification and to improve on the vertex position and particle direction from the track fit, a likelihood method is used. The method used is similar to those used in SNO [100] and MiniBoone [101]. The likelihoods are constructed from two separate probability distributions; the probability of observing the number of photoelectrons at each PMT and the probability of the time that each photoelectron is observed.

The likelihood values for the number of photoelectrons at each PMT are determined using probability density functions, generated by Monte-Carlo for a given particle type and energy, of the photon emission angle relative to the particle track (Cherenkov angle) and the distance along the track from the interaction vertex to the point of emission. These are then used to calculate the expected number of photons received at any given point, given its distance from the interaction vertex and angle between the particle's track and the line from the interaction vertex to this point. For each PMT together with a candidate vertex position, particle direction, particle type and energy, these geometric quantities are known, which allows the expected number of photoelectrons at the PMT to be looked up directly from these pre-calculated values. The difference for electrons

and muons is clearly seen in these distributions as shown in Figure 3.4. This arises due to a number of physical differences in the Cherenkov process for these particles; muons will travel a reasonable distance emitting photons close to the Cherenkov angle, which closes as the muon loses energy close to the threshold, while an electron will produce an electromagnetic shower, with each electron within the shower travelling in slightly different directions, giving a broader range of effective photon emission angles. Due to the non-Poissonian nature of the number of photoelectrons received at a PMT, it was found that the reconstruction performed better when only using the relative numbers of photoelectrons at each PMT, *i.e.* the expected number of photoelectrons at each PMT is normalised such that the total summed over all PMTs is equal to the observed total. The likelihood is then based on a multinomial distribution, where each photoelectron has a probability of appearing at each PMT, giving the log-Likelihood function for the pattern of PMT hits,

$$\log L_{\text{pattern}} = \sum_{i \in \text{PMT}} n_i \log p_i(x, E, l), \tag{3.3.4}$$

$$p_i(x, E, l) = \frac{\tilde{n}_i(x, E, l)}{\sum_j \tilde{n}_j(x, E, l)}, \tag{3.3.5}$$

where n_i is the observed number of photoelectrons at the ith PMT and p_i is the probability of an observed photoelectron at the ith PMT. The value $\tilde{n}_i(x, E, l)$ is the expected number of photoelectrons observed at a PMT coming from a lepton of type l with track starting at point x with energy E, taken from the pre-calculated lookup table produced by Monte-Carlo simulation. Due to the total number of photoelectrons not contributing to the likelihood fit in this form, the fit is not able to improve on the estimated particle energy since the most significant effect of the energy is on the total number of photoelectrons observed.

The likelihood for the time that a photoelectron is observed at a PMT is calculated using similar look-up tables to those used for the expected total number of photoelectrons observed at a PMT. Again using Monte-Carlo simulation a table is produced of expected arrival times of a photon at a point, given the photon's distance from the interaction vertex and the angle between the particle's track and the line from the interaction vertex to this point. This provides the mean for the probability distribution of the time that a photoelectron is observed in a PMT, which is taken as a Gaussian distribution with $\sigma = 4\,\text{ns} + \sigma_{\text{PMT}}$, where σ_{PMT} is the PMT timing resolution and the value of 4 ns was determined from the standard deviation of the distribution of timing residuals when using the true photon arrival time in simulated events. This gives the log-Likelihood function for the timing of PMT hits given by

$$\log L_{\text{time}} = -\sum_{i \in \text{PE}} \frac{(t_i - t_0 - \tilde{t}_i)^2}{2\sigma^2} \tag{3.3.6}$$

where t_i is the arrival time of the ith photoelectron, t_0 is the reconstructed interaction time and $\tilde{t}_i$ is the expected arrival time.

The total log-Likelihood $\log L = \log L_{\text{pattern}} + \log L_{\text{time}}$ is maximised, while allowing the reconstructed interaction vertex position, time and direction to vary, for both electron and muon hypotheses. This maximisation is completed using the same MIGRAD algorithm of MINUIT2 as for the track fit, and is completed in two minimisation passes;

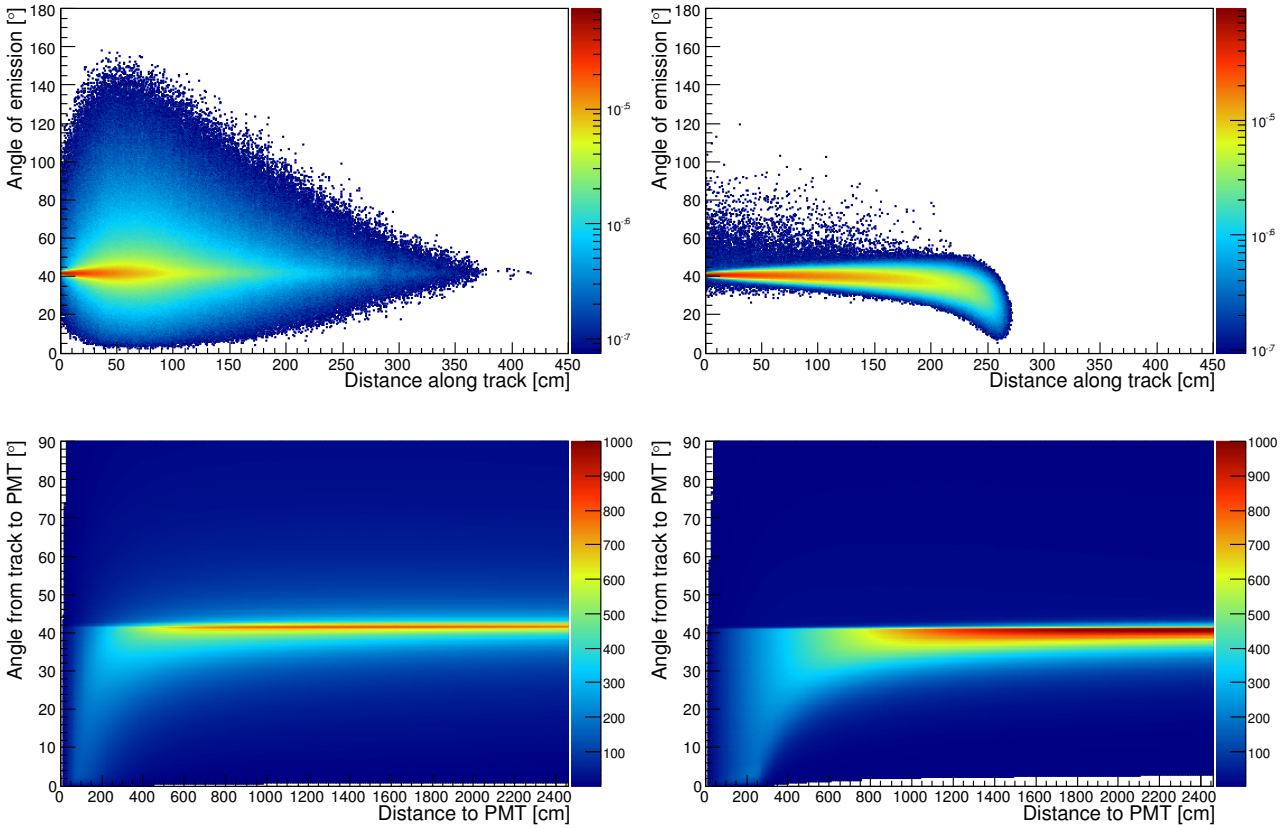

Figure 3.4: Probability density functions for photon emission at a given distance along particle track and angle of emission (top) and expected number of photons received at a PMT given its distance from and angle from the particle track (bottom) for electrons (left) and muons (right) with 600 MeV of kinetic energy.

first the direction is varied together with the interaction time and vertex position only along the track direction, to correct for biases along the track direction, before then also allowing the other components of the vertex position to also be varied in the second pass. The difference between the log-Likelihood value for the electron hypothesis and that of the muon hypothesis is used to discriminate between particle types and the final reconstructed vertex position and direction are taken to be those which maximise the log-Likelihood for the determined particle type.

3.3.5 Performance

The resolutions obtained for the vertex, direction and energy reconstruction are shown in Figure 3.5 with the particle identification performance shown in Figure 3.6, for muons and electrons generated with uniformly distributed random positions at least 1 m within the TITUS tank, isotropically distributed random directions, and kinetic energies of 50 MeV to 2 GeV. At low energies the reconstruction performs poorly, as seen in the three plots of Figure 3.5; this is mainly due to the small number of Cherenkov photons produced. For muons, the vertex reconstruction becomes poor below around 200 MeV, seen in the upper plot of Figure 3.5, and the direction and energy reconstruction fail at around 100 MeV, seen in the middle and lower plot of Figure 3.5. Above 200 MeV, the direction resolution is reasonable to high energies above 2 GeV, however the vertex resolution starts to become worse and energy reconstruction fails above around 1 GeV, resulting in the step-like behaviour of the lower plot of Figure 3.5. This is partly due to the long tracks of higher energy muons resulting in them exiting the tank before depositing the majority of their energy, and partly due to the energy reconstruction lookup tables focusing on the lower energy ranges resulting in inaccuracies from interpolation and extrapolation at higher energies. For those muons which exit the tank into the MRD it should be possible to use the additional information from the MRD to improve the reconstruction. Future improvements to the reconstruction by including the energy as a parameter in the likelihood fit should also improve the reconstruction, particularly at higher energies. For electrons, the resolutions are generally worse, but are stable for a wider range of energies; at low energies, the direction and energy resolutions start to become significantly poorer below around 100 MeV, while all parts of the reconstruction remain reasonable beyond 2 GeV. This is due to the electromagnetic showers depositing all the electron's energy within the tank, even for initially high energy electrons.

3.4 Event Selection

For these studies event selections have been developed for single ring muon and electron events, with binary neutron tagging (no tagged neutrons or at least one tagged neutron). Separate selections are produced for the beam in neutrino-enhanced mode and in antineutrino-enhanced mode. Since the number of interactions seen in TITUS will be dominated by ν_μ ($\bar{\nu}_\mu$) events with the beam in neutrino (antineutrino) mode, generating events according to this distribution would result in a much larger uncertainty on results for the non-dominant flavours. Events are instead generated with an equal number of each of the four neutrino flavours ($\nu_\mu, \nu_e, \bar{\nu}_\mu, \bar{\nu}_e$); 100,000 events of each flavour, for each beam mode, using the expected energy distribution of each respective flavour. The

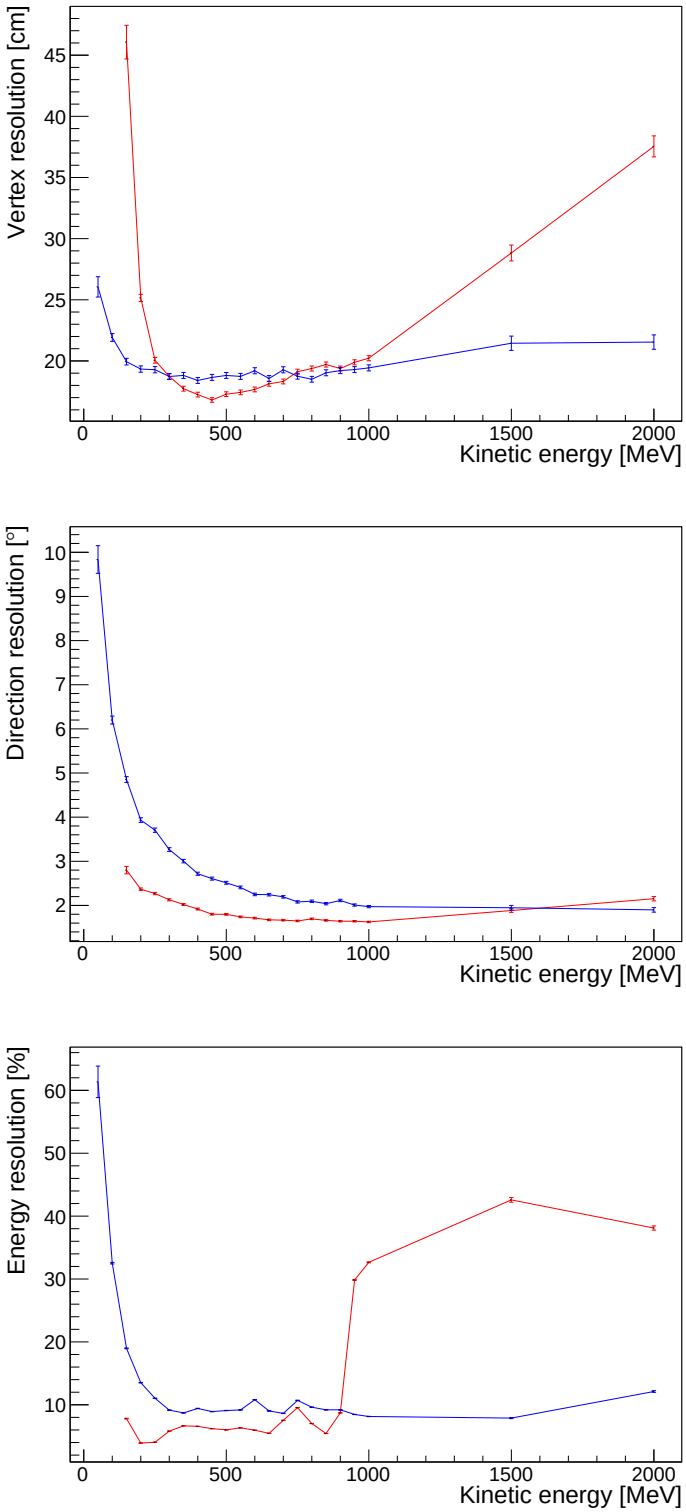

Figure 3.5: Resolutions of the reconstructed vertex position (top), lepton track direction (middle) and kinetic energy (bottom) for muons (red) and electrons (blue) generated at kinetic energies of 50 MeV to 2 GeV for electrons and 150 MeV to 2 GeV for muons.

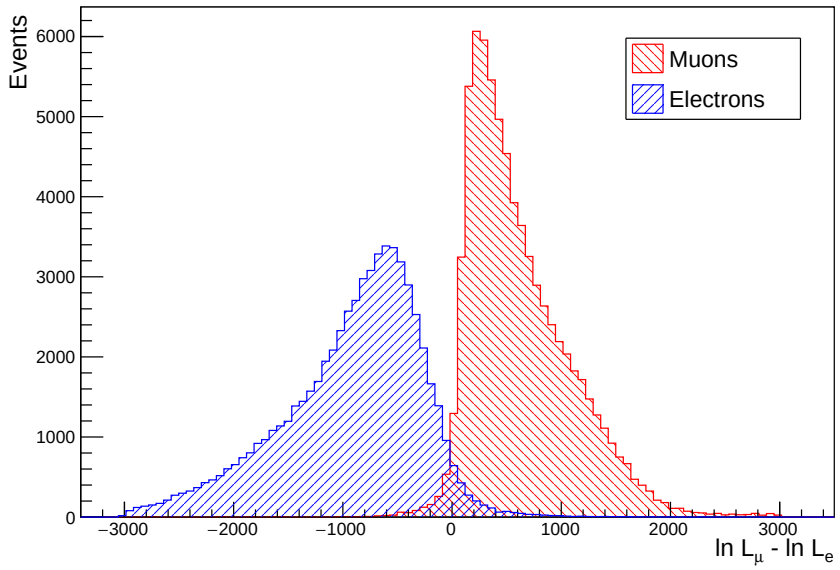

Figure 3.6: Particle identification for muon and electrons simulated in TITUS.

selected events are then normalised according to the correct flavour distribution to give the final selections.

The selection criteria are split into the charged-lepton selection, for selecting events that appear to contain a single muon-like or electron-like ring, and the neutron selection, for tagging those events that appear to contain at least one neutron in the final state.

3.4.1 Charged lepton selection

The primary goal of TITUS is to constrain the flux and interaction cross-sections of neutrinos coming from the J-PARC beam. Understanding both the ν_μ and ν_e flux and cross-section is important for determining their expected rates at Hyper-K, in particular for the $\nu_\mu \rightarrow \nu_e$ appearance measurement used for measuring δ. To achieve this it is important to obtain high-purity samples of CCQE events producing electrons and producing muons, where CCQE events are desired due to the ability to reconstruct the neutrino energy according to Equation (1.2.1). The charged lepton selection criteria have therefore been optimised according to the performance of the reconstructed lepton properties – most importantly the direction and energy, for neutrino energy reconstruction, and the particle identification to ensure high purity – while also considering the different expected fluxes for each flavour to optimize the cuts for the selection efficiency and purity of the flavour that is desired.

For both the muon and electron selections, the event must be identified as having a single Cherenkov ring, according to the ring searching described in Section 3.3.1. This increases the purity of the sample with respect to CCQE events, as other interaction modes may have several outgoing particles above Cherenkov threshold, or hadrons which decay into multiple Cherenkov-producing particles such as a neutral pion decaying to

two gammas, each resulting in an electromagnetic shower containing electrons that will appear as electron-like Cherenkov rings.

After selecting single ring events it is useful to define a fiducial volume within which the selected events must occur, so that events are discarded if they are reconstructed close to the wall of the tank where reconstruction performs poorly. In addition to using the distance between the interaction vertex position and the tank wall (*dwall*), it can also be useful to select events based on the distance the particle would need to travel along its track to reach the wall (*towall*). The effect of these cuts on the reconstruction is shown in Figure 3.7. The vertex reconstruction actually appears slightly worse further from the wall. This is understood to be due to the shorter time of flight from the interaction to the PMTs providing less possibility to vary the vertex position away from this, however the variation is small and the resolutions are reasonable throughout. For all other aspects of the reconstruction, there is significant improvement when excluding events close to the wall, with a *dwall* cut of 1 m sufficient for good reconstruction. Using a *towall* cut, unless very large, does not appear to allow a reduced *dwall* cut, and so only a *dwall* cut has been used for these selections. Figure 3.8 shows how the particle identification also becomes more difficult close to the wall of the tank.

Allowing for the potential need for different cuts for the μ-like and e-like samples, the sample purities and efficiencies are considered when determining the position of the cut for PID, together with the *dwall* cut. In Figures 3.9 and 3.10 it can be seen that when optimising the purity $\times$ efficiency, the loss of the efficiency with any *dwall* cut dominates over any gains in purity. However, from the reduction in reconstruction performance close to the wall noted earlier and the need to reduce backgrounds entering the tank which have not been simulated here, a cut of 1 m has been chosen. For the PID, for both samples the optimal point for purity $\times$ efficiency is to cut the log-likelihood difference at around -200. Since there will be such a small ν_e component of the beam, analyses requiring a higher purity in the e-like sample could use a tighter cut requiring a difference in log-likelihoods that more favours electrons, without too great a loss in efficiency.

In Section 3.3.5, it was seen that the performance of the reconstruction also depends on the lepton energy. Figure 3.11 shows how the vertex resolution varies with the reconstructed lepton and neutrino energy. The other reconstructed variables show similar trends but with a slightly smaller effect. At low energies, if a muon is reconstructed with energy below around 200 MeV or an electron reconstructed with energy below 100 MeV, then these events are cut due to the poor reconstruction. The reconstruction for electrons with energies above around 2 GeV also starts to deteriorate. For muons this is expected to also be the case but, due to these muons often ranging out of the detector before depositing the majority of their energy, their reconstructed energy is lower than the true value and so cutting the high energy muons does not give significant improvement. The reconstructed energy of the neutrino itself, E_ν^{rec}, can also be used, where the reconstruction is poor for ν_μ events with $E_\nu^{\text{rec}} \gtrsim 2\,\text{GeV}$ or for ν_e events with $E_\nu^{\text{rec}} \gtrsim 2.5\,\text{GeV}$. Requiring a lower reconstructed neutrino energy of $E_\nu^{\text{rec}} < 1.25\,\text{GeV}$ for the μ-like selection also significantly reduces the number of non-CCQE and wrong flavour events in the ν_μ ($\bar{\nu}_\mu$) samples when the beam is in neutrino (anti-neutrino) enhanced mode, due to their differing neutrino energy spectra, as seen in Figure 3.12.

The final selection criteria are summarised in Table 3.2, with the resulting resolutions for reconstructed quantities given in Table 3.1. Note that the signal rates for

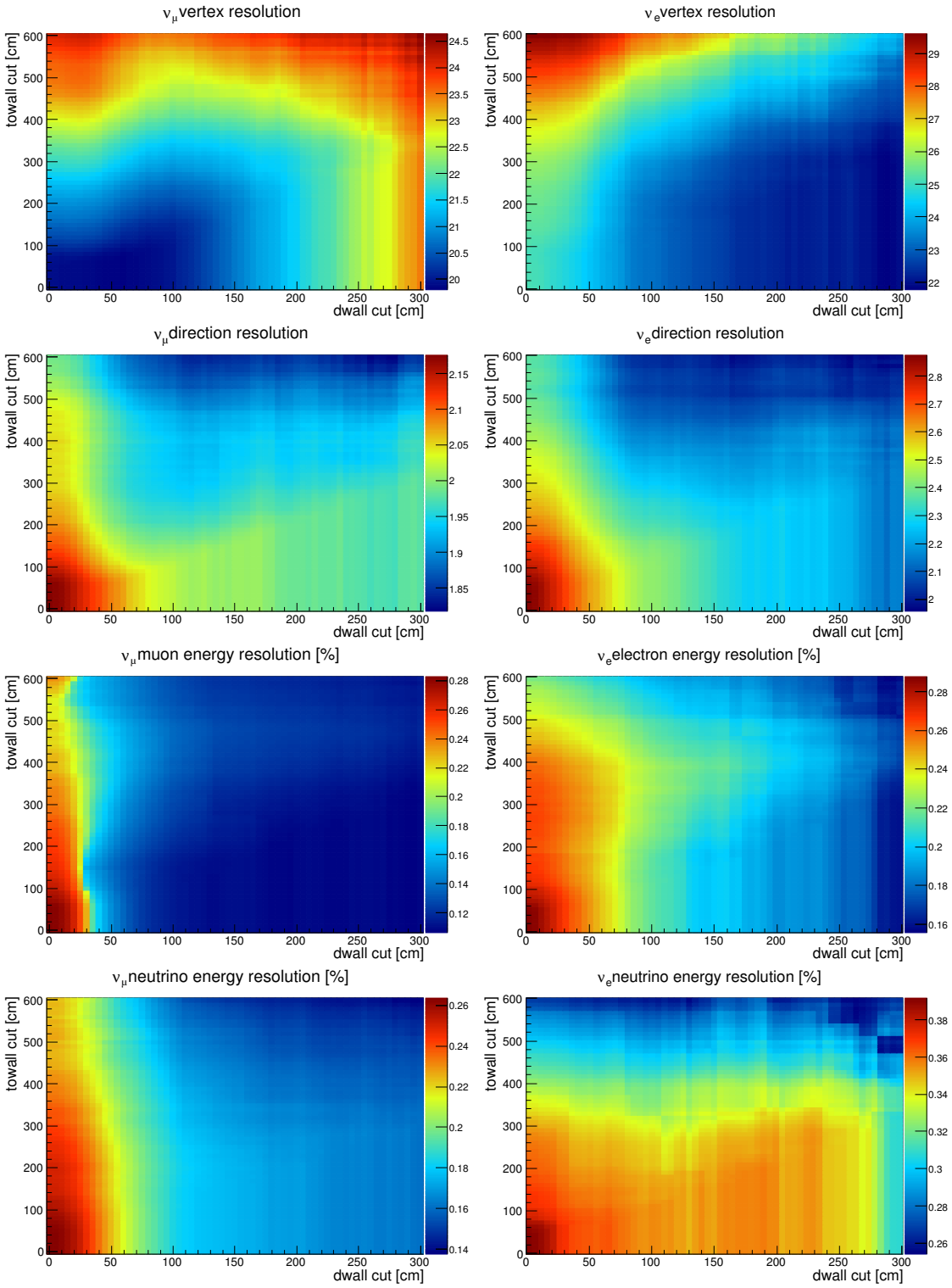

Figure 3.7: Reconstruction performance with varying *towall* and *dwall* cuts for simulated CCQE ν_μ (left) and ν_e (right) beam events in TITUS. In all cases except for the vertex resolution in ν_μ events, the reconstruction performs better when cutting events further from the wall.

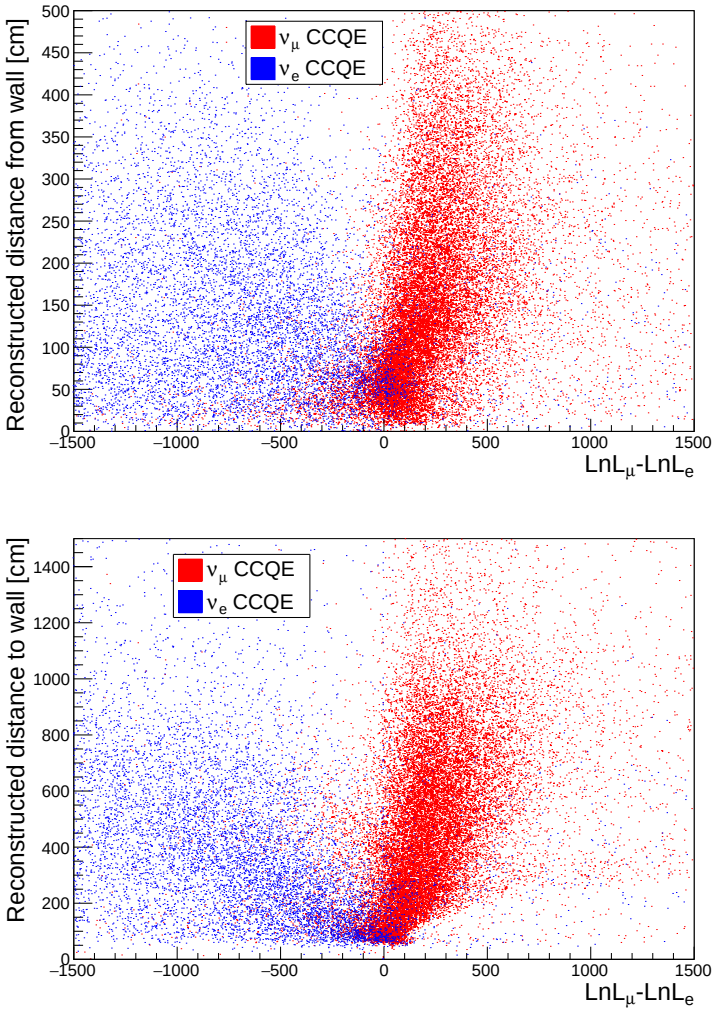

Figure 3.8: The likelihood difference used for particle identification of CCQE ν_μ events (red) and CCQE ν_e events (blue), against the distance from the interaction vertex to the nearest tank wall (top) or distance from the interaction vertex to the tank wall in the track direction (bottom). Close to the wall the two lepton flavours become less clearly separated.

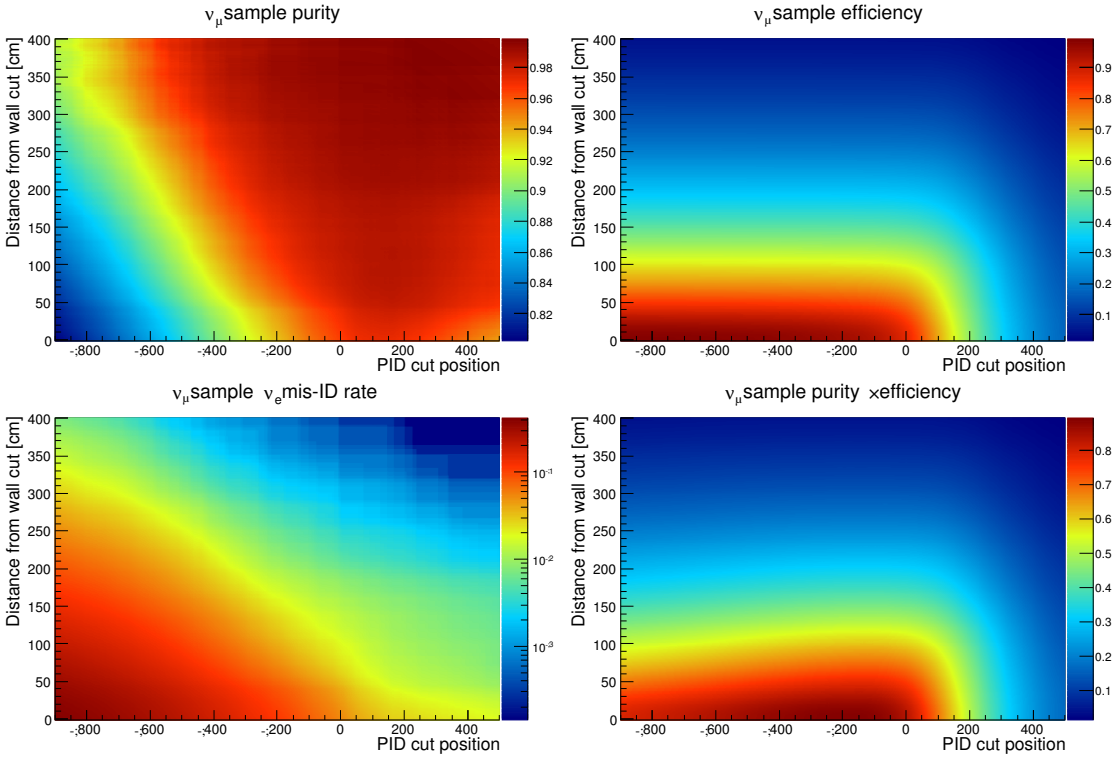

Figure 3.9: For CCQE ν_μ events, the sample purity (top left), efficiency (top right), ν_e mis-ID rate (bottom left) and purity $\times$ efficiency (bottom right), from equal numbers of simulated ν_μ and ν_e beam events, dependant on the position of the *dwall* and PID selection cuts.

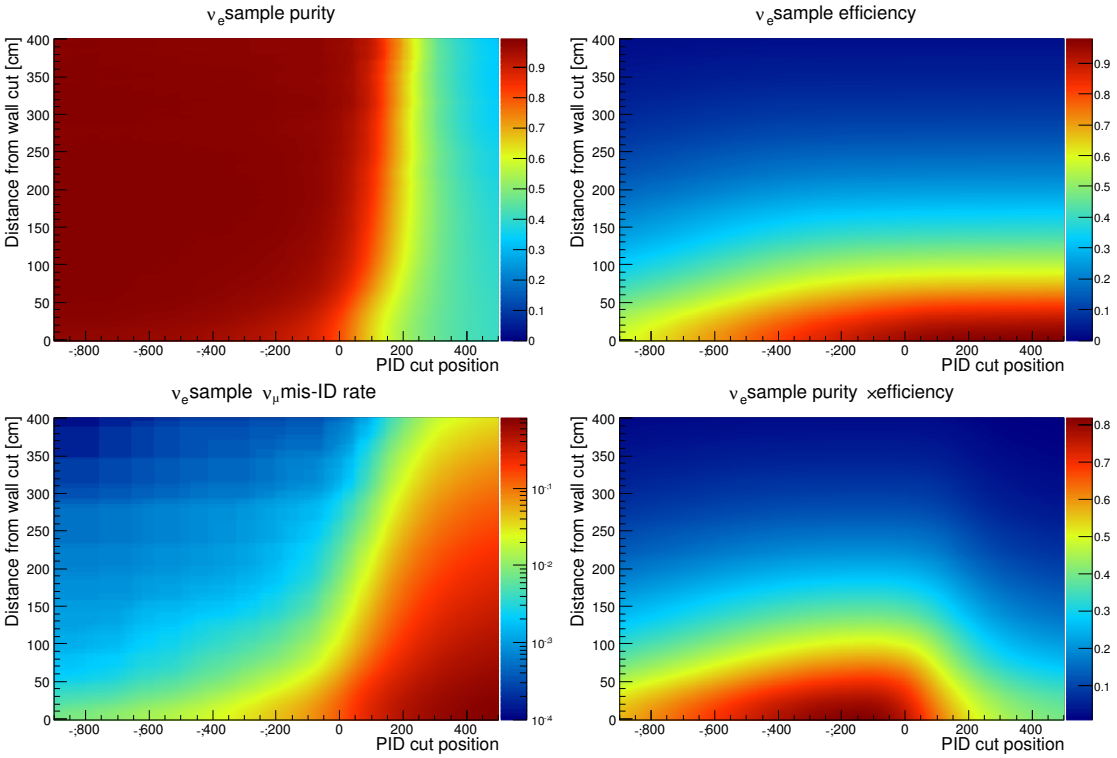

Figure 3.10: For CCQE ν_e events, the sample purity (top left), efficiency (top right), ν_μ mis-ID rate (bottom left) and purity $\times$ efficiency (bottom right), from equal numbers of simulated ν_μ and ν_e beam events, dependant on the position of the *dwall* and PID selection cuts.

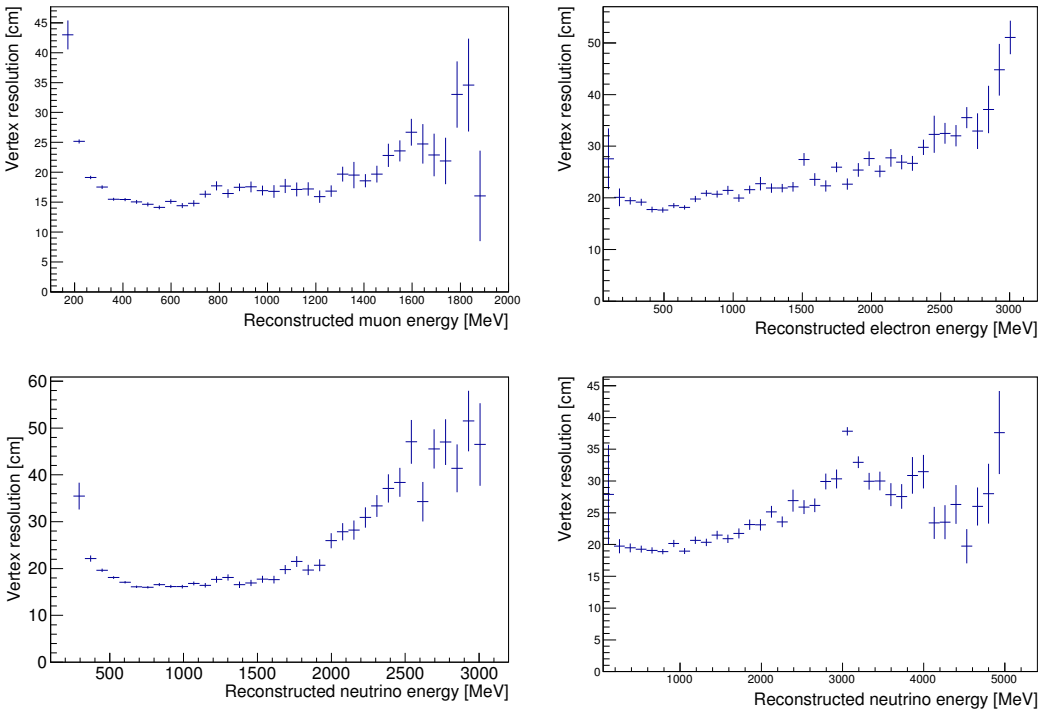

Figure 3.11: Vertex resolution for CCQE ν_μ events (left) and ν_e events (right), depending on the reconstructed electron/muon energy (top) and neutrino energy (bottom). At higher energies the reconstruction performs poorly for both flavours, as well as at low energies particularly for ν_μ events where the muon is close to the Cherenkov threshold.

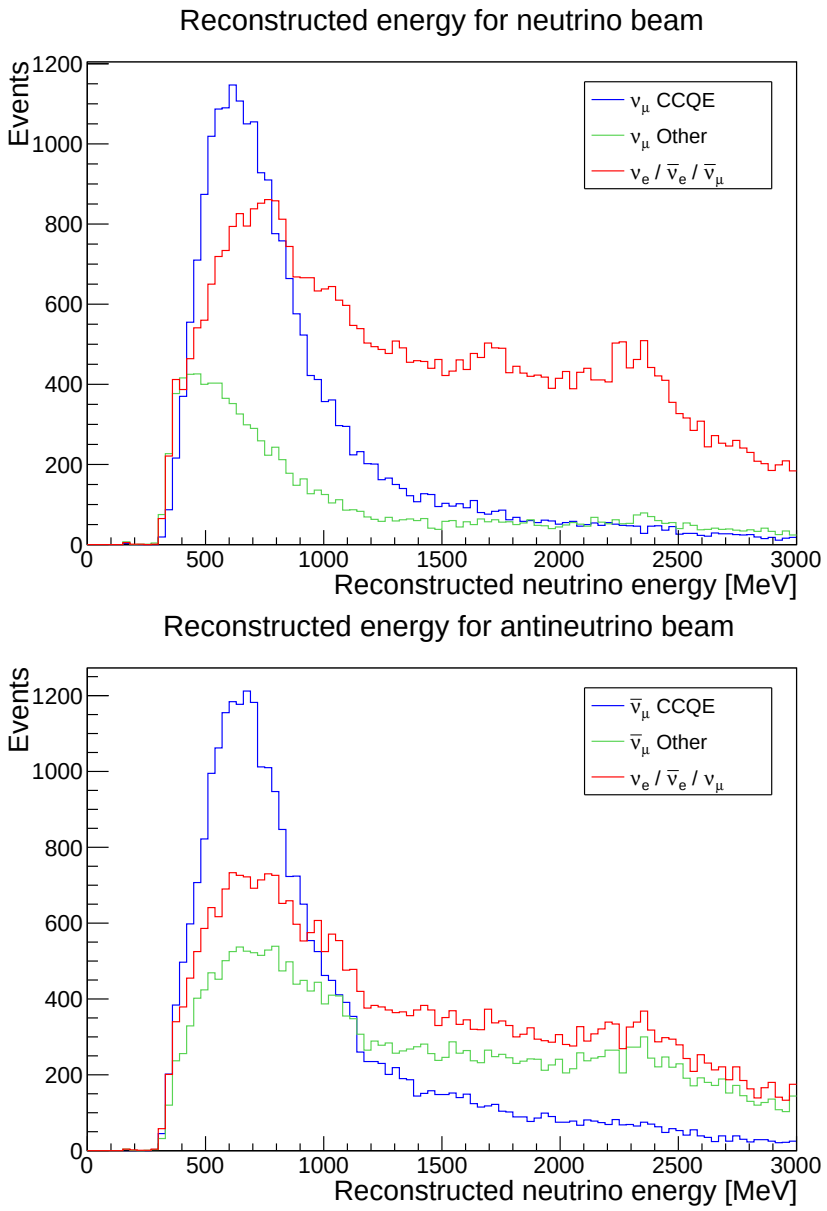

Figure 3.12: Reconstructed energy distributions for events identified with a single μ like ring from a neutrino-enhanced beam (top) and antineutrino-enhanced beam (bottom), with the events shown here normalised to give an equal number of each flavour prior to selection criteria.

the antineutrino-enhanced beam are significantly lower than the signal rates in the neutrino-enhanced beam due to a combination of two effects; the cross section is larger for neutrino interactions compared to antineutrinos in the detector and the flux of antineutrinos produced in the antineutrino-enhanced beam is smaller than the flux of neutrinos in the neutrino-enhanced beam, as discussed in Section 2.1.

	Reconstruction resolution		
Selection	Vertex [cm]	Direction [°]	Energy [%]
Single muon-like ring	18.4	2.1	11.8
Single electron-like ring	22.1	2.8	18.4

Table 3.1: Reconstruction resolutions for CCQE interaction beam events passing the single muon- and electron-like ring selections.

Single muon-like ring selection

	Neutrino-enhanced beam mode					Antineutrino-enhanced beam mode				
	Signal	Background				Signal	Background			
Selection	ν_μ CCQE	ν_μ CC other	$\bar{\nu}_\mu$ CC	$\nu_e + \bar{\nu}_e$ CC	NC	$\bar{\nu}_\mu$ CCQE	$\bar{\nu}_\mu$ CC other	ν_μ CC	$\nu_e + \bar{\nu}_e$ CC	NC
All	1 718 260	1 784 790	97 086	76 018	1 364 740	486 873	322 821	455 639	37 173	553 909
All in FV	1 090 130	1 133 550	61 622	48 149	867 219	308 239	206 129	288 673	23 641	353 630
dwall < 1 m	955 919	857 306	55 995	42 241	230 221	287 067	173 483	250 403	21 387	106 013
+ 1 ring	731 938	415 780	36 349	21 481	85 323	212 924	93 428	139 258	11 255	39 362
+ μ-like	723 484	303 093	31 984	1743	33 646	208 934	75 799	109 447	963	13 836
+ $E_\mu^{\mathrm{rec}} > 200$ MeV	692 934	240 457	23 322	688	27 732	196 807	59 779	81 210	292	11 570
+ $E_\nu^{\mathrm{rec}} < 1.25$ GeV	623 093	191 558	11 611	261	21 252	167 208	45 475	45 136	102	8878

Single electron-like ring selection

	Neutrino-enhanced beam mode					Antineutrino-enhanced beam mode				
	Signal	Background				Signal	Background			
Selection	ν_e CCQE	ν_e CC other	$\bar{\nu}_e$ CC	$\nu_\mu + \bar{\nu}_\mu$ CC	NC	$\bar{\nu}_e$ CCQE	$\bar{\nu}_e$ CC other	ν_e CC	$\nu_\mu + \bar{\nu}_\mu$ CC	NC
All	21 819	47 457	6742	3 600 140	1 364 740	6970	9688	20 514	1 265 330	553 909
All in FV	13 921	29 921	4307	2 285 290	867 219	4429	6136	13 076	803 041	353 630
dwall < 1 m	13 665	28 702	4301	1 994 500	271 715	4414	5956	12 819	748 300	124 884
+ 1 ring	8257	11 960	2392	1 225 620	92 886	2680	2944	6074	460 495	43 384
+ e-like	7559	11 105	2160	139 811	58 200	2427	2716	5579	55 592	28 951
+ $E_\mu^{\mathrm{rec}} > 100$ MeV	6302	6786	972	87 035	50 300	1832	1545	2913	34 343	25 182
+ $E_\nu^{\mathrm{rec}} < 2.5$ GeV	5510	5433	766	72 040	47 684	1644	1281	2232	27 477	23 295

Table 3.2: The number of expected events at TITUS, 2 km from a 1 MW beam running for 10^7 s, passing each selection criteria for single muon- and electron-like ring events. The signal is for CCQE events of the desired flavour; ν_μ ($\bar{\nu}_\mu$) or ν_e ($\bar{\nu}_e$) for the muon-like or electron-like selections respectively, with the beam in (anti)neutrino mode. The rates given in the fiducial volume (FV) are based on the true vertex position but the rates passing the selection criteria include those occurring outside the FV if reconstructed within the FV.

3.4.2 Neutron Tagging

To improve the purity of samples with respect to the wrong sign neutrino background, *i.e.* the antineutrino (neutrino) background contamination of the beam in (anti)neutrino enhanced mode, neutrons produced in the event are identified through the delayed signal after a neutron captures on Gadolinium. As described in Section 1.2.3, before final state interactions, there will be a single neutron produced for CCQE antineutrino interactions while none are produced for CCQE neutrino interactions. Although the number of neutrons in an interaction will change depending on final state interactions within the target nucleus, the purity of the samples can still be improved by requiring that there are no (at least one) neutron tagged in (anti)neutrino event samples.

To tag neutrons from their capture, a timing and energy window is chosen based on the distributions shown in Figure 1.4. The timing window used is 1 µs to 100 µs with a visible energy of 2 MeV to 10 MeV. For neutrons simulated with an initial energy of 50 MeV, randomly placed within the TITUS tank, the tagging efficiency using these criteria is 91 %. The majority of neutrons that were not tagged either captured on Hydrogen, converted into protons through interactions with nuclei, or escaped the water tank. The effect on the selections is shown in Table 3.4. For the neutrino beam the contamination of $\bar{\nu}_\mu$ ($\bar{\nu}_e$) events in the single muon-like (electron-like) sample is reduced by a factor of 9, while retaining 70 % (76 %) of CCQE ν_μ (ν_e) interactions. For the antineutrino beam the contamination of ν_μ (ν_e) events in the single muon-like (electron-like) sample is reduced by a factor of 2.5 (2.2), while retaining 85 % (86 %) of CCQE $\bar{\nu}_\mu$ ($\bar{\nu}_e$) interactions.

3.5 Effect on sensitivities of Hyper-K

The selections described in the previous section have been used in determining the effect of TITUS on oscillation sensitivities at Hyper-K; the full details of this analysis can be found in [71].

Using the VALOR framework, which is also used for official T2K analyses, the near and far detector samples are simultaneously fit to the expected rates, binned in reconstructed neutrino energy and accounting for both statistical and systematic uncertainties, to determine the oscillation parameters. A total of 189 systematic error sources are included coming from both TITUS and Hyper-K detector response as well as the neutrino beam flux prediction and neutrino interaction cross-section models. The parameters of these systematics are allowed to vary in the fit at the same time as the oscillation parameters, with the expectation that these systematic parameters will be constrained in the fit by the near and intermediate detector samples thereby reducing the overall errors in the oscillation parameters constrained by observations in the far detector. The fit has been performed using TITUS with Hyper-K, Hyper-K without TITUS, and Hyper-K without TITUS and without any systematic uncertainties, allowing the effect of the TITUS samples in reducing systematic uncertainties to clearly be seen. The results of the study are given in Figure 3.13 and Table 3.3. Improvements are seen in all of the main oscillation measurements; the precision measurement of δ, the search for CP violation, and the measurements of the atmospheric mixing parameters θ_{23} and Δm^2_{32}.

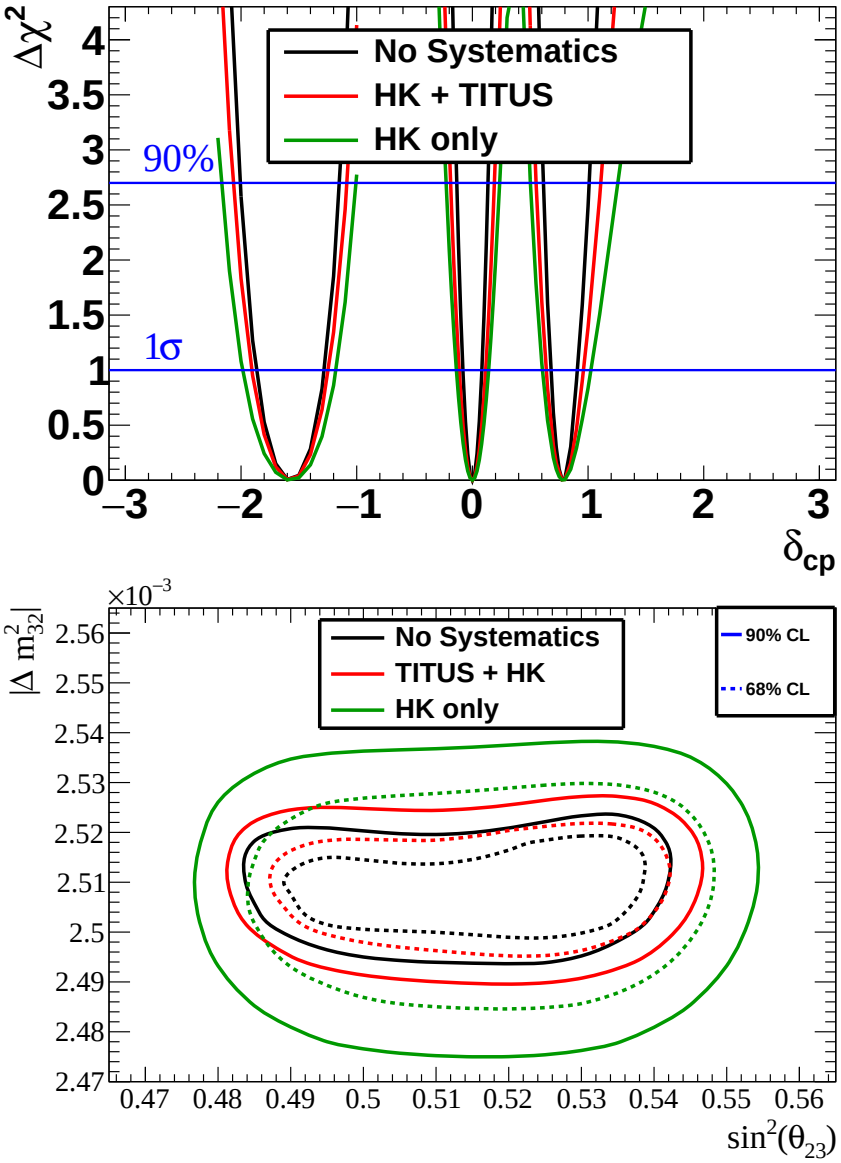

Figure 3.13: Sensitivities at Hyper-K only, Hyper-K with TITUS, and Hyper-K without systematic errors for excluding CP conserving values of δ (top) and for measurements of θ_{23} and Δm^2_{32} (right) [71].

	Error on δ			CP violation		Non-maximal θ_{32}	
	$\delta = 0$	$\delta = \frac{\pi}{4}$	$\delta = -\frac{\pi}{2}$	$3\,\sigma$	$5\,\sigma$	$3\,\sigma$	$5\,\sigma$
HK only	8.0°	12.1°	23.2°	73 %	51 %	90 %	87 %
TITUS + HK	6.6°	9.2°	19.0°	78 %	61 %	92 %	90 %
HK, no Systematics	4.7°	6.6°	16.9°	84 %	74 %	93 %	92 %

Table 3.3: Sensitivities at Hyper-K only, Hyper-K with TITUS, and Hyper-K without systematic errors. The the sensitivities shown are for the precision on the measurement of δ, the proportion of δ space for which the CP conserving values will be excluded, and the proportion of $\sin^2\theta_{23}$ space for which the value $\sin^2\theta_{23} = 0.5$ can be excluded.

Single muon-like ring selection

	Neutrino-enhanced beam mode					Antineutrino-enhanced beam mode				
	Signal	Background				Signal	Background			
Selection	ν_μ CCQE	ν_μ CC other	$\bar{\nu}_\mu$ CC	$\nu_e + \bar{\nu}_e$ CC	NC	$\bar{\nu}_\mu$ CCQE	$\bar{\nu}_\mu$ CC other	ν_μ CC	$\nu_e + \bar{\nu}_e$ CC	NC
All	1 718 260	1 784 790	97 086	76 018	1 364 740	486 873	322 821	455 639	37 173	553 909
All in FV	1 090 130	1 133 550	61 622	48 149	867 219	308 239	206 129	288 673	23 641	353 630
1 μ-like ring	623 093	191 558	11 611	261	21 252	167 208	45 475	45 136	102	8878
No neutron tag	438 500	99 382	1322	171	4396	24 859	2938	26 757	33	2056
1+ neutron tag	184 594	92 177	10 289	91	16 857	142 349	42 537	18 379	69	6822

Single electron-like ring selection

	Neutrino-enhanced beam mode					Antineutrino-enhanced beam mode				
	Signal	Background				Signal	Background			
Selection	ν_e CCQE	ν_e CC other	$\bar{\nu}_e$ CC	$\nu_\mu + \bar{\nu}_\mu$ CC	NC	$\bar{\nu}_e$ CCQE	$\bar{\nu}_e$ CC other	ν_e CC	$\nu_\mu + \bar{\nu}_\mu$ CC	NC
All	21 819	47 457	6742	3 600 140	1 364 740	6970	9688	20 514	1 265 330	553 909
All in FV	13 921	29 921	4307	2 285 290	867 219	4429	6136	13 076	803 041	353 630
1 e-like ring	5510	5433	766	72 040	47 684	1644	1281	2232	27 477	23 295
No neutron tag	4202	2512	83	37 844	23 246	236	97	1239	7692	13 361
1+ neutron tag	1308	2922	683	34 196	24 437	1408	1184	993	19 785	9934

Table 3.4: The number of expected events at TITUS, 2 km from a 1 MW beam running for 10^7 s, passing the selection criteria for single muon- and electron-like ring events, as in Table 3.2, with the addition of neutron tagging.

Conclusion

In this chapter, event selections of ν_μ, ν_e, $\overline{\nu}_\mu$ and $\overline{\nu}_e$ interactions have been developed, which have then been used to demonstrate the important role of an intermediate water Cherenkov detector for the Hyper-K oscillation analyses.

The selection criteria developed for these selections have demonstrated how the detector is capable of producing relatively pure, high-statistics data sets. In order to produce these samples, the requirement of a new high-energy reconstruction software package was met, providing fast, adaptable reconstruction suitable for the changing design of the detector.

While the design of the IWCD has changed since this analysis was produced, with a design now at a stage of development where the more advanced existing reconstruction software of Super-K and Hyper-K can be used, the tools and techniques described here could be applied to other detector design projects where speed and flexibility is a requirement. The reconstruction software developed for TITUS as part of this work was already been repurposed for use with the ANNIE experiment [60].

A simple neutron tag has also been implemented to demonstrate the possibilities of using the neutron capture signal on Gadolinium. The use of neutron tagging in this analysis is relatively basic, simply separating events by whether there appears to be a neutron capture anywhere in the tank within a fairly long time window, then using this to produce the two corresponding samples to include in the oscillation fit. However, there are a number of additional uses of neutron tagging expected to have a significantly greater impact in reducing errors at Hyper-K. A full neutron multiplicity measurement can provide new information to use in constraining cross-section models, which had not been implemented for the analysis of Section 3.5. Additionally, such a measurement could help understand the neutron capture signal that is intended to be used in the far detector (again not implemented for the analysis in Section 3.5) as well as to inform a more complete use of neutron tagging to statistically separate different interaction modes and separate neutrinos from antineutrinos. The next chapter investigates the possibility of producing such a neutron multiplicity measurement in the IWCD of Hyper-K.

Chapter 4

Measuring neutrons at E61

Introduction

As described in Section 2.4.2, the E61 experiment is the current design for an intermediate water Cherenkov detector as part of the Hyper-K project. The main motivation for these detectors is to perform measurements providing the inputs required to reduce systematic errors in measurements at the far detector. By providing measurements performed on the same water target, using the same Cherenkov ring imaging detector technology, the information provided by E61 can be applied to the far detector in a way which allows a greater reduction in systematic errors than existing near detectors have provided in the T2K experiment.

In T2K, the most significant sources of error come from uncertainties in the neutrino interaction cross-sections, the neutrino beam flux, the reconstructed incoming neutrino energy, and the contamination of neutrinos (antineutrinos) in the antineutrino (neutrino) beam. For the precision measurements of Hyper-K, these sources of error must be dealt with in order to reduce the total overall level of systematic errors to match the decrease in statistical errors from the increased event rate. The detection of neutron captures, in a water Cherenkov detector, tagged to specific neutrino interactions, has the potential to provide information helping to reduce all of these sources of errors; the details of this were covered in Section 1.2.3. To achieve this in practice, it is essential that the neutron capture signal is well understood, and it is hoped that this understanding can be gained through the observation of neutron captures in the E61 detector.

The benefits described previously of the E61 design in providing information on the neutrino beam flux and cross-sections would also apply to a neutron measurement; namely, the large sample of neutrino interactions from the largely unoscillated neutrino beam, the ability to make measurements over a range of different neutrino energy spectra through the varying off-axis angle, and the compatibility with far detector measurements due to having the same target and detector technology.

In this chapter, simulations of a neutron-capture measurement at E61 are presented, including event generation, detector simulation, reconstruction, selection and analysis, providing a proof-of-concept demonstrating the possibility of such a measurement and the information it could provide. The basic approach is to first identify and select primary events – the initial signal seen by the lepton (or other Cherenkov producing particles) produced by the initial neutrino interaction – then to search for neutron capture signals in a specified time window following the primary event. The primary event selection follows the same process as implemented for other E61 analyses, while neutrons are selected through a newly developed procedure attempting to maximise the efficiency and purity of the selected neutron capture samples. These results form a neutron multiplicity measurement, as a function of distance from the primary event and angle between the beam direction and the direction from the primary event vertex to the capture position. This can then be corrected to account for backgrounds and detector effects including efficiency and reconstruction resolutions.

Section 4.1 describes the tools used to produce the simulation and perform the reconstruction of both signal and background events. Section 4.2 details the event selections developed to separate the signal from background, with Section 4.3 discussing the methods used to correct for the signal efficiency of these selections and to subtract the remaining backgrounds. The results are then given in Section 4.4.

4.1 Event simulation and reconstruction

In order to perform the full analysis of this chapter, simulations are required to produce the flux of neutrinos entering the E61 detector tank, generate the neutrino interactions occurring in the detector, simulate the results of these interactions in the detector itself – the tracking of the particles through the detector, the detection of photons in the PMTs, and the subsequent electronics and data acquisition – and finally reconstruct the interactions from the detector simulation results.

2.39×10^{20} POT per off-axis position of simulated data has been produced for the signal neutrino interactions in the tank. The neutrino flux and interaction Monte-Carlo software used for this is the same as the previous chapter, except that the newer version 536 of NEUT [84] is used. The remaining software used for detector simulation and event reconstruction differ from those of the previous chapter.

4.1.1 WCSim detector simulation

The detector simulations performed for this analysis use the existing WCSim simulation package [102], which is the standard water cherenkov simulation package used by the Hyper-Kamiokande collaboration. The WCSim software itself has been modified to provide additional capabilities for the addition of Gadolinium to the water, and for the simulation (and for validating the simulation) of neutron captures. Additionally, the E61 detector geometry used within WCSim has been developed separately by the E61 collaboration. This geometry matches the description given previously in Section 2.4.2, with the assumption of 0.1 % Gadolinium doping (0.2 % Gadolinium sulphate) of the water in both the ID and OD. Further modifications to WCSim as well as the use of other simulation software allowed the simulation of various background events, which will be discussed in more detail in the next section.

To simulate events in WCSim, the incoming particles – either from the output of the neutrino interaction event Monte-Carlo or from separate background Monte-Carlo – are provided as the initial input. For each event, these particles are then simulated using Geant4 [92], version 4.10.1, in the same way as described for the WChSandbox simulation software in Section 3.1, up until each particle is either destroyed in a decay or interaction with the detector material, exits the detector volume or, for optical photons, enters a PMT. The standard Geant4 physics list `FTFP_BERT` is used by default in WCSim to define which physical processes are simulated and the models used. However, the high-precision `FTFP_BERT_HP` physics list is required to accurately model neutrons and so for the neutron simulations this has been used instead.

A more advanced treatment of the photodetectors themselves is employed in WCSim than in the WChSandbox software used in the previous chapter; in WCSim the detection, digitisation, triggering and data acquisition are all simulated. Each photon reaching a PMT has a chance of being registered as a hit, depending on the quantum efficiency and collection efficiency of the PMT, which varies with the incoming photon's wavelength as well as its incident angle on the PMT. The digitiser is then simulated, providing for each hit a delayed and smeared hit time and smeared observed charge. At this point, dark noise of each PMT is also simulated and included as additional hits, before the trigger and data acquisition simulation determines whether a collection of hits produce a

trigger event, or fail to trigger with these hits going unobserved. The models used for the PMT response, digitiser, trigger and data acquisition system are those of the nuPRISM branch of WCSim developed by the E61 (and previously nuPRISM) collaboration [103]. The only modification of these made for this analysis is the parameters of the trigger; in order to successfully observe the lower energy produced by neutron captures, a minimum of only 5 digitised hits above the expected dark rate (of 100Hz at each 3″ PMT) is required within a moving window of 50 ns, compared to the default requirement of 25 hits in 200 ns.

4.1.1.1 Neutron capture models in Geant4

An important consideration for this analysis is the modelling of neutron captures, which in Geant4 has some shortcomings that will need to be addressed for a neutron multiplicity measurement using neutron captures on Gadolinium. There are two existing models generally in use for simulations of Gd neutron captures, the default model of Geant4 and a custom model originally created to be used with the GLG4sim package [104], as well as a third model under development based on experimental data from the ANNRI experiment [105, 106].

In terms of the effect on the simulation and reconstruction of neutron captures, the difference between the models is in the number, individual energies, and total energy of the γ-rays emitted from the excited nucleus as a result of the capture. In all three models, for the case of more than one emitted photon, they are assumed to be emitted with no angular correlation.

Figure 4.1 shows the differences between the models, with all three models predicting different distributions of multiplicities and energies. For the default GLG4sim model, there are always at least two γs produced and the total energy is always one of the two correct values for the nuclear de-excitation of the two isotopes of Gadolinium, 8.5 MeV for ^{156}Gd and 7.9 MeV for ^{158}Gd, after neutron capture. The ANNRI model typically predicts a larger γ multiplicity, mostly with the same total energies, but with a small number of events having lower energies. The Geant4 model, however, predicts a much larger number of captures having lower energies, except when only a single γ is produced and the correct total energy is given to that γ. The Geant4 model also does not predict the specific γ lines in the individual γ energy spectrum, seen as spikes in the γ energy spectra, other than those for a single γ with the full energy. These spikes correspond to de-excitations between energy levels of the nucleus and have been included in the GLG4sim and ANNRI models based on experimental observation, having been added into these models explicitly but not included in the Geant4 model.

Since the charge seen in a PMT is directly correlated with the energy of the Cherenkov producing particles, both the total energy and how that energy is distributed amongst γs will affect this. An increased total charge provides more information for use in reconstruction and in Figure 4.2 the effect of the different models on the reconstructed capture position (vertex) can be seen. As expected from the typically lower total energy released in the default Geant4 model's captures, the reconstruction of these captures is significantly worse than the others. While the reconstruction of captures simulated using the ANNRI and GLG4sim models perform similarly, the GLG4sim captures do

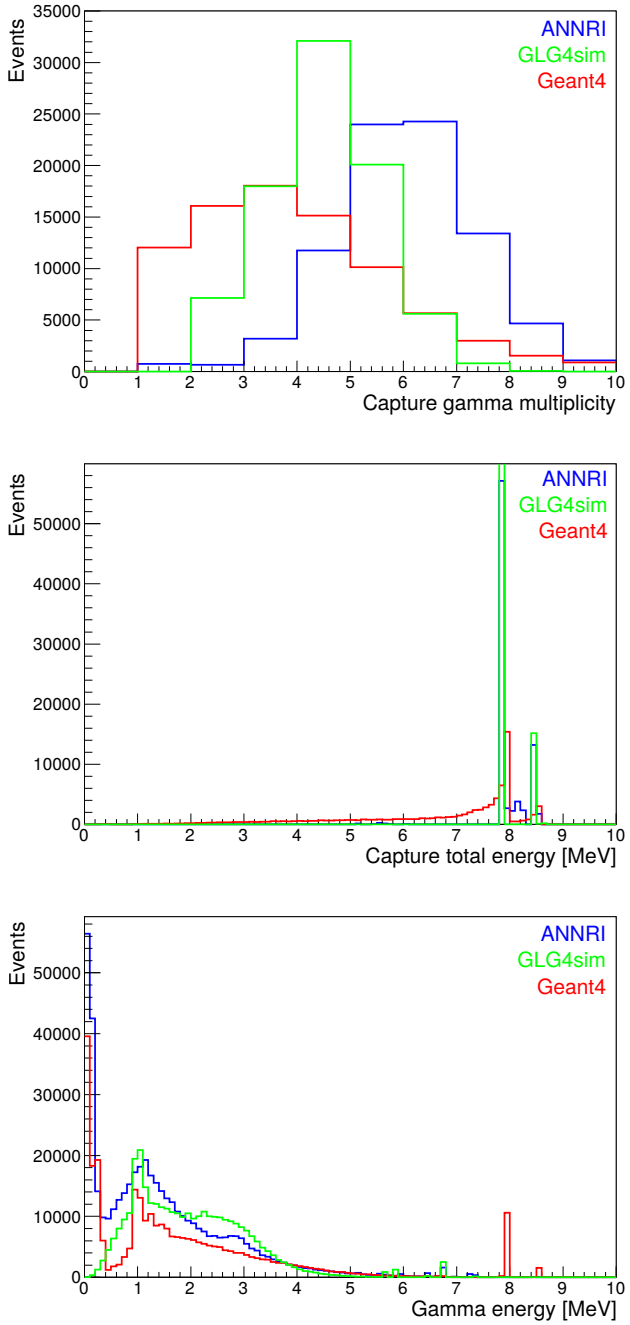

Figure 4.1: Comparison of the ANNRI, GLG4sim and Geant4 (default) models of Gadolinium neutron capture for 100 000 simulated events. The multiplicity (top), total energy (middle) and individual energy (bottom) of the γs emitted after simulated neutron captures are shown for the three models.

have slightly improved reconstruction, due to this model predicting fewer low-energy γs (below Cherenkov threshold).

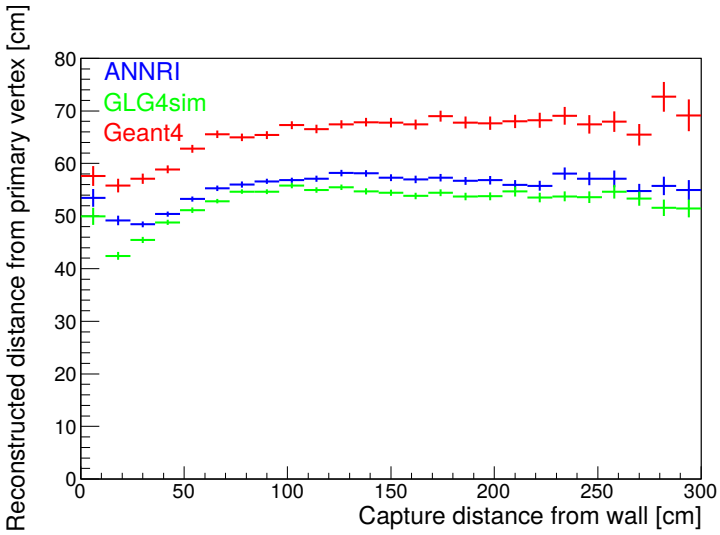

Figure 4.2: The vertex reconstruction as a function of capture distance from the tank wall for Gadolinium neutron captures simulated with the ANNRI, GLG4sim and Geant4 models.

With the current level of uncertainty in the number and energies of γs released after a capture on Gd, as demonstrated by the significant differences between these models, it will be important to take the effect of these into account as a source of systematic error on the neutron measurement. While this analysis does not include systematic errors, the conservative approach is taken of using the default Geant4 model (which produces captures with the least well-performing reconstruction). For future analyses the ANNRI model, once its development progresses and a full version of the model is released, would be preferred due to being based on experimental observation.

4.1.2 Low-energy background and background neutron simulations

The low energy background rates for a neutron capture measurement are expected to be significant, due to the relatively long time window required for the search for neutron captures, the relative proximity to the beam source resulting in a high rate of beam induced backgrounds, and the lack of overburden above the detector to protect from cosmic rays. While a cosmic ray muon may appear to mimic the muon coming from a neutrino interaction, they are high enough energy that they would be seen entering the OD region of the detector and can be vetoed. However they can still produce a background for the neutron measurement by interacting in the material surrounding the detector, producing neutrons which then travel undetected into the detector before capturing and appearing like a neutron produced in a neutrino interaction. In addition to backgrounds caused by incoming neutrons not associated with the signal neutrino interaction, any low-energy Cherenkov light producing particles can also mimic the signal of a neutron capture. The most significant source of this comes from the decays of radioactive isotopes from impurities within the detector. For this analysis, all the expected major sources of backgrounds have been fully simulated through custom software or

extensions of the WCSim simulation software described in the previous section. Background sources which form a significantly smaller contribution to the total rate have not been included; this includes skyshine neutrons (high-energy neutrons produced in the beamline at J-PARC and subsequently escaping into the air and propagating until they reach the detector), delayed decays of unstable nuclei activated in or near the detector by cosmic ray muon spallation, neutrons produced by decays of naturally occurring radioactive isotopes in the surrounding material and triggers produced purely through PMT dark-noise. Basic estimates of the rates of these backgrounds have suggested that their rates are at least two orders of magnitude smaller than the background sources that have been included. These estimates were based on extrapolations from measurements of the rates seen at other experiments; the decays of activated nuclei estimate is based on that seen at Super-K [107] and the neutron skyshine is based on that seen at K2K [108].

4.1.2.1 Neutrino beam induced backgrounds

The most significant source of background for this measurement comes from neutrons created in or near the detector tank as a result of neutrino beam interactions separate from the neutrino interaction identified in the primary event selection. This includes both neutrino interactions in the surrounding detector material, including the outer detector region of the tank and the sand and air surrounding the tanks, and neutrino interactions within the inner detector producing no detectable primary event (mostly NC events). Both of these sources have been simulated separately; for the 'invisible' interactions in the inner detector, no additional simulation was needed as these neutrons were included in the signal event simulation and so it is only required to identify the neutrons from those interactions with no visible primary event. For the neutrino interactions in the surrounding material, these were first generated using the same tools as the signal interactions in the tank, using a neutrino flux plane located 34 m upstream of the tank, with the simulation geometry extending from this plane to 5 m downstream of the tank, from 77 m below the surface to 25 m above the surface and a total of 22 m wide, centred horizontally with the detector. The products of these neutrino interactions are then simulated through a custom-built simplified Geant4-based software package which tracks all particles through the sand, air and water volumes, without simulating the entire detector geometry. This allows for a fast simulation to determine the particles entering the detector volume, which are then themselves entered into a full WCSim simulation. These simulations assume throughout that the volume below the surface, surrounding the pit, consists only of silica (SiO_2), with air above the surface. Below the OD down to the bottom of the 51 m pit is filled with pure water, as is up to 6 m of the pit above the top of the OD but no higher than the surface, with any remaining volume of the pit above this water filled with air. The water in the ID and OD detector volumes are Gadolinium doped, but any water above and below the OD is not. This geometry was shown for each off-axis angle position in Figure 2.8. A total of 10^{19} POT has been simulated for these interactions for each position of the detector.

4.1.2.2 Cosmic ray induced backgrounds

With the top positions of the detector having no overburden and the lower positions having only 6 m of water directly above, the rate of cosmic ray backgrounds will be large. For a neutron measurement, the majority of cosmic muons will not affect the measurement other than to temporarily blind the detector from observing low-energy events while muons pass through. However, these muons can also interact outside the detector, producing neutrons which may enter the detector, capture and produce the same signal as that of the neutrons from neutrino interactions. In order to simulate this background, the CRY library [109] has been used, within WCSim, to generate cosmic ray showers through a 50 m × 50 m plane at the surface (or at the top of the tank in the position where that is above the surface). The resulting particles of these showers are then simulated through the full WCSim simulation using an extended geometry, similar to that used by the beam induced background simulation described above, to include the sand and air surrounding the water tank. This has been performed for a total of 10 million cosmic ray muons and neutrons, corresponding to the amount expected through the 50 m × 50 m plane in approximately 3.3 s, then simulated with the detector at each of the seven off-axis positions.

4.1.2.3 Radioactive decays

The most significant source of non-neutron backgrounds to this measurement comes from electrons and gammas produced in decays of radioactive isotopes in the detector. A large proportion of the visible decays come from impurities in the PMT glass, however the smaller rate coming from impurities within the water itself is also significant due to the greater difficulty in separating these from signal events. In these simulations, only the impurities from these two sources have been considered, however additional impurities in the material surrounding the detector, the detector support structure and the materials of the multi-PMT modules may also contribute. A modified version of WCSim which uses the Geant4 radioactive decay models has been used to simulate the radioactivity background. The activity levels assumed are given in Table 4.1. The simulation runs for a fixed time window of 100 µs and was performed for 100 000 such windows.

	Isotope	Activity level
PMT glass	^{208}Tl	0.067 Bq/PMT
	^{214}Bi	0.64 Bq/PMT
	^{40}K	2.2 Bq/PMT
Water tank	^{214}Bi	940 Bq

Table 4.1: Activity levels of radioactive impurities simulated in E61.

4.1.3 Event reconstruction

As with the analysis in the previous chapter, separate reconstruction software is used for high energy or low energy events. Initially, all events are passed through the fiTQun

high-energy event reconstruction software, which was developed for use with the Super-K detector [110] and, like the high-energy reconstruction software described in the previous chapter, is based on the algorithms originally developed for the MiniBooNE experiment [101]. This is the standard reconstruction software which has been re-tuned by the E61 collaboration for use with the E61 detector. The results of this are used to identify and select the primary events, but are not used for subsequent triggers when looking for neutron captures.

The neutron capture reconstruction uses the BONSAI low-energy reconstruction software [111], also originally developed for the the Super-K detector; this has also been re-tuned for the E61 detector. All triggers with a total number of hits between 5 and 500 are passed through the BONSAI reconstruction and the results used in identifying and selecting neutron captures. Currently only the vertex position reconstruction of BONSAI is used. However, further work to tune the energy reconstruction for E61 could also provide more useful information than the total PMT charge which has been used here instead (the direction reconstruction is unlikely to be of much use due to the variable number of cherenkov-producing particles emitted after a neutron capture in different directions). The vertex reconstruction of BONSAI works by maximising a likelihood function based on the hit timing: A likelihood function of the timing residual of each hit, defined in the same way as previously in Equation (3.2.2), is fitted to the observed distribution for a large number of events simulated in the detector. This likelihood function differs only according to the detector geometry and so only needs to be computed once for a given detector design. The likelihood which BONSAI maximises for each event is then produced by computing the product of the likelihoods of the timing residual of each of the PMTs' hits, after a hit selection process which attempts to remove dark noise and other outliers. The maximisation algorithm itself is designed to deal with the large number of local maxima which frequently occur in low-energy events with a small number of hits. Initially a grid of candidate vertices is compiled using quadruplets of hits, in a similar process to the algorithm described in Section 3.2. Then, a search for progressively better candidates is performed, traversing a tree of the potentially local maxima and attempting to maximise the likelihood close to each of these, until the global maximum is determined.

4.2 Neutron selection and background rejection

For this analysis, there are two components to the event selection; the primary event selection to select *e.g.* CCQE ν_μ events, and the neutron selection to select the subsequent neutron captures associated with a given primary event. For measurements on other primary event types, such as ν_e events or non-CCQE events, both the primary and neutron selections could change, so long as the efficiency corrections are also changed accordingly (see next section).

The primary event selection used in this analysis is the standard E61 single ring muon-like selection, which was originally developed for the ν_μ flux and cross-section measurement at νPRISM. Except where stated otherwise, the results presented in the remainder of this chapter are only for events passing this selection and for the 2.5° off-axis position of the detector. The selection criteria for the primary event selection use the fiTQun reconstructed variables, with the following requirements:

1. A single muon-like Cherenkov ring is observed
2. The reconstructed muon momentum is at least 200 MeV
3. The muon is contained within the tank
4. The reconstructed interaction vertex is at least 1 m away from the tank wall
5. The vertex is at least 2 m away from the wall in the direction of the muon
6. There is no more than one sub-event (*i.e.* only no additional particles other than the decay electron)

This gives in an efficiency of 38 % for selecting fully contained CC ν_μ events while rejecting 99 % of other background events, resulting in a 97 % pure sample containing a total of 107 262 events from the 2.39×10^{20} POT simulated at 2.5° off-axis.

The above event selection has been performed for events which were simulated as occurring individually, with no pile-up of multiple events occurring together. To account for this, the rate is adjusted by assuming that if multiple visible events occur together in a single spill of the beam then both those events will be rejected. The rate of events within a given spill is assumed to be Poisson with the rate determined by the total number of visible events simulated divided by the number of spills corresponding to the simulated POT. The expected rate of visible events per spill is 0.94, giving the proportion of visible events occurring with no other visible events in the same spill of 39 %.

The neutron selection begins by searching for triggers which occur within a time window of 200 ns to 100 µs, the region in which the majority of captures occur while rejecting non-neutron triggers associated with the primary event, as shown in the upper plot of Figure 4.3. In order for the trigger to be passed to the low energy reconstruction, a total charge seen in the PMTs is required to be equivalent to between 10 and 100 photoelectrons; the lower plot of Figure 4.3 shows that this includes the vast majority of neutron captures while also ensuring reasonable reconstruction performance. This PMT charge cut will also help reduce the low-energy background from non-neutron sources such as radioactive decays.

The remaining selection criteria depend only on the time (in addition to the fixed timing cut above) and the reconstructed position, both relative to the reconstructed primary event position and relative to the tank's geometry. Since the majority of the remaining background are genuine neutron captures, but from neutrons produced from external sources, this timing and positional information is the only information that can be used to distinguish the signal from these backgrounds. In order to maximise the effectiveness of a cut using this information, a likelihood is constructed for each of the main background neutron sources (sand neutrons, NC event neutrons, and cosmic neutrons), as well as signal neutrons. In Figure 4.4, which shows the distributions of the time and distance from the primary event for signal and backgrounds, it can be seen how a likelihood cut that can follow the contours of these distributions has more power to separate signal from background than individual cuts.

The definitions of the quantities used to construct the likelihoods are given in Table 4.2. Each likelihood is then constructed as the product of four probability distributions – three for position and one for time – which may be simply flat distributions included to allow direct comparisons between likelihoods, as tabulated in Table 4.3. Additionally,

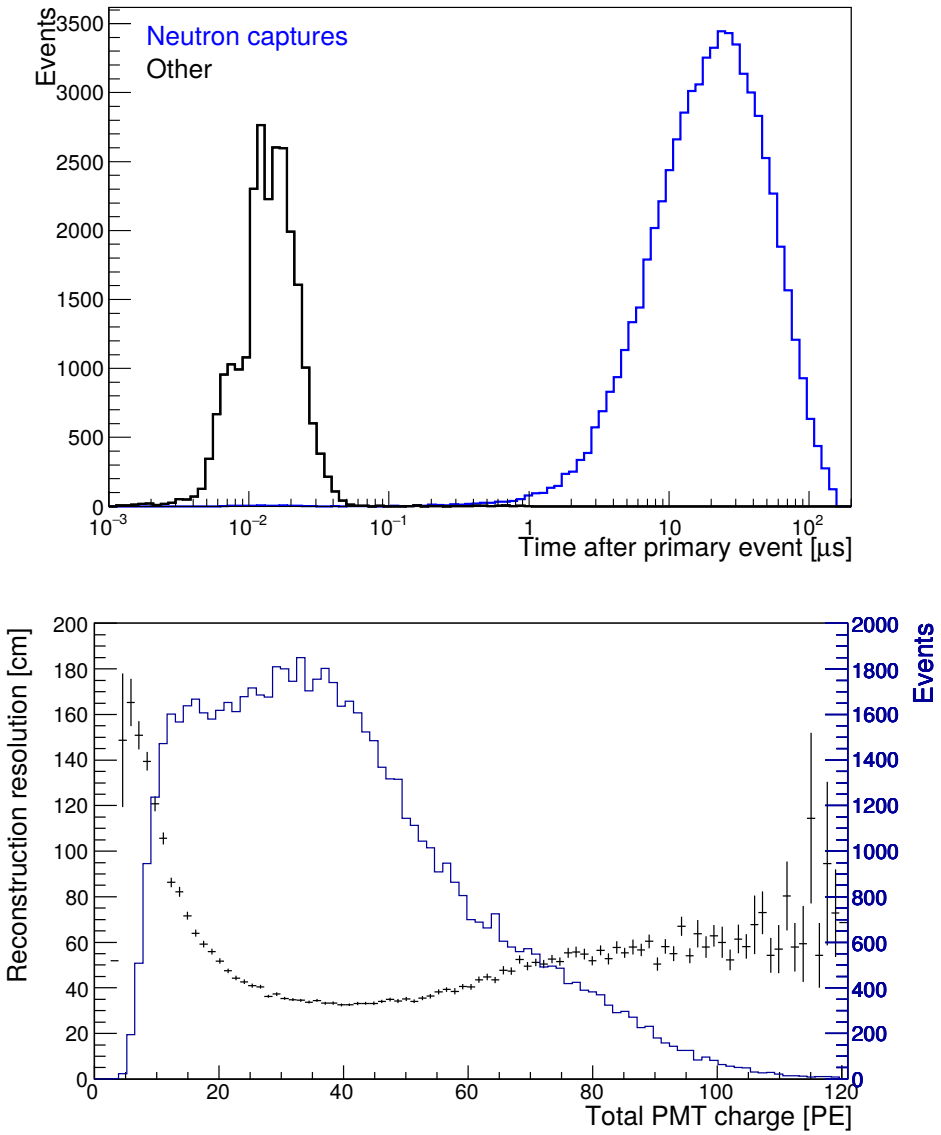

Figure 4.3: Top: Time distribution of neutron capture triggers (blue) and non-neutron triggers (black) after the primary event trigger. Bottom: Reconstructed distance from true capture position (black) and event rate (blue) against total PMT charge in units equivalent to single photoelectrons arriving at the PMT.

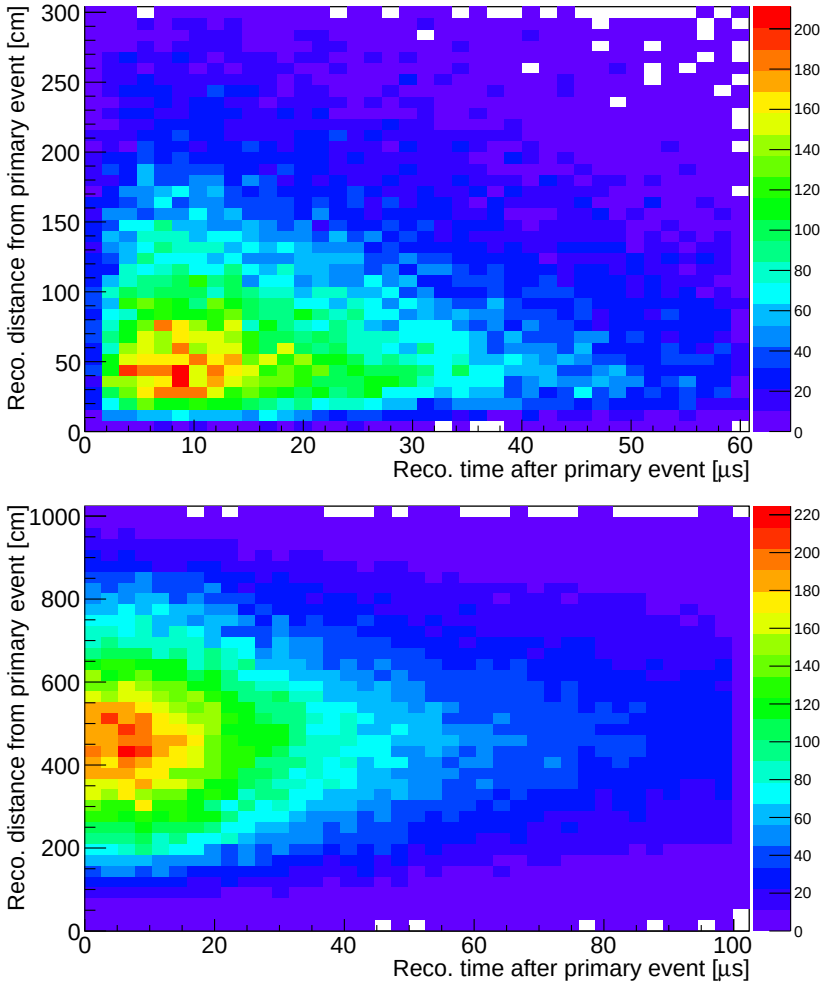

Figure 4.4: Distance and time relative to primary vertex for signal (top) and background (bottom) neutrons. The likelihood method used allows a cut which accounts for the shape of these distributions, providing better separation than individual cuts corresponding to vertical and horizontal cuts on these plots.

to ensure compatibility between likelihoods, although the spatial part of the likelihoods are each built using probability distributions of variables defined in polar or cylindrical coordinates, these must be reparametrised through a change of variable into probability distributions of a single consistent coordinate system. The probability distributions have been determined by fitting the various distributions using Monte-Carlo simulated events, as shown in Figures 4.5 to 4.8 with full details of the fitted distributions given in Appendix A. For the case of sand neutrons and NC event neutrons, the timing part of the likelihood is complicated by the possibility that these neutrons' primary events could have occurred at a different time in any of the beam spill's bunches[1]. It is constructed from the distribution of the time the neutron capture is observed relative to its primary event, convoluted with a uniform distribution corresponding to the time within the bunch that the primary event could have occurred, giving the time distribution relative to the start of the bunch, t_b. Assuming that the background neutron's primary event could then have occurred with equal likelihood in any of the eight bunches, a mixture distribution is constructed of the eight time-shifted distributions of t_b.

	Position relative to primary vertex
d	Distance from primary event to neutron capture
θ	Angle between beam direction and d
ϕ	Azimuthal angle about beam direction
	Position relative to tank geometry
y	Vertical position in tank
r	Radial position in tank
φ	Azimuthal angle about tank axis
	Time
t	Time relative to primary vertex
t_b	Time relative to start of each beam bunch

Table 4.2: Definitions of the parameters used to construct the likelihoods given in Table 4.3. All parameters are based on the reconstructed time and position of the neutron capture candidate and, where appropriate, the reconstructed time and position of the primary event vertex.

While these likelihoods have been built in this analysis using Monte-Carlo simulations, with separate likelihoods for each background type, the background distributions could instead be fit using data collected from spills in which no primary event is observed. This would remove the model dependence as well as provide a single full likelihood that includes all backgrounds from neutron sources as well as from other sources. With an expected visible primary event rate of 0.94 per spill, approximately 39 % of spills will have no visible primary event – slightly more than the number of spills with a single visible event, many more than the number of selected primary events – which should provide ample data to fit the distributions of the likelihood.

Calibration with neutron sources could also be used to help fit the likelihoods for the signal. Neutron sources are under development [17] which could be inserted into the

[1]The bunch structure of the T2K beam has been assumed, with eight bunches, each 58 ns long, separated by 581 ns gaps.

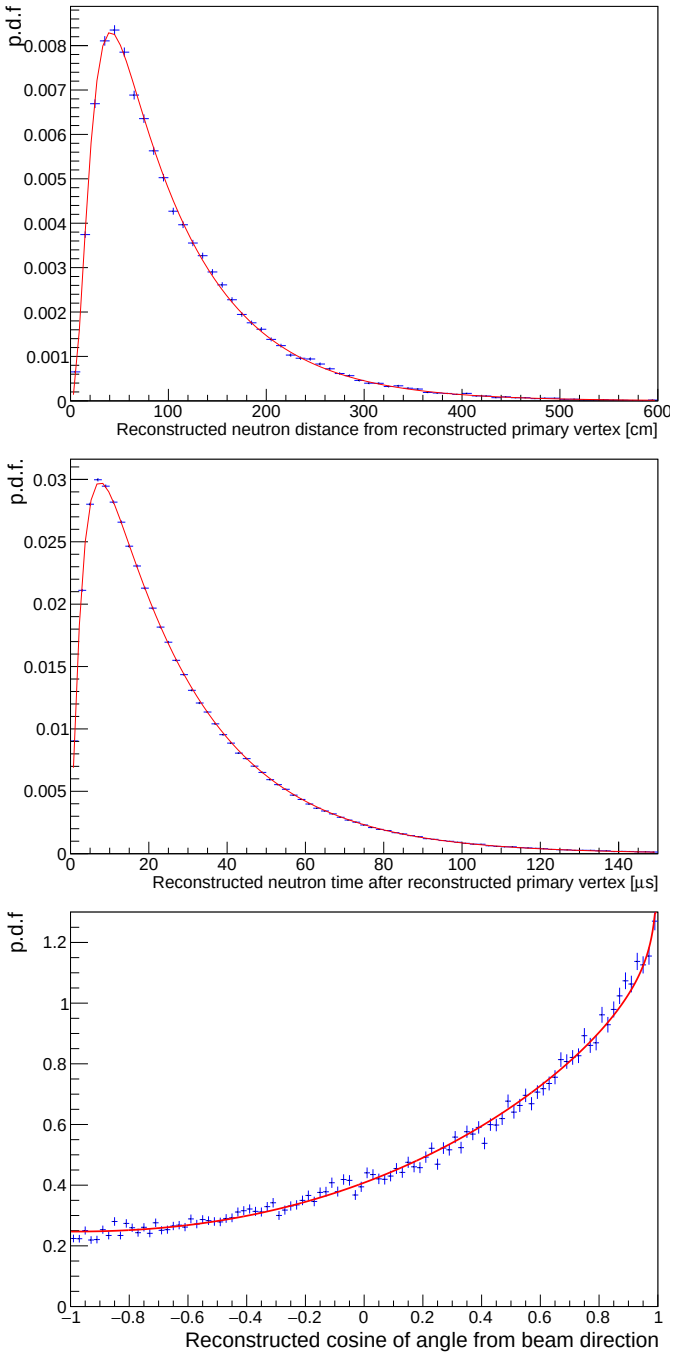

Figure 4.5: Distributions of the distance d to neutron capture (top), time t of neutron capture (middle) and angle θ of neutron capture (bottom) relative to primary event for signal neutrons, used to construct the signal neutron likelihood function. Fitted distributions are shown in red with Monte-Carlo simulated data shown in blue.

	Position from vertex			Position in tank			Time	
	d	θ	ϕ	y	r	φ	t	t_b
Signal	Fitted	Fitted	Flat	—	—	—	Fitted	—
Cosmic	—	—	—	Fitted	Fitted	Flat	Flat	—
Sand	—	—	—	Fitted	Fitted	Fitted	—	Fitted
NC	—	—	—	Fitted	Fitted	Fitted	—	Fitted

Table 4.3: Construction of the signal likelihood and sand neutron, cosmic neutron and NC event neutron background likelihoods using distributions of the quantities given in Table 4.2. Each likelihood is based on probability distributions corresponding to the position and time of the neutron capture candidate. The table shows which quantities are used and whether the distributions are fitted or flat.

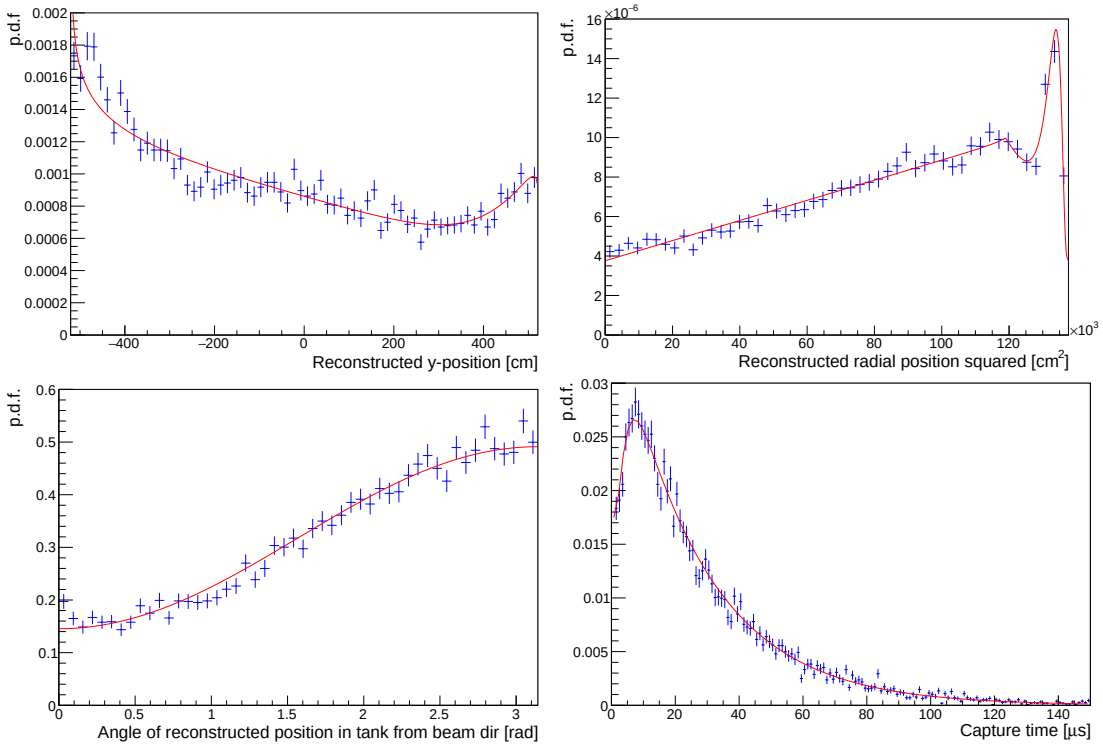

Figure 4.6: Distributions of the vertical position y (top left), radial position r^2 (top right), azimuthal angle φ (bottom left), and time t_b (bottom right) of neutron captures in the tank for sand neutrons, used to construct the sand neutron likelihood function. Fitted distributions are shown in red with Monte-Carlo simulated data shown in blue.

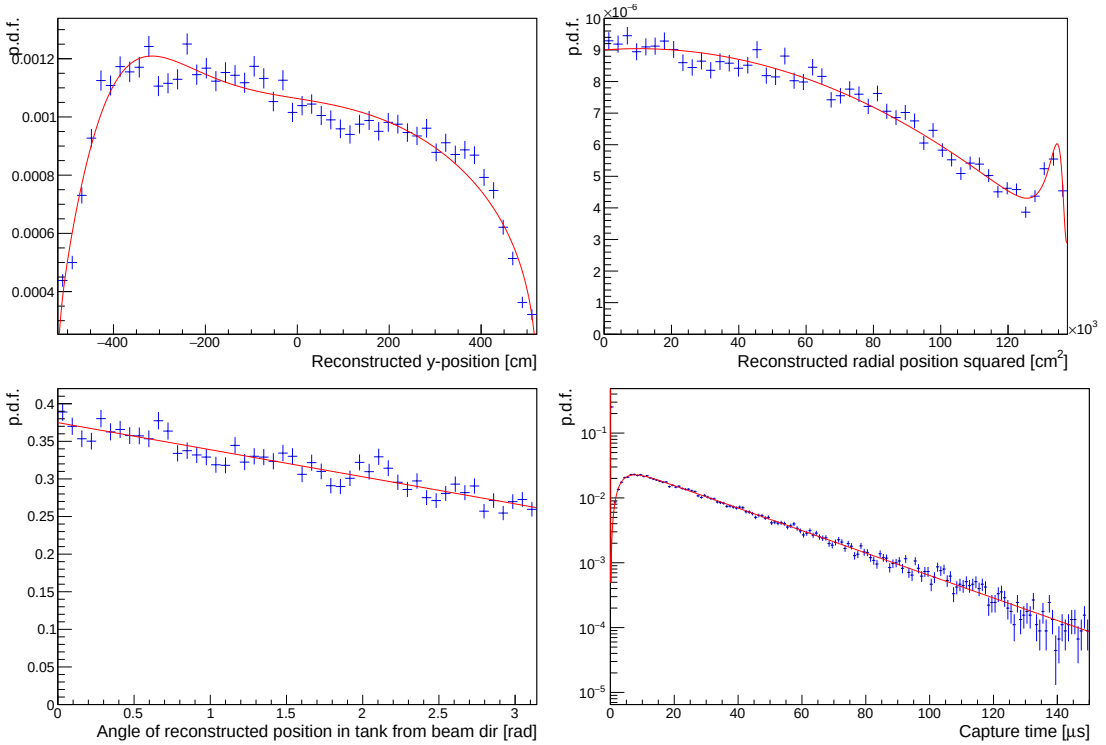

Figure 4.7: Distributions of the vertical position y (top left), radial position r^2 (top right), azimuthal angle φ (bottom left), and time t_b (bottom right) of neutron captures in the tank for NC event neutrons, used to construct the NC event neutron likelihood function. Fitted distributions are shown in red with Monte-Carlo simulated data shown in blue.

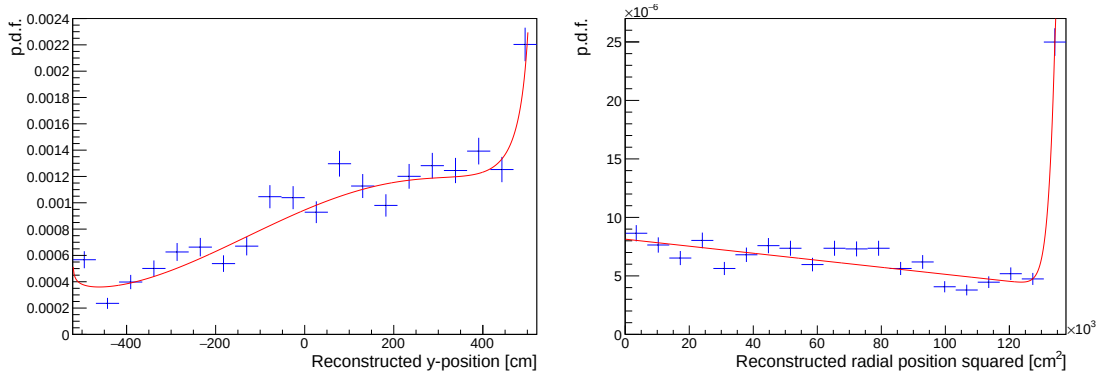

Figure 4.8: Distributions of the vertical position y (left) and radial position r^2 (right) of neutron captures in the tank for cosmic neutrons, used to construct the cosmic event neutron likelihood function. Fitted distributions are shown in red with Monte-Carlo simulated data shown in blue.

detector to emit neutrons at known energy, location and time, which could then be used to measure precisely the capture time and distance distributions. These distributions would then be used to form the likelihoods that in this analysis have been determined purely by simulation.

For each neutron capture candidate, a separate cut is then made on the difference between the signal log-likelihood and each of the three background log-likelihoods. Figure 4.9 demonstrates this, showing the signal neutron log-likelihood $\log L_{\text{sig}}$ against the sand neutron $\log L_{\text{sand}}$, with the cut on $\log L_{\text{sig}} - \log L_{\text{sand}}$. The value of each of these cuts has been optimised to maximize $S/\sqrt{S+B}$, where S and B are the accepted signal and background rates respectively.

Note that the use of the time and, in particular, the position of the neutron capture relative to the primary event vertex introduces a significant model dependence to the measurement. This is due to the large theoretical uncertainties in the momenta of neutrons produced in neutrino-nucleus interactions and will be dealt with as part of the efficiency corrections described in the next section.

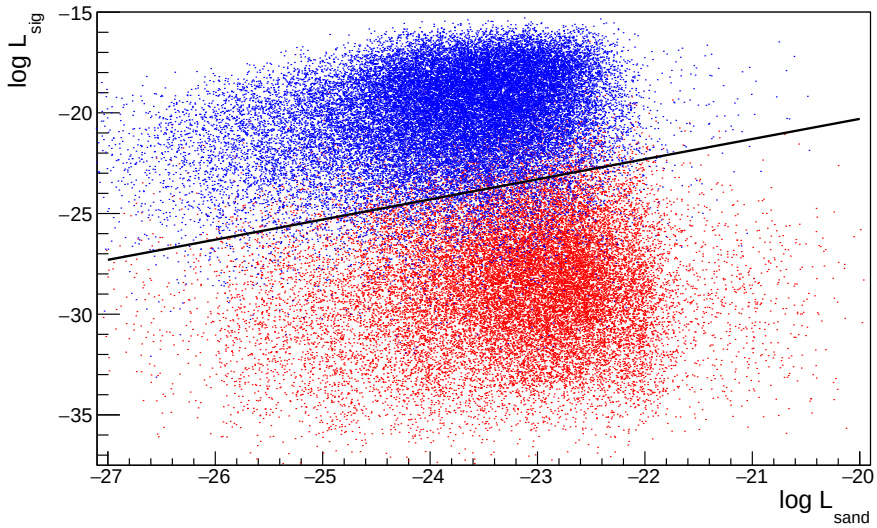

Figure 4.9: Signal neutron and sand neutron log-likelihoods for signal events (blue) and background events (red), with cut on the log-likelihood difference $\log L_{\text{sig}} - \log L_{\text{sand}}$ (black).

The final samples after likelihood cuts contain a total of 105 032 neutron capture candidates scaled to 10^{20} POT, with a sample purity of 92 % and efficiency[2] of 75.6 %. The effect of each of the cuts on the sample, with rates for signal and each type of background, are given in Table 4.4.

Despite the relatively high rate of incoming background neutrons, the selections used above demonstrate that it is still possible to make very pure samples, with high signal efficiency, of neutrons associated with neutrino interactions. The samples here are for ν_μ interactions, which are expected to generally produce fewer neutrons than $\overline{\nu}_\mu$ interactions or other interaction modes, so the neutron sample for $\overline{\nu}$ interactions is expected to have

[2]Efficiency here is defined as the number of selected signal neutron captures divided by the true number of signal neutrons which capture inside the ID.

	Signal			Background					
	Selected	Efficiency	Purity	Sand	Cosmic	NC	Radioactivity	Other	Total
All captures in ID	138939	—	—	80806	761	9497	—	—	91064
Captures on Gd	121830	—	—	67736	658	8253	—	—	76647
Captures on H	17087	—	—	13037	102	1240	—	—	14379
All triggers	132478	95.3 %	17.7 %	340828	36598	15336	159623	64875	617259
OD veto	131862	94.9 %	23.5 %	180017	8487	15336	159623	64826	428288
$10 <$ PMT charge < 100	125736	90.5 %	32.3 %	118131	1386	13423	86049	44574	263563
Reconstruct in ID	115225	82.9 %	40.6 %	86739	1371	10398	30223	39713	168445
$200\,\text{ns} < t < 100\,\mu\text{s}$	112621	81.1 %	48.6 %	78779	1368	8657	30165	0	118970
Likelihood	105032	75.6 %	92.1 %	5919	134	1106	1827	0	8986

Table 4.4: Table of signal and background true and selected neutron capture candidate rates for 10^{21} POT of running E61 at the 2.5° off-axis position. This corresponds to 175 402 selected primary events. Backgrounds include triggers from neutrino interactions in surrounding material (sand), cosmic rays, neutrino interactions in the tank with no visible primary event (NC), radioactive decay of impurities in PMT glass and water, and other non-neutron capture triggers from the signal primary event.

an even higher signal purity, allowing for less strict cuts to increase the amount of data available. However, in order to achieve the high purities and efficiencies seen here, a selection method has had to be used that produces efficiencies (and therefore event rates) that are highly model dependent, as mentioned above. To deal with this, a non-trivial method of background and efficiency correction needs to be used.

4.3 Background and efficiency correction

In order to understand the origin of the model dependencies introduced through the selection criteria of the previous section, and how they can be addressed, it is useful to look at the various sources of systematic effects that cause the shifts from the distributions of true variables to the distributions of observed variables. If the observables of interest are defined as the number of neutron captures and their positions relative to the primary event, then there are four main sources of these effects:

1. Increase in neutron multiplicity due to addition of background events.
2. Decrease in neutron multiplicity due to efficiency of signal events:
   (a) from neutrons failing to trigger or reconstruct
   (b) from neutrons failing to pass the selection cuts
3. Changes in reconstructed neutron capture position due to detector and reconstruction resolutions

Fundamentally, the size of each of these effects varies only according to the position of the neutron capture within the detector, *e.g.* the background rates, triggering efficiency and reconstruction resolutions all depend on the distance from the tank wall. In terms of the observables defined above, however, this dependence translates into a dependence on the capture position relative to the primary event, which is where the model dependence comes from: The overall effect of the above listed systematics depends on the capture position relative to the primary event, which depends on the direction neutrons are ejected from the nucleus and their momenta (which directly affects the distance they travel while thermalising before capturing), which both have large model uncertainties. The fact that these effects depend on the model due to the effective dependence on the distance d and angle θ of the emitted neutron means that even if only the total multiplicity is of interest, the multiplicity must be measured as a function of d and θ in order to correct for the effects in a way that takes this dependence into account.

In effect, the model dependence can be removed by performing the measurement as a function of d and θ, followed by a correction of the systematic effects which also depend on d and θ. The model dependence is effectively removed due to the fact that, once the position of the capture relative to the primary event is specified, *i.e.* the position of the capture within the tank is fixed, the size of the above effects for a given event do not depend on the models' predictions, only on the understanding of the detector's capabilities and the background rates at that position. This requires a thorough understanding of the how each of the above effects depends on the position within the tank. While Items 1 and 2b in the above list could be calculated using the likelihoods described in the previous section, which are required to perform the

selection anyway, a thorough understanding of Items 2a and 3 depend on the calibration programme of the detector, which is essential to producing a valid final result.

Performing the correction required to remove the model dependency is more complex for multiplicity measurements; whereas it is usually only the case that detector resolution effects like Item 3 cause migration between bins, with the background and efficiency effects of Items 1 and 2 only causing an increase or decrease in the observed event rate, for a multiplicity measurement all of these effects cause migration between bins, since the rate (*i.e.* multiplicity) is itself an observable whose distribution is being measured. So to correct for these effects, rather than simply subtracting the expected background rates and dividing by the expected efficiency, a method is required to correct for bin migration. In this analysis, the iterative unfolding method of D'Agostini[3] [112] is used, with the implementation provided by RooUnfold [113]. To simplify the analysis, the neutron capture position observables are left as reconstructed quantities, meaning that only Items 1 and 2 are corrected for and not Item 3, however a full analysis also unfolding the detector resolutions on capture position should be possible using the same approach.

The basic principle of this unfolding method is as follows: Both the true and observed distributions being measured are binned into N truth bins $T_i, i = 1 \dots N$ and M observed bins $O_j, j = 1 \dots M$ (here it is assumed that $N = M$). It is then assumed that the effects in Items 1 to 3 above are known and well understood, which allows the calculation of a response matrix describing the conditional probability $P(O_i|T_j)$ of an observation in bin O_i given that the truth was in bin T_i. The aim of unfolding is to find the inverse conditional probability $P(T_i|O_j)$ to use in statistically determining the true distribution $P(T_i)$ from the observed distribution $P(O_i)$. Bayes' theorem states that

$$P(T_i|O_j) = \frac{P(O_j|T_i)P(T_i)}{\sum_k P(O_j|T_k)P(T_k)}. \tag{4.3.1}$$

The iterative unfolding method initially assumes some prior distribution for $P_0(T_k)$, which can then be updated through the iterative procedure:

$$P_n(T_i|O_j) = \frac{P(O_j|T_i)P_{n-1}(T_i)}{\sum_k P(O_j|T_k)P_{n-1}(T_k)}, \tag{4.3.2}$$

$$P_n(T_i) = \sum_j P_n(T_i|O_j)P(O_j) \tag{4.3.3}$$

After a number of iterations, $P_n(T_i)$ gives the unfolded distribution. Using too high a number of iterations in this procedure can result in the amplification of statistical fluctuations, however in the case of the multiplicities being unfolded in this analysis, where the amount of data is fairly large, the number of multiplicity bins is small and with steeply falling distributions, this has not been observed to occur.

To implement the unfolding in this analysis, tables of signal efficiency $\epsilon(x, y, z, d, \theta)$ and expected background rates $\mu(x, y, z, d, \theta)$ are calculated, as a function of the primary event position in the tank (x, y, z) and of the bins in d and θ, using the likelihoods of the previous section. With the assumption that the number of observed signal events $N_{\text{obs}}^{\text{sig}}$ follows a Binomial distribution, $N_{\text{obs}}^{\text{sig}} \sim \text{B}(N_{\text{true}}, \epsilon)$, where N_{true} is the true number

[3] This is often referred to as *Bayesian unfolding* due to its use of Bayes' theorem in constructing the method.

of signal neutron captures, and the observed background rate $N_{\text{obs}}^{\text{bg}}$ follows a Poisson distribution, $N_{\text{obs}}^{\text{bg}} \sim \text{Pois}(\mu)$, the response matrix for the observed number of neutron capture candidates N_{obs} can be calculated as

$$\begin{aligned} P(N_{\text{obs}} = n_o | N_{\text{true}} = n_t) &= \sum_{n_s=0}^{\min(n_o,n_t)} f_{N_{\text{obs}}^{\text{sig}}}(n_s; n_t, \epsilon) f_{N_{\text{obs}}^{\text{bg}}}(n_o - n_s; \mu) \\ &= \sum_{n_s=0}^{\min(n_o,n_t)} \binom{n_t}{n_s} \epsilon^{n_s} (1-\epsilon)^{n_t - n_s} \frac{\mu^{n_o - n_s} e^{-\mu}}{(n_o - n_s)!}, \end{aligned} \tag{4.3.4}$$

where $f_{N_{\text{obs}}^{\text{sig}}}$ and $f_{N_{\text{obs}}^{\text{bg}}}$ are the binomial and Poisson probability mass functions, for $N_{\text{obs}}^{\text{sig}}$ and $N_{\text{obs}}^{\text{bg}}$, respectively, and the sum over n_s is over the possible number of observed neutrons that come from signal (with the remaining observed neutrons coming from background). This response matrix can then be used to unfold the multiplicity distribution in each bin of d and θ.

The approach described here differs from typical uses of unfolding in that the unfolding matrix is generated from analytic formulae of the distributions described above. Unlike the more common case where the unfolding matrix is generated by simply filling a histogram of the relevant quantities calculated by Monte-Carlo simulation, the approach used here helps avoid the problem of over-fitting of statistical fluctuations from the simulations. Note that this means that unfolding the same simulated sample of events used in generating the unfolding matrix, to reproduce exactly the true distributions, is not relevant for the unfolding used here.

Note that this unfolding procedure is only required for multiplicity distributions; for the distributions only of d and/or θ but not the multiplicity (*i.e.* the distribution of the position of a neutron capture, regardless of how many neutron captures occur in total), the correction is much simpler: The number of neutrons observed for each event can be corrected by simply subtracting the expected background and dividing by the efficiency in each bin of d and α.

4.4 Results

For the selections described in Section 4.2, the selected neutron capture candidates are binned in the reconstructed distance d from the primary event to the capture and the cosine of the reconstructed angle θ between the direction of the beam and the direction of d, according to the binning scheme given in Table 4.5. Distributions are then found for the observed multiplicity of neutron capture candidates per event in each bin of d and $\cos\theta$, with corrections applied as described in the previous section.

Figure 4.10 shows the unfolding of the multiplicity distributions themselves for several distance and angle bins. The effect of unfolding varies between bins, but overall it is found to improve with increasing number of iterations up to five iterations, beyond which there is no significant change. The remaining results in this section that use unfolding use a fixed number of five iterations.

Bins in d [cm]	Bins in $\cos\theta$
0 – 25	-1.00 – -0.60
25 – 40	-0.60 – -0.25
40 – 50	-0.25 – 0.00
50 – 60	0.00 – 0.25
60 – 75	0.25 – 0.40
57 – 95	0.40 – 0.55
75 – 115	0.55 – 0.70
115 – 140	0.70 – 0.80
140 – 180	0.80 – 0.90
	0.90 – 1.00

Table 4.5: Bins of distance d and angle $\cos\theta$ used in E61 neutron analysis

Using the multiplicity distributions in each distance and angle bin to produce a total multiplicity distribution, for the number of neutrons observed across all bins, is a complex challenge. This is because the rates of neutrons observed at each distance and angle are far from being independent of each-other; Appendix B discusses this in more detail, along with the approaches that could be used to address the problem.

Figure 4.11 shows the neutron multiplicity as a function of distance and as a function of angle. Comparing the signal-only and signal plus background distributions it can be seen that the background is mostly included at the larger distances, as could be expected due to the majority of signal neutrons capturing closer, as well as the primary event selection ensuring that primary events are at least 1 m from the wall, which is close to where the majority of background neutrons will capture. It can also be seen that the efficiency and background correction is successfully transforming the distribution closer to the true distribution, with some shift of the capture distance towards larger d remaining. This shift is mainly due to the smearing effect of the detector resolution, which has not been corrected for in this analysis, and is seen to also occur to a lesser extent in the angular distribution.

The multiplicity as a 2D function of both distance and angle is shown in Figure 4.12. Since the plots of both Figures 4.11 and 4.12 are not functions of the neutron multiplicity itself – they show the average multiplicity as a function of distance and angle – the full unfolding method of efficiency and background correction is not required, as described in the previous section. However, as an additional check of the full unfolding method (applied for the full 3D distributions of multiplicity, distance and angle), the average multiplicity in each distance and angle bin can be found by integrating over the multiplicity axis of the unfolded 3D distribution. This is also shown in Figure 4.12, alongside the equivalent plot using the simple correction, demonstrating that both methods of correcting for efficiency and background appear to work reasonably well.

The difference between the observed and the true distributions, before and after the efficiency and background correction, are shown in Figure 4.13. The correction is seen to remove the general reduction in rates due to efficiency, while some differences remain. The main difference is the shift from shorter to longer capture distances, and from more forward going to less forward going neutrons, due to the smearing effects of detector

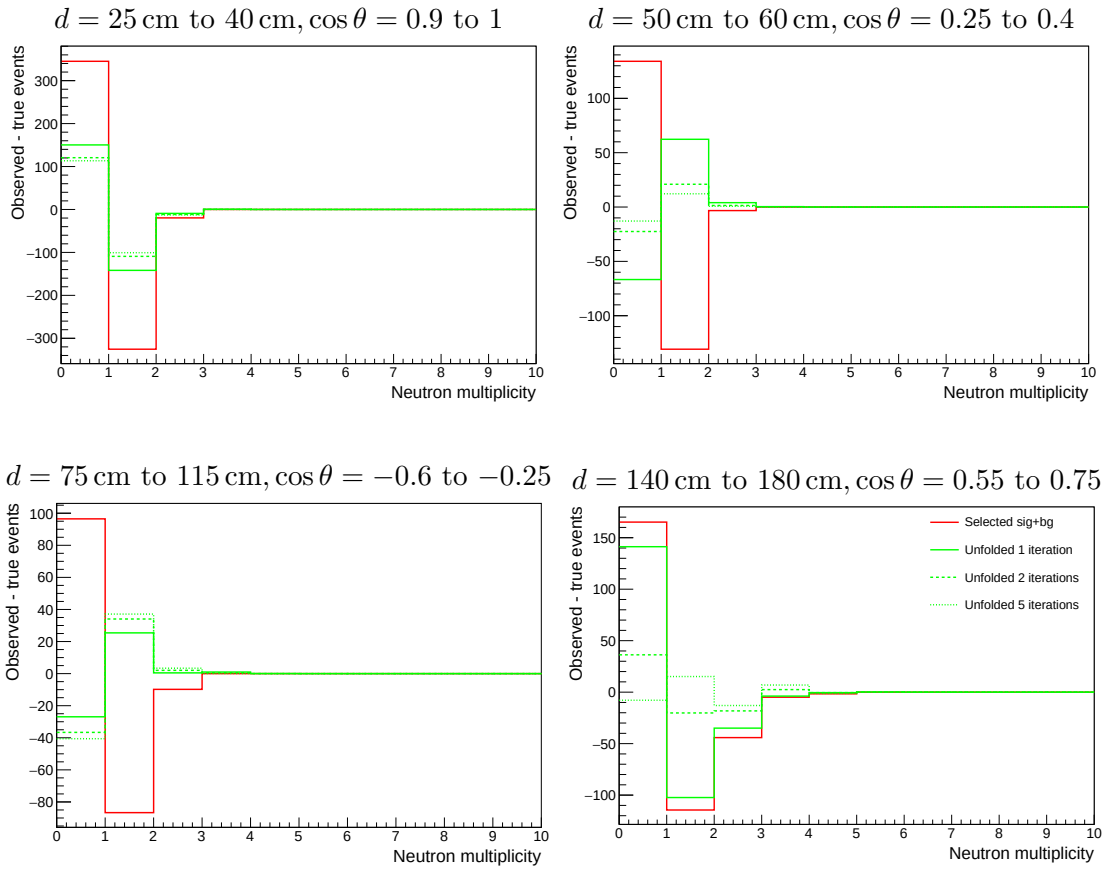

Figure 4.10: Effect of unfolding in various d and $\cos\theta$ bins of the full 3D multiplicity distribution. The difference between true and observed number of events against number of neutron captures is shown for selected signal plus background neutron capture candidates (red) and the unfolded rates after 1, 2 and 5 iterations (green solid, dashed and dotted respectively).

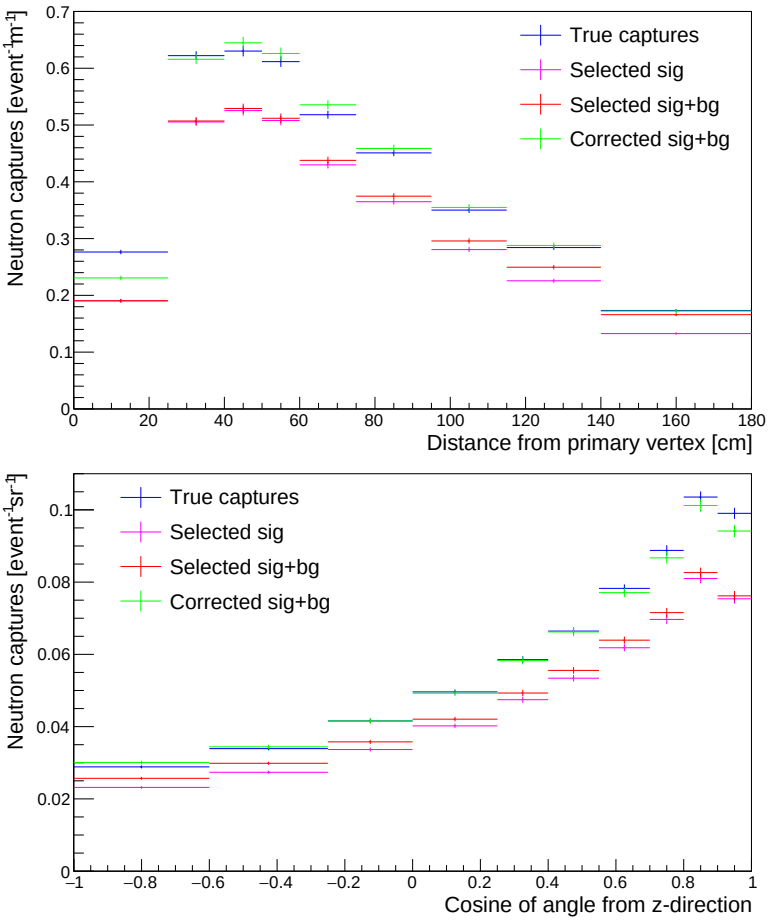

Figure 4.11: Neutron multiplicities as functions of distance d and of angle θ. Shown in blue is the true distributions, as a function of the true distance and angle from primary event. The observed signal-only distributions are shown in magenta, the signal with background distributions shown in red, and the background and efficiency corrected distributions shown in green, all as functions of the reconstructed distance and angle from the primary event. Errors on all distributions are statistical only.

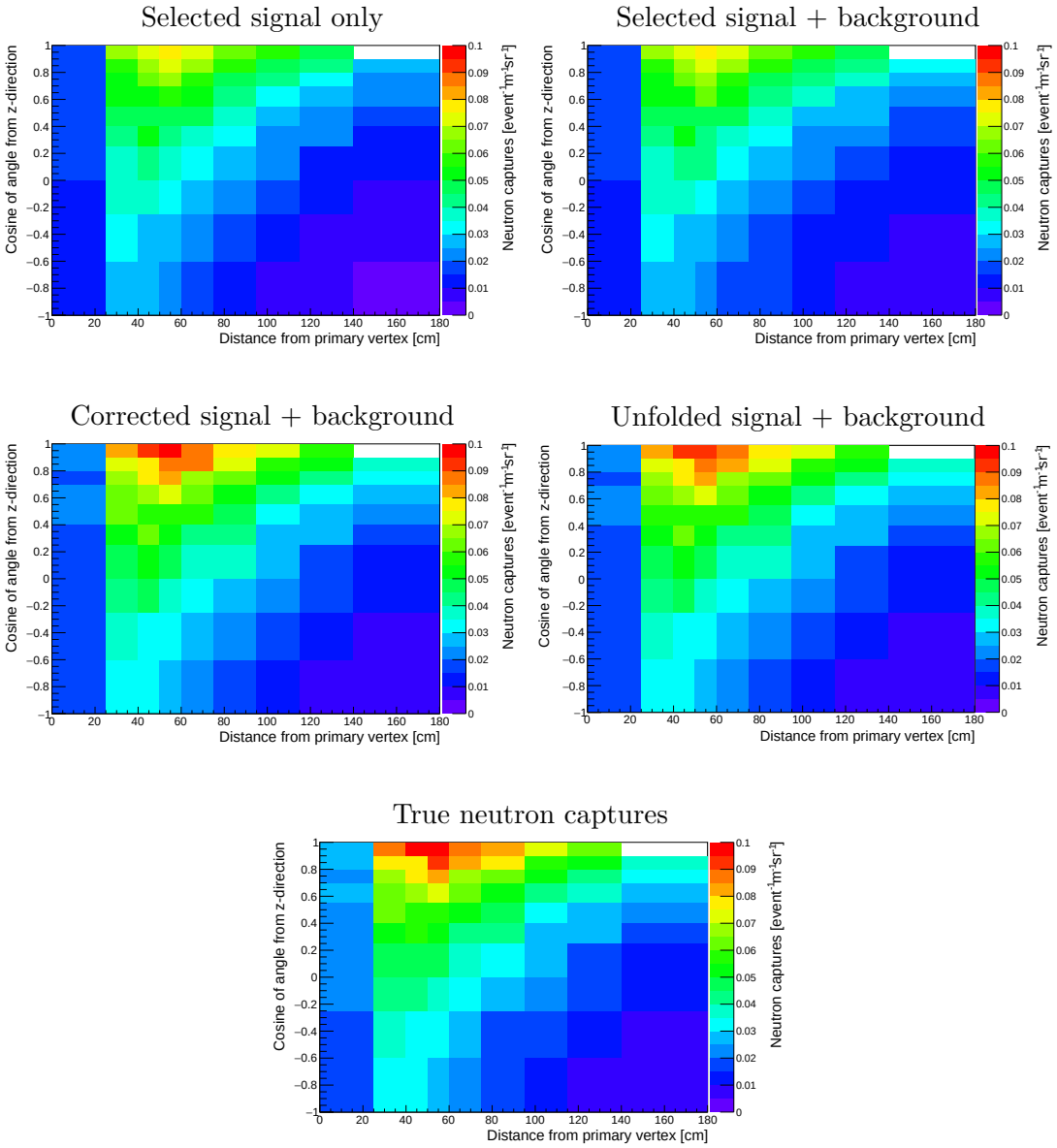

Figure 4.12: Neutron multiplicity as a function of distance d and angle θ. The observed signal-only distribution is shown on the top left and the signal with background distribution shown on the top right. The background and efficiency corrected distributions are shown in the middle, with the correction without unfolding on the left and the correction with unfolding on the right. All these distributions are given functions of the reconstructed distance and angle from the primary event. Also shown on the bottom is the true distribution, as a function of the true distance and angle from primary event.

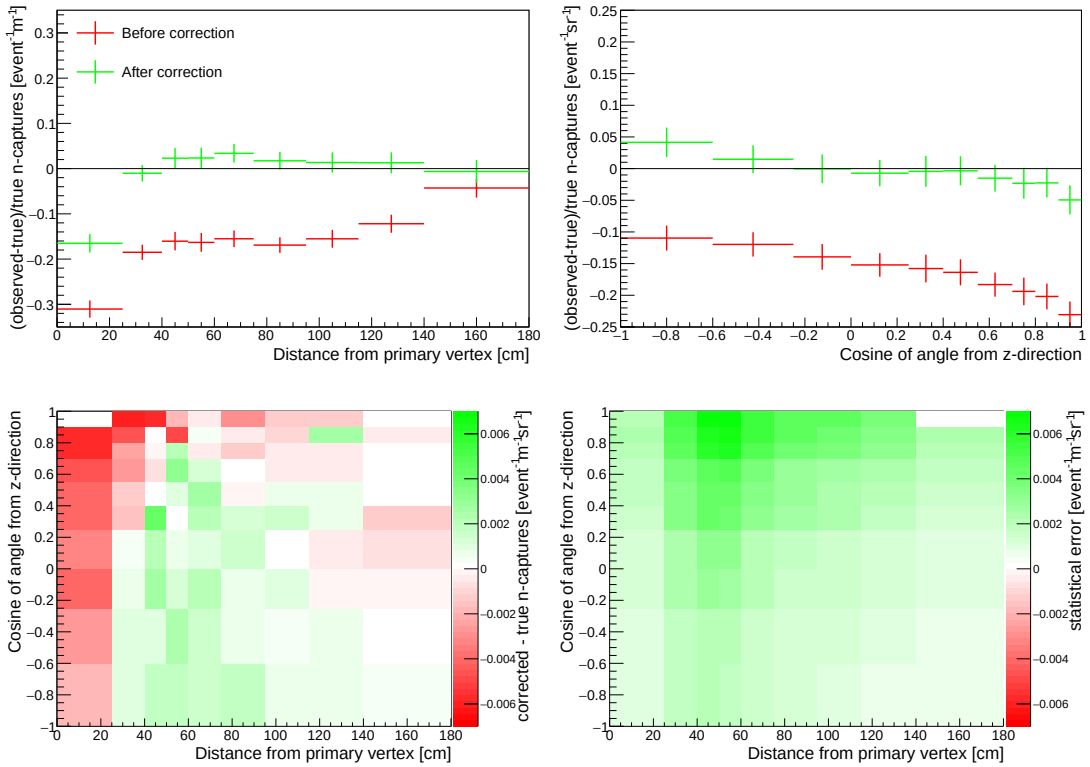

Figure 4.13: The difference between the observed and the true distributions of neutron capture distance (top left) and angle (top right), before and after the efficiency and background correction, with statistical errors, and the difference between the corrected and true 2D distribution (bottom left) with its statistical errors (bottom right).

resolution on the neutron capture position, which is not accounted for in the unfolding procedure used here. An extension of this procedure to account for these detector effects on the distance and angle, unfolding these quantities as well as the multiplicity at each distance and angle that is currently unfolded, should remove these effects and bring the overall difference to within the statistical errors. Already it can be seen that except at the extremes of the distributions the difference after unfolding is consistently smaller than the statistical errors; while the worst case is a 15 % reduction in the rate at the shortest distance and a 5 % reduction of the most forward going neutrons, in all bins other than the shortest distance (0 cm to 25 cm) and the two extremes in angle ($-1 < \cos\theta < -0.6$ and $0.9 < \cos\theta < 1$) the difference is within the statistical errors of around 2.5 %.

Conclusion

The intermediate water Cherenkov detector for Hyper-K aims to produce measurements to help constrain the systematic uncertainties at the far detector. In the previous chapter, the reduction in errors on oscillation analyses was seen when including these measurements, with additional information provided through neutron tagged samples.

In this chapter, a proof-of-concept analysis has shown that very pure samples of Gadolinium neutron captures in the IWCD can be produced, despite the significant background rates, while still retaining a large portion of the signal. In addition to providing neutron tagged samples, for which a demonstration of their effect on oscillation physics was given in the previous chapter, the large neutron samples also provide distributions of neutron capture distance, angle and multiplicity, giving additional input to various analyses at the far detector of Hyper-K.

The distributions can help understand the neutron capture signal at the far detector, to help improve the purity of samples produced there, as well as to enhance the ability to use neutron tagging at the far detector to reduce backgrounds for nucleon decay searches. The detection of neutrons at the Hyper-K far detector – whether through neutron captures on Gadolinium in doped water or on Hydrogen in undoped water – depends on understanding the positions the neutron are expected to capture. Understanding this through measurements like those presented in this chapter – the distance of captures from the primary event and the angle the neutron travels relative to the incoming neutrino – will allow for efficient selection of neutrons in the far detector, which will in turn provide purer samples for neutrino analyses, including separation of $\nu/\overline{\nu}$ discrimination which is not otherwise possible in water Cherenkov. This efficient selection of neutrons will also help maximise the sensitivity to nucleon decay by identifying and removing as much as possible of the main background coming from atmospheric neutrinos, as described in Section 2.5.2.

Additionally, these distributions of distance and angle of neutron captures can provide information related to the magnitude and direction of outgoing neutrons' momenta. Since neutrino interaction models currently have very high uncertainty in this area, improvements could be made to these models using the new information from neutron measurements. With the systematic uncertainties in the interaction models one of the most significant sources of error in oscillation analyses, any improvement to these models will help to improve the sensitivities of these analyses.

Although the analysis presented here has only been performed for the E61 CCQE ν_μ sample, the tools developed for this can be extended to other samples, to provide estimates of the ability to resolve the differences in the distributions for these other samples, and therefore the ability to use neutron captures to increase separation of interaction modes and neutrino flavours. The analysis can also be extended to the other off-axis angle positions of E61, to study the ability to use linear combinations of these positions to effectively measure different desired neutrino energy fluxes; for example, a combination could be chosen to more closely match the atmospheric neutrino flux in order to better understand the use of neutron tagging to reduce atmospheric neutrino backgrounds.

In order to fully study the sensitivities to neutrons of E61, a thorough understanding of the systematic uncertainties involved in neutron captures is required, which has not been included here. The number and type of these systematics depends on the analysis being performed, but in all cases the most important sources of uncertainty come from the modelling of neutrons propagating in the detector and their capture on Gadolinium, which was briefly investigated in Section 4.1.1.1. Additional systematics come from the methods used to separate signal from background; this includes both the modelling of backgrounds, or the ability to measure them in E61 independently through

background-only measurements, as well as an understanding of the detector resolutions and calibration which has a significant effect on the likelihood method used to remove backgrounds and also the background and efficiency corrections applied later on. Other sources of systematic errors are largely the same as other analyses of E61, such as the neutrino flux and interaction cross-sections, however since the overall primary event rate only affects the size of the samples and is not part of the measurement itself, these are less critical.

While further study is required to fully understand the benefits of Gadolinium doping and the neutron capture signal in the IWCD, the results of this chapter and the previous chapter have shown that high-quality neutron measurements are feasible and that they provide clear benefits to the Hyper-K project.

Chapter 5

Sensitivities and synergies of T2HK and DUNE

Introduction

For any future experiment, it is important to understand its capabilities not just in isolation, but also in the context of existing running experiment and future planned or proposed experiments. Through previous and current oscillation experiments, existing knowledge of the neutrino sector has undergone a sea-change over the last decade. The oscillation mechanism has been well established as the explanation of the anomalous solar and atmospheric neutrino flavour ratios, and the paradigm has been subjected to scrutiny from long-baseline accelerator and reactor experiments resulting in a measurement of the final mixing angle θ_{13} [13, 14, 114, 115]. Although some short-baseline anomalies still remain unexplained [116–118], the oscillation mechanism has leapt many hurdles to become a part of the new Standard Model (SM). However, some significant unknowns remain: the ordering of neutrino masses, the existence and extent of CP violation (CPV) in leptonic mixing, and the precise value, including crucially the octant, of θ_{23}. In addition, the current precision on the oscillation parameters is insufficient to rule out many theoretical models, for example those discussed recently in [2, 119–121].

With the intention of building on the progress of the oscillation programme, the international community has conceived of a range of future facilities with the potential to explore the final unknowns in the conventional oscillation paradigm, and to hunt for tensions in the data which might indicate that a richer extension of the SM is required. There are three major strands in the future experimental neutrino oscillation programme: short-baseline experiments such as those comprising the SBN programme [122], intermediate baseline reactor facilities, RENO-50 and JUNO [123–125], and long-baseline experiments such as LBNF-DUNE and T2HK [18, 126–130]. In this chapter the focus is on these latter two proposals for novel long-baseline facilities: Long-Baseline Neutrino Facility-Deep Underground Neutrino Experiment (LBNF-DUNE, referred to subsequently as DUNE) and the beam programme of Hyper-Kamiokande (referred to here as T2HK). DUNE is the flag-ship long baseline experiment of the Fermilab neutrino programme [18, 130]. It consists of a new beam sourced at Fermilab and a detector complex at Sanford Underground Research Facility (SURF) in South Dakota separated by a distance of 1300 km. Over this distance, neutrinos produced in the decays of secondary particles from proton collisions at Fermilab will propagate, undergoing oscillations and scattering processes in the matter of the Earth. The appreciable matter effects will modify the probability of detecting a given flavour of neutrino, in a way that will ultimately make the facility highly sensitive to the mass ordering, parametrized by the sign of Δm^2_{32}, while the broad spectrum of events arising from its on-axis flux also allows for significant sensitivity to the unknown CPV phase δ. The detector will use Liquid Argon Time Projection Chamber (LAr-TPC) technology, allowing for strong event reconstruction. As a result, a high signal to background ratio is expected. In contrast, as described in detail in Chapter 2, T2HK [129] was conceived with a smaller baseline of 295 km and a different detector technology, employing Water Cherenkov technology at a significantly larger scale. Matter effects for this facility will be smaller due to the shorter baseline (although non-negligible), and the significantly enhanced event rate will allow for a high-statistics comparison between neutrino and anti-neutrino modes, searching for fundamental asymmetries due to the CP violating phase δ. Another key difference between T2HK and DUNE is the narrow-band beam of T2HK versus the wide-band beam of DUNE. While the narrow-band beam provides

an energy spectrum which peaks in the oscillation maximum and at the energy where the clean CCQE interactions are dominant, as described in Section 2.1, a wide-band beam can provide a larger total neutrino flux with the possibility of measuring neutrino oscillations at different energies from one beam, at the expense of a larger uncertainty on the incoming neutrino energy. These two approaches can therefore be expected to provide complementary information.

Much work has been done over the years assessing the physics reach of T2HK [129, 131, 132] and DUNE [18, 133–136] (along with its predecessor designs LBNE [130, 132, 137–139] and LBNO [132, 140, 141]). This chapter is based on the work published in [1], where the physics sensitivity of DUNE and T2HK is revisited for key measurements relating to the mass ordering, δ phase and the mixing angle θ_{23}, focusing in particular on the combined reach of these designs. Recently, as the designs for T2HK and DUNE have matured, both collaborations have been considering significant alterations to the benchmark proposals in [129] and [18, 133]. The nuPIL (neutrinos from a PIon beam Line) design [142–144], developed by a working group of the DUNE collaboration, is a novel beam technology building on accelerator R&D work done for the neutrino factory [145]. It foresees the collection and sign selection of pions from a conventional beam, which are directed though a beam line and decay to produce neutrinos. This selection and manipulation of the secondary beam forces unwanted parent particles out of the beam resulting in a particularly clean flux. This screening process presents a particular advantage over conventional neutrino beams, where the contamination of the flux due to mesons of the wrong sign can limit the sensitivity of the antineutrino channel. In this case, the contamination from intrinsic ν_μ is effectively enhanced by the cross-section differences. This increases the relative number of wrong-sign events, and reduces the signal over background ratio. The simulated flux is also notably narrower than the DUNE reference design (although this could be changed through modification of the design) which will alter the sensitivity to the oscillation probability. In a parallel development, T2HK has reconsidered the location of its second detector module. The current design divides the detector into two modules installed at Kamioka following a staged implementation [17]: an initial data-taking period would use a single tank during which the second tank would be constructed and would start taking data after 6 years to further boost the statistical power of the experiment. Instead of this plan, the suggestion has been made to locate the second tank in South Korea at a baseline distance of between 1000 km to 1300 km from J-PARC [69]. This would allow T2HK + Korea (T2HKK) to collect data from two different baselines and with two different off-axis angles (and consequently energy spectra), crucially altering the phenomenology of the experiment. Work on both of these proposals is ongoing.

Although the question of the combined sensitivity of DUNE and T2HK has been studied before (most recently in [146]), this work brings three new elements to the discussion. Firstly, the significant redesign and development work that has been performed in the last few years on both designs has been incorporated. The simulation of T2HK is particularly noteworthy, departing significantly from those used in previous comparable analyses [146] by incorporating up-to-date information about detector performance from the collaboration's in-house simulation, and has been carefully calibrated against previously published results. Secondly, the precision measurement of δ and its phenomenology is thoroughly addressed, often deemed a secondary question in earlier studies that focus mainly on the discovery of CP violation, but one which is increasingly central to the

aims of the long-baseline programme. Finally, a detailed discussion is provided of the differences between the two designs as well as their possible redesigns (nuPIL, T2HKK) and a quantification of their complementarity in an attempt to identify the optimal choice from a global perspective.

This chapter begins with a brief recap of the relevant phenomenology of oscillation physics in Section 5.1. In Section 5.2, descriptions are provided of the details of DUNE and T2HK (including their alternative designs) taken into account in these simulations. Section 5.3 is devoted to the results of the simulations assuming the standard configurations of each experiment which look at mass ordering sensitivity, CP violation discovery, the ability to exclude maximally CP violating values of δ, the expected precision on θ_{23} and the ability to resolve the octant. An analysis of the complementarity for precision on δ is presented in Section 5.4, taking care to discuss the interplay of factors which influence this measurement. In Section 5.5, these physics goals are reconsidered in light of the alternative deigns for DUNE and T2HK.

5.1 Oscillation phenomenology at DUNE and T2HK

Long-baseline experiments such as DUNE and T2HK aim to improve knowledge of the PMNS mixing matrix U, as well as the atmospheric mass-squared splitting Δm^2_{32}, by the precision measurement of both the appearance $\nu_\mu \to \nu_e$ and disappearance oscillation channels $\nu_\mu \to \nu_\mu$, as well as their CP conjugates. In this section, the key aims of the long-baseline program will be discussed, along with the important design features of these experiments which lead to their sensitivities. To facilitate this discussion, the approximation of the appearance channel following [147] is used, which is derived by performing a perturbative expansion in the small parameter $\epsilon \equiv \Delta m^2_{21}/\Delta m^2_{31} \approx 0.03$ under the assumption that $\sin^2\theta_{13} = \mathcal{O}(\epsilon)$[1]. The expression for the oscillation probability is decomposed into terms of increasing power of ϵ,

$$P(\nu_\mu \to \nu_e; E, L) \equiv P_1 + P_{\frac{3}{2}} + \mathcal{O}\left(\epsilon^2\right), \tag{5.1.1}$$

where E is the neutrino energy, L the oscillation baseline, and the ordered terms $P_n = \mathcal{O}(\epsilon^n)$ are given by

$$P_1 = \frac{4}{(1-r_A)^2}\sin^2\theta_{23}\sin^2\theta_{13}\sin^2\left(\frac{(1-r_A)\Delta L}{2}\right), \tag{5.1.2}$$

$$P_{\frac{3}{2}} = 8J_r\frac{\epsilon}{r_A(1-r_A)}\cos\left(\delta+\frac{\Delta L}{2}\right)\sin\left(\frac{r_A\Delta L}{2}\right)\sin\left(\frac{(1-r_A)\Delta L}{2}\right), \tag{5.1.3}$$

where $J_r = c_{12}s_{12}c_{23}s_{23}s_{13}$, $r_A = 2\sqrt{2}G_{\mathrm{F}}N_eE/\Delta m^2_{31}$ and $\Delta = \Delta m^2_{31}/2E$. Using the same scheme, the disappearance channel can be written at leading order as

$$P(\nu_\mu \to \nu_\mu; E, L) = 1 - \sin^2(2\theta_{23})\sin^2\left(\frac{\Delta L}{2}\right) + \mathcal{O}(\epsilon). \tag{5.1.4}$$

For both channels, equivalent expressions for antineutrino probabilities can be obtained by the mapping $r_A \to -r_A$ and $\delta \to -\delta$.

[1] For alternative schemes of approximation, see [148–151].

5.1.1 Mass ordering, CPV and the octant of θ_{23}

The sensitivity of long-baseline experiments to the questions of the neutrino mass ordering, the existence of CPV and the octant of θ_{23}, are by now well studied topics (for a recent review see *e.g.* [152]). To help clarify the role of the designs of DUNE and T2HK, as well as their possible modifications, it is useful to understand how experiments on these scales derive their sensitivities using the approximate formulae expressed by Equations (5.1.2) to (5.1.4).

The dependence on the sign of Δm^2_{31}, and therefore the mass ordering, arises at long-baseline from the interplay with matter, where forward elastic scattering can significantly enhance or suppress the oscillation probability. This is governed by the parameter r_A in Equation (5.1.1), which for the experiments of interest is small, and goes to zero in the absence of matter. Changing from Normal Ordering (NO, $\Delta m^2_{31} > 0$) to Inverted Ordering (IO, $\Delta m^2_{31} < 0$) requires the replacements $\Delta \to -\Delta$ and $r_A \to -r_A$. However, in vacuum ($r_A = 0$) the leading-order term in Equation (5.1.1) remains invariant under this mapping. This invariance is broken once a matter term is included ($r_A \neq 0$), and the oscillation probability acquires a measurable enhancement or suppression dependent on the sign of Δm^2_{32}. The size of this enhancement increases with baseline length, and this effect is expected to be very relevant for appearance channels at a long-baseline experiment $\nu_\mu \to \nu_e$ and $\bar{\nu}_\mu \to \bar{\nu}_e$. However, the determination of the mass ordering is further facilitated by the contrasting behaviour of neutrinos and antineutrinos. Due to the dependence on r_A, larger values of the matter density cause an enhancement in the probability for $\nu_\mu \to \nu_e$ oscillation at the first maximum for NO, whilst suppressing the probability for $\overline{\nu}_\mu \to \overline{\nu}_e$. This behaviour is reversed for IO, with neutrinos seeing a suppression and antineutrinos, an enhancement. Moreover, matter effects also affect the energies of the first oscillation maxima for neutrinos and antineutrinos. Through precise measurements around the first maxima, these shifts can be observed allowing long-baseline oscillation experiments to determine the mass ordering. It is worth noting that an analogous analysis can be applied to the oscillations of atmospheric neutrinos, which can come either directly from the atmosphere above or through the Earth below, with the variable sized matter effect (and baseline) that this implies. Therefore the observation of atmospheric neutrinos at the same detectors as used in T2HK and DUNE could provide significant additional sensitivity to the mass ordering. In this study, however, only the long-baseline accelerator neutrino analysis has been included.

To detect CPV in neutrino oscillations an experiment requires sensitivity to δ. Unfortunately, the leading order appearance probability is independent of the CP phase δ, with CP asymmetries between neutrino and antineutrino channels first appearing with the subdominant term $P_{\frac{3}{2}}$. In the presence of a background medium, CP violating effects are instead introduced in P_1; however, these offer no sensitivity to the fundamental CP violating parameter δ, arising instead from the CP asymmetry of the background medium itself via the parameter r_A. As the sensitivity to δ is subdominant and masked by CP asymmetry arising from matter effects, extracting the CP phase is a more challenging measurement, requiring greater experimental sensitivity. Long baseline (LBL) experiments can obtain sensitivity to δ by looking not only at the first maximum but also at the spectral differences between CP conjugate channels. In particular, an important role is played by low-energy events in the sensitive determination of δ [139, 153–155]: around the second maximum, CP dependent terms of the oscillation probability are more sig-

nificant. Although accessing these events can be a challenging experimental problem, and low statistics or large backgrounds could limit their potential [153], their benefit is clear from recent experimental work [156].

The atmospheric mixing angle is known to be large and close to maximal $\theta_{23} \approx \pi/4$, but it is not currently established whether it lies in the first octant $\theta_{23} < \pi/4$ or the second octant $\theta_{23} > \pi/4$. It is seen in Equation (5.1.2) that the appearance channel is sensitive to the octant. However, it is also seen that changing the octant enhances or suppresses the first maximum of the appearance channel in much the same way as the matter enhancement. For this reason, the sensitivity to these two effects can be expected to be correlated and difficult to disentangle; however, this correlation will be reduced when data from both neutrino and antineutrino is available as this effect is the same in both CP conjugate channels. The determination of θ_{23} is also known to be beset by issues of degeneracy with δ which can complicate its determination [152, 157, 158]. As both of these parameters enter the second-order terms in Equation (5.1.2), the freedom to vary δ can be used to mask the effects of a wrong octant, making their joint determination more challenging. Fortunately, a precise measurement of $\sin(2\theta_{23})$ is possible through its leading-order dependence of the disappearance channel, seen in Equation (5.1.4). This helps to break this degeneracy and, along with spectral information, is expected to help mitigate this problem.

5.1.2 Precision on δ

Although the question of the *existence* of leptonic CP violation often dominates discussions about δ, the precision measurement of δ could prove to be the most valuable contribution of the long-baseline programme. To determine the existence of fundamental leptonic CP violation it suffices to exclude the CP conserving values $\delta = 0$ and $\delta = \pi$, those values corresponding to a vanishing Jarlskog invariant. Therefore the discovery potential of a facility to CP violation is fundamentally linked to the precision attainable for measurements of δ in the neighbourhood of 0 and π. However, the question of precision on δ goes beyond CP violation discovery. Many models of flavour symmetries, for example, are consistent with the known oscillation data and make predictions for δ.[2] No experiment on comparable time-scales will be able to compete with precision measurements of δ from DUNE and T2HK.

An understanding of precision measurements of δ can be developed analytically following the approach of [164]. The assumption can be made that the precision is dominated by events at a fixed energy, which could be due to a narrow beam or simply the predominance of the first maximum, and implies the number of events is proportional to the oscillation probability $P(\nu_\alpha \to \nu_\beta; E)$. Under the assumption that the statistical uncertainty dominates, and the number of events in that bin fluctuates in a Poissonian manner, the range of $\Delta\delta$ which corresponds to this statistical uncertainty can be inferred,

$$\Delta\delta \propto \frac{\sqrt{P}}{\frac{\partial P}{\partial \delta}}, \tag{5.1.5}$$

[2] For example, recent studies of mixing sum rules can be seen as predicting δ for long-baseline experiments [159–163]. For many more examples of predictive flavour symmetric models, see *e.g.* the review [44].

where the contribution from the higher order terms $\mathcal{O}\left(\Delta\delta^2\right)$ has been neglected. Combining neutrino and anti-neutrino channels, a simple formula can be derived for the precision on δ [164],

$$\Delta\delta \propto \frac{1}{\sqrt{1+\cos\left(2\delta\right)}}. \tag{5.1.6}$$

This approximate formula well describes the qualitative features of the precision on δ which are shown in Figure 5.1, and its general shape has been found in simulations of specific experiments [164].

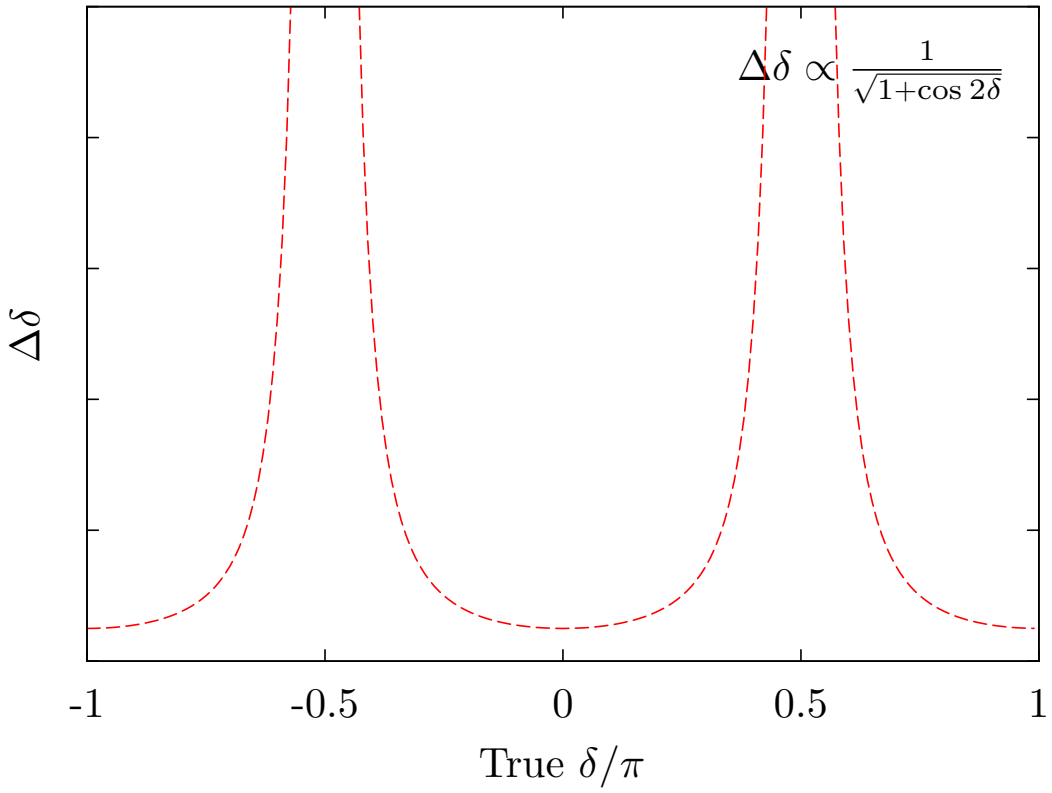

Figure 5.1: $\Delta\delta$ against δ for the measurement of neutrino and antineutrino appearance channels in vacuum. This is given by the approximation Equation (5.1.6) as discussed in more detail in [164]. Although matter effects and finite beam width modifies this shape, its characteristic peaks will still be discernible.

A notable feature of the analytic formula in Equation (5.1.6) is the total loss of sensitivity at values of δ which correspond to maximal CPV, $\delta \in \{\frac{\pi}{2}, \frac{3\pi}{2}\}$. These are seen as vertical asymptotes in Figure 5.1. Clearly this marks a breakdown in the approximations that have been made, but the general fact that the maximal CPV ($\delta = \pm\frac{\pi}{2}$) corresponds to the worst precision in δ is true in more realistic simulations. This can be understood qualitatively with reference to the approximate oscillation probability given in Equation (5.1.3). Looking at the CP sensitive term at energies around the first maximum, where $\Delta L/2 \approx \pi/2$, the probability can be approximated by

$$P_{\frac{3}{2}} \approx -8J_r \frac{\epsilon}{r_A(1-r_A)} \sin\delta \sin\left(\frac{r_A\Delta L}{2}\right) \sin\left(\frac{(1-r_A)\Delta L}{2}\right).$$

The highest sensitivity to δ is found when this function is most sensitive to changes in δ, information naturally encoded in the function's first derivative. Due to the sinusoidal nature of the function, when the CP term has its largest effect ($|\sin\delta| = 1$), it is at a maximum and consequently its gradient is at a minimum. Therefore, it is expected that the errors on δ will be small around 0 and π, when even though the absolute size of the CP sensitive terms are small, they are most sensitive to parameter shifts. Taking matter into account leads to a slight modification of the location of the worst sensitivity [164]. Assuming the measurement is close to the first oscillation maximum, and introducing a dimensionless parameter ξ to describe the deviation from this point (where $\xi = 0$ corresponds to the first maximum), the relevant parameter governing the phase of the sinusoidal terms can be expressed by

$$\Delta L = \pi \frac{1+\xi}{1-r_A}. \tag{5.1.7}$$

The value of δ for which the worst sensitivity is expected can then be found by minimising the gradient of Equation (5.1.3), which occurs for the values

$$\delta \approx -\frac{\pi}{2}\frac{1+\xi}{1-r_A} + \pi n, \tag{5.1.8}$$

for $n \in \mathbb{Z}$. From this formula it is clear that the value of δ with the worst sensitivity shifts away from $\frac{(2n+1)\pi}{2}$ in a direction governed by the signs of r_A and ξ. Specifically, the dependence on r_A means that the neutrino and anti-neutrino mode sensitivities at fixed energy have their worst sensitivity for different true values of δ. Running both CP conjugate channels in a single experiment allows each channel to compensate for the poorer performance of the other at certain values of δ, helping to smooth out the expected precision. In this way, the multichannel nature of LBL experiments allows for a greater physics reach than a single channel experiment.

The argument above assumed that all events came from a fixed energy defined implicitly by ξ in Equation (5.1.7). Due to the dependence on ξ in Equation (5.1.8), having information from different energies will also be complementary, acting analogously to the combination of neutrino and antineutrino data by mitigating the poorest performance. Although all LBL experiments aim to include the first maximum, where event rates are highest, none have a purely monochromatic beam and so-called wide-band beams include considerable information from other energies. Therefore such experiments can be expected to avoid the significant loss of sensitivity predicted by the simple analytic formula. It can be inferred, however, that a narrow beam focused on the first maximum in the presence of small matter effects should have a worse sensitivity at maximal values of δ compared to CP conserving values [164].

With reference to the traditional designs of T2HK and DUNE, from the above discussion it can be inferred that T2HK can be expected to have a greater range of expected precisions as δ is varied than DUNE. In particular, due to its narrower beam and small matter effects, markedly poorer performance is expected for T2HK at $\delta \in \{-\frac{\pi}{2}, \frac{\pi}{2}\}$ than at $\delta \in \{0, \pi\}$. DUNE on the other hand will be less variable as its broad band mitigates the total loss of sensitivity at certain energies, and its large matter effect helps to stabilise performance, but it can be expected to see its worst sensitivity at values of δ slightly displaced from 0 and π, where the sensitivity at the first maximum is worst. This suggests a degree of complementarity of the wide-band and narrow-band beams when

it comes to precision measurements of δ: a narrow-band focused on the first maximum is optimal for precision around 0 and π (and by implication, for CPV discovery) while a wide-band beam should perform better for precision measurements around $\delta = \pm\frac{\pi}{2}$. This general behaviour will be relevant not only for the traditional designs of DUNE and T2HK, but also their possible redesigns: nuPIL could lead to a narrowing of the neutrino flux, and T2HKK could see a wider-band component in its flux, or a narrow-band component focused away from the first maximum. The interplay of these factors will be explored in more detail in Section 5.4.

5.2 Simulation details

To better understand the sensitivities and complementarity of DUNE and T2HK (including their potential redesigns), simulation have been performed of the experiments in isolation and in combination. The General Long Baseline Experiment Simulator (GLoBES) libraries [165, 166] have been used and the following sections describe the features of the modelling of the two facilities and the statistical treatment.

5.2.1 DUNE

The DUNE experiment consists of a new neutrino source, known as Long Baseline Neutrino Facility (LBNF), a near detector based at Fermilab and a LArTPC detector complex located in SURF a distance of 1300 km away. Several variants of the LBNF beam have been developed. In this work, three neutrino fluxes are studied: a 2-horn reference beam design [18], a 3-horn optimised beam design [167], and the neutrinos from a PIon beam Line (nuPIL) [142–144]. All three fluxes used in these simulations are shown in Figure 5.2.

The reference beam uses a front-end design based on NuMI, which uses 2 magnetic horns, but with a thickened target to withstand the higher power beams of LBNF. In the GLoBES simulation, the proton energy is taken to be 80 GeV, the beam power 1.07 MW, and 1.47×10^{21} protons on target (POT) are assumed per year. Recent development work by the DUNE collaboration has led to the design of an optimised beam. This 3-horn design is based on the reference design, but has a stronger focus on producing lower energy events, leading to a substantial increase in flux between 0.5 GeV and 4 GeV. This leads to a greater number of expected events from around the second oscillation maximum, which is well-known to be particularly sensitive to the phase δ. For this design, the proton energy is assumed to be 62.5 GeV and the POT per year is taken as 1.83×10^{21}. The nuPIL design is also considered, which has been studied by a working group of the DUNE collaboration as a potential alternative design. nuPIL foresees the collection and sign selection of pions from proton collision with a target, which are then directed though a beam line and ultimately decay to produce neutrinos. This selection and manipulation of the secondary beam forces unwanted parent particles out of the beam, resulting in lower intrinsic contamination of the neutrino (antineutrino) flux by antineutrinos (neutrinos). In particular, this will improve the signal to background ratio of the antineutrino mode compared to a conventional neutrino beam. The proton energy for this design is assumed to be 80 GeV, and the corresponding POT per year is 1.47×10^{21}. Compared to the other two designs, nuPIL offers a lower intrinsic

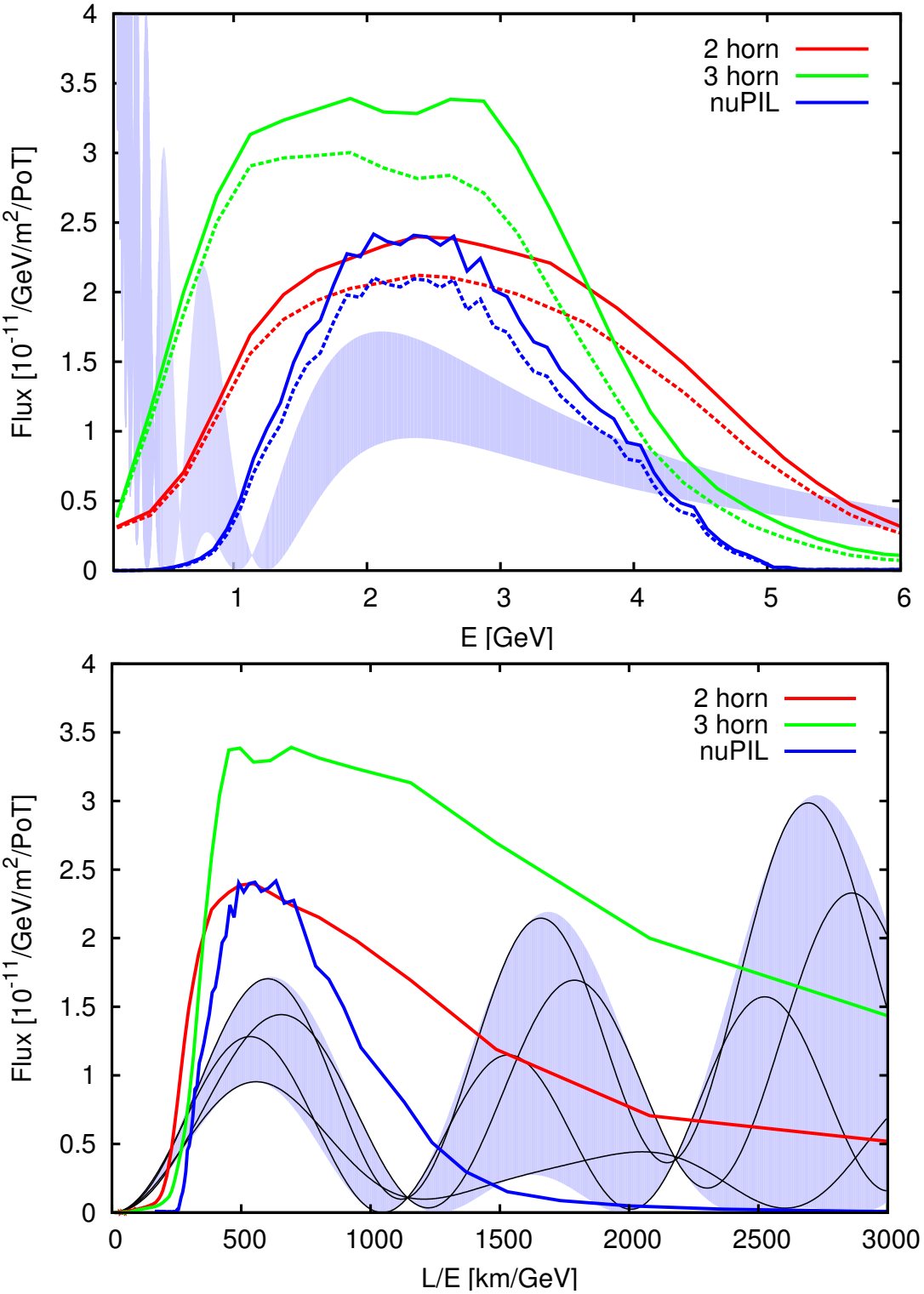

Figure 5.2: Top: ν_μ ($\overline{\nu}_\mu$) flux component in ν-mode ($\bar{\nu}$-mode) shown as solid (dashed) lines for 2-horn reference, 3-horn optimised, and nuPIL beam designs. Bottom: Fluxes for ν-mode shown as a function of L/E. In both panels, the shaded region shows the envelope of the oscillation probability as δ is varied over its full range. The black lines in the bottom panel show the probability for $\delta \in \{0, \frac{\pi}{2}, \pi, \frac{3\pi}{2}\}$.

contamination from other flavours and CP states while maintaining low systematic uncertainties. It is also noted that nuPIL expects a smaller total flux, although this might be avoidable through further design effort. Another characteristic of the nuPIL design is its notably narrower flux. As events from the second oscillation maximum are expected to be highly informative about the true value of δ, this may impact the sensitivity to δ. The coverage of first and second maxima is seen clearly in the bottom panel of Figure 5.2, where the fluxes are shown as a function of L/E. The first maximum ($L/E \approx 600\,\mathrm{km\,GeV^{-1}}$) is covered comparably well for all three flux designs, while the flux at the second maximum ($L/E \approx 1800\,\mathrm{km\,GeV^{-1}}$) varies significantly. The reference 2-horn design falls almost directly between the two alternatives: nuPIL offers far fewer events at this value of L/E and the 3-horn design, far more.

Although alternative fluxes are considered, the same detector configuration is always assumed of four 10-kiloton LArTPC detectors at 1300 km from the neutrino source. The possibility of staging is neglected, assuming that all four tanks are operational at the same time, and the expected improvement in performance throughout the lifetime of the detectors is not accounted for. LArTPC technology has a particularly strong particle identification capability as well as good energy resolution which are both crucial in providing high efficiency searches and low backgrounds. The LArTPC detector response is modelled with migration matrices incorporating the results of Monte Carlo simulations undertaken by the collaboration. These matrices quantify the migration of events from the true channel to the observed chanel, and from true to reconstructed incoming neutrino properties, due to the detector resolutions, backgrounds and efficiencies. Fourteen migration matrices are used – seven each for the disappearance and appearance channels – describing the detection and reconstruction of all three flavours of neutrino and antineutrino, as well as generic flavour blind NC events [168]. The channel specific efficiencies are taken from [18].

Both appearance and disappearance searches are included in this study. The appearance channel signal is taken as the combination of ν_e and $\bar{\nu}_e$ charged-current (CC) events. For the disappearance channel, ν_μ and $\bar{\nu}_\mu$ are studied for neutrino and antineutrino modes, respectively. The backgrounds to the appearance channel are taken as neutral-current (NC) events, mis-identified ν_μ CC interactions, intrinsic ν_e CC events, and ν_τ CC events. On the other hand, in ν_μ ($\bar{\nu}_\mu$) disappearance NC events, $\bar{\nu}_\mu$ (ν_μ) CC events, and ν_τ CC events are all considered. These considerations are the same as the study in [18]. The rates of these backgrounds are governed by the migration matrices.

The same systematic errors are then assumed for all beam designs. The reduction of the systematic errors is an ongoing task in the DUNE collaboration, and the values used are based on the conservative end of the current estimates of 1 % to 2 % [18]. As such, an overall normalization error is taken on the signal (2 % for appearance and 5 % for disappearance) and on the background rates (5 % for both channels). This accounts for fully correlated uncertainties on the event rates in each bin, and uncorrelated uncertainties are not considered. The nuPIL design could feasibly lower the systematic error with respect to the conventional design, although the extent of this is unknown, and beating 1 % systematics will be challenging.

5.2.2 T2HK

An up-to-date GLoBES implementation of T2HK has been developed, incorporating the collaboration's latest estimates for detector performance. The simulation is based on the GLoBES implementation of T2HK [169] with comprehensive modifications to match the latest experimental design. The beam power and fiducial mass have been updated to 1.3 MW and 187 kt per tank. For these studies, the staged design has been used with one tank operational for 6 years followed by two operational tanks beyond that time. In cases where results are shown against the run time of the experiment, additional simulations with just a single tank operational throughout have been included, to highlight the discontinuous nature of this design and the benefit gained from the introduction of the second tank. The neutrino flux and channel definitions have been updated to match those of [17], with separate channels for four interaction types (charged current quasielastic, charged current with one pion, other charged current and neutral current), for the $\nu_\mu \rightarrow \nu_e$ and $\overline{\nu}_\mu \rightarrow \overline{\nu}_e$ signals, and unoscillated ν_e, $\overline{\nu}_e$, ν_μ and $\overline{\nu}_\mu$ backgrounds. New tables of pre-smearing efficiencies and migration matrices have been created for each channel based on the full detector simulations used in [17]. New cross-sections for interactions on water for the four interaction types have been generated using version 2.8.4 of the GENIE Monte-Carlo neutrino interaction event generator [170].

The simulation determines the event rates for signal and background components for each of $\nu_\mu/\overline{\nu}_\mu \rightarrow \nu_e/\overline{\nu}_e$ appearance and $\nu_\mu/\overline{\nu}_\mu \rightarrow \nu_\mu/\overline{\nu}_\mu$ disappearance measurements in neutrino mode and antineutrino mode. The rates are determined for 12 energy bins, given in Appendix C. For the appearance measurements, the energy range is restricted to 0 GeV to 1.25 GeV, so only bins 1 to 8 are included. All bins are included in the disappearance measurements. Separate uncorrelated systematic errors are assumed on the total signal and background rates for each of the four measurements, where the size of the errors assumed, summarised in Table C.1, are the same as in the official Hyper-K studies after an adjustment to account for correlations between systematics not included in these simulations.

The design of T2HKK [69] and the location of the second detector module are still under development. As such, physics studies are being performed for a number of simulated fluxes with varying off-axis angles, generally ranging from on-axis to 2.5° off-axis, which is aligned with the first detector in Kamioka. The novelty of this design is not only the longer baseline distance, which will enhance the role of matter effects, but also the fact that the energy profile of the flux remains similar to that at the detector at 295 km, meaning that the oscillation probability is sampled at very different values of L/E. This is clearly seen in Figure 5.3, where the top panel shows how the flux aligns with the first maximum of the probability at Kamioka while the bottom panel shows that the fluxes align around the second maximum for the Korean detector. When plotted against L/E, as in Figure 5.4, it is seen that the T2HK flux has only minor coverage of the second maximum in contrast to T2HKK. The fluxes used in these simulations were provided by the T2HKK working group of the Hyper-Kamiokande proto-collaboration and were produced in the same way as the fluxes used in [17] but with a baseline of 1100 km and off-axis angles of 1.5°, 2.0° and 2.5°.

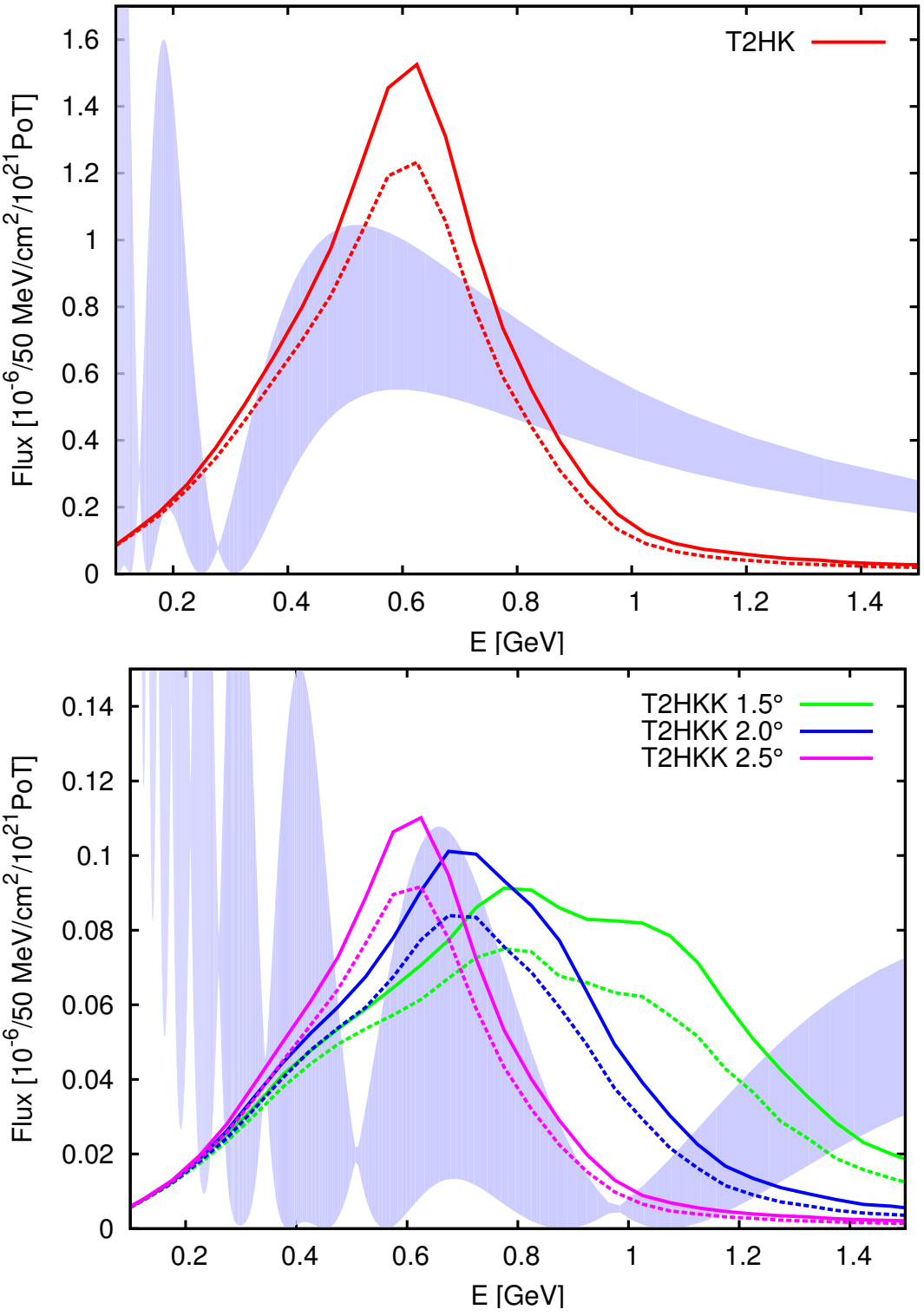

Figure 5.3: Top: T2HK's flux plotted against neutrino energy for ν-mode (solid) and $\overline{\nu}$-mode (dashed). Bottom: The T2HKK fluxes plotted against energy for ν and $\overline{\nu}$ modes. The shaded region shows the envelope of the probability found by varying the true value of δ. Due to T2HKK's longer baseline but comparable energy range to T2HK, the fluxes on the bottom sample a very different part of the probability.

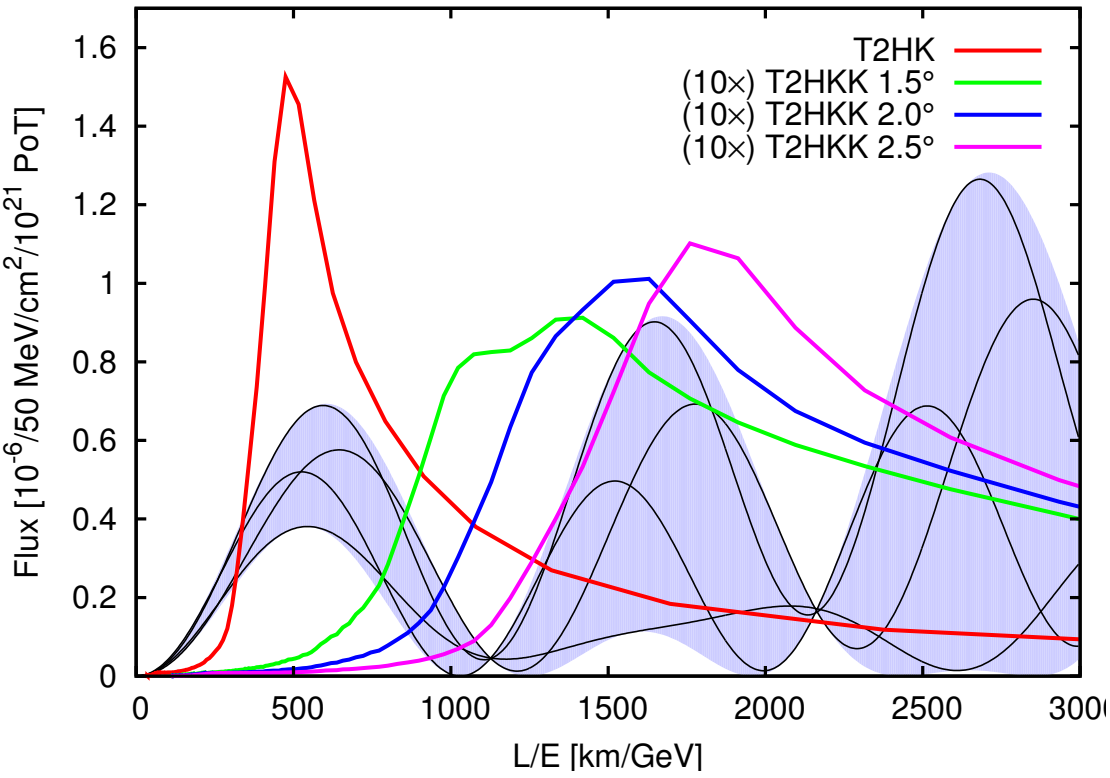

Figure 5.4: The T2HK and T2HKK fluxes shown as a function of L/E. The shaded region shows the envelope of the probability for $L = 1100\,\text{km}$ and the black lines indicate the specific behaviour for $\delta \in \{0, \frac{\pi}{2}, \pi, \frac{3\pi}{2}\}$. Note that the T2HK flux actually samples from the probability with a smaller matter effect corresponding to its shorter baseline $L = 295\,\text{km}$; however, on this scale the location of the first maximum does not deviate much from what is shown here.

5.2.3 Experimental run times and ν : $\overline{\nu}$ ratios

The previous sections have discussed the models of the experimental details of DUNE and T2HK. However, in the present study, a number of different exposures are considered for these experiments and their combination. This section is intended to clarify the terminology and explain the choices of run time, neutrino–antineutrino sharing, and detector staging adopted in the following analyses.

First, it is noted that although the ratio of the run time between ν and $\bar{\nu}$ beam modes is also known to affect the sensitivities of long-baseline experiments, only the ratios defined by each experiment's official designs are used throughout this work. For DUNE and T2HK, the ratio of ν to $\bar{\nu}$ are 1:1 and 1:3, respectively. The physical argument for the asymmetric run-time of T2HK is that, as described above, the use of both neutrino and antineutrino data is important in gaining precision on the measurement of δ, but the expected event rates for antineutrino interactions is around a third as large as the rates for neutrinos, due to the lower CCQE cross-section of antineutrinos and smaller antineutrino beam flux. For DUNE, however, due to its more limited statistics and its wide-band beam reaching higher energies, the CCQE interaction channel and the combination of neutrino and antineutrino data is less essential than obtaining a larger overall event rate by using an equal ratio of neutrino and antineutrino run times. The impact of changing these ratios was investigated, but found not to significantly impact the results, and for both experiments the optimal ratio was close to those assumed here. In the study for alternative designs, the same ratios as the standard configurations of DUNE and T2HK are assumed.

Most of the results in this chapter deal with three configurations labelled as DUNE, T2HK and DUNE + T2HK, and the sensitivities shown assume the full data taking periods for these experiments have ended. These are the standard configurations, and are defined in terms of run times and neutrino–antineutrino sharing in the rows labelled "fixed run time" in Table 5.1. It is noted that, as the intention is to compare experimental performance, the standard configuration of DUNE in these studies assumes 10 years of data taking, which differs for the 7 years considered in [18]. However, quantities are also plotted against run time, and for these figures the sharing of run time between components is defined in terms of a quantity defined here as the cumulative run time T; these are shown in the rows labelled "variable run time" in Table 5.1. The cumulative run time for the combination of DUNE and T2HK is defined to be the sum of the individual experiments' run times, *i.e.* if the two experiments were run back to back, with no overlapping period of operation, then this definition of cumulative run time is identical to the calendar time taken for the full data set to be collected[3]. Of course, if the experiments run in parallel, with identical start and end dates, this definition of cumulative run time would be double the calendar time required to collect the data. To make clear when this definition is used, the variable run time configuration is labelled as DUNE/2 + T2HK/2, as half of the cumulative run time goes to each experiment. Note also that, as per the official studies of each experiment, 10^7 s/year is assumed of active beam time for T2HK (2.7×10^{21} POT/year at 1.3 MW with 30 GeV protons) while combined

[3]In the interests of clarity, here the term *calendar time* is used to denote the actual time passed on the calendar. This is highly dependent on staging and the relative placements of individual experiment schedules, and is only used later in the text as an informal means of comparison for certain staging options.

accelerator uptime and efficiency of 56 % is assumed for DUNE (1.47×10^{21} POT/year at 1.07 MW with 80 GeV protons).

	Label	$\nu : \overline{\nu}$ at DUNE	$\nu : \overline{\nu}$ at T2HK
Fixed run time	DUNE	5 : 5	0 : 0
	T2HK	0 : 0	2.5 : 7.5
	DUNE + T2HK	5 : 5	2.5 : 7.5
Variable run time	DUNE	$T/2 : T/2$	0 : 0
	T2HK	0 : 0	$T/4 : 3T/4$
	DUNE/2 + T2HK/2	$T/4 : T/4$	$T/8 : 3T/8$

Table 5.1: The run times in years for each component of DUNE, T2HK, and their combination (DUNE + T2HK) for both the standard full data taking period (top 3 rows) and when considered with variable run times (bottom 3 rows). Plots with cumulative run time T on the x-axis are for the "variable run time" configurations, whilst all other plots are for the "fixed run time" configurations.

The possible staging options for the two modules of T2HK cause some added complication when plotting sensitivities against run time. In this study, it is assumed that the standard configuration of T2HK follows the staging suggested by the collaboration: 6 years of 1-tank running followed by 4 with an additional tank. In practice, this is implemented as an effective mass for T2HK which depends on the run time assigned to T2HK t defined by

$$M(t) = M_0 \left[1 + \Theta(t-6)\frac{t-6}{t}\right],$$

where M_0 is the mass of a single tank, defined above as 187 kt, and $\Theta(x)$ is the Heaviside step function. As the definition of cumulative run time T would require 12 years to pass before 6 years of data had been collected by T2HK in the combination of DUNE + T2HK, the discontinuity seen in sensitivity due to staging appear in two different places in plots against run time: one for T2HK alone, and one for DUNE + T2HK. This can be seen clearly in *e.g.* Figure 5.6, where the discontinuities are marked with vertical dashed lines. For comparison, also shown are the sensitivities against run time assuming there is no second tank. In this case, $M(t) = M_0$ for all values of t.

Finally, in Section 5.4 these configurations (and the labels in Table 5.1) will be deviated from as non-standard exposures are considered for the purpose of better exploring the complementarity of DUNE and T2HK. This will be discussed in more detail in Section 5.4.

5.2.4 Statistical method

The simulations of these studies use GLoBES [165, 166] to compute the event rates and statistical significances for the experiments discussed in the previous section. The salient details of the statistical model underlying the analysis are now described in this section.

Given the true bin-by-bin event rates, n_i, for a specific experimental configuration, a χ^2 function is constructed based on a log-likelihood ratio,

$$\chi^2(\vec{\theta}, \xi_s, \xi_b) = 2 \sum_i \left(\eta_i(\vec{\theta}, \xi_s, \xi_b) - n_i + n_i \ln \frac{n_i}{\eta_i(\vec{\theta}, \xi_s, \xi_b)} \right) + p(\xi_s, \sigma_s) + p(\xi_b, \sigma_b), \quad (5.2.1)$$

where i runs over the number of bins, $\eta_i(\vec{\theta}, \xi_s, \xi_b)$ is the hypothesis event rate for bin i and E_i is the central bin energy. The vector $\vec{\theta}$ has six components, corresponding to each of the three mixing angles, one phase and two mass-squared splittings of the hypothesis. The parameters ξ_s and ξ_b are introduced to account for the systematic uncertainty of normalization for the signal (subscript s) and background (subscript b) components of the event rate, and are allowed to vary in the fit as nuisance parameters. For a given hypothesised set of parameters $\vec{\theta}$, the event rate for bin i is calculated as

$$\eta_i(\vec{\theta}, \xi_s, \xi_b) = (1 + \xi_s) \times n_i + (1 + \xi_b) \times b_i,$$

where n_i and b_i are the expected number of signal and background events in bin i, respectively. The nuisance parameters are constrained by terms $p(\xi, \sigma) = \xi^2/\sigma^2$, representing Gaussian priors on ξ_s and ξ_b with corresponding uncertainties σ_s and σ_b. To test a given hypothesis against a data set, unwanted degrees of freedom are profiled out. This amounts to minimising the χ^2 function given in Equation (5.2.1) over these parameters whilst holding the relevant parameters fixed. The statistical parameters of interest will be detailed for each analysis in the following sections; however, as an example consider the study into how well different hypothesised values of δ fit a given data set. In this case, the quantity computed is

$$\chi^2(\delta) = \min_{\{\vec{\theta} \neq \delta, \xi_s, \xi_b\}} \left(\chi^2(\vec{\theta}, \xi_s, \xi_b) + P(\vec{\theta}) \right), \quad (5.2.2)$$

where the notation $\vec{\theta} \neq \delta$ means all parameters other than δ. The function $P(\theta)$ acts like a Bayesian prior, introduced to mimic the role of data from existing experiments during fitting. In all fits that are performed, unless explicitly stated otherwise, true values are used from the global fit NuFit 2.2 (2016) [171]. $P(\theta)$ comprises a sum of the 1D χ^2 data provided by NuFit for each parameter, except for δ, with either NO or IO priors used depending on the mass ordering of the hypothesis. [4] This includes the correlations which are currently seen in the global data, and this treatment goes beyond the common assumption of Gaussian priors, allowing for both the degenerate solution and its relative poorness of fit to be more accurately taken into account. The values of all parameters are permitted to vary, including the different octants for θ_{23}, the value of δ and the mass orderings, subject to the global constraints. The choice of true values depends on the mass ordering, and these are given explicitly in Table 5.2, unless stated otherwise.

Note that this treatment of the external data, which attempts to accurately model the global constraints beyond the approximation of independent Gaussians, leads to some differences between these results and those of previous studies [17, 18, 146]. The differences can be traced to two key features: First, the significantly non-Gaussian behaviour of the global constraints at higher significances is taken into account in these

[4] Implementing more recent versions of the NuFit global fit has been completed for part of the analysis, to verify that this does not make a significant difference for the results shown in this chapter.

Parameter	Normal ordering	Inverted ordering
θ_{12} [°]	$33.72^{+0.79}_{-0.76}$	$33.72^{+0.79}_{-0.76}$
θ_{13} [°]	$8.46^{+0.14}_{-0.15}$	$8.48^{+0.15}_{-0.15}$
θ_{23} [°]	$41.5^{+1.3}_{-1.1}$	$49.9^{+1.1}_{-1.3}$
Δm^2_{21} [$\times 10^{-5}$ eV^2]	$7.49^{+0.19}_{-0.17}$	$7.49^{+0.19}_{-0.17}$
Δm^2_{31} [$\times 10^{-3}$ eV^2]	$+2.526^{+0.039}_{-0.037}$	$-2.518^{+0.038}_{-0.037}$

Table 5.2: The true values used in the simulations, unless otherwise stated explicitly, with their uncertainties (the $1\,\sigma$ range of the priors used in the fit). These are based on NuFit 2.2 (2016) [171], and are similar to the parameters found in other recent global fits (see *e.g.* [172, 173]).

studies; this is particularly relevant for the prior on Δm^2_{21} and this is commented on in more detail in Section 5.3.1 and particularly in Section 5.3.1.1. The second important feature of the priors used in these studies is the strong correlation between mass ordering and the octant of θ_{23}. The current global data disfavours the combination of IO and first octant (or NO and second octant). This fact is reflected in the priors; although a visible local minimum is always present, it is never degenerate with the true minimum. In previous studies, various treatments of this degeneracy have been employed, some which do not allow the alternative minimum, and some which do not penalise it at all. The method used here interpolates between these two extremes, and attempts to faithfully describe the current global picture. More detail will be provided on the specific differences between these results and existing calculations of the sensitivity of DUNE, T2HK and their variant designs on a case-by-case basis in the following sections.

5.3 Sensitivity to mass ordering, CPV, non-maximal CPV, and octant

In this section, the results are presented of simulations studying the sensitivity of the standard configurations of DUNE and T2HK. This means using the 2-horn reference flux for DUNE, discussed in Section 5.2.1, while for the T2HK detector both the staged implementation of the two detector modules at Kamioka, as discussed in Section 5.2.2, but also the sensitivities for a single tank of 187 kt. The run time and neutrino–antineutrino sharing for these configurations are discussed in more detail in Section 5.2.3. After considering these benchmark configurations and their complementarity, the potential of alternative designs are returned to in Section 5.5.

5.3.1 Mass ordering sensitivity

The mass ordering is one of the central goals of the next generation of LBL experiments; it is also one of the easiest to measure with this technology. The ability to determine the mass ordering is quantified by computing the following test statistic,

$$\Delta\chi^2_{\text{MO}} = \min_{\{\vec{\theta},\xi_s,\xi_b\}} \left[\chi^2(\text{sgn}\Delta m^2_{31} = \text{true}) - \chi^2(\text{sgn}\Delta m^2_{31} = \text{false})\right]. \tag{5.3.1}$$

That is to say, the smallest value of the χ^2 function for any set of parameter values with the wrong ordering. All parameters are allowed to vary during marginalisation whilst preserving the ordering. Although this composite hypothesis violates the assumptions of Wilks' theorem [174,175], and therefore invalidates the mapping between $\sqrt{\Delta\chi^2}$ and σ-valued significance for discrimination of the two hypotheses, the work in this section sticks to convention, reporting the expected sensitivities for the median experiment in terms of $\sqrt{\Delta\chi^2}$ and discussing it in terms of σ. For details on the precise formulation of the statistical interpretation of $\sqrt{\Delta\chi^2}$, see *e.g.* [176].

The sensitivity found in Figure 5.5 is very strong. DUNE, with its large matter effects, can expect a greater than $6\,\sigma$ measurement of the mass ordering after 10 years for all values of δ, with an average sensitivity of around $8\,\sigma$ and a maximal sensitivity of around $13\,\sigma$. T2HK alone has limited access to this measurement due to its shorter baseline, but can still expect a greater than $3\,\sigma$ measurement for around 25 % of the possible values of δ after 10 years of data-taking. The combination of DUNE and T2HK running for 10 years each can reach sensitivities of at least $12\,\sigma$, with an average of around $14\,\sigma$ or $15\,\sigma$. Care should be taken when interpreting such large significances; however, it is clear that DUNE, and the combination of DUNE and T2HK, can expect a very strong determination of the mass ordering. The strong complementarity is also noteworthy: for the values of δ where DUNE performs the worst, the information from T2HK helps to raise the global sensitivity by almost $8\,\sigma$ to $9\,\sigma$. Despite this interesting interplay, the fact that this is such an easy measurement for DUNE means that the question of optimising such a measurement further is not investigated further.

The sensitivities in Figure 5.5 deviate from previous published values for DUNE, generally reporting a worse ability for DUNE to exclude the ordering, with lower average sensitivity and visibly discontinuous behaviour in the values of $\Delta\chi^2$. This is due to the priors that have been imposed. Instead of a Gaussian approximation to the global data, the global 1D χ^2 functions have been implemented, as provided by NuFit [171]. The true global data has strongly non-Gaussian behaviour at high significance, and there exist non-standard parameter sets which are not excluded at greater than $6\,\sigma$. These parameter sets sometimes become the best-fitting wrong-ordering solution, and must be excluded to rigorously establish the mass ordering. This is discussed in more detail in Section 5.3.1.1.

Another way to understand the complementarity of DUNE and T2HK is in terms of minimal run time necessary to ensure a $\sqrt{\Delta\chi^2} > 5$ measurement regardless of the true value of δ. This quantity is plotted in Figure 5.6, for normal ordering (left) and inverted ordering (right). The shaded bands take into account the variation in sensitivity due to the true value of θ_{23}. DUNE alone takes between 2 years and 10 years to reach this sensitivity, while the combination of DUNE and T2HK always takes less than 3 cumulative years (which if run in parallel is only 1.5 calendar years). T2HK running alone cannot ensure a measurement of this significance over any plausible run time. Shown explicitly is the difference in minimal sensitivity for T2HK with (dashed lines) and without (solid lines) a second staged detector module at Kamioka. This leads to a negligible increase in performance for T2HK in isolation, but a modest increase in the global sensitivity.

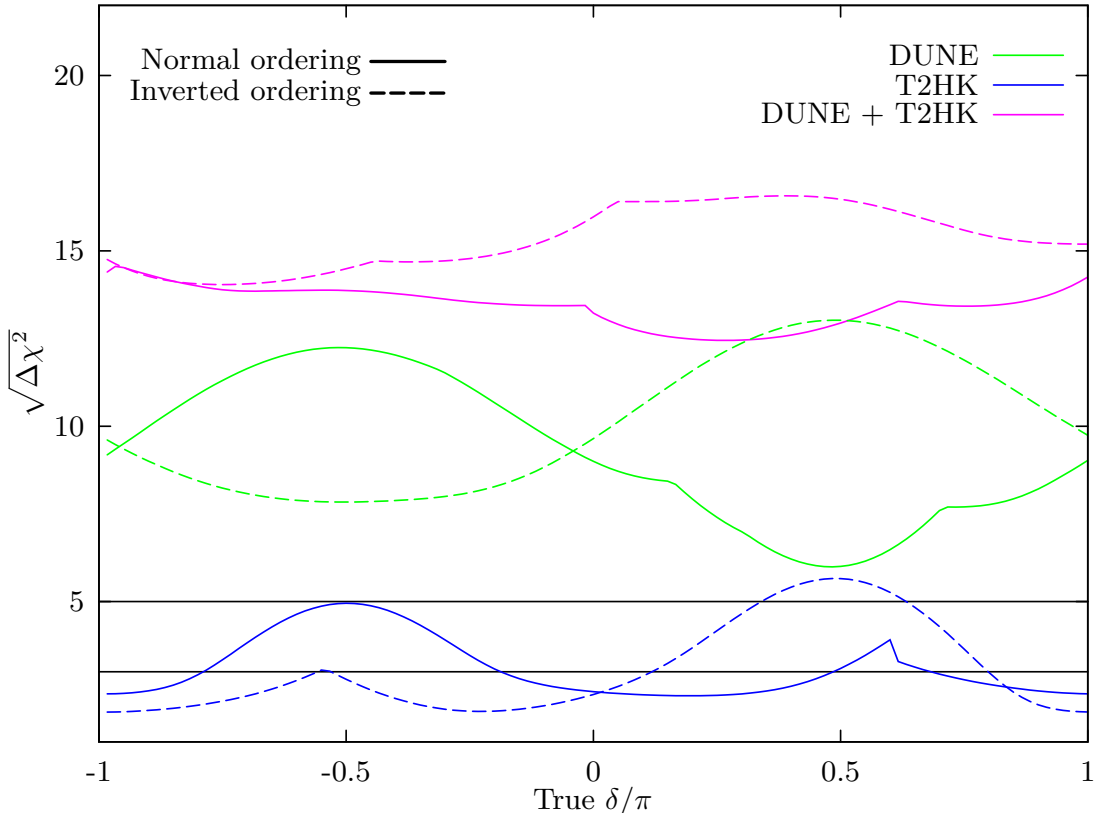

Figure 5.5: The sensitivity to the mass ordering for DUNE and T2HK in isolation and combined for true normal ordering (solid) and inverted ordering (dashed). This plot assumes the "fixed run time" configurations in Table 5.1 and the true oscillation parameters given in Table 5.2.

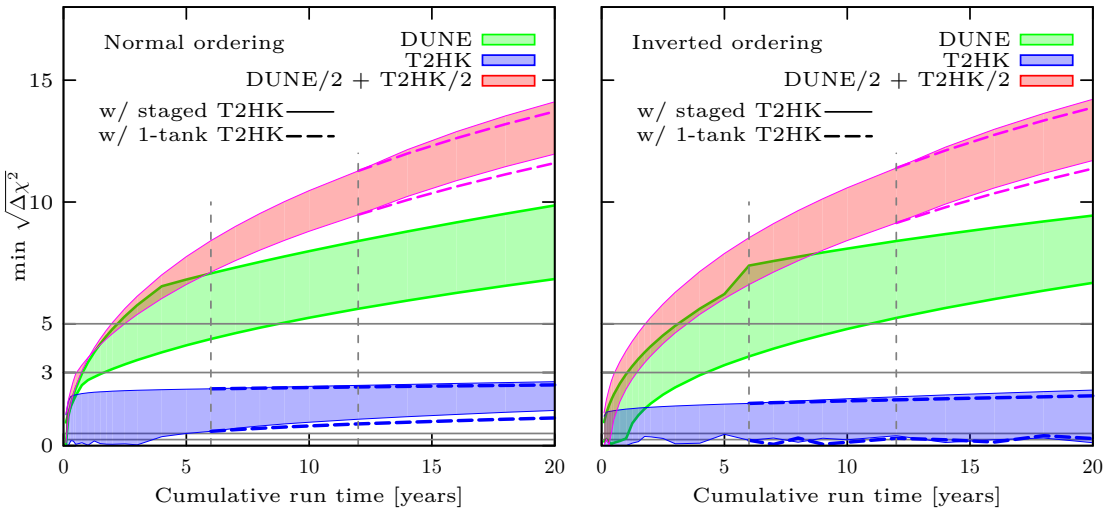

Figure 5.6: The least sensitivity for discovering mass ordering min $\sqrt{\Delta\chi^2}$ over values of true δ which can be reached by DUNE, T2HK and their combination as a function of cumulative run time. The width of the bands shows the sensitivity for $40° \leq \theta_{23} \leq 50°$. The left (right) panel assumes normal (inverted) ordering. These plots assume the "variable run time" configurations in Table 5.1 and the true oscillation parameters, apart from θ_{23}, given in Table 5.2. The vertical lines mark the introduction of a staged second detector for T2HK and leads to a notable discontinuity in sensitivity.

5.3.1.1 Mass ordering sensitivity at high significance

The sensitivity to mass ordering is conventionally reported as the difference between the value of a χ^2 statistic for the true parameter set and the close degenerate set with the atmospheric mass splitting changed by the following mapping,

$$\Delta m^2_{31} \rightarrow -\Delta m^2_{31} + \Delta m^2_{21}.$$

This local minimum becomes a worse and worse fit as data is collected, and reaches a $\Delta\chi^2$ value of above $8\,\sigma$ within a few years of running DUNE. This method computes the decreasing quality of a poor fit to the data; however, there are lots of parameter sets which are poor fits to the current data, and many cannot be excluded with a significance greater than $8\,\sigma$. Statistically speaking, to establish the mass ordering all possible parameter sets with that ordering must be excluded regardless of the other parameter values. In some circumstances, this may mean the local minimum identified above is not the true global wrong-ordering minimum. This problem is found to be relevant for DUNE as soon as the local minimum approaches a $5\,\sigma$ exclusion. This is because the global prior for the solar mass-squared splitting, Δm^2_{21} has a second minimum at around this significance. The long-baseline experiments considered in this chapter offer no sensitivity to this parameter themselves, and rely on the priors to help constrain it. The prior used in the simulations of this chapter has been plotted in the top panel of Figure 5.7, where the second minimum can be seen just above the global minimum. For DUNE to exclude the wrong mass ordering at above $5\,\sigma$, it must be ensured that it considers all values of Δm^2_{21} allowed by the global data at this significance. It is found that DUNE can often exclude this minimum only at lower significance than the more obvious local minimum corresponding to the expected degeneracy. This causes the lower significances, and discontinuous behaviour, that is reported in Section 5.3.1. On average, this reduces the expected significance of the mass ordering measurement by around $5\,\sigma$.

Of course, predicting any sensitivities at high significance requires good control over all other aspects of the statistical modelling, and it is not pretended that the method used in the simulations of this chapter correctly models all uncertainties up to very small fluctuations. However, this particular subtlety is pointed out as a concrete example of how the oft quoted sensitivity is not quite what it seems; it is the confidence at which it can be expected to exclude a particular local minimum, not to exclude the best-fitting set of parameters with the wrong ordering. The difference in these quantities starts to become relevant for DUNE at very modest exposures. The bottom panel of Figure 5.7 shows the difference in $\Delta\chi^2$ values for the local minimum (black) and the full set of wrong ordering parameter sets (green), which starts to be visible after only 2 years run time. It is hoped that this example helps to highlight some of the complexities of making precise statements with high confidence sensitivities.

5.3.2 CP violation sensitivity

To fulfil the central aim of the LBL programme, the experiments must be able to rule out CP conservation over a large fraction of the true parameter space. This would imply a non-zero Jarlskog invariant and rigorously establish CP violation in the leptonic sector.

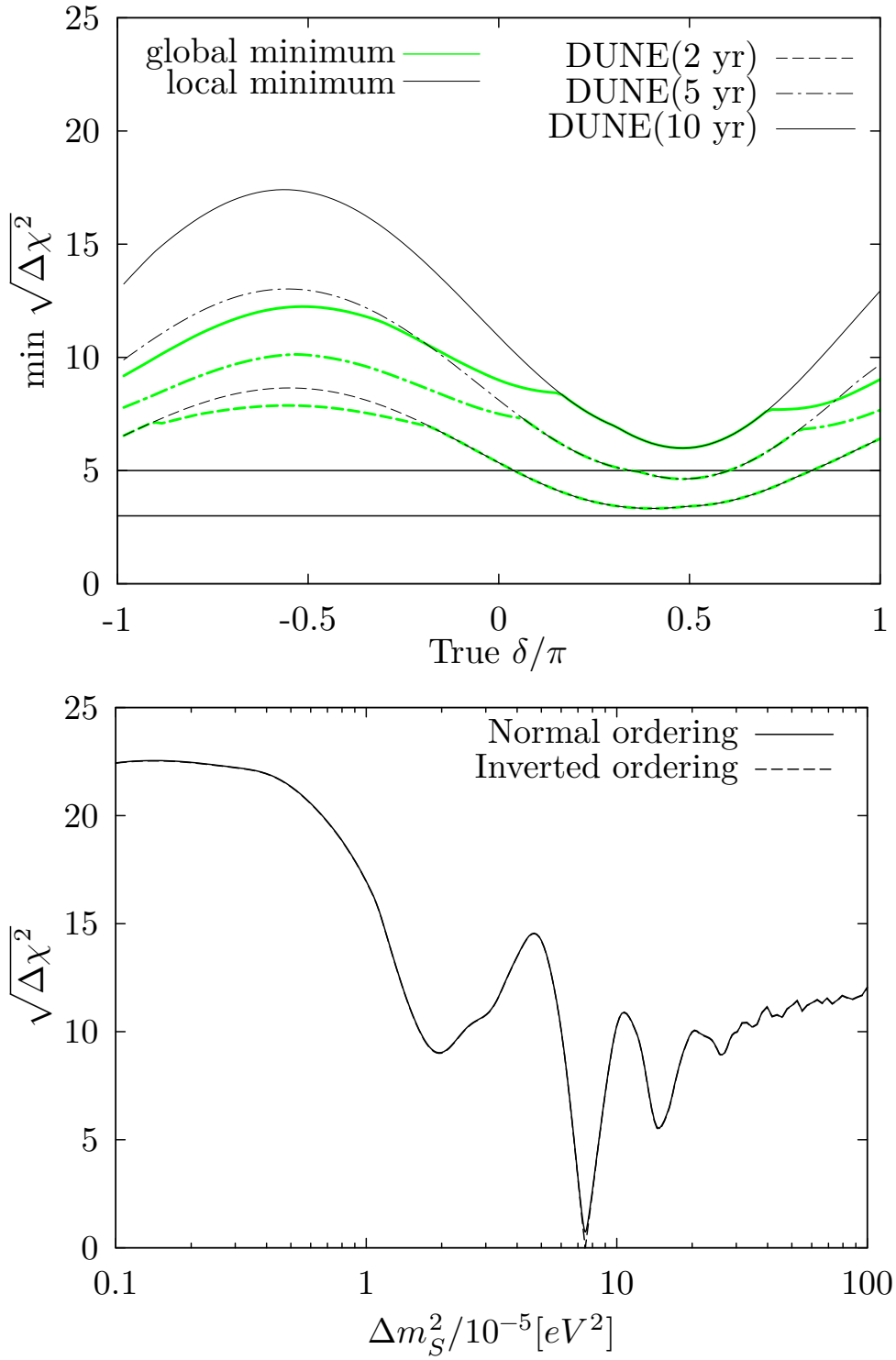

Figure 5.7: Top: The prior on Δm^2_{21} provided by the NuFit global fit [171]. The second local minimum with a significance around $5\,\sigma$ ($\Delta m^2_{21} \approx 1.6 \times 10^{-4}$ eV^2) leads to the unusual behaviour in the reported mass ordering sensitivities of this chapter. Bottom: Comparison of sensitivities based on the global minimum and more common published versions which show only a local minimum. This is due to the presence of additional wrong-ordering minima at high significance in the global data.

Once again the conventional test statistic is followed, defining the quantity

$$\Delta\chi^2_{\text{CP}} = \min_{\delta\in\{0,\pi\}} \Delta\chi^2(\delta), \tag{5.3.2}$$

which amounts to studying the composite hypothesis of CP conservation ($\delta = 0$ or $\delta = \pi$) [177]. Although at low-significance this test statistic is known to deviate from a χ^2 distribution [178], such effects are expected to be small for the experiments under consideration in this study.

For the discovery of CP violation, the true value of the mass ordering and octant are relevant. These values are not specified, and the sensitivity for all combinations of values are studied. Shown in the top panel of Figure 5.8 is the significance for exclusion of CP conservation for the standard designs of the two facilities, in isolation and combination. T2HK is found to have a better overall sensitivity than DUNE, with at least a $3\,\sigma$ ($5\,\sigma$) discovery of CPV over 63 % to 71 % (30 % to 47 %) of the parameter space for DUNE and 75 % to 81 % (55 % to 66 %) for T2HK. This can be understood by the discussion in Section 5.1.2. Discovery potential for CPV is closely related to the precision on δ at the CP conserving values; both rely on distinguishing between *e.g.* $\delta = 0$ and other values. The best sensitivity to CP conserving values of δ is at the first maximum, where the majority of T2HK events are found and consequently it sees a better sensitivity.

As mentioned in the last paragraph of Section 5.2.4, the prior used in these fits correlates the allowed octant to the mass ordering, and this is responsible for differences between these results and previously published work. In Figure 6 of [146], there is almost no CPV sensitivity for $0 < \delta < \pi$ for T2HK, which has not been found in the results presented here, while the results for DUNE are similar. This feature is explained as being due to the lack of MO sensitivity at T2HK, allowing for degeneracies to limit the sensitivity. In the simulation use here, however, T2HK avoids this problem by its strong determination of the octant and the correlation of the global data, which is included in this study but not in [146]. This lifts the degeneracy, and allows a higher sensitivity to be obtained. DUNE is found to perform slightly better in these simulation than is reported in the left panel of Fig 3.13 in [18]. Around $\delta = \pi/2$ ($-\pi/2$), their result shows the sensitivity is about $5.4\,\sigma$ ($3.8\,\sigma$).[5] However, this work's simulations find a range of between $5.0\,\sigma$ to $6.5\,\sigma$ for both $\delta = -\pi/2, \pi/2$. There are two sources for this discrepancy. Firstly, a longer run time (10 years) is assumed, for the purposes of comparison between T2HK and DUNE. Secondly, the degeneracy which impacted the T2HK simulation is also relevant here, albeit only at higher significances. The CPV sensitivity for DUNE does not peak around $\delta = -\pi/2$ in the left panel of Fig 3.13 in [18] like these results, due to the correlation described earlier. DUNE does not have as strong octant sensitivity as for the mass ordering, and without this correlation DUNE data prefers the forbidden minimum around $\delta = -\pi/2$. Finally, agreement is found between these results and those of Fig. 119 in [17]. This is largely because the mass ordering is fixed during fitting in [17], which mitigates the impact of the mass ordering degeneracy. This leads to superficial agreement between the two sets of results; although, these new results show the sensitivity which is possible assuming only the current global data, whereas assuming the MO is known would require new external data, perhaps from another long-baseline experiment.

[5] The range given in their work is for various beam designs.f For the design considered in the simulations presented here, the result is at the bottom of the range.

Shown in the bottom panel of Figure 5.8 is the fraction of values of δ for which a $5\,\sigma$ exclusion of CP conservation can be made as a function of run time. DUNE requires between 7 years and 10 years of data-taking to reach at least a $5\,\sigma$ measurement for 25 % of the possible values of δ, while T2HK alone expects to be able to make at least a $5\,\sigma$ measurement for more than 50% of the parameter space in less than 7 years. The combination of DUNE and T2HK is shown as a function of cumulative run time, the sum of the individual run times for each experiment, and as such interpolates the two sensitivities. However, if run in parallel, the combination of the two experiments performs stronger than either in isolation, and expects a greater than $5\,\sigma$ measurement for more than 50 % of the parameter space after at most 5 years of parallel data-taking.

5.3.3 Sensitivity to maximal CP violation

Although the search for any non-zero CPV is the principle goal of the next LBL experiments, understanding the value of δ is also highly relevant. Current global fits [6,172,173] point towards maximal values of δ, $\delta = \pm\pi/2$. Of course, these should be treated with some scepticism; no single experiment can claim evidence for this at an appreciable level. However, determining if a maximal CP violating phase exists will remain a high priority for the next generation of long-baseline experiments. If established, it could be seen as an "unnatural" value advocated as evidence against anarchic PMNS matrices. Indeed, it is also one of the most common predictions in flavour models with generalised CP symmetries.

This question is studied in Figure 5.9 where the quantity

$$\Delta\chi^2_{\text{MCP}} = \min_{\delta\in\{-\frac{\pi}{2},\frac{\pi}{2}\}} \Delta\chi^2(\delta) \tag{5.3.3}$$

is defined. This is analogous to $\Delta\chi^2_{\text{CP}}$ defined earlier, and gives a measure of the compatibility of the data with the hypothesis of maximal CP violation. On the top panel, the ability to exclude maximal CPV is shown as a function of the true value of δ. There is a similar sensitivity for both facilities, with T2HK being better for true values of δ around the CP conserving points 0 and π, while DUNE can slightly improve on this sensitivity for those values of δ closest to maximal CP violation. In this way, the two experiments once again exhibit a complementarity, and the combination of DUNE and T2HK inherits the best sensitivity of its two component parts, expecting a $3\,\sigma$ exclusion of MCP for over 58% of the parameter space.

The bottom panel of Figure 5.9 shows the fraction of true values of δ for which a $5\,\sigma$ exclusion of maximal CP violation can be achieved. By running in parallel for 10 years, DUNE and T2HK can expect a coverage at this significance of around 39 % to 48 % of the parameter space with a second detector at Kamioka, or 36 % to 45 % of the space with a single tank. DUNE alone would struggle to compete on this measurement, after 10 years only covering a fraction of between 10 % to 23 %.

5.3.4 Octant degeneracy and the precision on θ_{23}

Although it is known that θ_{23} is around 45°, the current global fit data allows for two distinct local minima, one below and one above 45°. This ambiguity is known as the

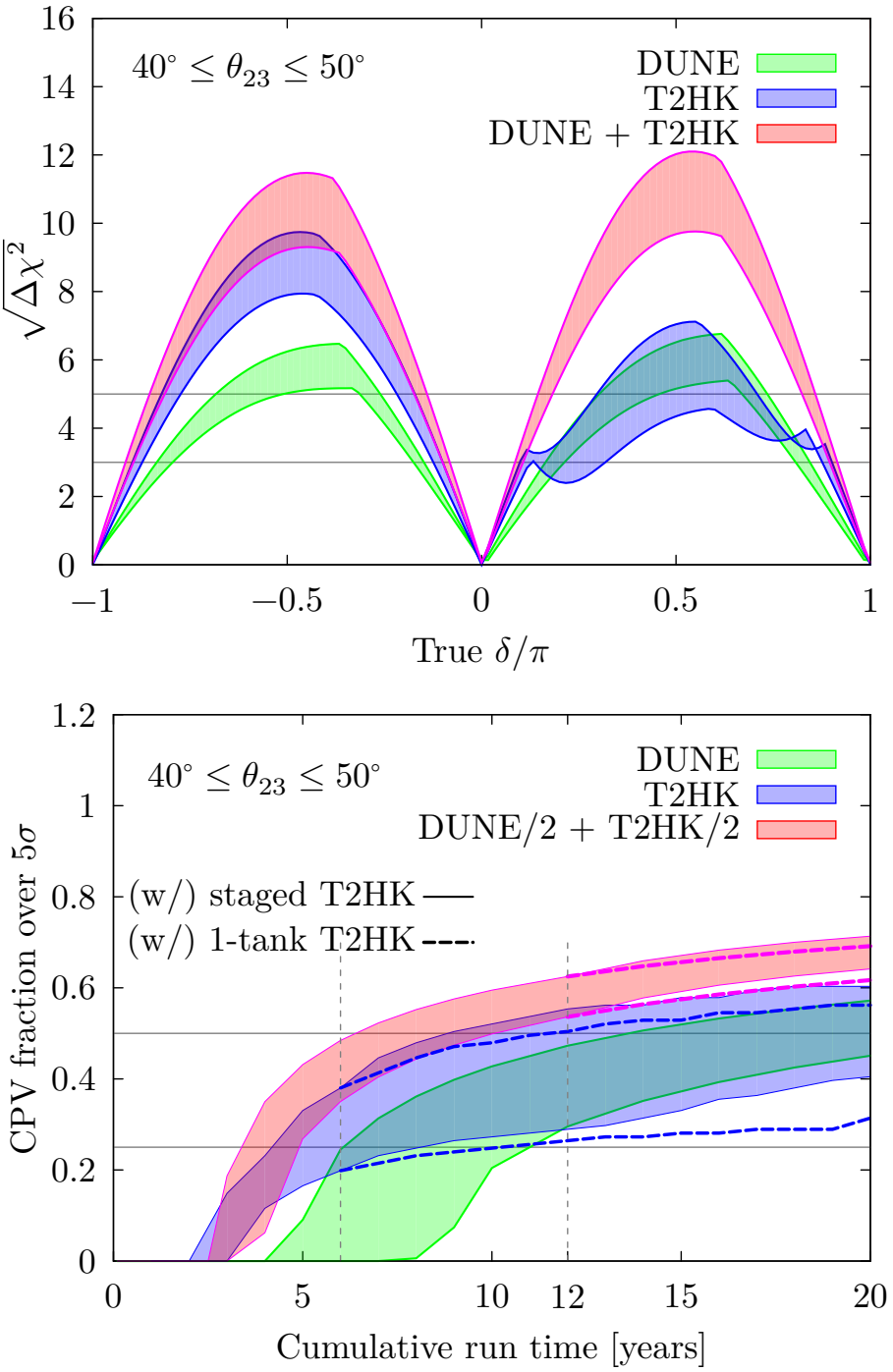

Figure 5.8: The sensitivity to CP violation for DUNE and T2HK in isolation and combined as a function of delta (top) and the fraction of δ parameter space for which greater than $5\,\sigma$ CPV discovery is expected (bottom). A range of true θ_{23} is considered spanning both octant solutions. The lower edge of the shaded regions corresponds to $\theta_{23} > 45°$ due to a decrease in sensitivity arising from the relative suppression of the CP sensitive terms in Equation (5.1.1). The top (bottom) plot assumes the "fixed run time" ("variable run time") configurations in Table 5.1 and the true oscillation parameters, apart from θ_{23}, specified in Table 5.2.

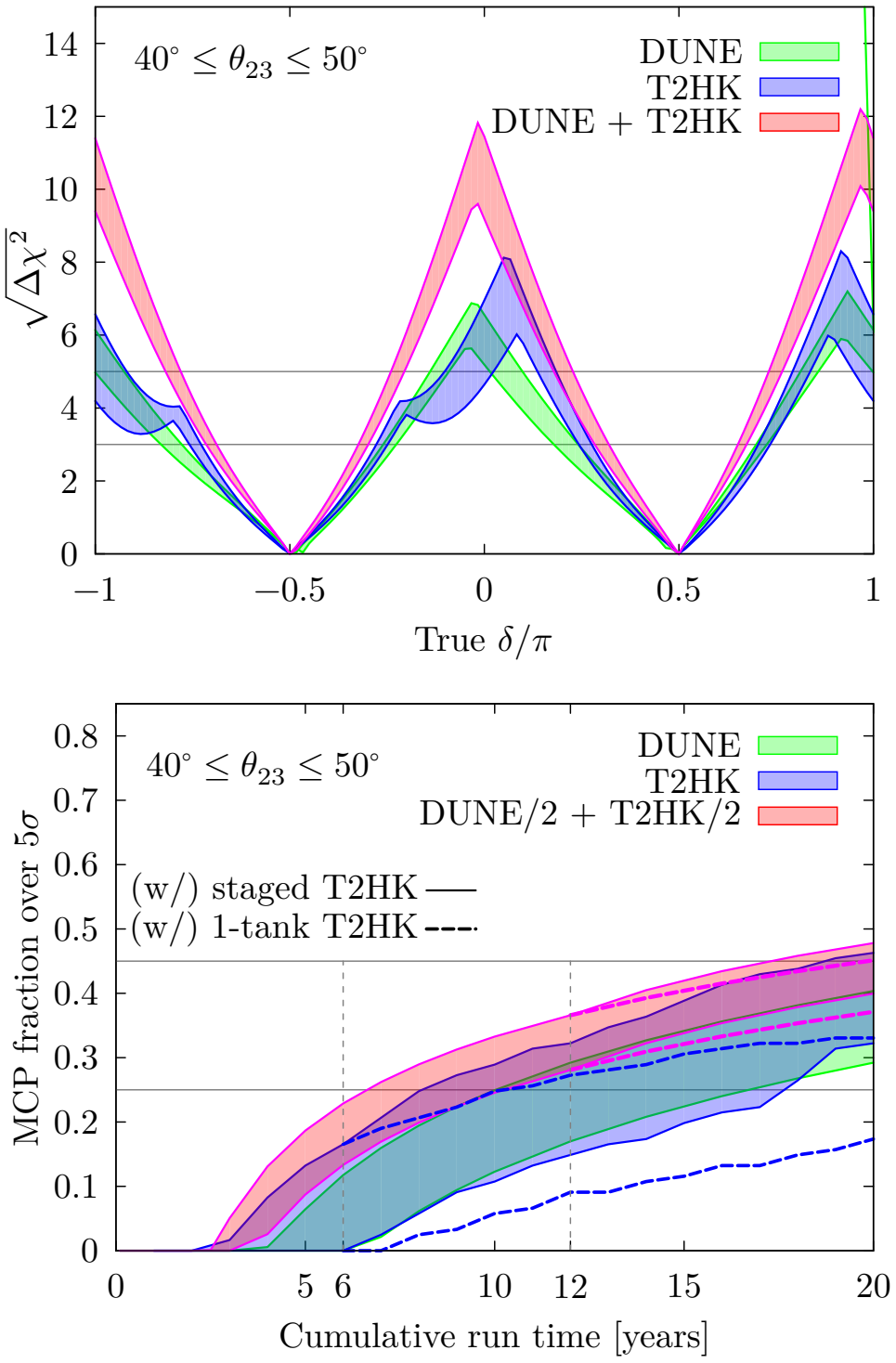

Figure 5.9: Top: The significance at which maximal CP can be excluded for DUNE and T2HK in isolation and combined as a function of true δ. Bottom: The fraction of δ-parameter space for which maximal CP can be excluded as a function of run time. The top (bottom) plot assumes the "fixed run time" ("variable run time") configurations in Table 5.1 and the true oscillation parameters, apart from θ_{23}, specified in Table 5.2.

octant degeneracy and arises as the disappearance channel of $\nu_\mu \to \nu_\mu$ is sensitive at leading-order only to $\sin^2 2\theta_{23}$. However, the appearance channel breaks this degeneracy at leading-order, and future long-baseline experiments are expected to significantly improve knowledge of θ_{23}. This section studies how well DUNE and T2HK will be able to measure θ_{23} as well as settling two central questions: Is θ_{23} maximal, and which is its correct octant?

The ability to exclude the wrong octant for DUNE, T2HK and their combination is shown in Figure 5.10. Shown on the top is the sensitivity as a function of the true value of θ_{23}. In these plots a fixed value of $\delta = 0$ is assumed. The impact of varying δ for these measurements is small, as the degeneracy is broken at leading-order in the appearance channel, and the subdominant effects of δ are less relevant. The ability to exclude the wrong octant can reach up to $8\,\sigma$ at the extremes of the current $3\,\sigma$ range of θ_{23}, and it is seen that $3\,\sigma$ determinations of the upper (lower) octant can be expected for true values of $\sin^2\theta_{23}$ less than 0.47–0.48 (greater than 0.54–0.56). This corresponds to a $3\,\sigma$ determination of the octant for all values of θ_{23} in the ranges $\theta_{23} \lesssim 43.3°$ to $43.8°$ or $\theta_{23} \gtrsim 47.3°$ to $48.4°$. On the bottom, the true value of θ_{23} is fixed while showing how the sensitivity depends on cumulative run time. The sensitivity is seen to quickly plateau, and the staging options for T2HK make little difference. Overall, the experiments expect to be able to establish the octant for this value of θ_{23} after only 2 years to 5 years. Although this plot assumes $\theta_{23} = 40°$, changing the true value of θ_{23} leads to a predictable change in sensitivity, as indicated in the top panel, but does not qualitatively change the behaviour against run time. Overall, T2HK is seen to perform better than DUNE for the determination of the octant. However, the difference in performance is marginal, and their combination after 10 years of data for each experiment, outperforms either experiment running alone for 20 years.

In this simulation, a prior has not been imposed on θ_{23}. This process differs from [18], in which they give a gaussian prior for θ_{23}. It also differs from the fitting method in [17], where they fit θ_{13}, θ_{23} and the value of Δm^2_{31} without implementing any priors, but fix θ_{12}, Δm^2_{21} and the mass ordering. In [146], the details of the fitting process are not specified. Despite these differences, qualitatively similar behaviour is seen between the three sets of results. The regions of θ_{23} where the octant cannot be determined at $5\,\sigma$ are found to be $\theta_{23} \in [41.1°, 49.8°]$, $\theta_{23} \in [42°, 48.9°]$, and $\theta_{23} \in [42.3°, 48.9°]$ for DUNE, T2HK, and their combination, respectively. In Fig. 3.18 of [18], the equivalent region for DUNE is $\theta_{23} \in [41°, 50°]$, which is comparable to this work. In the middle panels of Fig. 5 in [146], the authors estimate the region as $42.5° < \theta_{23} < 48.5°$ for T2HK and the combination of DUNE and T2HK, while for DUNE alone the range is slightly smaller than in this work's simulation at $42° < \theta_{23} < 49°$.

In Figure 5.11, the analogous plots are shown for the exclusion of maximal θ_{23}. It is seen that maximal θ_{23} can generally be excluded at greater significance than the octant. As before, T2HK dominates the measurement and can reach $5\,\sigma$ sensitivity for $\sin^2\theta_{23} \lesssim 0.47$ as well as for $\sin^2\theta_{23} \gtrsim 0.55$. DUNE in contrast can make a $5\,\sigma$ exclusion for $\sin^2\theta_{23} \lesssim 0.43$ and $\sin^2\theta_{23} \gtrsim 0.56$. Due to its poorer sensitivity, DUNE plays less of role in the combination and DUNE + T2HK follows the sensitivity of T2HK. On the bottom, the sensitivity against cumulative run time is shown. Again, the combination of DUNE + T2HK performs similarly to T2HK when the cumulative run time is divided by two, while DUNE performs slightly worse. The staging of T2HK is seen to play a notable role, leading to significantly higher sensitivities.

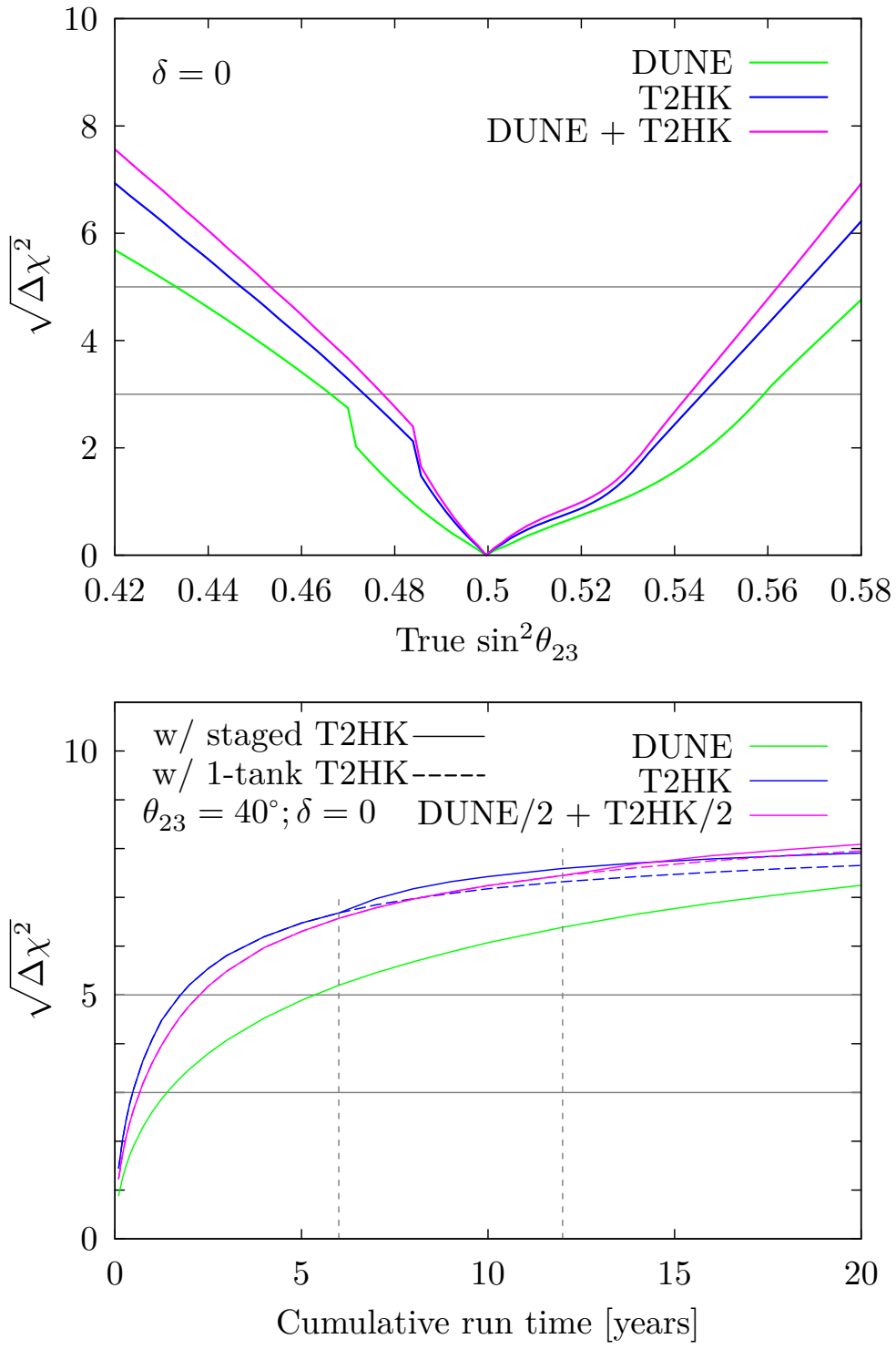

Figure 5.10: The sensitivity to exclude the wrong octant for DUNE, T2HK and their combination, as a function of $\sin^2\theta_{23}$ (top) and the cumulative run time (bottom). These plots assume $\delta = 0$ and normal mass ordering. The top (bottom) plot assumes the "fixed run time" ("variable run time") configurations in Table 5.1 and the true oscillation parameters, apart from θ_{23}, specified in Table 5.2.

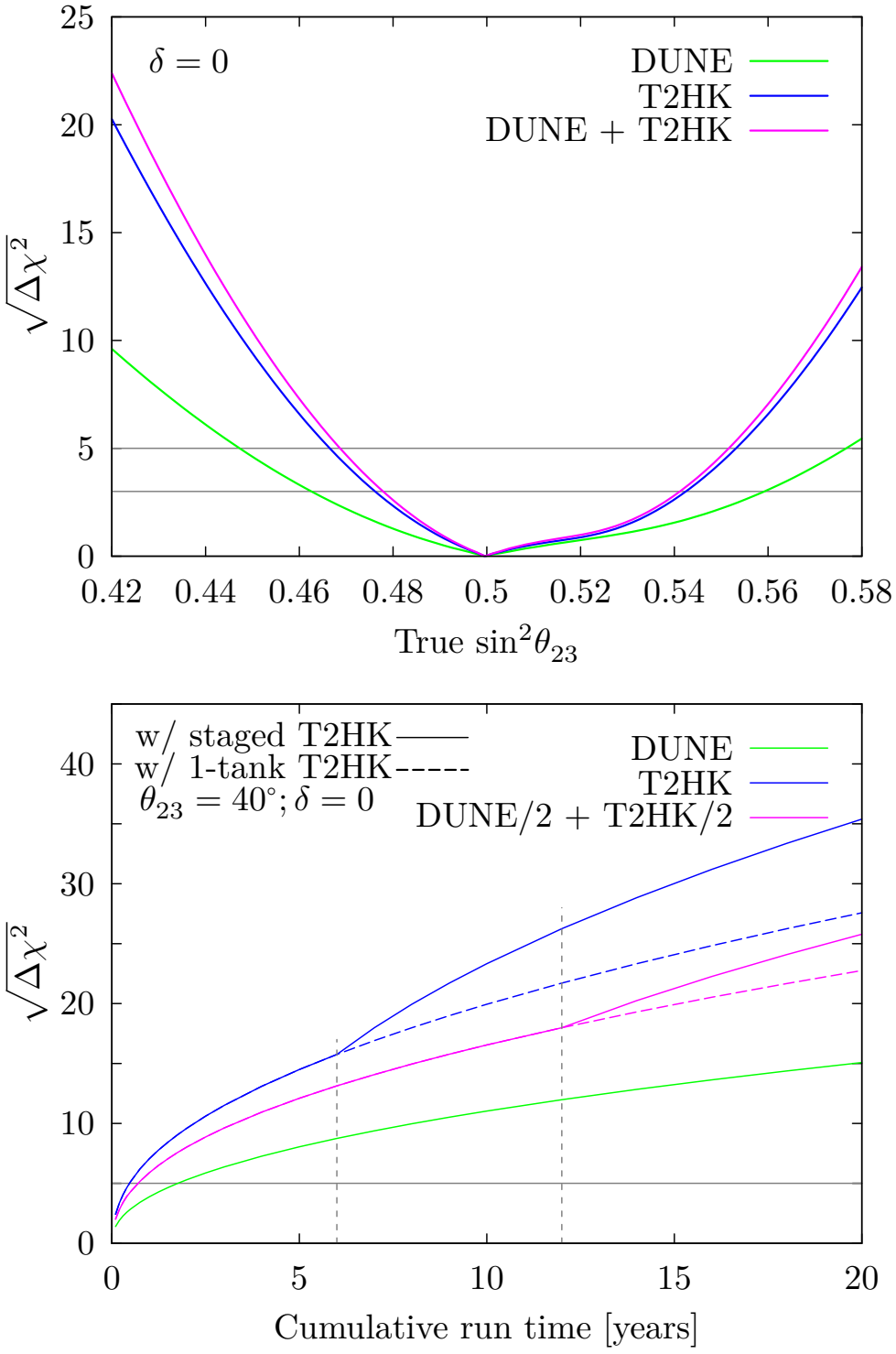

Figure 5.11: The ability to exclude $\theta_{23} = 45°$ for DUNE, T2HK and their combination, against the true value of $\sin^2\theta_{23}$ (top) and the cumulative run time (bottom). These plots assume $\delta = 0$ and normal mass ordering. The top (bottom) plot assumes the "fixed run time" ("variable run time") configurations in Table 5.1 and the true oscillation parameters, apart from θ_{23}, specified in Table 5.2.

The attainable precision on $\sin^2\theta_{23}$ is studied in Figure 5.12, where $\Delta(\sin^2\theta_{23})$ is plotted against the true value of $\sin^2\theta_{23}$ for normal mass ordering. For all configurations, the same behaviour is found: The uncertainty climbs up from about $\sin^2\theta_{23} = 0.48$ and falls down around $\sin^2\theta_{23} = 0.54$, peaking at $\sin^2\theta_{23} \sim 0.51$. This is expected for a measurement dominated by the disappearance channel, where the probability is proportional to $\sin^2(2\theta_{23})$ and a leading-order analytic treatment implies the relation

$$\Delta(\sin^2\theta_{23}) \propto |\tan(2\theta_{23})|\,,$$

which naively predicts a total loss of sensitivity at maximal mixing, analogous to $\Delta\delta$ at $\delta = \pi/2$. This is mitigated by higher-order effects, as well as the information from the appearance channel, which becomes important around these values. The drop in sensitivity seen in Figure 5.12 is quite sharp, and for values of $\sin^2\theta_{23}$ away from maximal mixing there is only modest variation in precision. For DUNE, $\Delta(\sin^2\theta_{23})$ is about 0.01 at the boundaries, and peaks up to the value ~ 0.045. T2HK has better performance, with $\Delta(\sin^2\theta_{23}) \sim 0.005$ for $\sin^2\theta_{23} = 0.43,\ 0.585$. As with DUNE, the worst performance for T2HK is near the peak at $\sin^2\theta_{23} = 0.5$ with $\Delta(\sin^2\theta_{23}) \sim 0.03$. The combination of DUNE and T2HK performs very similarly to T2HK; although the additional information from DUNE helps to improve this measurement, the sensitivity is seen to be dominated by T2HK. In these plots, the value $\delta = 0$ is fixed, although qualitatively similar behaviour holds for other choices. There is, however, a correlation between the precision on θ_{23} and δ.

An estimate of the joint precision on θ_{23} and δ attainable at DUNE and T2HK is presented in Figure 5.13. In this plot, each ellipse shows the $1\,\sigma$ allowed region for a set of true values inside its boundary taken from the sets $\delta \in \{0°, \pm 90°, \pm 180°\}$ and $\theta_{23} \in \{40°, 45°, 50°\}$. T2HK performs best for this measurement, however the combination of additional data from DUNE helps to reduce the contours slightly. It can also be seen that the precision measurement of these two parameters are largely independent, although DUNE exhibits a stronger correlation due to its reliance on data from both the appearance and disappearance channels. The best measurements will be obtained for large deviations from θ_{23}-maximality and values of δ close to the CP conserving values, where DUNE (T2HK) can expect precisions on θ_{23} of $\Delta\theta_{23} = 0.8°$ ($\Delta\theta_{23} = 0.5°$). Conversely, the worst precision comes from the values of θ_{23} near maximal mixing where DUNE (T2HK) can expect larger uncertainties by a factor of around 3 with $\Delta\theta_{23} = 2.3°$ ($\Delta\theta_{23} = 1.5°$). Comparing the result in Figure 5.13 to Fig. 123 in [17], the value found in this work for $\Delta\sin^2\theta_{23}$ is very close to the official result for T2HK, despite the differences in treatment of external data mentioned previously.

5.4 Complementarity of precision measurements of δ

For the reasons outlined in Section 5.1.2, an interesting interplay of sensitivities is expected for a narrow-band and wide-band beam for the determination of δ. In this section, the complementarity of DUNE and T2HK is studied for precision measurements of δ. Figure 5.14, shows the $1\,\sigma$ precision on δ, which is attainable by the standard configurations of DUNE and T2HK and their combination. A range of true values of θ_{23} is considered as this significantly affects the ultimate precision. It is seen that for most of the parameter space T2HK can attain a better precision, with values of $\Delta\delta$ between 6°

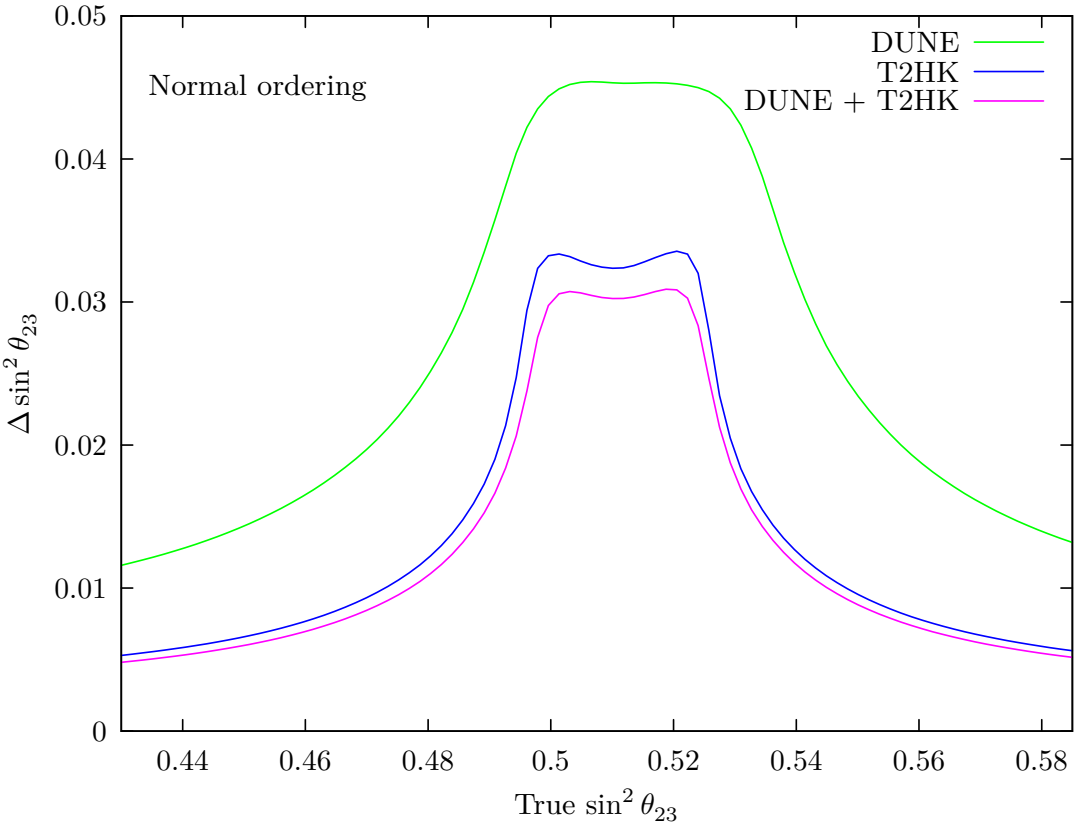

Figure 5.12: The expected $1\,\sigma$ precision on $\sin^2 \theta_{23}$ as a function of true value of $\sin^2 \theta_{23}$ from 0.43 to 0.585 for DUNE, T2HK, and their combination, under the assumption of normal ordering. This plot assumes the "fixed run time" configurations in Table 5.1 and the true oscillation parameters, apart from θ_{23}, specified in Table 5.2.

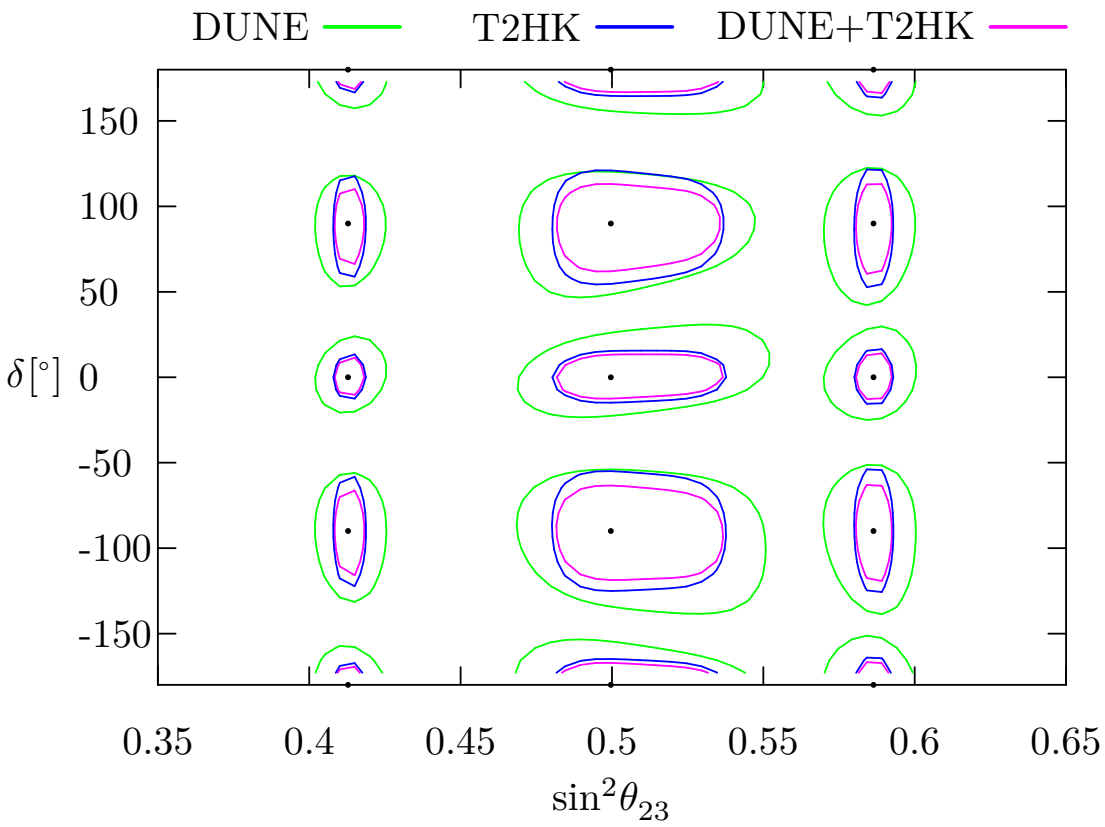

Figure 5.13: The attainable $1\,\sigma$ precision on $\sin^2\theta_{23}$ and δ for DUNE, T2HK, and their combination. In each case, the contours enclose the assumed true values for θ_{23} and δ, marked with a point. This plot assumes the "fixed run time" configurations in Table 5.1 and the true oscillation parameters, apart from θ_{23}, specified in Table 5.2.

and 7° compared to between 9° and 11° for DUNE, for the CP conserving values of δ. However, DUNE performs slightly better than T2HK for maximally CP violating values of δ. This leads to an effective complementarity between the two experiments, and their combined sensitivity reduces $\Delta\delta$ as compared to the two experiments in isolation by between 1° and 4° depending on the value of δ.

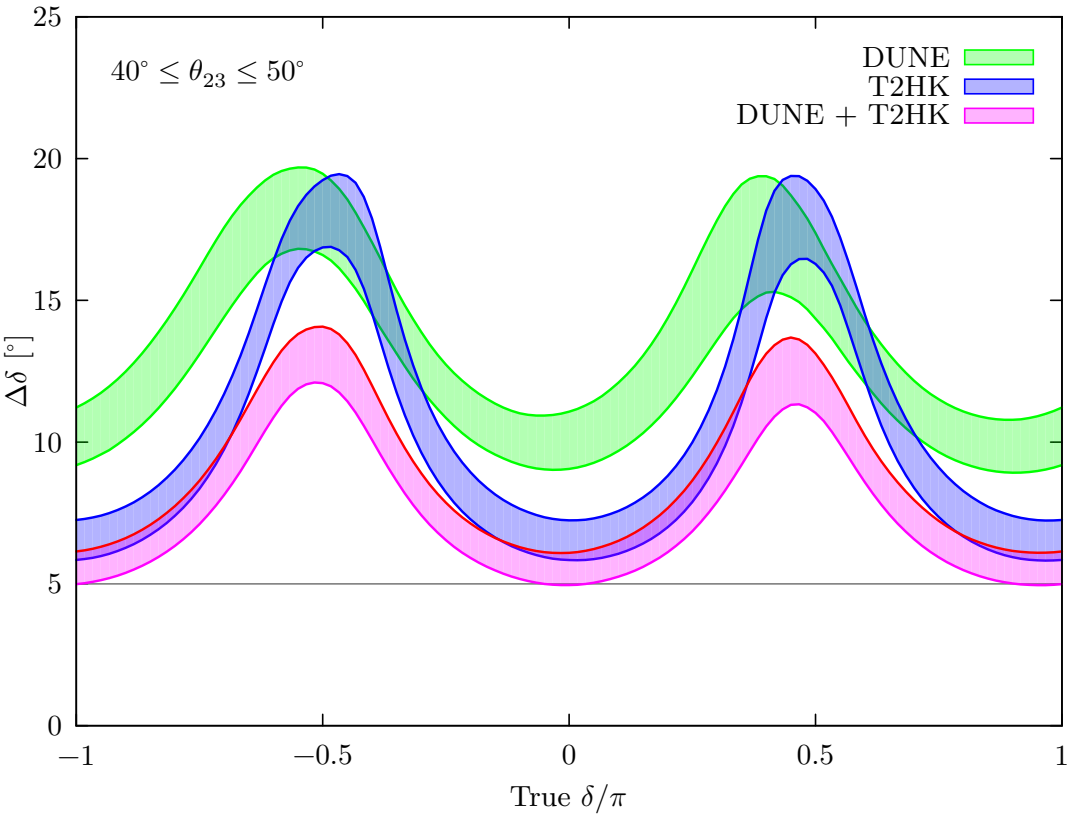

Figure 5.14: The $1\,\sigma$ precision on δ for DUNE and T2HK in isolation and combined. This plot assumes the "fixed run time" configurations in Table 5.1 and the true oscillation parameters, apart from θ_{23}, specified in Table 5.2.

An improvement is therefore seen when combining the data from the two experiments. This was to be expected for a number of reasons: Firstly, there is a simple statistical benefit of combination – an increase in data reduces the statistical uncertainty and allows for a more precise measurement. On top of this, there is a synergistic benefit, where the two experiments mutually improve the reconstruction of the parameter of interest. To try to understand the synergy between DUNE and T2HK, the statistical advantage can be mitigated in simulations using normalization procedures intended to expose the complementarity shown by the information available in each data set. As the experiments operate under such different assumptions, there is no universal way to do this. There are many factors which influence an experiment's sensitivity; for example, the total flux produced by the accelerator, the effects of baseline distance on the flux, the detector's size, technology and analysis efficiencies, not to mention the purely probabilistic effects of the oscillation itself, which occurs over different baseline distances and at different energies. In the next two sections, different ways to normalise the experiments are considered, which reveal different aspects of their sensitivities.

5.4.1 Normalising by number of events

The statistical advantage of combining two experiments can be removed by fixing the number of events. Two ways of doing this are considered, with both based on the total number of signal events S, composed of genuine appearance channel events and mis-reconstructed background events in the detectors.

The first of the two normalization methods fixes S. This is, of course, an unrealistic goal in practice. However, it answers an interesting hypothetical question: Would a fixed number of events be more informative if they came from DUNE or T2HK? The simulations of T2HK and DUNE have been produced while fixing the number of events in the appearance channel. This number varies with δ, and so the effective run time has been modified for each value of δ to keep the observed events constant. In the left-hand panel of Figure 5.15, the number of appearance events has been fixed to 8000 for each configuration, roughly what is expected for the combination of events from 10 years each at DUNE and T2HK. For a fixed number of observed events, DUNE is seen to dominate the sensitivity. In this sense, events at DUNE are more valuable than events at T2HK. This effect is quantitatively assessed in the right-hand panel of Figure 5.15. This plot compares the performance of DUNE with a fixed 8000 events, with T2HK for increasing numbers of events. To reach a comparable precision on δ T2HK needs between 2 and 3 times the number of events as DUNE. For T2HK to outperform DUNE for all values of δ it needs more than 4 times the number of events collected by DUNE.

The second normalization scheme is designed to remove the effect of the probability from the comparison with fixed event rates. The number of appearance channel events, S, is to a good approximation proportional to the oscillation probability,

$$S \propto P(\nu_\mu \to \nu_e; \langle E \rangle),$$

where $\langle E \rangle$ denotes the average energy of the flux, and a quantity N is introduced denoting signal events with the probabilistic effects removed,

$$N(\langle E \rangle) = S/P(\nu_\mu \to \nu_e; \langle E \rangle). \tag{5.4.1}$$

N can be thought of as the constant of proportionality between the number of signal events and the oscillation probability, and it is affected by many factors, whose product is often referred to as the *exposure* of the experiment. These factors, such as run time, detector mass and power of the accelerator, describe technical aspects of the experimental design and the exposure is often taken as a proxy for run time in phenomenological studies of neutrino oscillation experiments. However, there are other factors affecting the coefficient N such as the effects of cross-sections and detector efficiencies, which also vary from experiment to experiment. This definition of N accounts for all of the factors which affect the signal, apart from the fundamental effect of the oscillation probability. Equating N assumes that all technical parameters are identical between the experiments, allowing the effect of the oscillation probability to be studied alone. Whereas normalising by S puts the experiments on an equal *statistical* footing, normalising by N puts them on more of an equal *technical* footing; the statistical advantage is still removed, except where that statistical advantage is due to the actual physics (a higher oscillation probability, as opposed to higher beam power or larger detector, for example).

The performance of DUNE, T2HK and their combination is studied here with a constant value of N. In practice, as the detector models have binned energy spectra, an analogous

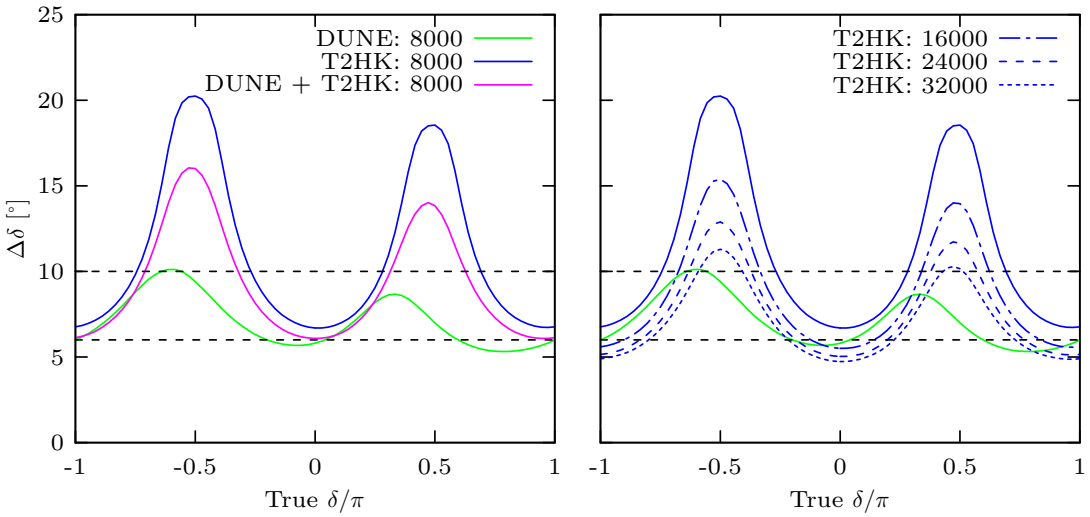

Figure 5.15: Left: The precision attainable by DUNE, T2HK and their combination with a fixed number (8000) of appearance channel events. On the left, DUNE + T2HK denotes the "fixed run time" configuration in Table 5.1, which expects around 8000 events. The DUNE configuration shown here is the corresponding "variable run time" entry in Table 5.1. For T2HK, an average detector mass of 1.4 times a single tank's mass is assumed. In both cases, the cumulative run time for the experiment has been increased until it has 8000 events. Right: The performance of T2HK with increasing numbers of appearance events (in brackets) compared to DUNE with 8000 events. T2HK is seen to need between 3 and 4 times the number of events to achieve a similar performance to DUNE for all δ. In both plots, all unspecified parameters take the true values given in Table 5.2.

quantity N_i is defined for each energy E_i and N is defined as the sum over N_i. An additional advantage of this normalisation is that, unlike when fixing S, fixing the value of N for a given experiment corresponds to equivalent experimental run time; the time required of an experiment to obtain a given number of events depends on the true values of the oscillation parameters, whereas the time required to obtain a given value of N is constant for a given experiment. Of course, the two experiments investigated here require quite different run times in their standard configurations to generate a comparable value of N. T2HK has considerably higher event rates and a 5+5 year run of DUNE contributes the same N as 0.96+2.88 at T2HK. In Figure 5.16, the sensitivities are shown for the combination of 5+5 years of DUNE with 2.5+7.5 years of T2HK, compared to the two experiments running in isolation with run times to ensure the same N: 3.46+10.38 years for T2HK, and 18+18 years for DUNE. The figure shows that for a fixed N the combination of T2HK and DUNE always outperforms T2HK running alone. However, for values of δ around the maximal CP violating values, DUNE outperforms the combination by up to 3°. This comparison shows that given a fixed N, DUNE generally outperforms T2HK and on average has a better sensitivity than the combination of DUNE and T2HK, although not at CP conserving values of δ. This suggest that events at DUNE are more informative about the value of δ than at T2HK. However, it is worth pointing out that the run times assumed here lead to quite an asymmetric comparison: for T2HK to see the same N factor as DUNE it needs to run only approximately 40 % of DUNE's run time. Comparing this to the results in Section 5.3.2, it is possible to conclude that a key advantage of T2HK is precisely that it has larger event numbers despite an intrinsically less sensitive observable.

Comparing the expected precision on δ under the two different normalization conditions gives an idea of the role played by the probability. Generally, the conclusions are seen to be similar: when arranged to have equal normalizations, T2HK does worse than DUNE for most of the parameter space. However, the behaviour around the CP conserving values of δ depends subtly on the normalization condition, and therefore the probability itself. When a fixed number of appearance events are considered (fixed S), DUNE outperforms T2HK, yet for the probability independent normalization (fixed N), T2HK performs best. This shows that the sensitivity of the probability itself is a key factor in explaining DUNE's performance. This section is concluded by noting that both normalization methods highlight the same aspect of the two experiments: events at DUNE have more information on δ; however, it is already apparent that events are harder to produce at DUNE. This will be studied in more detail in the next section.

5.4.2 Normalising by run time

Of course, one of the most pragmatic ways to normalise the experiments is by run time. Would a decade of both experiments running in parallel be better than two consecutive decades of DUNE or of T2HK? To make this comparison, the same cumulative run time is assumed for the combination of experiments as the individual run time for each of the experiments running alone. Figure 5.17 shows the results of this simulation. The combination of DUNE and T2HK outperforms either experiment running for twice as long, but T2HK reproduces the combination for most values of δ. There are some small regions of parameter space where 20 years of DUNE outperforms not only T2HK but also the combination of DUNE and T2HK, focused around the maximal CP violating

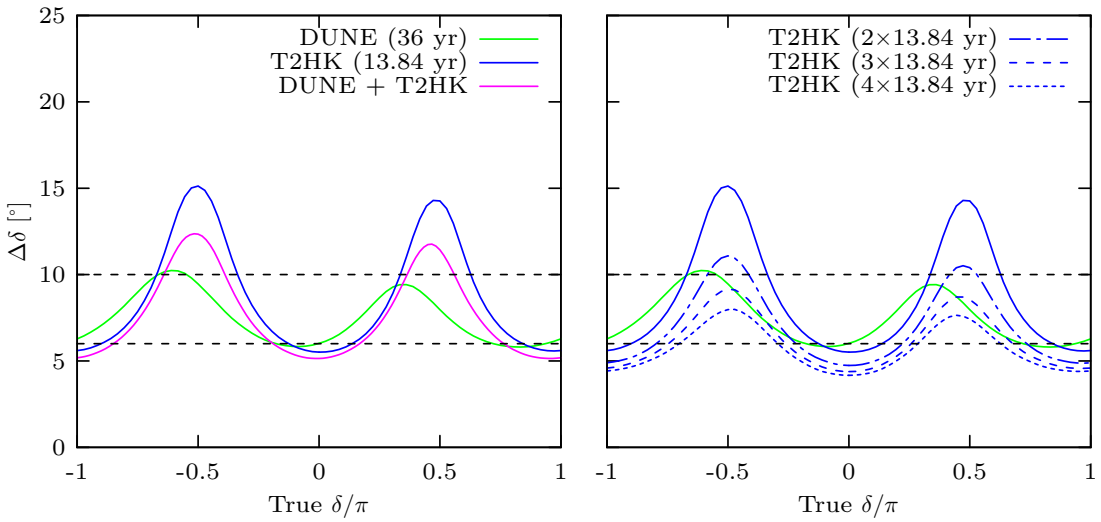

Figure 5.16: Left: The expected precision on δ as a function of the true value of δ for the standard configurations of DUNE, T2HK and their combination assuming all experiments have the same value of N. See Equation (5.4.1) for a definition of N. The DUNE + T2HK configuration is used as a reference, defined by the "fixed run time" entry in Table 5.1. The DUNE configuration is the "variable run time" configuration in Table 5.1 with the cumulative run time required to achieve the same N as the DUNE + T2HK reference, specified in brackets after the name. For T2HK, the number in brackets also denotes the cumulative run time, the staging is simplified by assuming an average detector mass of 1.4 times a single tank. Right: The precision on δ for T2HK with an increasing run time up to the point where it consistently outperforms DUNE (36 yr). In both of these plots, the true oscillation parameters are given in Table 5.2.

values of δ. At these values of δ, DUNE's wide-band beam performs best by incorporating information from other energies. This benefit is also seen in the combination of DUNE and T2HK, which outperforms 20 years of T2HK. This results indicates that the combination offers two advantages. First, running the experiments in parallel allows the collection of two decades of data in half the calendar time. This explains a significant part of the sensitivity improvement; however, there is also a complementarity arising from the different sensitivities of the two experiments. This is especially marked for this measurement about the maximally CP violating values of δ.

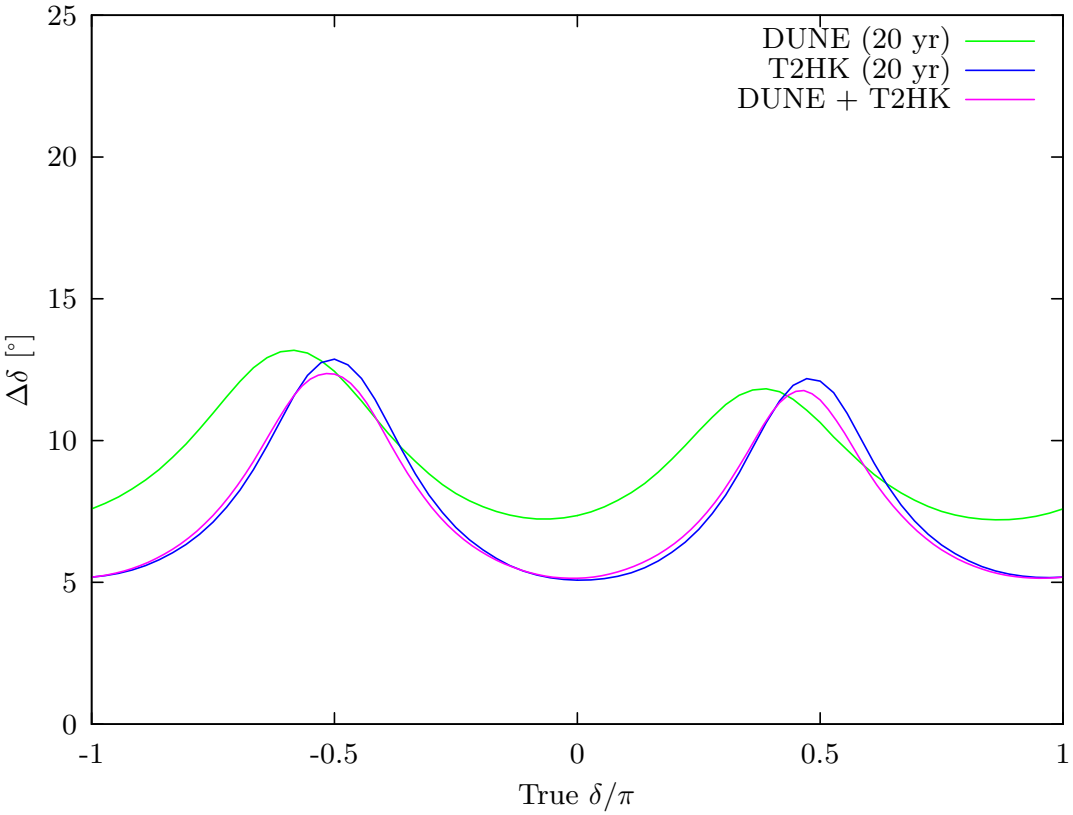

Figure 5.17: The $1\,\sigma$ precision on δ as a function of the true value of δ for DUNE, T2HK and their combination with the same cumulative run time of 20 years. The configuration of DUNE (10) is defined by the "variable run time" entry in Table 5.1, with T given in brackets after the experiment's name, whereas DUNE + T2HK is the corresponding "fixed run time" entry. For T2HK, the run time is also denoted in brackets, the scaling is simplified by assuming an average detector mass of 1.4 times a single tank. This plot assumes normal mass ordering and all other unspecified true parameters are given in Table 5.2.

The behaviour of $\Delta\delta$ for different experimental configurations as a function of run time is shown in Figure 5.18. The staging of T2HK leads to a strong improvement in the sensitivity, which is comparable to that of DUNE for large run times at $\delta = \frac{3\pi}{2}$ and consistently better for CP conserving values. This has been studied for two representative values of δ, around 0 and $\pi/2$, where the greatest difference in sensitivity for the two experiments is found. Running in parallel, the combination of DUNE and T2HK

expects $\Delta\delta \lesssim 6°$ around CP conserving values, and $\Delta\delta \lesssim 14°$ for maximally violating values after 20 years.

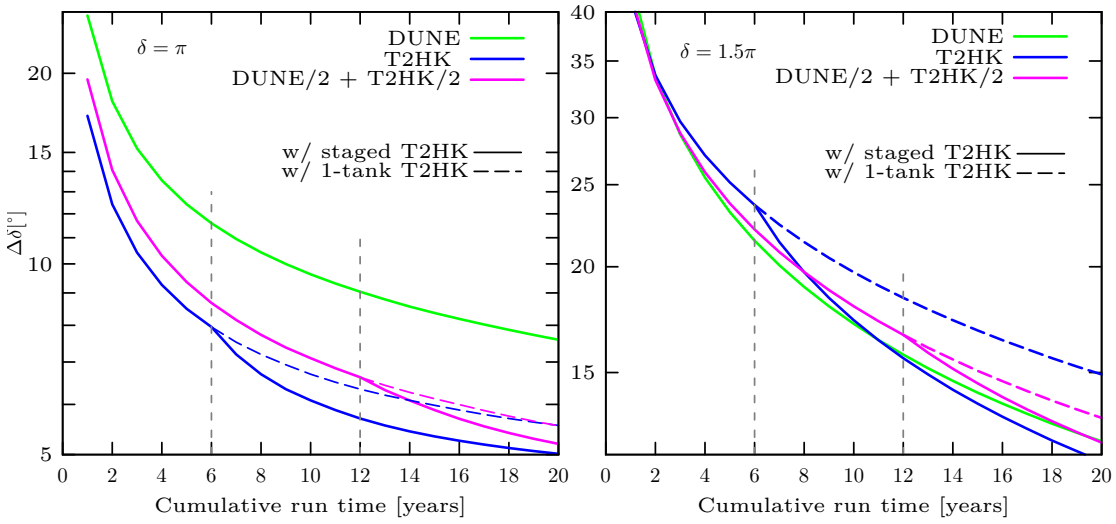

Figure 5.18: Left (right): $\Delta\delta$ for $\delta = \pi$ ($\delta = 3\pi/2$) at DUNE, T2HK and their combination as a function of run time. These plots assume the "variable run time" configurations in Table 5.1 and the true oscillation parameters appropriate for normal ordering as given in Table 5.2. Similar behaviour was also obtained for inverted ordering.

To end this section, the performance of the two experiments and their combination is compared through the minimal exposures required to obtain certain physics goals. Table 5.3, shows the value of N, see Equation (5.4.1), the number of signal events S and the cumulative run time required to reach a precision on δ of 10° for a CP conserving value of δ and a maximally CP violating value. It is clear from the study in this section that to achieve a precision of 10° for maximally CP violating values of δ will be a challenging measurement: around 30 years of data is necessary, requiring at least 15 years of both experiments running in parallel. For $\delta = \pi$ this is, however, a feasible goal. DUNE expects a similar measurement after a full 10 years data-taking period, while T2HK can achieve this goal in less than 2.5 years. The combination of DUNE and T2HK marginally improves on this, requiring only 1.8 years.

	$\delta = \pi$			$\delta = \frac{3\pi}{2}$		
	DUNE	T2HK	Both	DUNE	T2HK	Both
N	50939	31353	31440	159085	449537	260761
S	1981	2814	2378	7179	42113	23163
Run time [years]	10.33	2.44	3.54	32.29	35.07	32.78

Table 5.3: Exposures required to reach a precision of $\Delta\delta = 10°$ for a true value of δ of π or $3\pi/2$. T2HK has the best precision on reasonable time scales due to its very high event rate especially at $\delta = \pi$. DUNE marginally out performs T2HK for maximally violating values of δ. The combination "Both" assumes a scaling of the standard configuration of DUNE/2 + T2HK/2, with the run time being the cumulative run time of these two experiments, and can be seen to track the best performing experiment.

5.4.3 Impact of systematic errors

The previous section has looked at the precision on δ under a number of different assumptions. It has been seen that T2HK has a larger number of events, but that they are relatively less valuable. However, the balance of these factors is in T2HK's favour for most of the parameter space, and it expects better precision on δ. This means that the relationship between statistical and systematic uncertainty will be quite different at the different experiments and any assumptions about systematics, always a contentious issue, may be significant. This section tries to understand these effects and explores the impact on the expected precision on δ under differing systematics assumptions for the combination of DUNE and T2HK.

A feel for the relevance of statistical versus systematic uncertainty can be obtained by seeing how the sensitivity scales with run time. In the model of the systematics used in this study, only effective signal and background normalisation systematics are considered for both DUNE and T2HK. In Figure 5.19, the sensitivity to δ is shown for different run times of the two experiments in isolation, with and without systematic uncertainties. It is seen that there is little impact from the systematic uncertainty at DUNE, and it continues to further its sensitivity as its run time is increased. This effect is quite different for T2HK where systematics clearly have a more important role; for CP conserving values, there is no significant improvement in sensitivity after extensions of the experiment run time by a factor of 4. This result neatly shows that DUNE is statistically limited while T2HK has more reliance on its systematic assumptions. It is interesting to note that in both cases, neither DUNE nor T2HK taken as a single experiment running for 40 years is comparable at CP conserving values with the combination of DUNE and T2HK running for only 10 years each.

Due to the limiting effect of systematic uncertainties suspected at T2HK, it can be expected that its performance is quite sensitive to the assumptions made in the models used. To understand how the combination of DUNE and T2HK can help reduce this sensitivity, simulations have been run while varying the value of the normalization systematics in T2HK. The case of 2 %, 4 %, 6 % and 8 % normalization uncertainty have been studied, in combination with DUNE and in comparison to T2HK running for twice as long. The results are shown in Figure 5.20. It is seen that for 2 % systematic uncertainty, T2HK dominates the precision on δ and is limited strongly by the systematics, meaning that doubling the run time leads to scant improvement. As the systematic uncertainty on T2HK increases, there is more of an advantage of including DUNE. For 6 % systematics, the improvement in precision at $\delta = 0$ is around 2° (around 25 % improvement). It can be concluded that as $\Delta\delta$ by T2HK is systematically limited around $\delta = 0, \pi$, including DUNE data can help to mitigate the effect of larger uncertainties.

5.5 Impact of potential alternative designs

As part of their continual optimisation work, both the DUNE and T2HK collaborations have considered modifications of their reference designs, aiming to further the physics reach of their experiments. As mentioned in Section 5.2.1, DUNE has considered an optimised beam based on a 3-horn design as well as a novel beam concept, nuPIL. For T2HK, the redesign efforts are focused on the location of the second tank. Originally

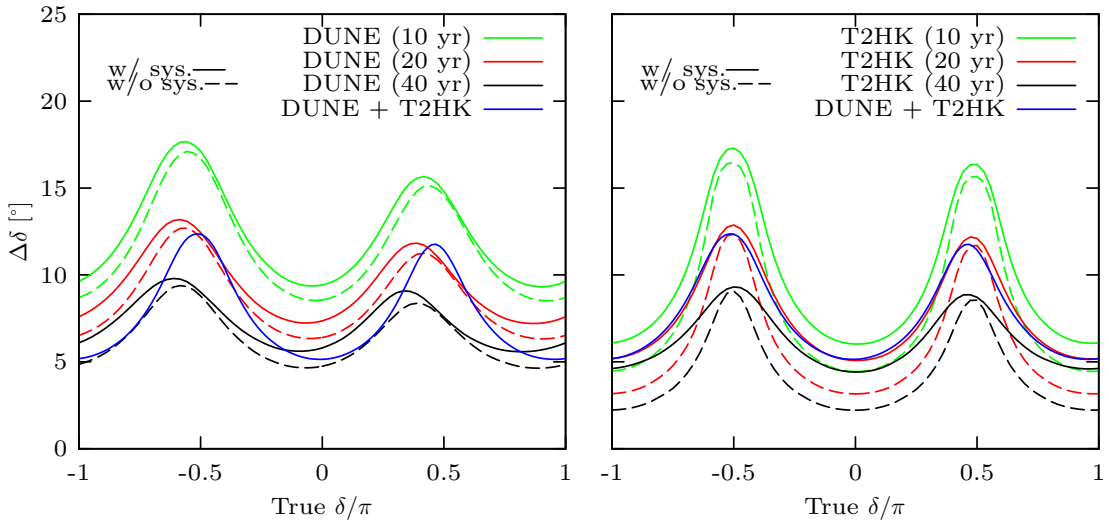

Figure 5.19: Left (right): The expected $1\,\sigma$ precision on δ for DUNE (T2HK) with different run times with and without systematics (solid and dashed, respectively) compared to a reference design of the "fixed run time" configuration of DUNE + T2HK from Table 5.1. The DUNE configuration assumed here is defined in Table 5.1 with their cumulative run time T denoted in brackets after their names. For T2HK, the number in brackets also denotes the run time, but these plots simplify the staging of the detectors by taking a total mass of 1.4 times a single tank. All unspecified parameters are given in Table 5.2.

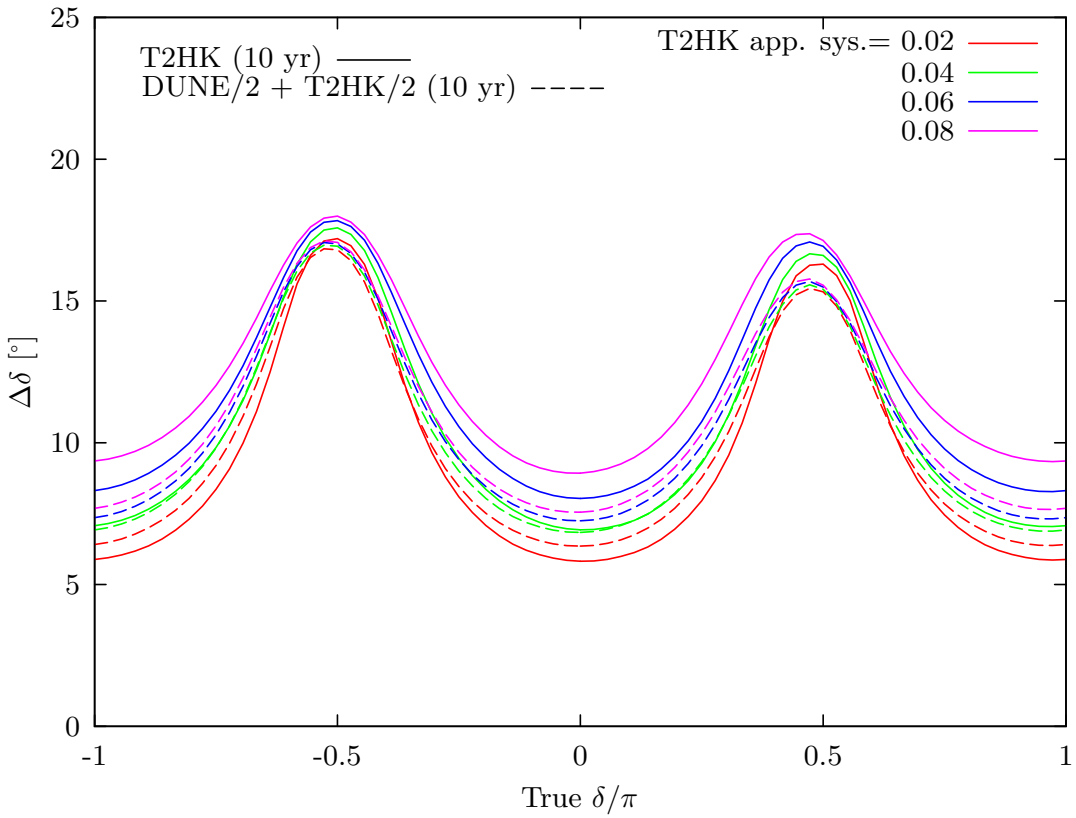

Figure 5.20: $\Delta\delta$ for T2HK and the combination of DUNE/2 + T2HK/2 each with 10 years cumulative run time for different normalization systematic uncertainties on the appearance channel in T2HK (2 %, 4 %, 6 % and 8 %). The normalization systematics are held at 2 % for the appearance channels of DUNE. The configurations in this plot are labelled "variable run time" in Table 5.1 with the cumulative run time denoted in brackets after their names. This plot assumes normal ordering, but all other true parameters follow Table 5.2.

foreseen as being installed at Kamioka 6 years after the experiment started to take data, the possibility of installing the detector in southern Korea has been mooted. This section discusses the impact of these redesigns on the physics reach of the experiments, both alone and in combination, via the results of the phenomenological discussion and simulations in the previous sections of this chapter. The focus of this section is on the mass ordering, CPV discovery, MCP and precision measurements of δ. Measurements of θ_{23} are not discussed further, as it was found that there is little difference between the alternative designs under consideration.

5.5.1 Experimental run times and ν : $\overline{\nu}$ ratios

In all plots that follow, it is assumed that DUNE and its variants will run with equal time allocated to neutrino and antineutrino mode, while T2HK and T2HKK will always follow the 1:3 ratio of their standard configuration. It is also assumed that there is no staged implementation of any of the variants of T2HKK, and that both detector modules start collecting data at the same time.

The run time configurations for these alternative designs follow those of the "variable run time" options in Table 5.1, albeit with variant fluxes for each experiment. All variants of DUNE, T2HK and T2HKK when run on their own are assumed to have a cumulative run time of 10 years. When a variant of DUNE is run in combination with a variant of T2HK, the cumulative run time is divided equally between the two experiments in the same way as DUNE/2 + T2HK/2 in Table 5.1. This means that when not plotted against T, the combination of DUNE and T2HK will have $T = 20$, or 10 years running time for each of the two experiments.

5.5.2 Mass ordering

As shown for the standard configurations in Section 5.3.1, identifying the mass ordering is almost guaranteed for experiments on this scale. However, a large difference is seen in performance between DUNE and T2HK due to the difference in baseline distance. The alternative beams of the DUNE collaboration do little to change this picture.

The results of the simulations are shown in Figure 5.21, which show the minimum sensitivity to the mass ordering as a function of cumulative run time. The left column of panels shows the performance of the alternative designs for DUNE (top) and T2HK (bottom). It is seen that for DUNE, the 3 horn design improves the minimum sensitivity by about $1\,\sigma$ compared to the 2 horn design, whilst nuPIL performs almost identically to the 2 horn design. The 3 horn design is seen to reach greater than $5\,\sigma$ significance after around 3 years run time, whereas the other two experiments require 4.5 years to 5 years.

For T2HK and its alternative designs the picture is quite different. Placing a second tank in Korea will allow T2HKK to see large matter effects over the 1000 km to 1200 km baseline, the sure-fire way to strong sensitivity to the mass ordering. Moreover, the possibility of placing the second detector at a different off-axis angle, could produce a wider beam, or a narrow beam whose peak is shifted away from the first maximum. This interplay of factors could qualitatively alter the picture of mass ordering sensitivity

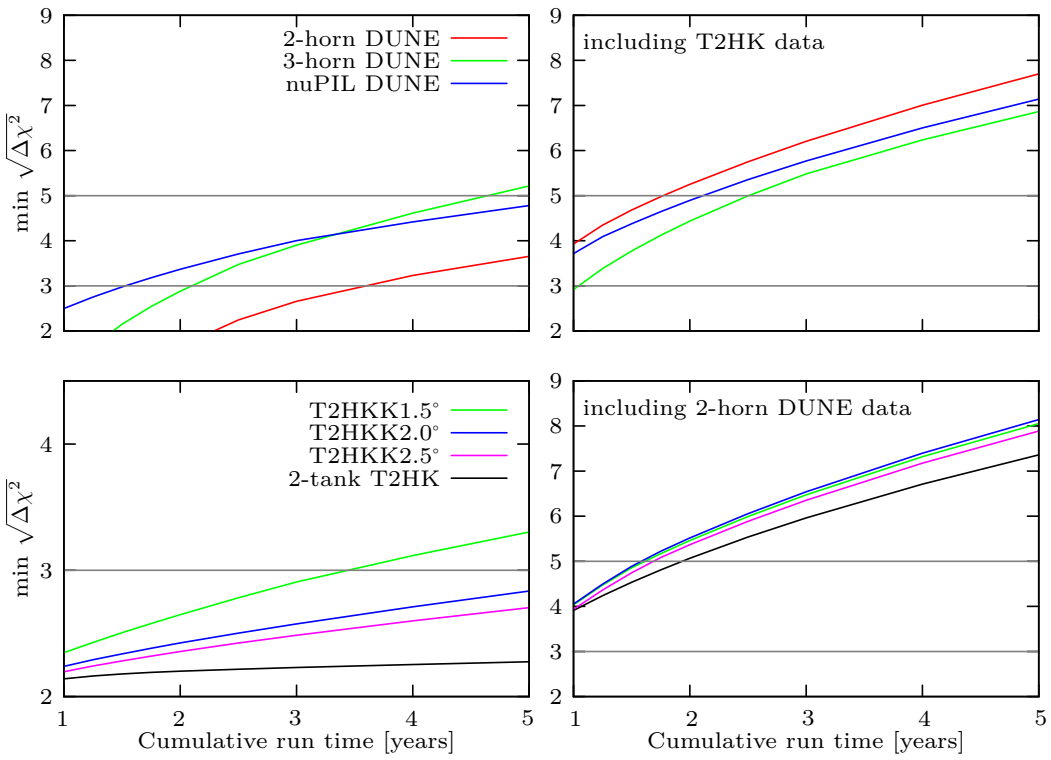

Figure 5.21: Top (bottom) row: The minimum statistical significance of mass ordering discrimination for DUNE (T2HK) with various beam designs. On both rows, the left-hand panels show the performance of the alternative designs in isolation, while the right-hand panels show the impact of an alternative design on the combination of DUNE and T2HK by incorporating the standard T2HK and DUNE designs on the top and bottom rows, respectively. The configurations assumed here are described in Section 5.5.1 and the true oscillation parameters are given in Table 5.2.

at T2HK(K). A greater variation in performance is seen as the fluxes are varied but, as seen before, lower overall sensitivities. Due to the sizeable matter effects associated with the Korean detector, there is significantly increased sensitivity to the mass ordering over the standard T2HK design, but this does not strongly enhance the sensitivity. This effect is understood to be due to the limited data collected by T2HKK at the longer baseline. Fewer events associated with neutrinos travelling the longer baseline are detected as the beam suffers significant suppression due to dispersion over the longer distance[6]. With WC technology, the advantage is known to come from scale, and such a limitation on event numbers means that longer baselines will not be competitive unless operated for a longer period of time. That said, the T2HK1.5° option does push the sensitivity above $3\,\sigma$ after around 5 years. Although the full MO sensitivity against δ is not shown in Figure 5.21, a limited comparison can be drawn between this work and Fig. 18 in [69]. The results presented here find slightly lower sensitivities: For T2HKK1.5°, the difference is about $1\,\sigma$, while for off-axis angles of 2.5° and 2.0° the difference is smaller than $1\,\sigma$.

The sensitivity is seen to increase as the Korean detector is moved to smaller off-axis angles. This can be explained by the different flux profiles of the T2HKK options. As the detector is moved towards the beam axis, the events sample the oscillation probability increasingly close to the first maximum. This is where the mass ordering is most visible in the presence of matter effects and an accordingly stronger discovery potential is seen.

The right column of Figure 5.21 shows how the alternative designs impact the combination of the two experiments. As DUNE dominates the measurement of the ordering, these figures most closely resemble the top-left panel. Including T2HK data reduces the difference in performance between the three DUNE beam designs, which all expect a minimum sensitivity of $5\,\sigma$ after 2.5 years. For T2HK, the inclusion of DUNE data, pushes the overall sensitivity above $5\,\sigma$ for the first time, with an extra Korean detector, DUNE + T2HKK expects a greater than $5\,\sigma$ measurement for all values of δ with less than 2 years run time.

5.5.3 CPV and MCP sensitivity

The sensitivity to CPV is understood to depend upon the energy of the events observed, meaning that modifying the flux spectrum, for example with a narrower beam from nuPIL or a beam located at the second maximum for T2HKK, could lead to significant changes in the physics reach of the design. In the top-left panel of Figure 5.22 the performance of the standard and alternative DUNE designs are compared. CPV and MCP sensitivities are shown for the three beam options as a function of δ in solid and dashed lines, respectively. The lower energy focus of the 3-horn optimised design is seen to lead to an increase in sensitivity to both quantities, reaching a maximal sensitivity of between $6.5\,\sigma$ and $6.8\,\sigma$. This increase is as expected due to the heightened sensitivity of the second maximum to δ. The top-right panel shows how these sensitivities are changed as information from the standard configuration of T2HK is included. It is seen that due to T2HK's strong sensitivity to the parameter δ, the impact of alternative designs for

[6]The flux is dispersed by an inverse square law as baseline increases; subsequently, a Korean detector sees around 11 % of the flux seen at Kamioka assuming the same off-axis angle.

DUNE is greatly reduced. Maximal sensitivities to CPV of above $11\,\sigma$ are found for the maximal values of $\delta \in \{\frac{\pi}{2}, \frac{3\pi}{2}\}$.

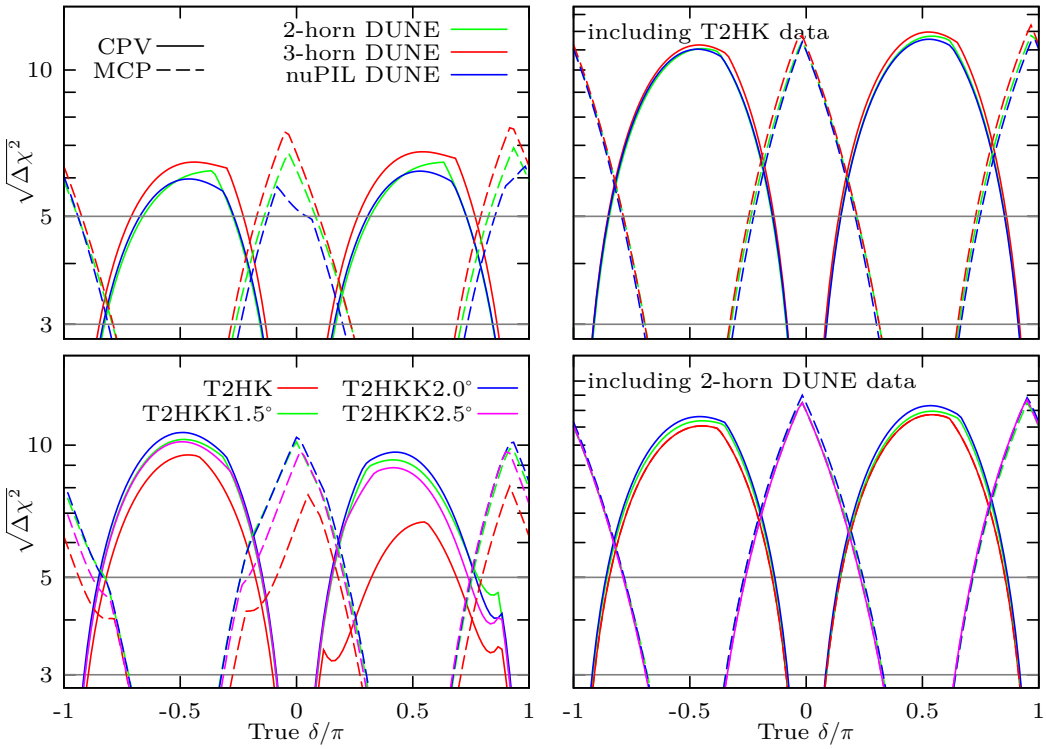

Figure 5.22: The sensitivity to CPV (solid) and MCP (dashed) as a function of δ for various designs of DUNE (top row) and T2HK (bottom row). The configurations assumed here are described in Section 5.5.1 and the true oscillation parameters are given in Table 5.2.

For T2HKK three off-axis angles for the Korean detector are compared to the standard configuration in the bottom row of Figure 5.22. The left panel, shows the performance of these alternative designs in isolation. The experiments are seen to perform comparably, but the best performance comes from the T2HKK2.0° flux. As can be seen in Figure 5.4, this flux is the best aligned with the second maximum, suggesting that it is the access to events which sample this part of the oscillation spectrum which lead to the increase in sensitivity. Despite this, the increase remains modest. This is understood to be again due to the suppression in event rates for a Korean detector: Although possessing valuable information, they are seen in relatively small numbers, and their impact is limited. The bottom-right panel of Figure 5.22 shows the sensitivity to CPV and MCP for combinations of DUNE and T2HKK. As T2HKK dominates this measurement, there is little impact of including DUNE data aside from an overall improvement in the sensitivities by between $1\,\sigma$ and $2\,\sigma$.

In Figure 5.23, the fraction of values of δ have been computed for which CP conservation or maximal CP violation can be excluded at great than $5\,\sigma$ confidence. The top-left panel shows the performance of the alternative DUNE beam designs in isolation. The 3

horn design has a significantly higher sensitivity for all run times, with a CPV fraction higher by between 10 % to 30 % and an MCP fraction higher by around 10 %. The 2 horn design and nuPIL perform comparably for most run times. Considering 30 % to be a benchmark CPV fraction, the 3 horn design expects to reach this sensitivity after around 6 years, while the other two designs take 8 years. Excluding MCP is a harder measurement for all beam designs, and exposures of greater than 10 years would be required to achieve a 30 % coverage of δ parameter space at $5\,\sigma$. The top-right panel shows how the alternative DUNE designs are affected by the inclusion of T2HK data. As it has already been seen that T2HK has a superior sensitivity to the phase δ, it is no surprise that the sensitivity is significantly higher for these combinations than the DUNE variants in isolation. A relative suppression of the difference between variants is also found; ultimately, DUNE offers less to this configuration and its precise design is less important. These combinations expect to reach a CPV fraction of 30 % (50 %) after about 4 years (6 years). For the exclusion of MCP, these values will be approximately reached after 10 years run time.

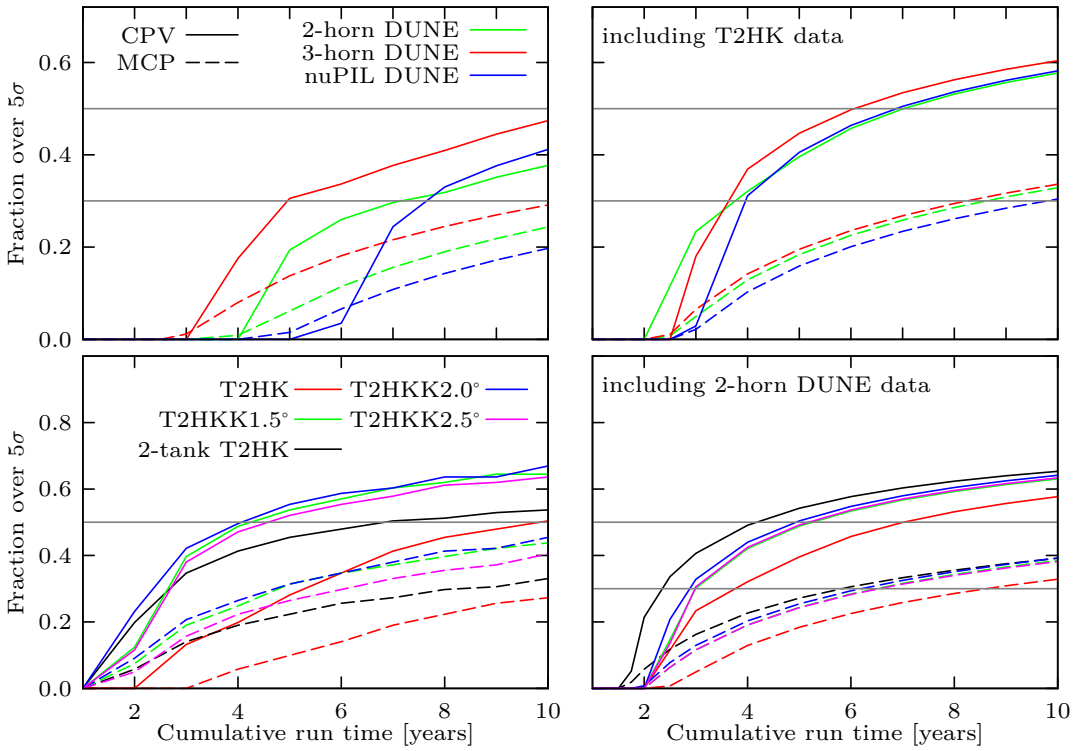

Figure 5.23: The fraction of true δ values where a CPV sensitivity (solid) and MCP sensitivity (dashed) is expected to be over $5\,\sigma$, against cumulative run time. The configurations assumed here are described in Section 5.5.1 and the true oscillation parameters are given in Table 5.2.

The bottom row of Figure 5.23 shows analogous plots for T2HK and T2HKK. On the left, these alternative designs are considered in isolation. There is very little difference between the T2HKK designs, although they all show an increase in CPV and MCP fraction over the T2HK design. T2HKK expects a CPV fraction of over 50 % after

less than 4 years, while T2HK requires around 6 years for the same sensitivity. MCP fractions of greater than 30 % are possible after 5 years and 8 years for T2HKK and T2HK, respectively. Compared with the results shown in the upper panels in Fig. 20 in [69], the same ranking of designs is found. However, sensitivities around $2\,\sigma$ higher are found near $\delta = \pm\pi/2$. This quantitative difference is suspected to be due to the priors used, since in [69] priors for δ, θ_{23} and Δm^2_{31} are not implemented. However, the studies presented in this chapter use priors on all variables apart from δ, and the simulations have slightly less leeway to accommodate degenerate solutions, and a correspondingly improved ability to exclude CP conserving parameter sets.

The right panel shows the performance for the combination of DUNE data with the T2HK variants. As in the bottom-left panel, it is seen that the T2HKK designs perform similarly, with T2HKK2.0 performing marginally the best. The inclusion of DUNE data here makes little change to the sensitivities. In fact, as cumulative run time is defined as the sum of the individual DUNE and T2HKK run times, an apparent decrease in performance is seen. Scaled appropriately for parallel data collection, DUNE + T2HKK are found to expect a $5\,\sigma$ CPV fraction of greater than 50 % after around 2.5 years compared to 3.5 years for T2HKK alone.

To conclude this section, it is noted that the experiments running in isolation can expect the exclusion of one of CP conservation or maximal CP violation for all values of δ at $3\,\sigma$ and $5\,\sigma$ for DUNE and T2HK, respectively. This can be seen clearly in Figure 5.22, where the intersections between CPV and MCP lines are above the $3\,\sigma$ or $5\,\sigma$ horizontal lines. This is true for all alternative designs, while the combination of DUNE and T2HK ensures that one of these facts would be established with a significance greater than $6\,\sigma$.

5.5.4 Precision on δ

The difference in $\Delta\delta$ is shown for the alternative designs in the left column of Figure 5.24. The top row shows that, as for CPV discovery, the 3 horn design performs best, marginally improving $\Delta\delta$ by between 0.5° and 1.5° over that of the 2 horn design. These designs expect a precision on δ somewhere between 8° and 16° after their full data taking period. The performance of the nuPIL design depends significantly on the true value of δ. For values near maximal CP violation $\delta = \pm\frac{\pi}{2}$, nuPIL performs worse than the standard design. This can be understood due to the narrowing of the beam, which when focused on first maximum, has insufficient events from other energies to mitigate the poor sensitivity around maximal CP violating phases. The top-right panel of Figure 5.24 shows the impact that the DUNE redesigns have on the combination of DUNE and the standard configuration of T2HK. As shown in Section 5.4, T2HK dominates the significance for these measurements and a correspondingly small impact is seen of alternative beam designs for DUNE, but a significantly better precision than for DUNE alone. Notably, the worsening of performance is however seen around maximal CP violating values of δ for the combination of nuPIL and T2HK.

The expected sensitivity of $\Delta\delta$ for the alternative designs for T2HKK are shown on the bottom-left panel of Figure 5.24. Here it is seen that all designs with a far detector allow for a significant improvement in the precision on δ, generally seeing the best performance coming from the 1.5° or 2.0° off-axis angle fluxes. A slight loss of performance is seen for larger off-axis angles, which may be associated with the peak of the flux falling beyond

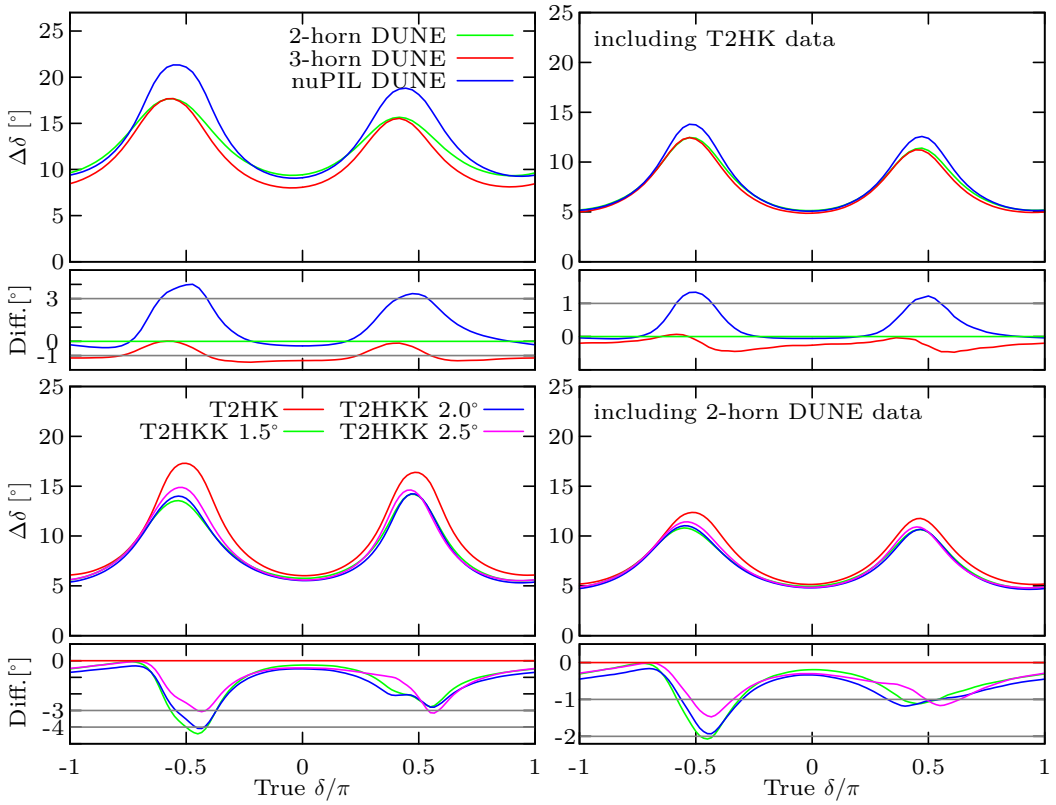

Figure 5.24: The $1\,\sigma$ precision on δ for variants of DUNE (top row) wand T2HK (bottom row). In the left column, these designs are considered in isolation while on the right, variant designs of one experiment are combined with the standard configuration of the other. The configurations used are described in Section 5.5.1. These plots assume normal mass ordering and the remaining true parameters are specified in Table 5.2.

the second maximum into a region of hard to identify, fast oscillations. The results for $\Delta\delta$ are very close to those shown in the upper panels of Fig. 23 in [69], with agreement on the ranking among alternative designs. This is notable, given the differences induced by the priors in other variables of interest, but is explained by the fact that the priors differ in their global structure more than in their local structure. It is this local structure which dictates $\Delta\delta$, as at low significance the Gaussian approximation works well and multiple minima are irrelevant. On the right panel of Figure 5.24, the combination is shown with different T2HKK fluxes and the standard DUNE configuration. Once again, it is seen that T2HKK dominates the combination, and therefore the shapes of these curves closely follow those on the left panel.

5.5.5 Optimal configuration

The preceding sections have studied how the alternative designs of T2HKK and DUNE could impact the physics reach for key measurements, considering both the experiments in isolation and in certain combinations. It was seen that the best option for DUNE is the 3 horn design, which excels at measurements of the mass ordering, and precision measurements of δ for values around $\delta \in \{\frac{\pi}{2}, \frac{3\pi}{2}\}$. T2HKK in contrast performs best with a flux positioned between 1.5° and 2.0° degrees off axis. Here it maximizes its sensitivity to CP violation, its ability to exclude maximal CP violation and to make precision measurements of δ around CP conserving values. Whereas so far alternative designs have only been considered for one experiment in combination with the standard design of the other, in this section the physics reach is reported of the optimal combination of DUNE 3-horn and T2HKK1.5 (and T2HKK2.0).

Figure 5.25 shows the minimum sensitivity expected for the mass ordering for this optimal configuration of DUNE + T2HKK. A $3\,\sigma$ measurement is expected after less than a year, which increases to $5\,\sigma$ after around 1.8 years. Figure 5.26 shows the significance at which the experiments are expected to exclude CP conservation (solid) and maximal CP violation (dashed). These are expected to reach a maximal significance of $11\,\sigma$ and $12\,\sigma$, respectively. The advantage of the combination is clearer when the performance is viewed in terms of the minimal run time required for the exclusions to be made at $5\,\sigma$. The combination of DUNE + T2HKK expects to have greater than $5\,\sigma$ exclusion of CP conservation for more than 25 % (50 %) of the parameter space after 2.5 years (5 years). For the exclusion of maximal CP violation, longer run times are required: about 6 years ensures the exclusion for more than 25 % of values of δ. For the precision on δ, shown in Figure 5.27, it is found that the optimal combination of DUNE + T2HKK could expect a measurement around a CP conserving value with an uncertainty of only 4.5°. This worsens for maximally CP violating values of δ to around 11°.

Conclusion

DUNE and T2HK will lead the way in key measurements of the neutrino oscillation parameters. These long-baseline experiments will make high statistics determinations of the mass ordering, the first precision measurements of δ, and have an excellent chance to establish the presence of fundamental CP violation in the leptonic sector. In this chapter, the expected performance of these two experiments has been studied, including

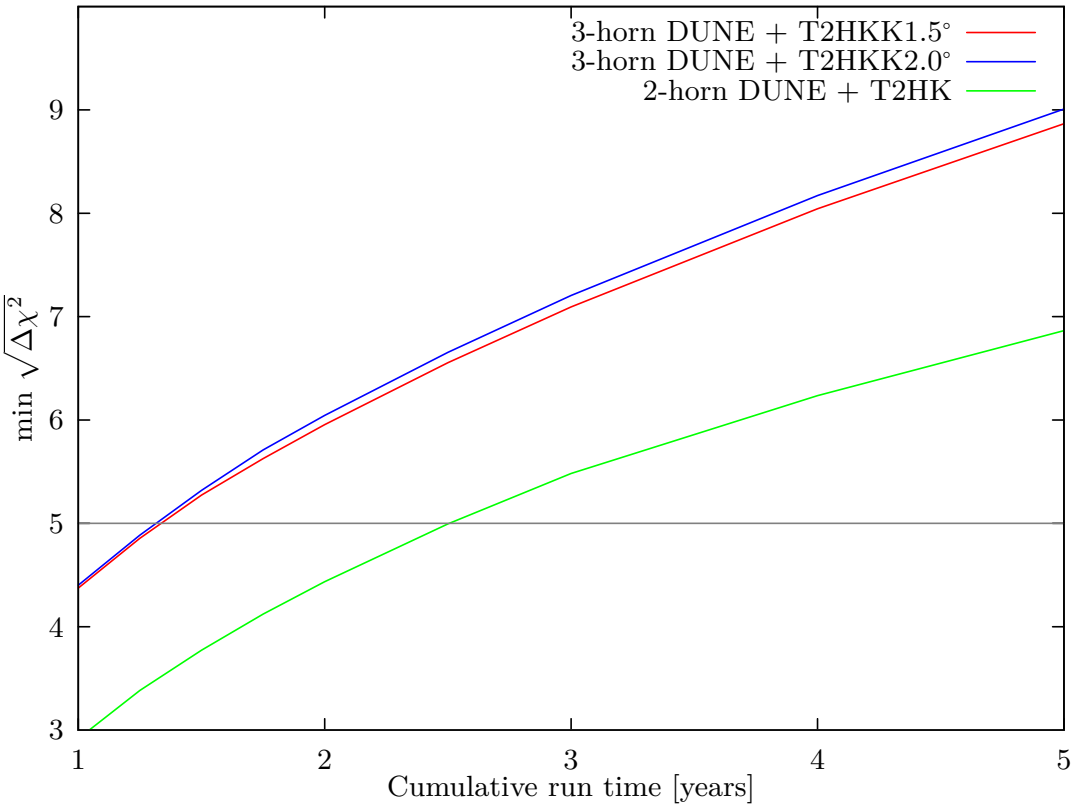

Figure 5.25: The minimum mass ordering sensitivity for the combination of DUNE with the 3 horn flux and T2HKK1.5° (red) and T2HKK2.0° (blue) compared with the standard configurations of DUNE with 2 horn flux and T2HK with a single tank at Kamioka (green). The configurations assumed here are described in Section 5.5.1 and the true oscillation parameters are given in Table 5.2.

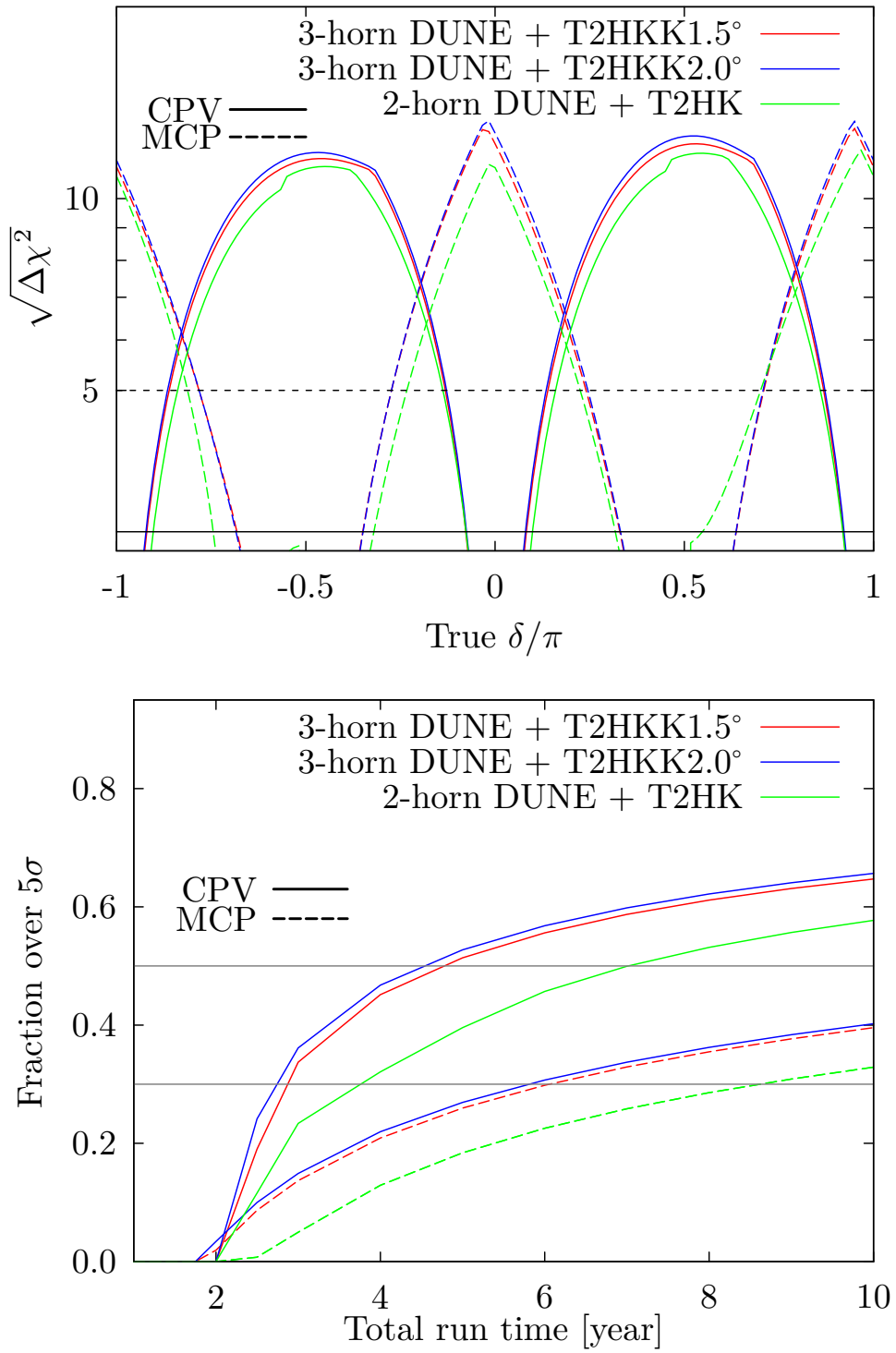

Figure 5.26: Top: The CPV and MCP sensitivity for the combination of DUNE with the 3 horn flux and T2HKK1.5°(2°) shown in red (blue). For reference, the combination of the two standard designs are also shown: DUNE with 2 horn beam and T2HK (green). Bottom: The fraction of δ parameter space for CPV (MCP) sensitivity over $5\,\sigma$ for the same configurations as on the top panel. The configurations assumed here are described in Section 5.5.1 and the true oscillation parameters are given in Table 5.2.

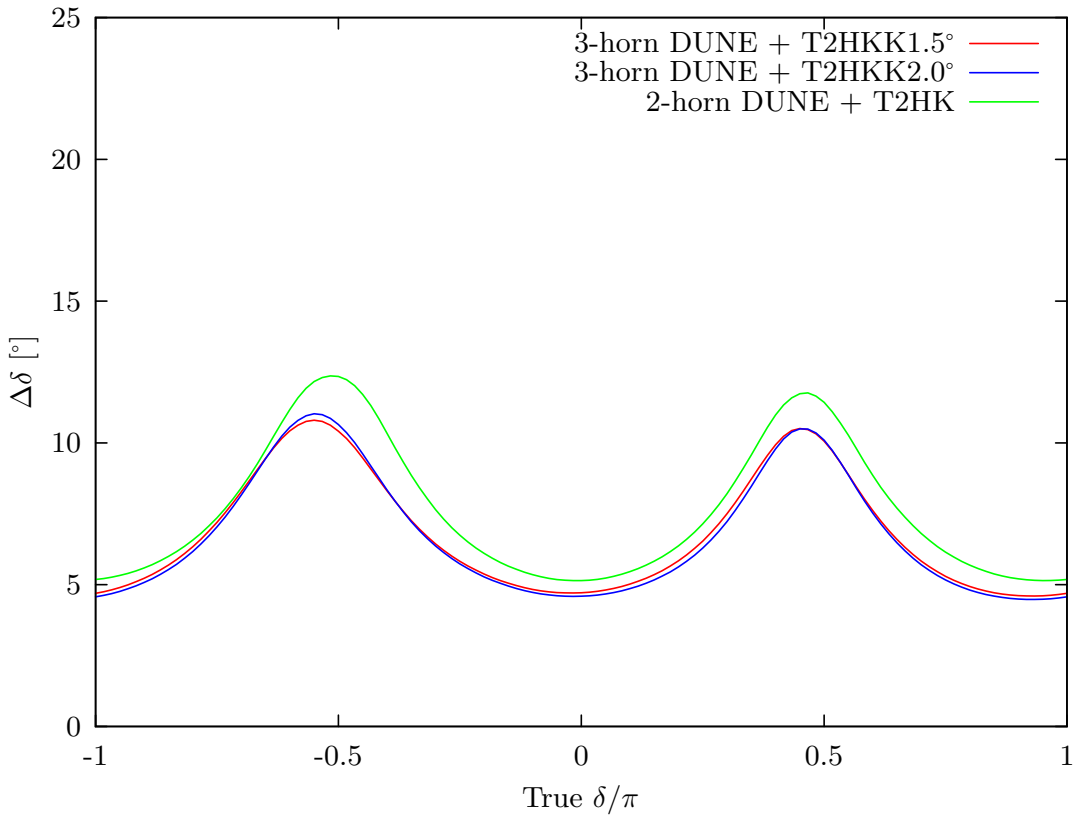

Figure 5.27: The $1\,\sigma$ error on δ for the combination of DUNE with the 3 horn flux and T2HKK1.5°(2.0°) shown in red (blue). For reference, also shown are the combination of the two standard designs: DUNE with 2 horn beam and T2HK with one tank (green). The configurations assumed here are described in Section 5.5.1 and the true oscillation parameters are given in Table 5.2.

possible alternative designs which have been recently suggested. It is seen that thanks to their different designs, both the energy profiles of the beam and the different baseline distances chosen, DUNE and T2HK have different sensitivities to the mass ordering and the value of δ, leading to a natural complementarity.

DUNE, with its long baseline and significant matter effects, excels at measuring the mass ordering. It can expect a greater than $5\,\sigma$ measurement after between 2 years and 7 years depending on the true value of θ_{23}. T2HK is limited in its sensitivity for this measurement, but the combination of data collected at T2HK with the DUNE data reduces the impact of the worst-case scenario, significantly reducing the required run times. DUNE+T2HK can expect the same measurement in less than 3 years regardless of θ_{23}. The roles are reversed for measurements of the CP phase δ. T2HK dominates this measurement, thanks to its high statistics. In isolation, T2HK expects to be able to exclude CP conservation at greater than $5\,\sigma$ for more than 50 % of the parameter space after around 7 years. DUNE alone would require between 10 years to 15 years of data for the same measurement, but the combination of the two experiments, assumed to collect data in parallel, would take at most 5 years. For the measurement of the octant sensitivity, it is found that the large event numbers in the disappearance channel of T2HK lead to better performance than at DUNE. For example, to exclude the upper octant solution at $5\,\sigma$ with a true value of $\theta_{23} = 40°$, T2HK needs about 2 years, while DUNE requires 5 years of data. This pattern is repeated for the exclusion of maximal mixing, where for the true value $\theta_{23} = 40°$, $5\,\sigma$ exclusion at DUNE takes 2 years, while T2HK can make this exclusion in only 1 year. For these measurements, T2HK dominates the performance of the combination of DUNE and T2HK, although some small benefit is found from the inclusion of extra data. Also studied is the precision on $\sin^2\theta_{23}$, where there is a strong dependence on the true value of θ_{23}, with the worst precision close to maximal mixing, as expected for a measurement driven by the disappearance channel. At the peak, $\Delta(\sin^2\theta_{23})$ for DUNE is about 0.045 while T2HK can significantly improve this, peaking around 0.032. Extending the study to the $1\,\sigma$ joint precision on δ and $\sin^2\theta_{23}$, the measurement of these two parameters are seen to be largely independent, due to the disappearance channel driving the fits to θ_{23} while the appearance channel dictates δ. The precision gets worse at $\theta_{23} = 45°$, as seen before, and improves upon moving away from this maximal value. For $\theta_{23} = 40°$ or $50°$, the precision on θ_{23} is around $0.8°$ ($0.5°$) for DUNE (T2HK). However, near maximal mixing the value increases to $\Delta\theta_{23} = 2.3°$ ($1.5°$) for DUNE (T2HK).

In particular the sensitivity to δ has been stressed, studying the behaviour of the $1\,\sigma$ uncertainty on δ, $\Delta\delta$, in some detail. For most of the parameter space, T2HK outperforms DUNE if both are operated in isolation, expecting $\Delta\delta$ to lie between $6°$ and $18°$. It was shown that T2HK is intrinsically less sensitive to δ, but increases its sensitivity through large statistics. DUNE on the other hand, is limited by lower event rates. To reach comparable precision on δ, T2HK requires between 2 and 3 times as many events as DUNE. Beyond the question of statistics, the complementarity of the two experiments for precision measurements of δ was discussed. DUNE's wide-band beam helps to compensate for a loss of sensitivity at the first oscillation maximum, which hampers T2HK's performance. It was found that DUNE performs best for maximally CP violating values of δ and T2HK, in contrast, prefers CP conserving values. When combined, these experiments complement each other, and the global sensitivity to δ is well covered

by the two technologies: DUNE + T2HK is expected to reach $\Delta\delta \lesssim 6°$ (14°) for CP conserving (maximally violating) values of δ after 10 years of running in parallel.

Also considered were the potential alternative designs for T2HK and DUNE. T2HK may locate its second detector module in southern Korea, while DUNE is considering two beams beyond its standard 2 horn reference, a 3 horn optimised and the nuPIL design. The ability of these designs to determine the mass ordering, to exclude CP conservation and maximal CP violation, and to measure δ was investigated. These alternatives are promising extensions of the current physics programme, and lead to modest improvements in all measurements studied in this work. The combination of DUNE (3 horn) and T2HKK with a flux between 1.5° and 2.0° off-axis was identified as the optimal choice, based on the measurements considered in this work. This combination expects to discover the mass ordering at $5\,\sigma$ after only 1.8 years, to be able to exclude CP conservation at $5\,\sigma$ for more than 50 % of the parameter space after 5 years, and to measure δ around CP conserving (maximally violating) values with an uncertainty of around 4.5° (11°) after its full data-taking period.

In conclusion, it has been shown that DUNE and T2HK have a natural complementarity, thanks to key differences in their designs. Although design modifications, such as nuPIL for DUNE or the location of T2HK's second detector in Korea, have quite distinct features which could upset the existing synergy, the combination of the two experiments is found to be quite robust. Sensitivity to the mass ordering will come primarily from DUNE, sensitivity to CP conservation is dominated by T2HK, but precision on δ is a bit more nuanced with wider-band information being preferred for maximally CP violating values of δ, and high statistics first maximum measurements preferred for CP conserving values. Overall, the global physics program benefits from the breadth and variation in design of these experiments.

Chapter 6

Testing Littlest Seesaw models of lepton flavour

Introduction

While the immediate goals of the future long-baseline neutrino experiments were examined in the previous chapter, the broader motivation for these measurements is more fundamental: Rather than simply increasing our knowledge of the properties of neutrinos, it is hoped that this will help further our understanding of these particles and the mechanisms which underlie their physics, perhaps even paving the way to a successor to the Standard Model of particle physics. The framework of neutrino masses and mixing for explaining neutrino oscillations – the first direct experimental evidence for physics beyond the Standard Model – is now firmly established [179]. All three mixing angles together with the size of the two mass-squared differences have been measured, with experimental efforts now focused on determining the final few unknowns: the ordering and scale of the neutrino masses, the value of the Dirac phase δ, and a precision measurement of the angle θ_{23} including, if non-maximal, its octant. Although there is some as yet inconclusive evidence for δ in the third or fourth quadrant, as well as for normal ordering (NO) and non-maximal atmospheric mixing, the next generation of oscillation experiments is relied upon to set these issues to rest. In Chapter 5 it was seen that, with the exception of only the scale of the neutrino masses, all of these measurements are within reach.

On the theoretical side, however, the origin of neutrino masses and mixing remains unknown, with many possible models considered viable (for reviews see *e.g.* [38, 44, 180–182]). A large proportion of these models are based on the classic seesaw mechanism, involving heavy right-handed Majorana neutrinos [183–188], providing both a mechanism for generating the neutrino masses and a natural explanation for their smallness. However, in order to make predictions that can be probed experimentally, seesaw models require additional assumptions or constraints [189].

To accommodate the three distinct light neutrino masses which drive the oscillation phenomenon, the seesaw mechanism requires at least two right-handed neutrinos [190]. In order to reduce the number of free parameters still further to the smallest number possible, and hence increase predictivity, various approaches to the two right-handed neutrino seesaw model have been suggested[1], such as postulating one [191] or two [192] texture zeroes in the Dirac mass matrix in the flavour basis (*i.e.* the basis of diagonal charged lepton and right-handed neutrino masses). However, such two texture zero models are now phenomenologically excluded [193] for the case of a normal neutrino mass hierarchy. The minimal two right-handed neutrino model with normal hierarchy which can accommodate the known data of neutrino mixing involves a Dirac mass matrix with one texture zero and a characteristic form known as the Littlest Seesaw model [194]. The Littlest Seesaw model may be embedded in unified models of quarks and leptons in [195, 196]. It leads to successful leptogenesis where the sign of baryon asymmetry is determined by the ordering of the heavy right-handed neutrinos, and the only seesaw phase η is identified as the leptogenesis phase, linking violation of charge parity symmetry (CP) in the laboratory with that in the early universe [197]. The Littlest Seesaw

[1] In seesaw models with two right-handed neutrinos, including those discussed in this chapter, a hierarchical spectrum of left-handed neutrino masses is obtained where the lightest left-handed neutrino is massless. This is always the case since to the Dirac mass matrix connecting the two right-handed and three left-handed neutrinos is 3×2, and so there can only be two non-zero eigenvalues in the 3×3 effective light neutrino mass matrix.

model can be understood as an example of sequential dominance (SD) [198,199] in which one right-handed neutrino provides the dominant contribution to the atmospheric neutrino mass[2], leading to approximately maximal atmospheric mixing, while the second right-handed neutrino gives the solar neutrino mass and controls the solar and reactor mixing as well as the magnitude of CP violating effects via δ. SD generally leads to normal ordering and a reactor angle which is bounded by $\theta_{13} \lesssim m_2/m_3$ [191], proposed a decade before the reactor angle was measured [179]. Precise predictions for the reactor (and solar) angles result from applying further constraints to the Dirac mass matrix, an approach known as constrained sequential dominance (CSD) [200]. For example, keeping the first column of the Dirac mass matrix proportional to $(0,1,1)^T$, a class of CSD(n) models has emerged [194, 200–205] corresponding to the second column proportional to $(1, n, (n-2))^T$, with a reactor angle approximately given by [47] $\theta_{13} \sim (n-1)\frac{\sqrt{2}}{3}\frac{m_2}{m_3}$. The Littlest Seesaw model corresponds to $n = 3$ with a fixed seesaw phase $\eta = 2\pi/3$.

It was recently realised that the alternative form of the Littlest Seesaw model with second column $(1,1,3)^T$ and seesaw phase $\eta = -2\pi/3$ (also proposed in [194]) may be enforced by an $S_4 \times U(1)$ symmetry, putting this version of the Littlest Seesaw model on a firm theoretical foundation [48] in which the required vacuum alignment emerges from symmetry as a semi-direct model [206]. In general the Littlest Seesaw model is an example of trimaximal TM_1 mixing [207–213], in which the first column of the tri-bimaximal mixing matrix [46] is preserved, similar to the semi-direct model of trimaximal TM_1 mixing that was developed in [214]. To fix the seesaw phase, one imposes a CP symmetry in the original theory which is spontaneously broken, where, unlike [215], there is no residual CP symmetry in either the charged lepton or neutrino sectors, but instead the phase η in the neutrino mass matrix is fixed to be one of the cube roots of unity due to a Z_3 family symmetry, using the mechanism proposed in [216].

As explained in more detail later in this chapter, the Littlest Seesaw model predicts all neutrino masses and mixing parameters in terms of two or three parameters, and it has been shown that the model is in agreement with all existing data, for a suitable range of its internal parameters [205]. The model makes some key predictions about the neutrino mass spectrum, that the lightest neutrino is massless $m_1 = 0$ and that normal ordering[3] obtains $\Delta m^2_{31} > 0$, which offer a means to exclude it via the observation of neutrinoless double beta decay[4], the measurement of the beta-decay end-point, or from cosmological measurements, as well as any measurement of inverted ordering from neutrino oscillation searches. However, the model also provides a rich set of predictions and correlations for the mixing angles and phases. This chapter covers the work published in [2], which studies how the future long- and medium-baseline oscillation programme will be able to

[2]With the lightest neutrino massless, $m_1 = 0$, the two non-zero masses are referred to as the *solar neutrino mass* and the *atmospheric neutrino mass*, corresponding to the square roots of the experimentally measured solar and atmospheric neutrino mass splittings $m_2 = \sqrt{\Delta m^2_{21}}$ and $m_3 = \sqrt{\Delta m^2_{31}}$ respectively.

[3]The prediction of NO is a general consequence of Sequential Dominance upon which the model is built [198, 199]. In the case of the Littlest Seesaw models in this chapter, having only two RH neutrinos leads to one massless neutrino, $m_1 = 0$, as explained above, while the model's Sequential Dominance assumption of one RH neutrino being dominant for m_2 and a second heavier RH neutrino dominant for m_3 leads directly to $\Delta m^2_{32} > 0$, *i.e.* normal ordering [191].

[4]The masslessness of the lightest neutrino leads to a neutrinoless double beta decay rate far smaller than could foreseeably be observed [205].

test this model, under the assumption of Normal Hierarchy ($m_1 = 0$ and NO), through the precision measurement of the oscillation parameters.

The layout of the chapter is as follows: in Section 6.1 the Littlest Seesaw models discussed above are defined and some of the predictions are expressed in terms of exact sum rules of the neutrino oscillation parameters. In Section 6.2 the Littlest Seesaw models are confronted with existing oscillation data, showing the precise predictions made once this data is taken into account. Section 6.3 then covers how the predictions of the models could be probed at future experimental facilities, showing the sensitivities of experiments to exclude the models and the combined measurements required to do so.

6.1 Littlest Seesaw models of neutrinos

Sequential dominance models of neutrinos arise from the proposal that, via the type-I seesaw mechanism, a dominant heavy right-handed (RH) neutrino is mainly responsible for the atmospheric neutrino mass, a heavier subdominant RH neutrino for the solar neutrino mass, and a possible third largely decoupled RH neutrino for the lightest neutrino mass [198, 199]. This leads to the prediction of normal neutrino mass ordering and, in the minimal case containing just the dominant and subdominant right-handed neutrinos, the masslessness of the lightest neutrino. Constrained sequential dominance (CSD) constrains these models further through the introduction of family symmetry, with the indirect approach used to fix the mass matrix from vacuum alignments of flavon fields [200]. A family of such models, parametrised by n, either integer or real using the family symmetry groups S_4 or A_4 respectively, predicts the CSD(n) mass matrix for left-handed neutrinos [47, 194]. Following the notation introduced in Section 1.1.3, the RH neutrino Majorana mass matrix, for the case of just two RH neutrinos, is given by

$$M_R = \begin{pmatrix} M_{\text{atm}} & 0 \\ 0 & M_{\text{sol}} \end{pmatrix}, \tag{6.1.1}$$

where M_{atm} and M_{sol} are the masses of the RH neutrinos responsible mainly for the atmospheric and solar neutrino masses respectively. The form of the Dirac mass matrix is determined by the family symmetry and is given by

$$m_D = \begin{pmatrix} 0 & a \\ e & na \\ e & (n-2)a \end{pmatrix}, \tag{6.1.2}$$

with the two additional complex parameters a and e. Following through the steps of the seesaw mechanism outlined in Section 1.1.3, this results in the left-handed light effective Majorana neutrino mass matrix in the charged-lepton flavour basis given by

$$m^\nu = m_a \begin{pmatrix} 0 & 0 & 0 \\ 0 & 1 & 1 \\ 0 & 1 & 1 \end{pmatrix} + m_b e^{i\eta} \begin{pmatrix} 1 & n & (n-2) \\ n & n^2 & n(n-2) \\ (n-2) & n(n-2) & (n-2)^2 \end{pmatrix}, \tag{6.1.3}$$

where in addition to n there are three free real parameters: two parameters with the dimension of mass $m_a \equiv \frac{e^2}{M_{\text{atm}}}$ and $m_b \equiv \frac{a^2}{M_{\text{sol}}}$, and a relative phase η determined by $\arg\left(\frac{a}{e}\right)$. A second version of this model has also been proposed, based on an $S_4 \times$

$U(1)$ symmetry, where the second and third rows and columns of the mass matrix are exchanged [48]. In this work, both these versions are discussed for the case where $n = 3$, since it has been shown that $n = 4$ is disfavoured and other values of n are already excluded [48, 205]. These models are also known as Littlest Seesaw (LS) models since they provide physically viable seesaw models with the fewest number of free parameters. The two versions of the model used are denoted here as LSA and LSB;

$$m^{\nu}_{\mathrm{LSA}} = m_a \begin{pmatrix} 0 & 0 & 0 \\ 0 & 1 & 1 \\ 0 & 1 & 1 \end{pmatrix} + m_b e^{i\eta} \begin{pmatrix} 1 & 3 & 1 \\ 3 & 9 & 3 \\ 1 & 3 & 1 \end{pmatrix}, \tag{6.1.4}$$

$$m^{\nu}_{\mathrm{LSB}} = m_a \begin{pmatrix} 0 & 0 & 0 \\ 0 & 1 & 1 \\ 0 & 1 & 1 \end{pmatrix} + m_b e^{i\eta} \begin{pmatrix} 1 & 1 & 3 \\ 1 & 1 & 3 \\ 3 & 3 & 9 \end{pmatrix}. \tag{6.1.5}$$

Although, in the most minimal set-up, the relative phase η is a free parameter, it has been shown that in some models the presence of additional Z_3 symmetries can fix the phase $e^{i\eta}$ to a cube root of unity [215], with $\eta = 2\pi/3$ the preferred value for LSA and $\eta = -2\pi/3$ for LSB as determined by current data [205]. This restriction gives the model greater predictivity by reducing the number of free parameters to two. These cases are therefore given special attention, while also showing results for the case with η left free.

Diagonalising the mass matrices above leads to predictions for the neutrino masses as well as the angles and phases of the unitary PMNS matrix, U_{PMNS}, which describes the mixing between the three left-handed neutrinos

$$U^{T}_{\mathrm{PMNS}} m^{\nu} U_{\mathrm{PMNS}} = \begin{pmatrix} m_1 & 0 & 0 \\ 0 & m_2 & 0 \\ 0 & 0 & m_3 \end{pmatrix}, \tag{6.1.6}$$

where U_{PMNS} is defined by

$$U_{\mathrm{PMNS}} = \begin{pmatrix} c_{12}c_{13} & s_{12}c_{13} & s_{13}e^{-i\delta} \\ -s_{12}c_{23} - c_{12}s_{13}s_{23}e^{i\delta} & c_{12}c_{23} - s_{12}s_{13}s_{23}e^{i\delta} & c_{13}s_{23} \\ s_{12}s_{23} - c_{12}s_{13}c_{23}e^{i\delta} & -c_{12}s_{23} - s_{12}s_{13}c_{23}e^{i\delta} & c_{13}c_{23} \end{pmatrix} \begin{pmatrix} e^{i\frac{\beta_1}{2}} & 0 & 0 \\ 0 & e^{i\frac{\beta_2}{2}} & 0 \\ 0 & 0 & 1 \end{pmatrix} \tag{6.1.7}$$

with $s_{ij} = \sin\theta_{ij}$ and $c_{ij} = \cos\theta_{ij}$. All of the parameters in this decomposition are therefore predicted in terms of the 2 (or 3) real parameters in Equations (6.1.4) and (6.1.5). Due to the minimal assumption of only two right-handed neutrinos, the lightest neutrino is massless $m_1 = 0$ and the mass-squared differences, which are the only combinations of masses accessible to neutrino oscillation experiments, are predicted to be $\Delta m^2_{21} = m^2_2$ and $\Delta m^2_{31} = m^2_3$. Of the remaining parameters, θ_{12}, θ_{13}, θ_{23} and δ, are also experimentally accessible via neutrino oscillation, while the Majorana phases β_1 and β_2 are not.

As will be seen in more detail in the next section, due to their similar forms, LSA and LSB make similar predictions. However, the process of diagonalisation reveals that the octant of θ_{23} is reversed, along with the sign of δ, while all other parameters are unchanged. Changing the sign of η, however, also reverses the sign of δ, with no other effect, and so with the sign of η not fixed by the model the only physical difference between LSA and LSB is the octant of θ_{23}.

6.1.1 Sum rules of LS

Before probing the viability of the LS models using experimental data, it is useful to summarize the hard predictions of the model irrespective of the predictions made once existing observations are enforced. In addition to the predictions of normal ordering and the lightest neutrino being massless, the form of the PMNS matrix given above enforces relationships, known as sum rules, between the neutrino mixing parameters. While the exact values of the parameters are not predicted, the relationships described in this subsection give testable predictions of the model that will be investigated throughout the remainder of this chapter.

It has already been shown that, since the first column of the LS mixing matrix U_{PMNS} is equal to that of the tri-bimaximal mixing matrix, LS (both LSA and LSB for all values of η) obeys the TM1 sum rules [47, 48]

$$\tan\theta_{12} = \frac{1}{\sqrt{2}}\sqrt{1-3s_{13}^2}, \qquad \sin\theta_{12} = \frac{1}{\sqrt{3}}\frac{\sqrt{1-3s_{13}^2}}{c_{13}}, \qquad \cos\theta_{12} = \sqrt{\frac{2}{3}}\frac{1}{c_{13}}, \tag{6.1.8}$$

$$\cos\delta = -\frac{\cot 2\theta_{23}(1-5s_{13}^2)}{2\sqrt{2}s_{13}\sqrt{1-3s_{13}^2}}, \tag{6.1.9}$$

where $s_{ij} = \sin\theta_{ij}$ and $c_{ij} = \cos\theta_{ij}$, and the forms in Equation (6.1.8) are equivalent.

For LSA with $\eta = \frac{2\pi}{3}$ or LSB with $\eta = -\frac{2\pi}{3}$, there are several additional sum rules, which have been newly derived and are presented here. A set of these additional sum rules can be derived using the fact that the only two remaining input parameters m_a and m_b have dimensions of mass, so all the mixing angles and phases must depend only on the (unitless) ratio $r \equiv \frac{m_b}{m_a}$. The exact expressions for the mixing angles and Dirac phase as a function of r can be found in Appendix D, along with new exact sum rules derived using these expressions. These results make clear the difference between predictions of LSA and LSB; while θ_{13} and θ_{12} remain unchanged, $\cos 2\theta_{23}$ and $\cos\delta$ differ by a change of sign.

An exact expression for the Jarlskog invariant J has previously been given as [47, 48]

$$J = s_{12}c_{12}s_{13}c_{13}^2 s_{23}c_{23}\sin\delta = \mp\frac{24m_a^3m_b^3(n-1)\sin\eta}{m_3^2m_2^2\Delta m_{32}^2}. \tag{6.1.10}$$

with the negative sign taken for LSA and positive for LSB. For both LSA with $\eta = \frac{2\pi}{3}$, and LSB with $\eta = -\frac{2\pi}{3}$, the new relation

$$m_2m_3 = 6m_am_b \tag{6.1.11}$$

is found. Using this relation and inserting $n = 3$ into Equation (6.1.10) leads to the new relation for the Jarlskog invariant J

$$J = -\frac{\sqrt{\Delta m_{21}^2\Delta m_{31}^2}}{3\sqrt{3}\Delta m_{32}^2} \tag{6.1.12}$$

and hence the new sum rule,

$$\sin\delta = -\frac{\sqrt{\Delta m_{21}^2\Delta m_{31}^2}}{3\sqrt{3}\Delta m_{32}^2 s_{12}c_{12}s_{13}c_{13}^2 s_{23}c_{23}}, \tag{6.1.13}$$

which is valid for both LSA with $\eta = \frac{2\pi}{3}$ and LSB with $\eta = -\frac{2\pi}{3}$.

6.2 Probing LS with existing data

Existing measurements of the neutrino mixing parameters have been shown to be in good agreement for CSD(n) for the $n = 3$ case [205]. The best-fit value of η is found to be close to $\pm\frac{2\pi}{3}$, with the positive sign for LSA and the negative sign for LSB, which has been theoretically motivated as one of the cube roots of unity required due to an additional Z_3 symmetry as part of a larger GUT model [47]. This section, studies both the case where η is fixed by symmetry and the case where it is left as a free parameter of the theory.

6.2.1 Predictions of oscillation parameters with fixed $\eta = \pm 2\pi/3$

In the $n = 3$ case of LSA with $\eta = \frac{2\pi}{3}$ (or LSB with $\eta = -\frac{2\pi}{3}$), all neutrino masses, mixing angles and phases are fully determined from the two remaining parameters m_a and m_b and the three most precisely measured of these parameters, θ_{13}, Δm^2_{31} and Δm^2_{21}, currently provide the strongest test of the LS model. Exact expressions are used for all mixing angles and neutrino masses, derived in [47, 48], to study these predictions of the LSA and LSB models. Figure 6.1 shows how these parameters vary in the $m_a - m_b$ plane, along with the regions corresponding to the $1\,\sigma$ and $3\,\sigma$ ranges for these parameters from the NuFit 3.2 (2018) global fit [6], assuming normal mass ordering and a lightest neutrino mass of $m_1 = 0$. The SD proposal requires m_a to be significantly larger than m_b and for this portion of the parameter space the approximate proportionality relations of $m_2 \sim m_b$ and $m_3 \sim m_a$ can be seen, verifying the approximations previously derived in [47].

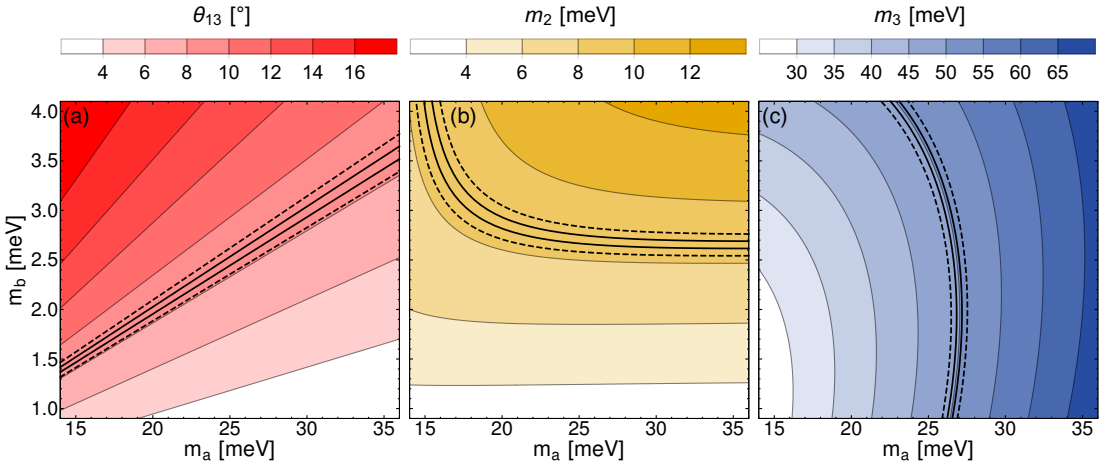

Figure 6.1: Predicted values from LSA with $\eta = \frac{2\pi}{3}$ (or LSB with $\eta = -\frac{2\pi}{3}$) of oscillation parameters depending on the input parameters m_a and m_b. Regions corresponding to the experimentally determined $1\,\sigma$ (solid lines) and $3\,\sigma$ (dashed lines) ranges for each parameter are also shown.

Even at $1\,\sigma$ the three allowed regions coincide at a single point, as can be seen in Figure 6.2, and so this benchmark point can be used to make predictions of the remaining angles θ_{12} and θ_{23} and the Dirac phase δ. As described in Section 6.1 these parameters, along with θ_{13}, depend only on the ratio $r = m_b/m_a$; this dependence, given by the relations in Equation (D.0.1), is shown in Figure 6.3, with the $1\,\sigma$ and $3\,\sigma$ NuFIT 3.2 ranges and reference point at $m_b/m_a = 0.1$. For θ_{23} and δ, the predictions of both LSA and LSB are shown. At this point it can be seen that all mixing angles θ_{13}, θ_{12} and θ_{23} lie within their $1\,\sigma$ ranges and a prediction on the value of the Dirac phase is made of $\delta \simeq -90°$.

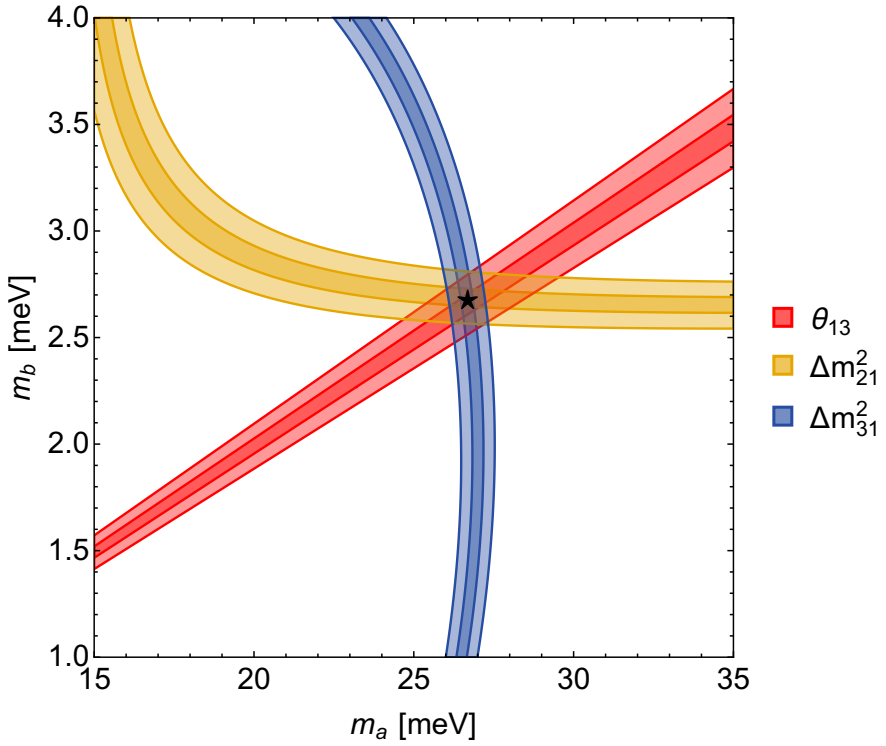

Figure 6.2:
Regions in the m_a-m_b plane with fixed $\eta = 2\pi/3$ ($\eta = -2\pi/3$) for LSA (LSB) corresponding to the experimentally determined $1\,\sigma$ and $3\,\sigma$ ranges for θ_{13}, Δm^2_{21} and Δm^2_{31}.

Combining these results for all parameters that have been experimentally measured, displayed together in Figure 6.4, the predictions for θ_{12} and θ_{23} are seen to lie within the current $1\,\sigma$ bounds for both LSA and LSB.

6.2.2 Predictions of oscillation parameters with η as a free parameter

In the versions of the LS models with η as an additional free parameter, the mixing angles and phases now depend on both the ratio $r = m_b/m_a$ and η. The masses m_3 and m_2 depend on all three input parameters; however, their ratio m_2/m_3 (and therefore the ratio $\Delta m^2_{21}/\Delta m^2_{31}$) will depend only on r and η. As previously, the strongest constraints come from the very precise measurements of θ_{13} and the mass-squared differences Δm^2_{21} and Δm^2_{31}. Figure 6.5 shows the regions corresponding to the $1\,\sigma$ ranges for all the

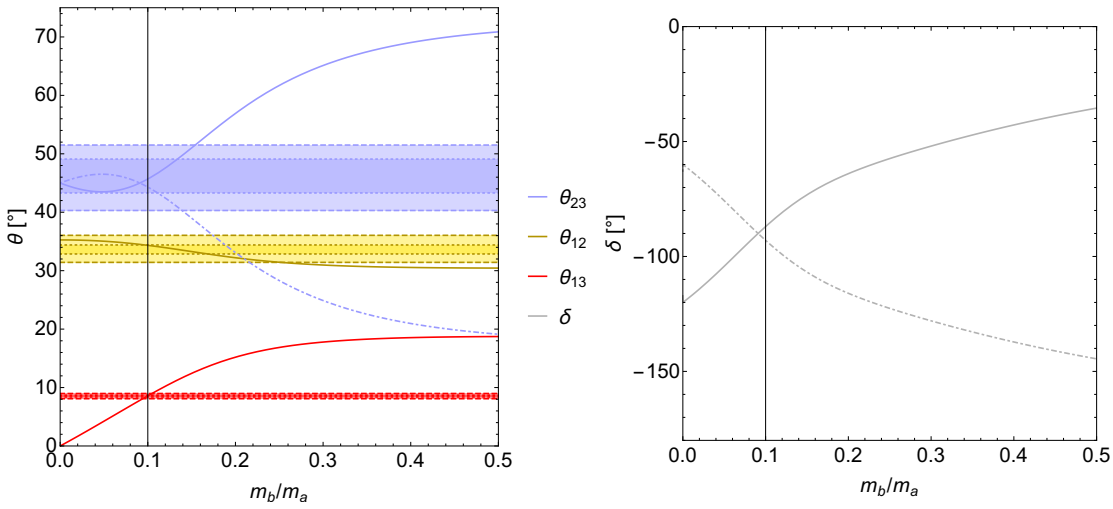

Figure 6.3: Predicted values from LS with fixed $\eta = 2\pi/3$ for LSA (solid) and $\eta = -2\pi/3$ for LSB (dot-dashed) of the mixing angles and delta as a function of the ratio m_b/m_a. Note that only θ_{23} and δ differ between LSA and LSB. Horizontal bands show the experimentally determined $1\,\sigma$ and $3\,\sigma$ ranges for each parameter. A reference point giving a good prediction for all parameters is shown at $r = m_b/m_a = 0.1$.

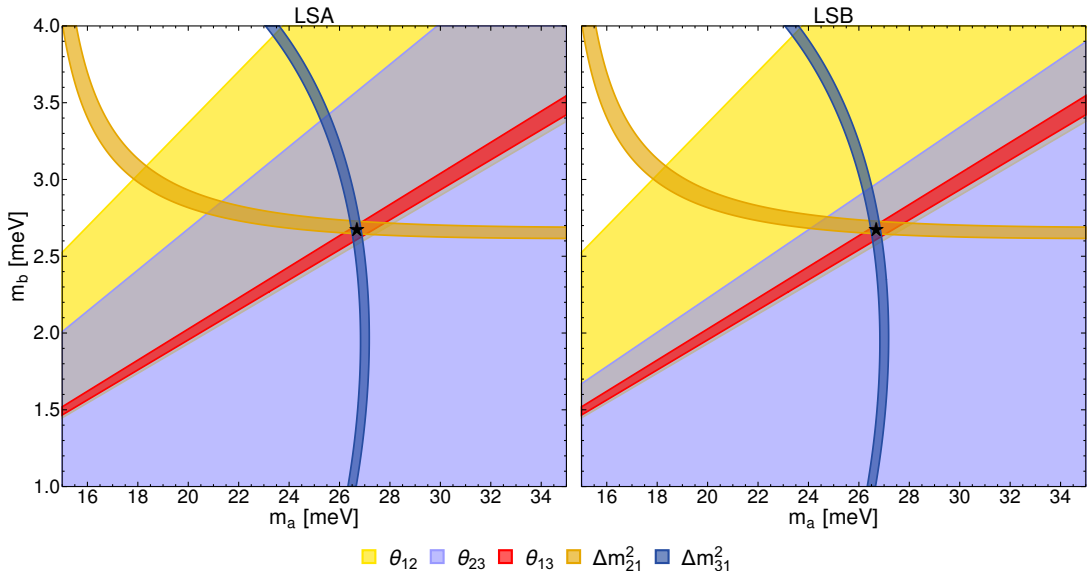

Figure 6.4: Regions in the m_a-m_b plane with fixed $\eta = 2\pi/3$ ($\eta = -2\pi/3$) for LSA (LSB) corresponding to the experimentally determined $1\,\sigma$ ranges for solar and reactor mixing angles and mass-squared differences. The θ_{23} regions shown are in tension with other measurements, however, extending to $2\,\sigma$ these regions become far larger, covering the entire parameter space shown in these plots.

mixing angles, δ and m_2/m_3, where it is seen that all the five regions overlap at a region around $\eta = \pm 2\pi/3$ for LSA and LSB, respectively. That two input parameters should give a good description of five observables, within their one sigma errors, is ostensibly a remarkable achievement, indeed perhaps better than might be expected on statistical grounds.

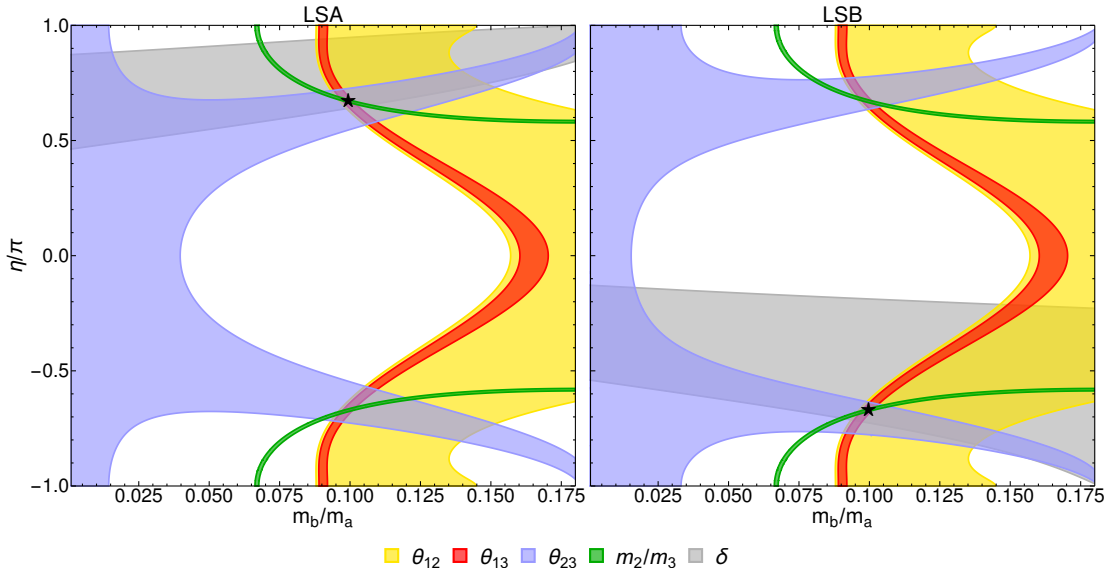

Figure 6.5: Regions in the (m_b/m_a) - η plane corresponding to the experimentally determined $1\,\sigma$ ranges for all mixing angles, δ and the ratio of neutrino masses m_2/m_3 for LSA (left panel) and LSB (right panel).

6.2.3 Fitting LS models to global fit data

In order to provide a more concrete measure of the agreement between the predictions of the model and existing data, as well as to make further predictions of the less well measured parameters, a χ^2 fit is performed to the four cases discussed above: LSA and LSB with η fixed and free. As a proxy for the full data sets of previous experiments, these fits use the results of the NuFIT 3.2 global analysis [6]. This analysis combines the results (as of early 2018) of solar, atmospheric, long baseline accelerator, and long, medium and short baseline reactor neutrino experiments, to obtain a combined fit to the six standard neutrino oscillation parameters. The χ^2 data provided by NuFIT[5] is used, for the case where normal mass ordering is assumed, combining both the 1D χ^2 data for each mixing parameter with the 2D χ^2 data to include correlations between parameter measurements

$$\chi^2_{\rm Fit}(\Theta) = \sum_{\theta_i \in \Theta} \chi^2_{\rm 1D}(\theta_i) + \sum_{\theta_i \neq \theta_j \in \Theta} \left(\chi^2_{\rm 2D}(\theta_i, \theta_j) - \chi^2_{\rm 1D}(\theta_i) - \chi^2_{\rm 1D}(\theta_j) \right), \tag{6.2.1}$$

where the first sum in this expression combines each of the 1D χ^2 data into a first approximation of the full 6D χ^2 while the second sum provides corrections to this coming

[5]The full data used for one- and two-dimensional $\Delta\chi^2$ projections of the NuFIT analysis, available at http://www.nu-fit.org

from the 2D correlations between each pair of parameters. This procedure is used since the full 6D χ^2 data is not available and so using the 1D and 2D data together in this way provides the best possible approximation. The more simple (and more commonly applied) method of using only the 1D χ^2 data for each parameter would be insufficient for our case, since it is often the correlations between parameters, rather than their values independently, that are testing the model predictions.

This result is then applied first to the standard mixing case, then to the LS model case as follows:

- For the case of standard mixing $\Theta = \Theta_{\text{PMNS}} \equiv \{\theta_{12}, \theta_{13}, \theta_{23}, \Delta m^2_{21}, \Delta m^2_{31}, \delta\}$ and the NuFIT 3.2 results are simply combined as shown above, in order to include correlations, and use this to calculate $\chi^2\left(\Theta_{\text{PMNS}}\right) \equiv \chi^2_{\text{Fit}}(\Theta)$ for this case.
- For the LS model $\Theta = \Theta_{LS} \equiv \{m_a, m_b, \eta\}$ (or $\Theta_{\text{LS}} = \{m_a, m_b\}$ when fitting with η fixed) is used instead, which is then minimised over the LS parameter space, using the analytic relations to calculate standard mixing parameters from LS parameters and hence calculate $\chi^2\left(\Theta_{\text{LS}}\right) \equiv \chi^2_{\text{Fit}}(\Theta)$ for this case.

The test statistic used for a particular LS model is then given by:

$$\sqrt{\Delta\chi^2} = \sqrt{\min_{\Theta_{\text{LS}}}\left[\chi^2\left(\Theta_{\text{LS}}\right)\right] - \min_{\Theta_{\text{PMNS}}}\left[\chi^2\left(\Theta_{\text{PMNS}}\right)\right]}. \tag{6.2.2}$$

While a number of the assumptions in Wilks' theorem [217] are broken by the parameter space of the LS models (and indeed standard neutrino mixing), Monte-Carlo simulations of randomised experimental data were used to confirm that Wilks' theorem holds well for this statistic, *i.e.* it is approximately distributed according to a chi-squared distribution. This allows the statistic to be used to quote results in terms of a number of σ in the conventional way.

The best fit LSA and LSB points for fits with η left free or with η fixed at $\frac{2\pi}{3}$ are given in Table 6.1 together with errors on the predicted parameters corresponding to the $1\,\sigma$ allowed ranges. The number of degrees of freedom (d.o.f.) is either 3 or 4, which is just the difference between the number of observables (which is taken to be the parameters in Θ_{PMNS}) and the number of LS parameters (namely the parameters in Θ_{LS}, which is either 3 or 2, depending on whether η is free or fixed). For LSA a best fit is found with $\Delta\chi^2 = 1.6$ (3 degrees of freedom) with η free and $\Delta\chi^2 = 1.9$ (4 degrees of freedom) fixing $\eta = \frac{2\pi}{3}$, while slightly better fits are found for LSB, with $\Delta\chi^2 = 1.5$ (3 degrees of freedom) and $\Delta\chi^2 = 1.7$ (4 degrees of freedom) for η free and $\eta = -\frac{2\pi}{3}$ respectively.

Figure 6.6 shows the best fit points with $1\,\sigma$ and $3\,\sigma$ contours of the fits in the $m_a - m_b$ plane for fixed η and in the $r - \eta$ plane for free η. The significance at which a LS model is allowed is determined from the distribution of the $\Delta\chi^2$ test statistic, where $N\sigma$ has been calculated assuming that Wilks' theorem applies.

The fit can also be used to identify the regions of standard neutrino mixing parameter space predicted by LS, once existing data has been taken into account. This corresponds to mapping the regions of LS input parameter space allowed by the fit onto the standard mixing parameter space.

Figure 6.7 shows the predictions of LS (for the fixed η case) in the planes made from each pair of mixing angles and δ. Since these values all depend only on the single parameter

	LSA		LSB		NuFIT 3.2
	η free	η fixed	η free	η fixed	global fit
m_a [meV]	26.80	26.61	26.74	26.64	
m_b [meV]	2.666	2.670	2.669	2.673	—
η [rad]	0.672π	$2\pi/3$	-0.670π	$-2\pi/3$	
θ_{12} [°]	$34.34^{+0.03}_{-0.03}$	$34.33^{+0.02}_{-0.02}$	$34.33^{+0.04}_{-0.03}$	$34.33^{+0.02}_{-0.03}$	$33.62^{+0.78}_{-0.76}$
θ_{13} [°]	$8.57^{+0.13}_{-0.16}$	$8.61^{+0.11}_{-0.10}$	$8.59^{+0.13}_{-0.16}$	$8.61^{+0.11}_{-0.10}$	$8.54^{+0.15}_{-0.15}$
θ_{23} [°]	$45.46^{+0.52}_{-0.56}$	$45.72^{+0.11}_{-0.10}$	$44.45^{+0.60}_{-0.52}$	$44.28^{+0.10}_{-0.11}$	$47.2^{+1.9}_{-3.9}$
δ [°]	$-88.0^{+2.2}_{-2.4}$	$-86.9^{+0.4}_{-0.4}$	$-92.4^{+2.6}_{-2.2}$	$-93.1^{+0.4}_{-0.4}$	-126^{+43}_{-31}
Δm^2_{21} [10^{-5}eV^2]	$7.396^{+0.203}_{-0.209}$	$7.311^{+0.155}_{-0.136}$	$7.379^{+0.204}_{-0.199}$	$7.328^{+0.150}_{-0.145}$	$7.40^{+0.21}_{-0.20}$
Δm^2_{31} [10^{-3}eV^2]	$2.485^{+0.029}_{-0.029}$	$2.485^{+0.030}_{-0.027}$	$2.485^{+0.030}_{-0.028}$	$2.490^{+0.027}_{-0.030}$	$2.494^{+0.033}_{-0.031}$
$\Delta\chi^2$ / d.o.f	1.6 / 3	1.9 / 4	1.5 / 3	1.7 / 4	—

Table 6.1: Results of the fit of existing data to LSA and LSB with η left free and for $\eta = \frac{2\pi}{3}$ for LSA and $\eta = -\frac{2\pi}{3}$ for LSB. The best fit values are given for both the input parameters, m_a, m_b and η, and the output parameters, θ_{ij}, Δm^2_{ij} and δ, together with the $\Delta\chi^2$/ degrees of freedom for the best fit. For the output parameters, errors are also given corresponding to the $1\,\sigma$ ranges of the fit. The results of the NuFIT 3.2 (2018) global fit to standard neutrino mixing for the normal ordering case are shown for comparison.

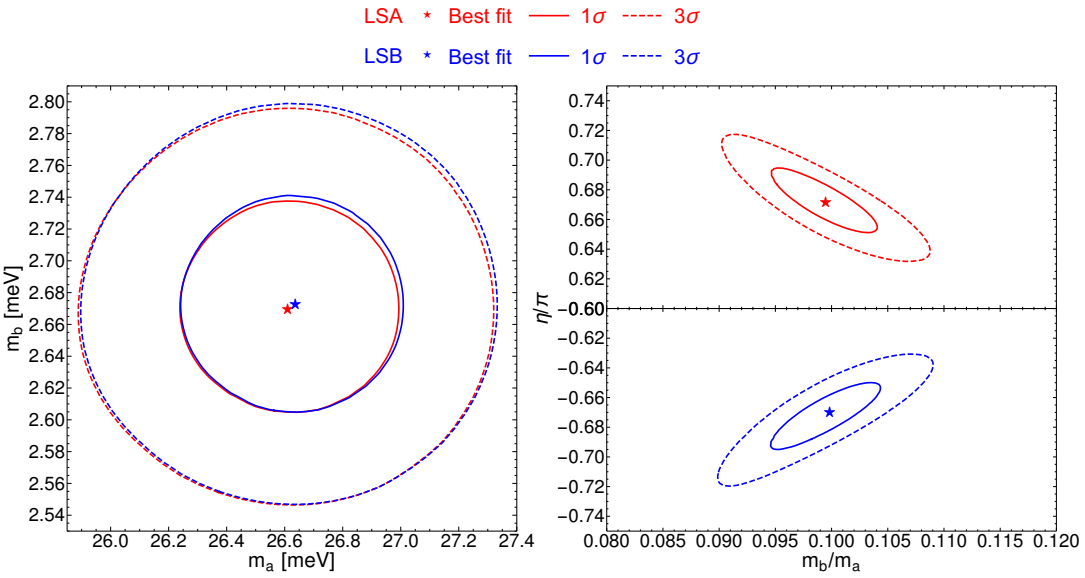

Figure 6.6: Results of the fits to LS of the NuFIT 3.2 (2018) global neutrino oscillation data. Left: LS fit with fixed $\eta = 2\pi/3$ ($\eta = -2\pi/3$) for LSA (LSB). Right: LS fit with η as a free parameter.

r, the predictions of LS form lines of allowed solutions in each plane, corresponding to sum-rules between the oscillation parameters. For example, Figure 6.7a corresponds to the TM1 sum rule in Equation (6.1.8), while Figures 6.7b to 6.7f correspond to those in Equation (D.0.6) or to combinations of these sum rules. It can be seen that very strong restrictions are placed on the allowed values of the less well measured parameters, θ_{12}, θ_{23} and δ. For the remaining angle, θ_{13}, the majority of the NuFIT 3.2 range remains viable in LS.

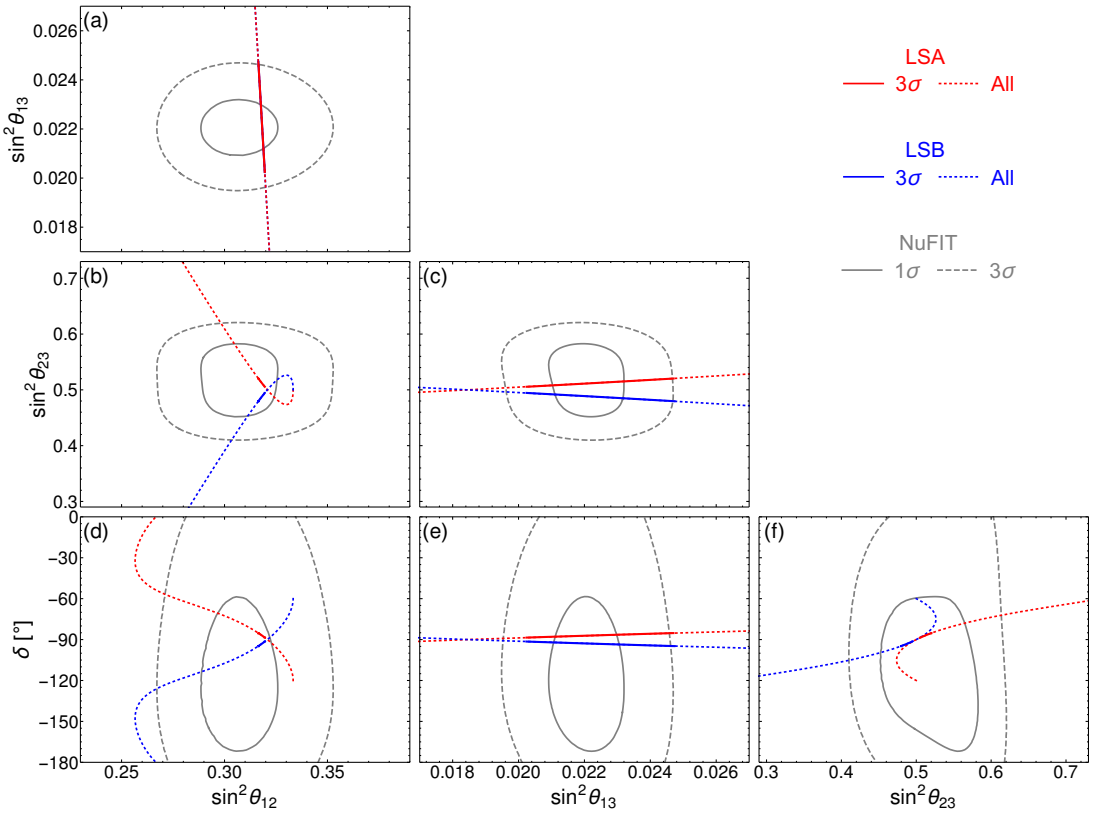

Figure 6.7: Allowed values for LSA (red) and LSB (blue) with $\eta = 2\pi/3$ and $\eta = -2\pi/3$ respectively. The dotted lines labelled "All" show all possible values allowed by the model, corresponding to the solutions of the sum rules in Equations (6.1.8) and (D.0.6)) or combinations thereof without any constraints from experimental data, with the solid segments showing those values allowed experimentally at $3\,\sigma$. Also shown are the $1\,\sigma$ (solid) and $3\,\sigma$ (dashed) regions from the NuFIT 3.2 2018 global fit (grey).

Figure 6.8 shows the allowed regions of parameter space for pairs of variables including the mass-squared differences. In these plots, as the mass-squared differences can depend on both m_a and m_b independently, regions of allowed values are seen instead of lines. For each of these planes, any point will fully determine both input parameters m_a and m_b, and so these contours correspond exactly to the equivalent regions shown in Figure 6.6. In addition to the tight constraints on θ_{12}, θ_{23} and δ already mentioned, in Figures 6.8b and 6.8e it can be seen that the allowed range of θ_{13} is correlated with that of both Δm^2_{21} and Δm^2_{31}, suggesting that combining future measurements of these parameters could provide a better probe of LS than the individual parameter measurements alone. The ability of future experiments to exclude the model then depends on both the predictions

of the model seen here, combined with the sensitivity of experiments to measurements of the parameters in the region of interest predicted by LS, which is the focus of the next section.

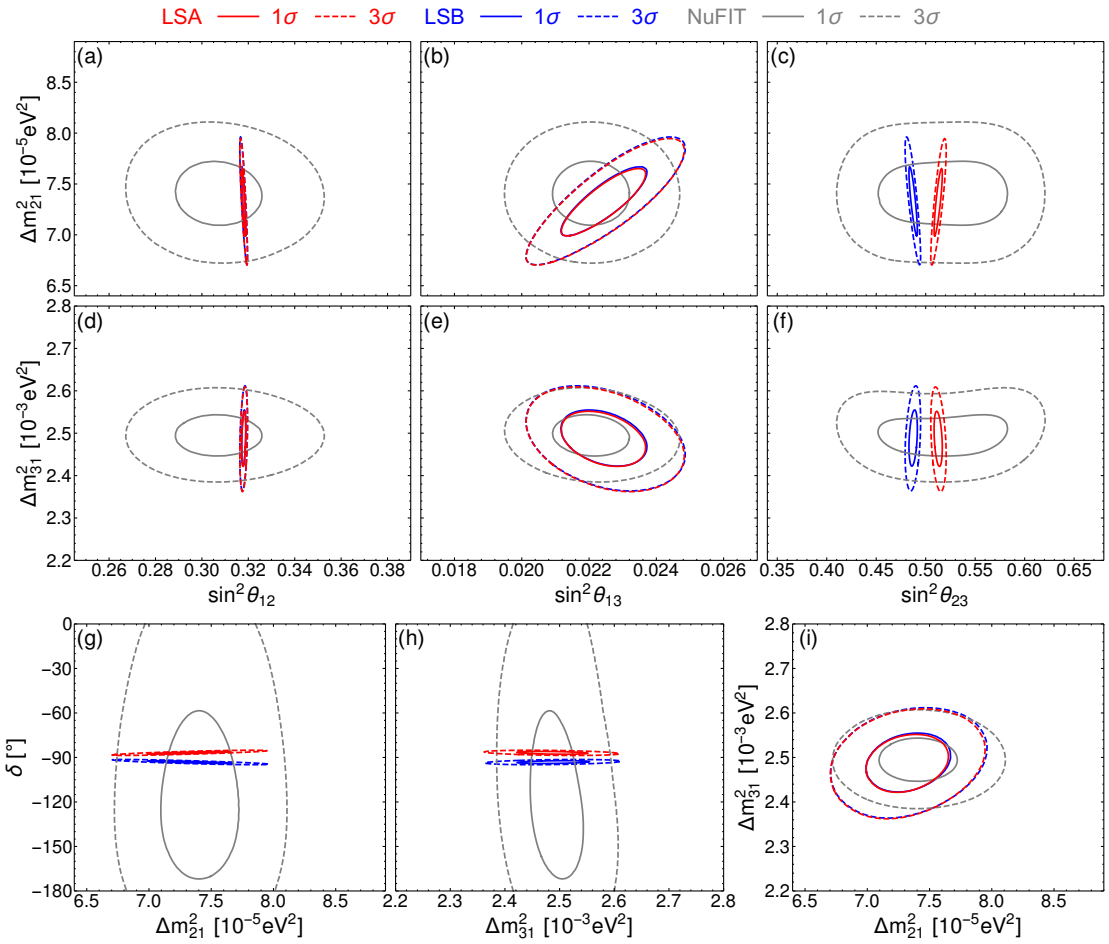

Figure 6.8: Allowed $1\,\sigma$ (solid) and $3\,\sigma$ (dashed) regions for LSA (red) and LSB (blue) with $\eta = 2\pi/3$ and $\eta = -2\pi/3$ respectively. Also shown are the current allowed regions from the NuFIT 3.2 2018 global fit (grey).

6.3 Sensitivity of future experiments

In order to understand the potential for future experiments to exclude the LS models, simulations are performed of a combination of accelerator and reactor experiments, modelling the experimental data expected over the next two decades. The General Long Baseline Experiment Simulator (GLoBES) libraries [165, 166] are used to simulate future experiments and to fit the simulated data to both standard mixing and the LS models. In all these simulations it is assumed that the mass ordering is known to be normal ordering, as this is a requirement of the LS models; a measurement of inverted ordering would immediately exclude the models.

6.3.1 Future neutrino oscillation experiments

The combination of experiments included in the simulations of this section use the same detailed models of the T2HK and DUNE long-baseline accelerator experiments as used in Chapter 5, to provide precision measurements of Δm^2_{31}, θ_{23} and δ, together with basic constraints on θ_{13} from the Daya Bay short baseline reactor experiment and on θ_{12} and Δm^2_{21} from the JUNO and RENO-50 medium baseline reactor experiments. Details of the models for T2HK and DUNE are provided in Section 5.2; the remaining experiments and the treatment of them in these simulations are now described below.

6.3.1.1 Short baseline reactor experiments

By observing the oscillations of the $\bar{\nu}_e$ produced in nuclear reactors, short baseline reactor neutrino experiments are able to measure the mixing angle θ_{13} with particularly high accuracy. The Daya Bay experiment [218] currently has the most precise measurement of this parameter with the aim to achieve a precision on $\sin^2\theta_{13}$ of better than 3 % [219]. The experiment measures anti-neutrinos produced in six nuclear reactors in south China. A total of eight 20 t liquid scintillator detectors are used; two are located at each of two near detector sites and four at a far detector site L =1.5 to 1.9 km from the reactors near the first atmospheric neutrino oscillation maximum for $\Delta m^2_{31} \sim 2.5 \times 10^{-3}$ eV^2, given the low nuclear energy of the neutrino beam $E \sim$ few MeV. Results of the Double Chooz [220] and RENO [125, 221] short baseline reactor experiments also contribute to the precision obtained on θ_{13} combined with the Daya Bay result. Although DUNE and T2HK will also measure this parameter with high precision, the measurement of the short baseline reactor programme by that time is expected to be at least as precise, and will provide a measurement independent of the other parameters which influence the appearance channel at long-baseline accelerator experiments.

6.3.1.2 Medium baseline reactor experiments

The Jiangmen Underground Neutrino Observatory [124] (JUNO) and the future plans of the Reactor Experiment for Neutrino Oscillation (RENO-50) [125] are medium baseline reactor neutrino experiments which, like the Daya Bay experiment, will observe the oscillations of electron anti-neutrinos produced in nuclear reactors. The JUNO experiment will use a 20 kt liquid scintillator detector approximately L =53 km from two planned nuclear reactors in southern China, while RENO-50 will use an 18 kt liquid scintillator detector approximately L =50 km from a nuclear reactor in South Korea. Given the low nuclear energy of the neutrino beam $E \sim$ few MeV, these longer baselines correspond to the first solar neutrino oscillation maximum for $\Delta m^2_{21} \sim 7.5 \times 10^{-5}$ eV^2, where the higher frequency atmospheric oscillations appear as smaller fluctuations in the probability as L/E is varied. Thus the longer baseline than at Daya Bay gives greatest sensitivity to a different set of oscillation parameters, in particular θ_{12} and Δm^2_{21}. The precision on the measurements of both $\sin^2\theta_{12}$ and Δm^2_{21} is expected to reach 0.5 % [124, 125].

6.3.1.3 Details of experimental simulation

Complete simulations of the latest designs for both DUNE and T2HK are used with the assumption that both experiments run for 10 years. For the short and medium baseline reactor experiments, basic constraints are included on the values of $\sin^2\theta_{13}$, $\sin^2\theta_{12}$ and Δm^2_{21}; since these measurements are expected to be approximately independent of other parameters these are implemented as simple Gaussian measurements with a mean of the true simulated value and error as given in Table 6.2.

Experiment	Parameter	Precision
Short baseline reactor	$\sin^2\theta_{13}$	3 %
Medium baseline reactor	$\sin^2\theta_{12}$	0.5 %
Medium baseline reactor	Δm^2_{21}	0.5 %

Table 6.2: Precision on oscillation parameter measurements expected by future reactor experiments, which have been used as constraints in these simulations.

6.3.2 Statistical method

To determine the statistical significance with which the LS model could be excluded based on simulated data, a minimum-χ^2 fit is performed to both standard three neutrino mixing and to the LS model. As in Section 6.2.3, for the case of standard mixing $\Theta = \Theta_{\text{PMNS}} \equiv \{\theta_{12}, \theta_{13}, \theta_{23}, \Delta m^2_{21}, \Delta m^2_{31}, \delta\}$ is used, while for LS $\Theta = \Theta_{LS} \equiv \{m_a, m_b, \eta\}$ (or $\Theta_{\text{LS}} = \{m_a, m_b\}$ when fitting with η fixed) is used. The test statistic for the significance to exclude the LS model is then given by

$$\sqrt{\Delta\chi^2} = \sqrt{\min_{\Theta_{\text{LS}}} \left[\chi^2\left(\Theta_{\text{LS}}\right)\right] - \min_{\Theta_{\text{PMNS}}} \left[\chi^2\left(\Theta_{\text{PMNS}}\right)\right]}. \tag{6.3.1}$$

The significance at which LS is excluded is then determined from the distribution of the $\Delta\chi^2$ test statistic; where sensitivities are given in terms of $N\sigma$, this quantity has been calculated assuming the that Wilks' theorem applies. Wilks' theorem states that when comparing nested models, the $\Delta\chi^2$ test statistic is a random variable asymptotically distributed according to the χ^2-distribution with the number of degrees of freedom equal to the difference in number of free parameters in the models. In this case the LS models, with two or three free parameters, are treated as sub-models of standard neutrino mixing with six free parameters, leading to a χ^2-distribution with 4 degrees of freedom when η is kept fixed or 3 degrees of freedom when η is left as a free parameter. As for the fit in the previous section, Monte-Carlo simulations were used to verify that the distribution of this $\Delta\chi^2$ test statistic is well approximated by these distributions.

In applying the above formula, the $\chi^2(\Theta)$ is minimised over the parameters Θ in the fits and is built from three parts;

$$\chi^2(\Theta) = \chi^2_{\text{LB}}(\Theta) + \chi^2_{\text{R}}(\Theta) + P(\Theta), \tag{6.3.2}$$

with $\chi^2_{\text{LB}}(\Theta)$ for the full simulations of the long-baseline experiments DUNE and T2HK, $\chi^2_{\text{R}}(\Theta)$ for the constraints from reactor experiments Daya Bay and JUNO, and $P(\Theta)$

for a prior intended to include information from the results of existing experimental measurements.

For the long-baseline experiments the statistical model of the GLoBES library [165,166] is used, where the $\chi^2_{LB}(\Theta)$ is a sum of contributions from each of the experiments' channels. The individual contributions are constructed as

$$\chi^2_c(\Theta) = \min_{\xi=\{\xi_s,\xi_b\}} \left[2 \sum_i \left(\eta_i(\Theta,\xi) - n_i + n_i \ln \frac{n_i}{\eta_i(\Theta,\xi)} \right) + p(\xi,\sigma) \right], \tag{6.3.3}$$

where χ^2_c denotes the contribution from a given channel of a given experiment. The sum in this expression is over the i energy bins of the experimental configuration, with simulated true event rates of n_i and simulated event rates $\eta_i(\Theta,\xi)$ for the hypothesis parameters Θ and systematic error parameters ξ. The systematic errors of the experiments are treated using the method of pulls, parametrised as ξ_s for the signal error and ξ_b for the background error. These parameters are given Gaussian priors which form the term $p(\xi,\sigma) = \xi_s^2/\sigma_s^2 + \xi_b^2/\sigma_b^2$, where $\sigma = \{\sigma_s, \sigma_b\}$ are the sizes of the systematic errors given by the experiment.

For the reactor experiments independent Gaussian measurements are assumed such that

$$\chi^2_{\mathrm{R}} = \frac{\left(\sin^2\theta_{13} - \sin^2\overline{\theta_{13}}\right)^2}{\sigma^2_{\theta_{13}}} + \frac{\left(\sin^2\theta_{12} - \sin^2\overline{\theta_{12}}\right)^2}{\sigma^2_{\theta_{12}}} + \frac{\left(\Delta m^2_{21} - \overline{\Delta m^2_{21}}\right)^2}{\sigma^2_{\Delta m^2_{21}}}, \tag{6.3.4}$$

where $\overline{\theta_{13}}$, $\overline{\theta_{12}}$ and $\overline{\Delta m^2_{21}}$ are the true parameter values and $\sigma_{\theta_{13}}$, $\sigma_{\theta_{12}}$ and $\sigma_{\Delta m^2_{21}}$ the corresponding experimental measurement uncertainties.

The prior $P(\Theta)$ provides information from existing experimental measurements and is calculated using the results of the NuFIT 3.2 global fit in the same way as the fit in Section 6.2.3, so that $P(\Theta) = \chi^2_{\mathrm{Fit}}(\Theta)$ as defined in Equation (6.2.1).

In all these simulations, the true parameters are taken to be the best-fit values from the appropriate LS fit results given in Table 6.1, except where stated otherwise. During minimisation of $\Delta\chi^2$, the test parameters are allowed to vary with no restriction on their values. This means that m_a and m_b for LS and the mass-squared differences for standard mixing can have any value greater than 0, with η for LS and the mixing angles and phase δ for standard mixing taking any value from $-\pi$ to π. However, in all cases in these simulations the parameter values at the $\Delta\chi^2$ minimum remained close to the specified true values (for standard mixing parameters) and the physically viable ranges found in the fits of the previous section (for LS parameters).

6.3.3 Results

The sensitivity to exclude either version of the LS model is shown as a function of the true value of each parameter in Figure 6.9, where the range along the horizontal axes has been set to the range given by the currently allowed at $3\,\sigma$ by the NuFIT 3.2 global fit. In each case, the parameters not shown are assumed to take their best-fit values from the fit to LS described in Section 6.2.3.

In the upper panels in Figure 6.9, θ_{12}, θ_{23} and δ are seen to provide the strongest tests of the model, with there only being a relatively small portion of the presently allowed true

parameter space where the model would not be excluded. This is due to the strong predictions of these parameters by the LS models, as discussed in Section 6.2.1. Note that these parameters are those that will be measured most precisely by the next-generation experiments used in the simulations, θ_{12} by JUNO and RENO-50, θ_{23} and δ by DUNE and T2HK. For these three parameters, allowing η to vary does not significantly change the sensitivity other than the additional solution (currently disfavoured by experiment) with $\delta = +90°$, which occurs when changing the sign of η. For θ_{12} in particular there is no effect of allowing η to vary. This is due to the sum rule in Equation (6.1.8) which relates θ_{12} with θ_{13} independently from the value of η; the precise measurement of θ_{13} then fixes the value of θ_{12} to a narrow range such that a measurement of θ_{12} outside of this would exclude the LS model regardless of the LS parameter values. Similarly the precise measurements of θ_{13}, Δm^2_{21} and Δm^2_{31} strongly constrain the magnitude (but not sign) of η, so that the LS allowed regions of the other variables are not significantly changed when η is allowed to vary, with the noted exception that changing the sign of η allows the sign of δ to also change.

In the lower panels in Figure 6.9, it is seen that the sensitivity to exclude LS from measurements of θ_{13}, Δm^2_{21} or Δm^2_{31} is much less than for the other three parameters and the sensitivity is also significantly reduced when allowing η to vary. By the converse argument to that used above, this is due to these three parameter measurements driving the fit to m_a and m_b (and η), and so a measurement of these parameters will tend to move the fitted LS parameter values rather than exclude the model, particularly when fitting the extra free parameter η. However, a particularly small measurement of θ_{13} or particularly large measurement of Δm^2_{21}, relative to their current allowed range of values, may still exclude the fixed η version of the models.

The results shown in Figure 6.9 show only the dependence of the significance to exclude LS on the true value of each variable individually. However, the sensitivity will generally have a strong dependence on the true values of the other parameters. The significance to exclude the LS models depending on the true values of each pair of variables, for the cases where η is kept fixed, is shown in Figures 6.10 and 6.12 for LSA and in Figures 6.11 and 6.13 for LSB.

Each panel of Figures 6.10 and 6.11 includes two dimensionless variables (*i.e.* angle or phase) which both depend only on the ratio of LS input parameters $r = m_b/m_a$, and so, in a LS model, a measurement of any one of these parameters corresponds to a measurement of $r = m_b/m_a$ (see Figure 6.3). Combining two of these parameter measurements therefore gives two measurements of $r = m_b/m_a$, with any conflict between them providing strong evidence to exclude the model. For this reason the significance to exclude the models is close to being simply the combined significance from individual measurements implied by Figure 6.9.

By contrast, each panel of Figures 6.12 and 6.13 shows the results for the pairs of variables including at least one dimensionful mass-squared difference. Here it can be seen in Figures 6.12b, 6.12e and 6.12i for LSA, and in Figures 6.13b, 6.13e and 6.13i for LSB, that there is a strong correlation between the measurements of θ_{13}, Δm^2_{21} and Δm^2_{31}. This shows clearly that, although individual measurements of these parameters cannot exclude a LS model (since the parameters of the LS model could be adjusted to accommodate any of them individually) a *combined* measurement of two of them could

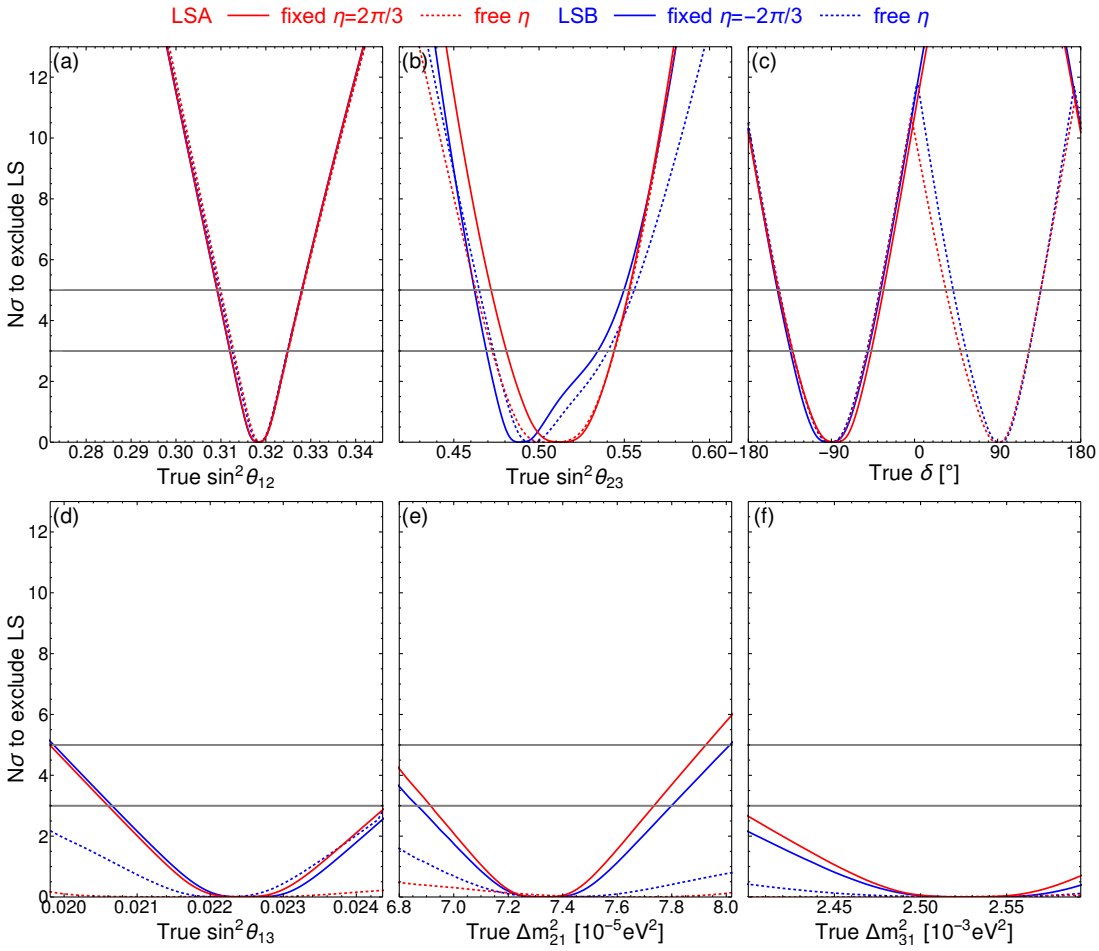

Figure 6.9: The predicted sensitivity of future experiments to excluding LSA (red) and LSB (blue), shown as a function of the true value of each parameter. Solid curves correspond to the case with η fixed at $\eta = \frac{2\pi}{3}$ for LSA or $\eta = -\frac{2\pi}{3}$ for LSB, while dashed curves correspond to the case with η left free. The ranges of true parameters shown in the plots corresponds to the current three sigma allowed NuFIT 3.2 regions.

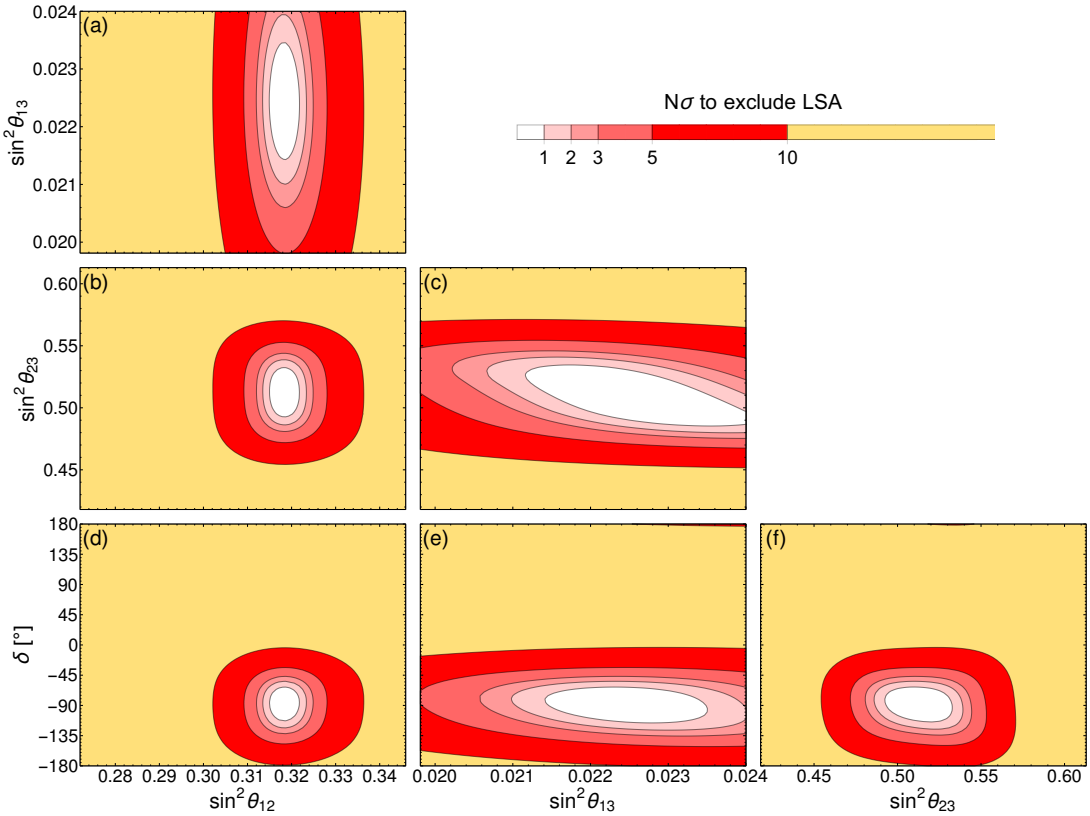

Figure 6.10: The predicted sensitivity of future experiments to excluding LSA, with η fixed at $\eta = \frac{2\pi}{3}$, shown as a function of each pair of true parameters. The ranges of true parameters shown in the plots corresponds to the current three sigma allowed NuFIT 3.2 regions.

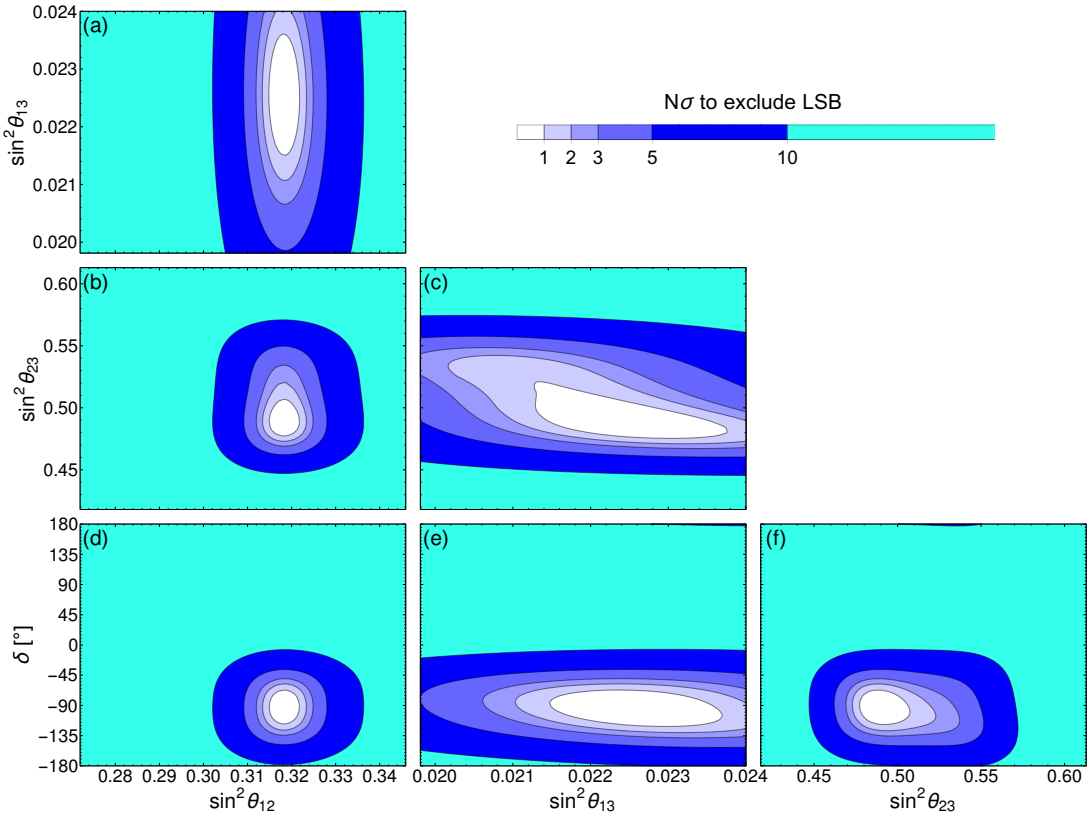

Figure 6.11: The predicted sensitivity of future experiments to excluding LSB, with η fixed at $\eta = -\frac{2\pi}{3}$, shown as a function of each pair of true parameters. The ranges of true parameters shown in the plots corresponds to the current three sigma allowed NuFIT 3.2 regions.

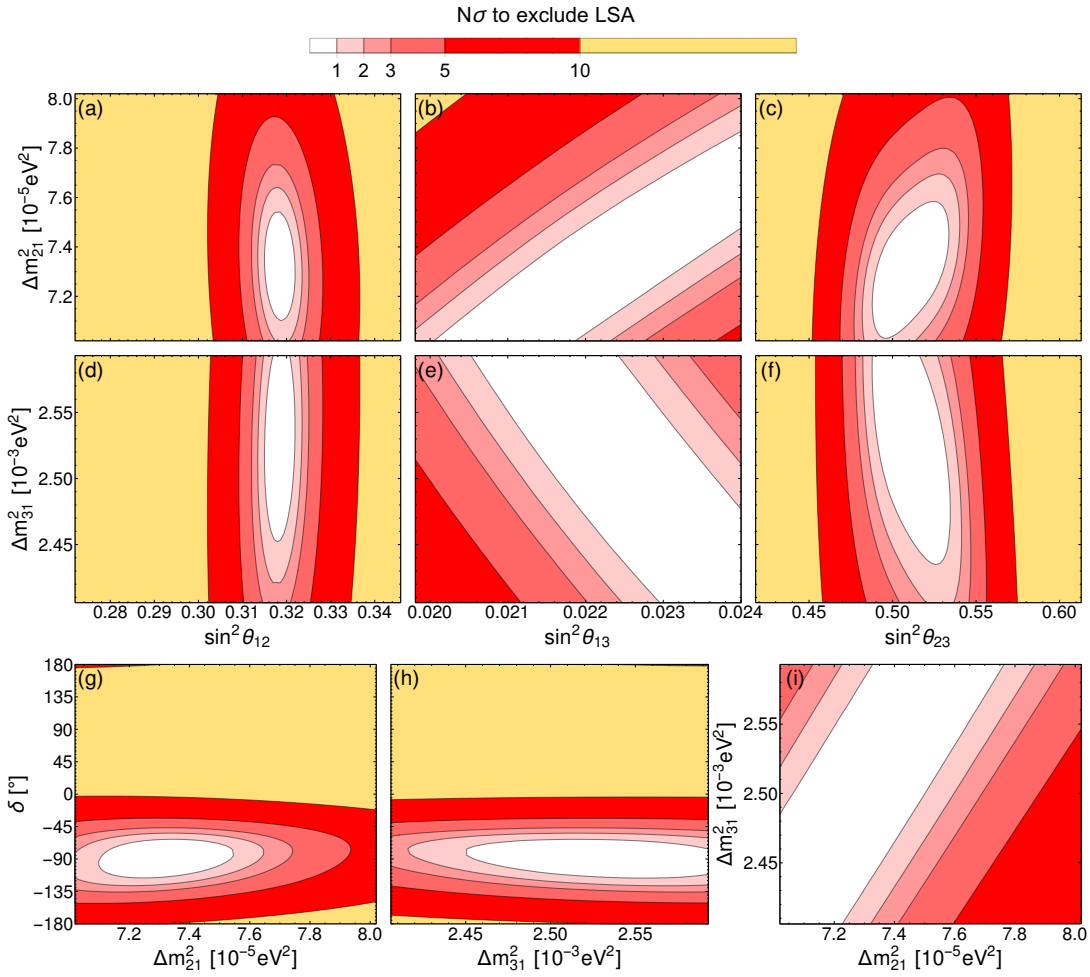

Figure 6.12: The predicted sensitivity of future experiments to excluding LSA, with η fixed at $\eta = \frac{2\pi}{3}$, shown as a function of each pair of true parameters. The ranges of true parameters shown in the plots corresponds to the current three sigma allowed NuFIT 3.2 regions.

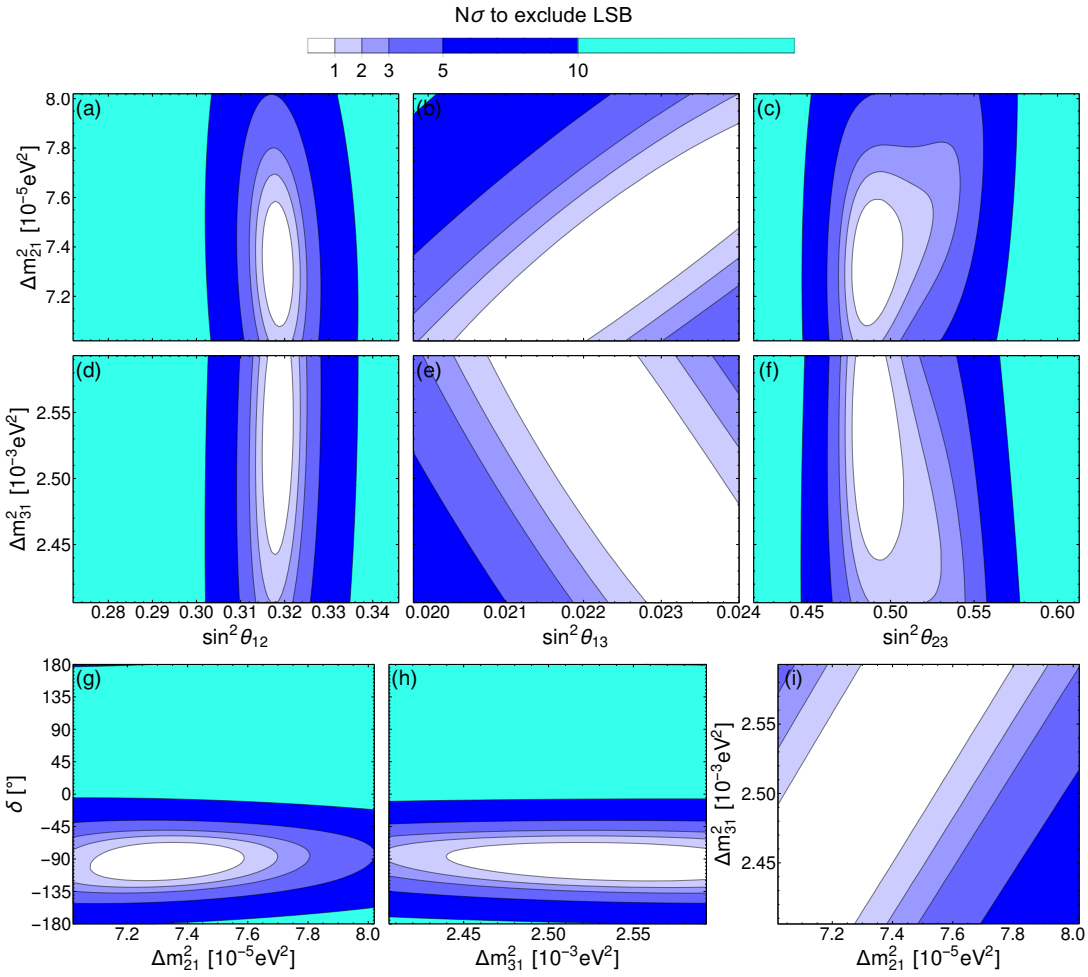

Figure 6.13: The predicted sensitivity of future experiments to excluding LSB, with η fixed at $\eta = -\frac{2\pi}{3}$, shown as a function of each pair of true parameters. The ranges of true parameters shown in the plots corresponds to the current three sigma allowed NuFIT 3.2 regions.

serve to exclude the model. This is the reason for presenting these combined sensitivity plots.

Of the three parameters for which such *combined* measurements provide the strongest test of the model, it is interesting that each pair includes measurements from different experiments, with θ_{13} coming mainly from the short-baseline reactor measurement such as Daya Bay, Δm^2_{21} from a medium-baseline reactor measurement of JUNO or RENO-50, and Δm^2_{31} from a long-baseline accelerator measurement of DUNE and T2HK. This demonstrates a strong synergy between all these experiments in attempts to exclude the LS models.

Conclusion

In this chapter, the ability to probe one of the most predictive viable neutrino mass and mixing models, the Littlest Seesaw, with future neutrino oscillation experiments, has been investigated. The LS models work within the framework of the Type I seesaw mechanism, using two right-handed neutrinos to generate the left-handed neutrino masses. Combined with constraints from family symmetries, the neutrino mixing angles and phases can be predicted from a small number of parameters; in its most constrained form all neutrino masses, angles, and phases are determined from just two input parameters. In fact, it was shown that while the neutrino masses depend on the two mass parameters independently, the mixing angles and phases depend only on a single dimensionless quantity, the ratio of these two input parameters.

Two versions of this model (LSA and LSB) have been studied, which use different family symmetries to enforce constraints which result in different permutations of the second and third rows and columns of the neutrino mass matrix, leading to different predictions for the octant of θ_{23}. Using the results of a recent global fit of neutrino oscillation experiments, it was found that both versions can well accommodate the parameter values as measured by experiment, with no tension between the model and experimental measurements even at the $1\,\sigma$ level. The LSB version, predicting a value of θ_{23} in the lower octant, was found to be slightly preferred.

The ability of future experiments to exclude these models then comes from a convolution of the strength of the predictions of the model with the sensitivity of the experiments in measuring those parameters. Through fitting the models to current global neutrino oscillation data, it was seen that the LS models make strong predictions for the values of θ_{12}, θ_{23}, and δ, the three parameters for which current measurements are weakest. In addition it was found that, for certain combinations of the remaining observables, θ_{13}, Δm^2_{21} and Δm^2_{31}, the LS models predict strong correlations.

With future experiments expected to improve precision on all six parameters measured through oscillations, the simulations presented here have shown that the LS models can be thoroughly tested through future precise individual measurements of θ_{12}, θ_{23}, and δ. This can be readily understood since the free parameters of the LS models are currently most constrained by the precise measurements of θ_{13}, Δm^2_{21} and Δm^2_{31}, leading to predictions for the currently less well determined parameters θ_{12}, θ_{23}, and δ.

The predictivity of the LS models means that an even higher precision measurement of those parameters which currently drive the fit of the input parameters, namely θ_{13}, Δm^2_{21} and Δm^2_{31}, could still exclude the LS models when considered in combination with each other. For example, the combination of any two of them could require a region of LS parameter space already excluded by the third.

These above results all highlight the strong complementarity between different classes of oscillation experiment. While the long baseline accelerator experiments DUNE and T2HK are expected to provide the strongest measurements of θ_{23} and δ (two of those that can *individually* test the model's viability) the third, θ_{12}, will come from medium baseline reactor experiments such as JUNO and RENO-50. The strongest complementarity, however, comes from combining precision measurements of Δm^2_{21}, Δm^2_{31} and θ_{13}, where any pair of these measurements relies on the results from all the different experiments: long-baseline accelerator experiments for Δm^2_{31}, medium-baseline reactor experiments for Δm^2_{21}, and short-baseline reactor experiments for θ_{13}.

In summary, the work presented in this chapter shows that the most straightforward way to exclude the LS model is to provide a better *individual* determination of the three currently less precisely measured parameters θ_{12}, θ_{23}, and δ, which requires both medium baseline experiments such as JUNO and RENO-50, and long baseline experiments such as DUNE and T2HK, where the synergy between the latter two experiments is thoroughly explored in the previous chapter. In addition, the LS model could be constrained by *combined* measurements of the three remaining parameters Δm^2_{21}, Δm^2_{31} and θ_{13}, where an even higher precision of the latter reactor parameter at the short baseline Daya Bay experiment can also play an important role.

Note that, although the above conclusions have been established for the LSA and LSB models, similar arguments could be expected to apply to any highly predictive flavour models which determine the oscillation parameters from a smaller number of input model parameters. In any such model, the input parameters will tend to be tuned to fit the strong constraints from the most precisely measured parameters, leading to testable predictions of the other parameters. If the models can accommodate individual measurements in this way, distinguishing between them using those parameters which drive the fit is still possible, if those models are highly constrained, but this requires the parameter measurements to be considered in combination.

In conclusion, the need for future reactor and accelerator experiments to measure individually θ_{12}, θ_{23} and δ, plus combinations of θ_{13}, Δm^2_{21} and Δm^2_{31}, may be considered to be general requirements in order to probe predictive flavour symmetry models. Therefore a broad programme of such precision experiments seems to be essential in order to take the next step in understanding neutrino oscillations in the context of the flavour puzzle of the Standard Model.

Conclusions

This thesis has explored the future of neutrino oscillation physics through studying the next-generation long-baseline neutrino beam experiments. Since providing the first and only observation of particle physics beyond the Standard Model, neutrino oscillations have been thoroughly examined through a broad programme of experiments detecting the interactions of a diverse spectrum of neutrino types and energies. The panoramic view of neutrino oscillations provided thanks to these efforts leaves only a few aspects of the phenomenon still unknown, with the next generation of experiments expected to begin to probe all of these in the next decade.

The main focus of this thesis has been to examine the measurement of the Dirac phase of neutrino oscillations by the Hyper-Kamiokande experiment, both alone and in combination with other measurements and experiments, in the search for CP violation in the leptonic sector. The design of Hyper-K and its intermediate water Cherenkov detector has been studied to investigate possible improvements in sensitivities of its measurements, followed by studies into where these measurements of Hyper-K stand in combination with other experiments. The complementarity of these experiments has been identified both in determining oscillation parameter values themselves and the resulting ability to probe theoretical models introduced in attempting to gain a more fundamental understanding of neutrino mass and mixing.

Chapter 3 has documented the development of a new high-energy reconstruction package used to aid the development of the intermediate detector of Hyper-K. This software, which is essential in allowing the positions, directions, energies and types of particles to be determined, also met the additional requirements of speed and adaptability that the changing detector design demanded. The construction of selection criteria for samples of neutrino interaction events seen in the intermediate detector was also detailed, culminating in the use of these selections in producing improved sensitivities of the oscillation analyses of Hyper-K.

With the intermediate detector having progressed to the later stages of its design process, the use of advanced detector-specific software has taken over, however the techniques developed are still applicable to other water Cherenkov detector design projects; that the reconstruction software developed in this work has also been used in the design stage of the ANNIE detector provides a case in point.

Chapter 4 has then described a full analysis of a possible measurement of neutron captures with a Gadolinium doped intermediate detector. This measurement was motivated by the benefits it can bring to various analyses at the far detector of Hyper-K. Measuring neutrons in the intermediate detector, with its large event rate, will provide two

main benefits: Firstly, the additional information related to the number, energies and directions of neutrons produced in neutrino interactions allows the interaction cross-sections to be constrained, thereby reducing systematic uncertainties in analyses that rely on these models. Secondly, a thorough understanding can be gained of the ability to measure neutrons in the far detector, where the neutrino flux is greatly reduced, allowing the use of neutron tagging to improve the purity and reconstruction of neutrino interaction events, as well as significant reduction in the atmospheric neutrino background of nucleon decay searches.

The analysis of Chapter 4, saw that despite the large rate of external backgrounds, including incoming neutrons capturing in an identical way to that of the signal neutrons, the measurement can provide a high level of detail on the signal neutron captures' properties: Through the development of a likelihood-based selection method, backgrounds were separated from signal neutrons allowing very pure samples to be produced while retaining the vast majority of signal neutron captures. A method developed to correct for the remaining background and selection efficiency was then seen to work as expected, demonstrating the ability to successfully reproduce the true joint distributions of multiplicities, distance and angle of the neutron captures following neutrino interactions in the detector. Although this analysis has begun to demonstrate the potential of such a measurement, extensions to provide a total neutron capture multiplicity measurement and to correct for additional detector effects seen in the results should provide further improvements, while a thorough study of the effects of systematic uncertainties not currently included in the analysis is required to truly prove the measurement's feasibility.

In Chapter 5, a full analysis of the neutrino beam oscillation measurements of Hyper-K is then presented in combination with the other planned next-generation accelerator neutrino experiment, DUNE. Due to the significant differences in design of these two experiments, a strong synergy between them was seen to emerge. Most significantly, the longer baseline of DUNE provides it with strong matter effects to enhance its sensitivity to determining the mass ordering, to which the beam programme of Hyper-K has little sensitivity. Conversely, Hyper-K's high statistics and narrow-band beam focused around the oscillation maximum give it the strongest sensitivity in measuring the Dirac phase. The complementarity of these two strengths of the experiments is striking when combined; the precision constraint on δ from Hyper-K allows an even greater sensitivity to the mass ordering at DUNE, by helping to exclude degeneracies between Δm^2_{32} and δ, while this also works in reverse where the mass ordering measurement at DUNE resolves these same degeneracies and greatly improving the sensitivity to δ at Hyper-K. The potential redesigns of both Hyper-K and DUNE, with a second detector placed in Korea and with an optimised 3-horn beam, respectively, was also investigated; the best combination of these two experiments was found to be able to determine the mass-ordering in under 2 years and to have the potential to discover CP violation at $5\,\sigma$ for 50 % of the parameter space after just 5 years. This analysis has demonstrated the clear benefits of both of these experiments and their synergistic nature in resolving the remaining unknowns of neutrino oscillations, however only the beam programme of these experiments has been included and the two experiments were assumed in simulations to have entirely uncorrelated errors. Extending the analysis to include other aspects of the experiments, such as the atmospheric neutrino programme of Hyper-K that can provide sensitivity to the mass ordering, and to include a full analysis of the correlations

between systematic error sources such as the use of common interaction models, could result in modifications to these conclusions.

Finally, in Chapter 6, the Littlest Seesaw models of neutrino flavour, mass and mixing was investigated in the context of measurements of current and future oscillation experiments. The highly predictive models were found to be in good agreement with existing data; no tension is found even at the $1\,\sigma$ level between experiments' measurements and the models' predictions. With these models' predictions fitting well with current data, the ability of future experiments to probe the models, by attempting to exclude them through oscillation parameter measurements, was investigated. It was found that the three strands of neutrino oscillation experiments – long baseline beam experiments, medium baseline reactor experiments and short baseline reactor experiments – each provide unique tests of the models both in isolation and when combined with each other: The measurements of the three less-precisely known parameters, δ and θ_{23} at the long-baseline beam experiments and θ_{12} at the medium baseline reactor experiments, can all individually provide tests of the LS models, while more precise measurements of the already well-known parameters, θ_{13} at short baseline reactor experiments, Δm^2_{21} at medium baseline reactor experiments and Δm^2_{31} at long baseline beam experiments, can also test the model when at least two of any of these measurements are combined. This is due to the few free parameters of the models being highly constrained by fitting to the precisely measured oscillation parameters, effectively providing predictions of the less constrained parameters as well as making the fit fragile to more precise measurements of the other parameters. While the analysis has shown the impressive ability of the various experiments to potentially exclude these models, a plethora of other models exist making different predictions. Further work to investigate the ability to exclude other sets of models, and to discriminate between the various models, will be required to meet the goal of moving towards a more complete fundamental understanding of the origin of neutrino mass and mixing.

In conclusion, the state of neutrino oscillation physics has come a long way in a relatively short time, with only a handful of unknowns left, all expected to be resolved with the next generation of experiments. This thesis has documented some of the essential work going towards the optimisation of the sensitivities of these experiments. But despite the experimental progress, on the theoretical side there are many potential explanations for what the mechanism is that determines the parameters of neutrino oscillations, and where the neutrino mass comes from to enable the phenomenon to occur. To make progress in this area, with the eventual hope of finding a successor to the Standard Model of particle physics, the measurements of the next generation of experiments will be essential.

Appendices

Appendix A

Further details of likelihood distribution fits

The details of the fitted functions of the distributions used in the likelihoods of Section 4.2 are summarised below, for the fitted variables listed in Tables 4.2 and 4.3. Table A.1 describes the fitted distributions and the fitted parameter values with the definitions of the probability distributions given in Table A.2. For sand and neutral current backgrounds, the timing distribution was fitted separately for those coming from neutron or from non-neutron sources, due to the significantly longer times for neutrons to be observed in the detector, while the position distributions will be approximately similar. Where the distributions are described as convolutions, this is a convolution of two probability density functions physically implying the sum of two random variables, for example the time for a high energy neutron to thermalise plus the time for the thermal neutron to capture. Where the distributions are described as mixtures, this is a weighted sum of probability density functions physically implying the event could have come from different possible sources with different distributions.

Quantity	Distribution	Fitted parameters	
Signal t	Convolution of $\mathrm{Exp}(\lambda)$	λ	0.039 61
	$\Gamma(k, \theta)$	k	1.1648
		θ	2.750
		χ^2 / d.o.f	2.0
Signal d	Convolution of $\mathrm{Exp}(\lambda)$	λ	0.011 80
	$\Gamma(k, \theta)$	k	2.714
		θ	8.219
		χ^2 / d.o.f	1.7
Signal $\cos\theta$	Mixture of $\mathrm{U}(-1, 1)$ weight w	w	0.5059
	$\mathrm{B}(\alpha, \beta)$ weight $1 - w$	α	3.162
		β	0.9166
		χ^2 / d.o.f	1.4

Quantity	Distribution		Fitted parameters	
Sand t_b (neutron)	Convolution of Exp(λ) and $\Gamma(k,\theta)$		λ	0.038 16
			k	1.632
			θ	2.032
			χ^2 / d.o.f	1.3
Sand t_b (other)	Mixture of Exp(λ_1)	weight w	w	0.6660
			λ_1	19.95
	Exp(λ_2)	weight $1-w$	λ_2	0.5779
			χ^2 / d.o.f	0.9
Sand y	Mixture of B(α_1,β_1)	weight w	w	0.086 86
			α_1	10.58
			β_1	1.005
	B(α_2,β_2)	weight $1-w$	α_2	0.8713
			β_2	1.363
			χ^2 / d.o.f	2.0
Sand r^2	Mixture of U($0, r_{\max}^2$)[1]	weight $w_1 w_2$	w_1	0.4463
	Tri(c)	weight $(1-w_1)w_2$	w_2	0.9351
			c	118 967
	LN(μ,σ^2)	weight $(1-w_2)$	μ	3.287
			σ^2	0.6032
			χ^2 / d.o.f	1.0
Sand φ	Cos(α)		α	0.5431
			χ^2 / d.o.f	1.3
NC t_b (neutron)	Convolution of Exp(λ) and $\Gamma(k,\theta)$		λ	0.039 90
			k	1.3524
			θ	2.433
			χ^2 / d.o.f	1.0
NC t_b (other)	Convolution of Exp(λ) and U($0, T_b$)[2]		λ	164.0
			χ^2 / d.o.f	1.0
NC y	Mixture of B(α_1,β_1)	weight w	w	0.084 00
			α_1	2.731
			β_1	11.18
	B(α_2,β_2)	weight $1-w$	α_2	1.332
			β_2	1.365
			χ^2 / d.o.f	2.9

[1] $r_{\max} = 371$ cm is the radius of the tank.
[2] $T_b = 0.058$ µs is the length of each bunch

Quantity	Distribution	Fitted parameters	
NC r^2	Mixture of Quad(a, b) weight w_1	w_1	0.9819
		a	-1.0081
		b	0.1483
	LN(μ, σ^2) weight $(1 - w_1)$	μ	3.362
		σ^2	0.7020
		χ^2 / d.o.f	1.5
NC φ	Lin(a)	a	$-0.036\,01$
		χ^2 / d.o.f	1.4
Cosmic y	Mixture of B(α_1, β_1) weight w	w	0.3834
		α_1	3.051
		β_1	2.013
	B(α_2, β_2) weight $1 - w$	α_2	0.8966
		β_2	0.4506
		χ^2 / d.o.f	2.7
Cosmic r^2	Mixture of Lin(a) weight w	w	0.8357
		a	-4.949×10^{-6}
	B(α, β) weight $1 - w$	α	86.17
		β	1.574
		χ^2 / d.o.f	2.8

Table A.1: Fitted distributions and parameter values for for quantities used in likelihoods for the E61 neutron selection.

Distribution		Probability density function	Range
Exponential	$\mathrm{Exp}(\lambda)$	$f(x;\lambda) = \lambda e^{-\lambda x}$	$0 < x$
Gamma	$\Gamma(k,\theta)$	$f(x;k,\theta) = \frac{1}{\Gamma(k)\theta^k} x^{k-1} e^{-\frac{x}{\theta}}$	$0 < x$
Uniform	$\mathrm{U}(a,b)$	$f(x) = \frac{1}{a+b}$	$a < x < b$
Beta	$\mathrm{B}(\alpha,\beta)$	$f(x;\alpha,\beta) = \frac{\Gamma(\alpha+\beta)}{\Gamma(\alpha)\Gamma(\mathrm{B})} x^{\alpha-1}(1-x)^{\beta-1}$	$0 < x < 1$
Triangular	$\mathrm{Tri}(c)$	$f(x;c) = \begin{cases} \frac{2(x-a)}{(b-a)(c-a)} \\ \frac{2(b-x)}{(b-a)(b-c)} \end{cases}$	$a < x < c$ $c < x < b$
Logit-normal	$\mathrm{LN}(\mu,\sigma^2)$	$f(x;\mu,\sigma^2) = \frac{1}{\sigma\sqrt{2\pi}} \frac{e^{-\frac{(\log(x/(1-x))-\mu)^2}{2\sigma^2}}}{x(1-x)}$	$0 < x < 1$
Cosine	$\mathrm{Cos}(\alpha)$	$f(x;\alpha) = \frac{1+\alpha\cos(x)}{\pi}$	$0 < x < \pi$
Quadratic	$\mathrm{Quad}(a,b)$	$f(x;a,b) = ax^2 + bx + 1 - \frac{a}{3} - \frac{b}{2}$	$0 < x < 1$
Linear	$\mathrm{Lin}(a)$	$f(x;a) = ax + 1 - \frac{a}{2}$	$0 < x < 1$

Table A.2: Definitions of the probability density functions used in the distributions of Table A.1. For bounded distributions, the ranges are adjusted according to the relevant range of each fit; for the vertical position from $-y_{\max}$ to $y_{\max} = 521\,\mathrm{cm}$, for the radial position from 0 to $r_{\max} = 371\,\mathrm{cm}$.

Appendix B

Obtaining total multiplicity distributions

Section 4.4 provides results of an example neutron measurement at E61, including a full 3D distribution of neutron capture multiplicities as a function of distance from the primary event and angle to the beam. This distribution has been corrected for efficiency and background using an unfolding method. However, a total neutron multiplicity distribution across all angles and distances is difficult to obtain either through combining the unfolded rates at each angle and distance or through applying an efficiency and background correction to the observed total multiplicity distribution.

The total multiplicity is accumulated over all bins in d and/or θ, but the unfolding method must be applied with a dependence on d and θ, *i.e.* it must be applied to each bin individually, due to the model dependence, as described in Section 4.3.

The difficulty comes from the fact that the rates of neutrons observed at each distance and angle are highly inter-dependent; The number of neutrons produced in an interaction can be correlated with their energies, and therefore the distance they travel, for example. The most significant dependence between rates at different angles and distances simply comes from the fact that fundamentally a number of neutrons is produced in an interaction that then capture at some position; once a neutron is observed at one position, however, this drastically reduces the likelihood of another neutron being observed at some other position, since this would require that another neutron was actually produced by the original interaction in addition to it capturing at the new position. This results in large anti-correlations between the probabilities of positive neutron capture multiplicities in different bins of distance and angle, and positive correlations between a positive multiplicity in one bin and zero multiplicity in other bins.

In the absence of this inter-dependence, to obtain an unfolded total neutron multiplicity distribution, the unfolding matrix $P_n(T_i|O_j)$ in Equation (4.3.3) for each d and α bin (determined when producing the unfolded distribution of each bin for the full 3D distribution) could be applied to each event individually. This gives a probability $P_i(n_i)$, for a given event, of the true number of neutrons n_i in the bin i, where $i = 1 \ldots N$ numbers the N bins of d and α. The probability of the *total* multiplicity $P(T)$, for a given event,

can then be determined as

$$P(T) = \sum_{n_1=0}^{T} \sum_{n_2=0}^{T-n_1} \cdots \sum_{n_N=0}^{T-\sum_{i=1}^{N-1} n_i} P_1(n_1)P_2(n_2)\cdots P_N(n_N), \tag{B.0.1}$$

which sums over all possible combinations of multiplicities in each bin that sum to T. This could then be summed over each event, to give the total unfolded multiplicity distribution.

To account for the dependence between the $P_i(n_i)$, the above method would need to be modified, replacing the product of independent probabilities $\prod_{i-1}^{N} P_i(n_i)$ in Equation (B.0.1) with the full joint probability $P(n_1, n_2, \ldots, n_N)$ of observing n_i neutrons in the i bins. This full joint probability is not simple to calculate taking into account all correlations between bins; there are a total of N^M terms in the above sum (where M is the maximum multiplicity in a given bin), which cannot be determined as the product of independent probabilities.

Alternatively, a more feasible approach may be to attempt to simply unfold the observed total multiplicity distribution. In this case, the distance and angle dependence of the background rates and efficiencies would need to be taken into account in the construction of the response matrix. Fundamentally, the response could be constructed in exactly the way that was done for unfolding individual bins, through Equation (4.3.4), with the μ now being the total background rate across all distances and angles, and ϵ now being the overall efficiency of all neutron captures at all positions. In practice, although the total background rate can be determined simply by integrating the background estimates over all positions (*i.e.* summing over the bins of distance and angles), determining the overall efficiency is more complex; a weighted average would need to be taken over the distance and angle bins, weighted by the likelihood of signal neutrons capturing in that position.

The distribution of signal neutrons' positions is another part of the measurement, and the unfolding of this true distribution was found to work well, as presented in Section 4.4. These results – specifically the 2D unfolded distribution of signal neutrons distance and angle, given in Figure 4.12 – could be used to provide the weighting of each distance and angle to perform the weighted average of the efficiencies described above. The response matrix can then be constructed in the same way as for the unfolding of individual bins, for the same unfolding procedure to be applied to the total multiplicity distribution. However, attempts at using this method have so far not been successful at reproducing the true total multiplicity distribution from the observed distribution.

Appendix C

Further details of T2HK GLoBES simulation

The model of the T2HK detector used in Chapter 5 significantly deviates from previous work using the GLoBES software and is much closer to the models used in official Hyper-Kamiokande simulations. In this appendix, some further details of its implementation which where glossed over in the main text and a comparison with the collaboration's simulation.

C.1 Energy bins

This model of the T2HK detector(s) features 12 energy bins. Bin 1 collects all events below 0.35 GeV. The next 5 bins are 0.1 GeV wide, collecting events from 0.35-0.85 GeV. The next two bins are 0.2 GeV wide, followed by a single bin of 0.25 GeV width. There are then 3 increasingly broad bins, from 1.5 to 3.5, 3.5 to 6 and an overspill bin from 6 to 10 GeV.

C.2 Channel systematic uncertainties

The model of the systematic uncertainty at T2HK uses two general normalisation systematics for the signal and background of each channel. The precise systematic errors used in this simulation are given, channel by channel, in Table C.1.

	$\nu_\mu \to \nu_e$	$\nu_\mu \to \nu_\mu$	$\overline{\nu}_\mu \to \overline{\nu}_e$	$\overline{\nu}_\mu \to \overline{\nu}_\mu$
Signal	2.4 %	2.7 %	2.925 %	2.7 %
Background	2.4 %	2.7 %	2.925 %	2.7 %

Table C.1: Systematic errors used for T2HK simulation.

C.3 Comparison with published event rates

Figure C.1 compares the event rates from this simulation to the official rates published by T2HK. The official simulation does not use GLoBES, and the reproduction is a non-trivial check to show that the signal and background modelling in this GLoBES simulation is faithful. Additional checks have also been made to ensure that these simulations are able to reproduce the final sensitivities of official simulations, after modifications to match the priors and chosen fitted parameters of the official simulations.

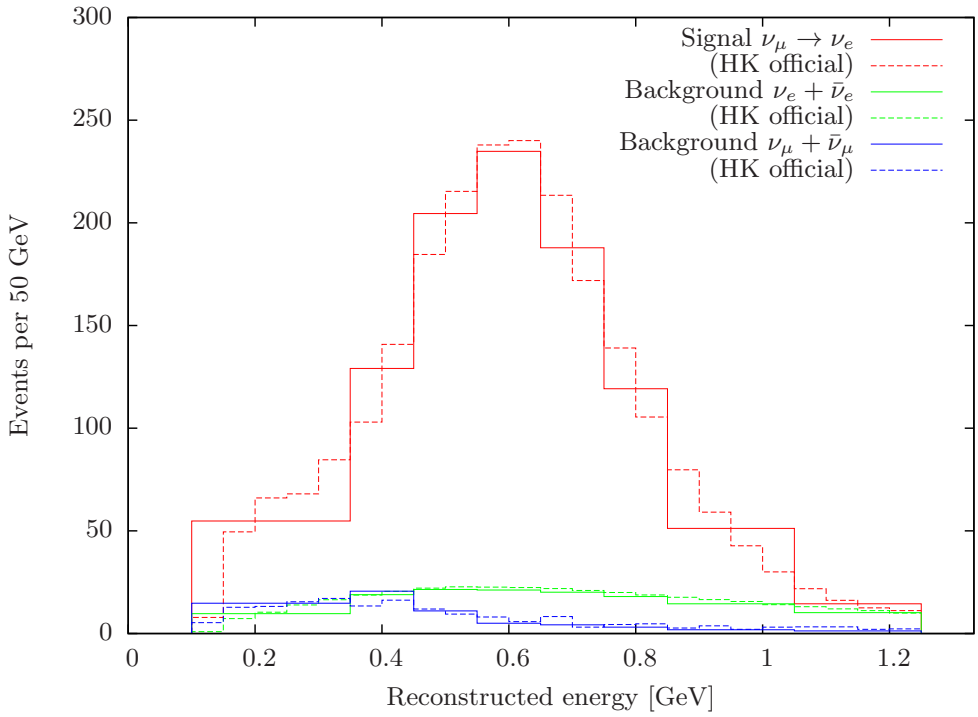

Figure C.1: T2HK appearance spectrum from the GLoBES simulations used in Chapter 5 compared to official event rates [64].

Appendix D

Exact expressions for LS sum rules

The following expressions represent relations between the neutrino mixing parameters in the Littlest Seesaw models, derived to be used in the work of Chapter 6. The angles and Dirac phase can be written as

$$\sin^2\theta_{13} = s(r), \qquad \tan^2\theta_{12} = t(r), \qquad \cos 2\theta_{23} = \pm c(r), \qquad \cos\delta = \pm d(r), \tag{D.0.1}$$

with positive signs taken for LSA and negative for LSB and where

$$s(r) = \frac{1}{6}\left(1 - \frac{55r^2 + 4(1-4r)}{\sqrt{\left((11r)^2 + 4(1-7r)\right)\left((11r)^2 + 4(1-r)\right)}}\right) \tag{D.0.2}$$

$$t(r) = \frac{1}{4}\left(1 + \frac{55r^2 + 4(1-4r)}{\sqrt{\left((11r)^2 + 4(1-7r)\right)\left((11r)^2 + 4(1-r)\right)}}\right) \tag{D.0.3}$$

$$c(r) = \frac{2r(11r-1)\left(55r^2 - 16r + 4 - 5\sqrt{\left((11r)^2 + 4(1-7r)\right)\left((11r)^2 + 4(1-r)\right)}\right)}{\left((11r)^2 + 4(1-7r)\right)\left((11r)^2 + 4(1-r)\right) + 4r^2\left((11r)^2 + 2(2-11r)\right)} \tag{D.0.4}$$

$$d(r) = -\frac{c(r)(1-5s(r))}{2\sqrt{2s(r)(1-c(r)^2)(1-3s(r))}}. \tag{D.0.5}$$

Similar expressions for the Majorana phases also possible. Combining these, expressions relating any two of the angles and/or phases can be found. The first such relation, relating θ_{13} and θ_{12}, is the same as Equation (6.1.8), which is general for all CSD(n). New exact relations between θ_{13} and θ_{23} or θ_{12} and θ_{23}, as well as the relation between δ and θ_{12}, true for LSA with $\eta = \frac{2\pi}{3}$ or LSB with $\eta = -\frac{2\pi}{3}$, are found of the form

$$f_\pm(\theta_{13}, \theta_{23}) = 0, \qquad g_\pm(\theta_{12}, \theta_{23}) = 0, \qquad h_\pm(\delta, \theta_{12}) = 0, \tag{D.0.6}$$

where again the positive (negative) sign is used in the functions valid for LSA (LSB). Exact expressions are given as

$$f_{\pm}(\theta_{13},\theta_{23}) = \frac{44 s_{13}^2\sqrt{1-3s_{13}^2}}{4(1-6s_{13}^2)\mp 3c_{13}^2\cos 2\theta_{23}} \pm \frac{c_{13}^2\cos 2\theta_{23}}{\sqrt{1-3s_{13}^2}} - \sqrt{\frac{8s_{13}^2}{3} - \frac{c_{13}^4\cos^2 2\theta_{23}}{3(1-3s_{13}^2)}}, \tag{D.0.7}$$

$$g_{\pm}(\theta_{12},\theta_{23}) = \frac{22 s_{12}^2\sqrt{1-3s_{12}^2}}{2(5s_{12}^2-1)\mp \cos 2\theta_{23}} \pm \frac{\cos 2\theta_{23}}{\sqrt{1-3s_{12}^2}} - \sqrt{4s_{12}^2 - \frac{\cos^2 2\theta_{23}}{3(1-3s_{12}^2)}}, \tag{D.0.8}$$

$$h_{\pm}(\delta,\theta_{12}) = \frac{5s_{12}^2-1}{s_{12}\sqrt{1-3s_{12}^2}} \pm \frac{\sqrt{3}\cos\delta}{\sqrt{1-12(s_{12}^2-3s_{12}^4)\sin^2\delta}} + \frac{11\sqrt{1-12(s_{12}^2-3s_{12}^4)\sin^2\delta}}{2(6s_{12}^2-1)\sin\delta\mp 2\sqrt{3}\cos\delta}. \tag{D.0.9}$$

Bibliography

[1] Peter Ballett, Stephen F. King, Silvia Pascoli, Nick W. Prouse, and TseChun Wang. Sensitivities and synergies of DUNE and T2HK. *Phys. Rev.*, D96(3):033003, 2017. 2, 119

[2] Peter Ballett, Stephen F. King, Silvia Pascoli, Nick W. Prouse, and TseChun Wang. Precision neutrino experiments vs the Littlest Seesaw. 2016. 2, 118, 175

[3] Y. Fukuda et al. Evidence for oscillation of atmospheric neutrinos. *Phys.Rev.Lett.*, 81:1562–1567, 1998. 17, 21

[4] C.L. Cowan, F. Reines, F.B. Harrison, H.W. Kruse, and A.D. McGuire. Detection of the free neutrino: A Confirmation. *Science*, 124:103–104, 1956. 17, 20

[5] Wolfgang Pauli. Letter to Tübingen conference participants, December 1930. 17, 20

[6] Ivan Esteban, M. C. Gonzalez-Garcia, Michele Maltoni, Ivan Martinez-Soler, and Thomas Schwetz. Updated fit to three neutrino mixing: exploring the accelerator-reactor complementarity. *JHEP*, 01:087, 2017. 17, 23, 23, 24, 141, 179, 182

[7] S. Fukuda et al. Solar B-8 and hep neutrino measurements from 1258 days of Super-Kamiokande data. *Phys. Rev. Lett.*, 86:5651–5655, 2001. 17, 21

[8] Q. R. Ahmad et al. Measurement of the rate of $\nu_e + d \rightarrow p + p + e^-$ interactions produced by ^8B solar neutrinos at the Sudbury Neutrino Observatory. *Phys. Rev. Lett.*, 87:071301, 2001. 17, 21

[9] Q. R. Ahmad et al. Direct evidence for neutrino flavor transformation from neutral current interactions in the Sudbury Neutrino Observatory. *Phys. Rev. Lett.*, 89:011301, 2002. 17, 21

[10] K. Eguchi et al. First results from KamLAND: Evidence for reactor anti-neutrino disappearance. *Phys. Rev. Lett.*, 90:021802, 2003. 17

[11] M. H. Ahn et al. Measurement of Neutrino Oscillation by the K2K Experiment. *Phys. Rev.*, D74:072003, 2006. 17

[12] D. G. Michael et al. Observation of muon neutrino disappearance with the MINOS detectors and the NuMI neutrino beam. *Phys. Rev. Lett.*, 97:191801, 2006. 17

[13] F.P. An et al. Observation of electron-antineutrino disappearance at Daya Bay. *Phys.Rev.Lett.*, 108:171803, 2012. 17, 118

[14] K. Abe et al. Indication of Electron Neutrino Appearance from an Accelerator-produced Off-axis Muon Neutrino Beam. *Phys.Rev.Lett.*, 107:041801, 2011. 17, 118

[15] N. Agafonova et al. Observation of a first ν_τ candidate in the OPERA experiment in the CNGS beam. *Phys. Lett.*, B691:138–145, 2010. 17

[16] M. G. Aartsen et al. First observation of PeV-energy neutrinos with IceCube. *Phys. Rev. Lett.*, 111:021103, 2013. 17

[17] K. Abe et al. Hyper-Kamiokande Design Report. 2018. 17, 40, 43, 45, 45, 49, 50, 53, 53, 54, 55, 55, 56, 57, 58, 59, 101, 119, 128, 133, 140, 144, 147

[18] R. Acciarri et al. Long-Baseline Neutrino Facility (LBNF) and Deep Underground Neutrino Experiment (DUNE). 2015. 17, 118, 119, 125, 127, 131, 133, 140, 144

[19] J. Chadwick. Possible Existence of a Neutron. *Nature*, 129:312, 1932. 20

[20] E. Fermi. Trends to a Theory of beta Radiation. (In Italian). *Nuovo Cim.*, 11:1–19, 1934. [,535(1934)]. 20

[21] E. Fermi. An attempt of a theory of beta radiation. 1. *Z. Phys.*, 88:161–177, 1934. 20

[22] Steven Weinberg. A Model of Leptons. *Phys. Rev. Lett.*, 19:1264–1266, 1967. 20

[23] Abdus Salam. Weak and Electromagnetic Interactions. *Conf. Proc.*, C680519:367–377, 1968. 20

[24] Raymond Davis, Jr., Don S. Harmer, and Kenneth C. Hoffman. Search for neutrinos from the sun. *Phys. Rev. Lett.*, 20:1205–1209, 1968. 21

[25] B. Pontecorvo. Mesonium and anti-mesonium. *Sov. Phys. JETP*, 6:429, 1957. [Zh. Eksp. Teor. Fiz.33,549(1957)]. 21, 21

[26] Ziro Maki, Masami Nakagawa, and Shoichi Sakata. Remarks on the unified model of elementary particles. *Prog. Theor. Phys.*, 28:870–880, 1962. 21, 21

[27] J. Beringer et al. Review of Particle Physics (RPP). *Phys.Rev.*, D86:010001, 2012. 22

[28] Makoto Kobayashi and Toshihide Maskawa. CP Violation in the Renormalizable Theory of Weak Interaction. *Prog. Theor. Phys.*, 49:652–657, 1973. 22

[29] Rabindra N. Mohapatra and Goran Senjanovic. Neutrino Mass and Spontaneous Parity Violation. *Phys. Rev. Lett.*, 44:912, 1980. 22

[30] Evgeny Kh. Akhmedov and Alexei Yu. Smirnov. Paradoxes of neutrino oscillations. *Phys. Atom. Nucl.*, 72:1363–1381, 2009. 22

[31] Evgeny Kh. Akhmedov and Joachim Kopp. Neutrino oscillations: Quantum mechanics vs. quantum field theory. *JHEP*, 04:008, 2010. [Erratum: JHEP10,052(2013)]. 22

[32] Nov 2017. NuFit v3.1, http://www.nu-fit.org. 23

[33] K. Abe et al. Indication of Electron Neutrino Appearance from an Accelerator-produced Off-axis Muon Neutrino Beam. *Phys. Rev. Lett.*, 107:041801, 2011. 23

[34] F. P. An et al. Observation of electron-antineutrino disappearance at Daya Bay. *Phys. Rev. Lett.*, 108:171803, 2012. 23

[35] S. Pascoli, S. T. Petcov, and Antonio Riotto. Connecting low energy leptonic CP-violation to leptogenesis. *Phys. Rev.*, D75:083511, 2007. 23

[36] S. Pascoli, S. T. Petcov, and Antonio Riotto. Leptogenesis and Low Energy CP Violation in Neutrino Physics. *Nucl. Phys.*, B774:1–52, 2007. 23

[37] C. Jarlskog. Commutator of the Quark Mass Matrices in the Standard Electroweak Model and a Measure of Maximal CP Violation. *Phys. Rev. Lett.*, 55:1039, 1985. 24

[38] Stephen F. King and Christoph Luhn. Neutrino Mass and Mixing with Discrete Symmetry. *Rept. Prog. Phys.*, 76:056201, 2013. 25, 30, 32, 174

[39] L. Wolfenstein. Neutrino Oscillations in Matter. *Phys. Rev.*, D17:2369–2374, 1978. 25, 27

[40] S. P. Mikheyev and A. Yu. Smirnov. Resonant neutrino oscillations in matter. *Prog. Part. Nucl. Phys.*, 23:41–136, 1989. 25, 26, 27

[41] S. P. Mikheev and A. Yu. Smirnov. Resonance Amplification of Oscillations in Matter and Spectroscopy of Solar Neutrinos. *Sov. J. Nucl. Phys.*, 42:913–917, 1985. [,305(1986)]. 25

[42] Steven Weinberg. Baryon and Lepton Nonconserving Processes. *Phys. Rev. Lett.*, 43:1566–1570, 1979. 28

[43] André de Gouvêa. Neutrino Mass Models. *Ann. Rev. Nucl. Part. Sci.*, 66:197–217, 2016. 28

[44] Stephen F. King. Models of Neutrino Mass, Mixing and CP Violation. *J. Phys.*, G42:123001, 2015. 30, 122, 174

[45] S. F. King. Unified Models of Neutrinos, Flavour and CP Violation. *Prog. Part. Nucl. Phys.*, 94:217–256, 2017. 30

[46] P. F. Harrison, D. H. Perkins, and W. G. Scott. Tri-bimaximal mixing and the neutrino oscillation data. *Phys. Lett.*, B530:167, 2002. 32, 175

[47] Stephen F. King. Littlest Seesaw. *JHEP*, 02:085, 2016. 32, 175, 176, 178, 178, 179, 179

[48] Stephen F. King and Christoph Luhn. Littlest Seesaw model from $S_4\times$ U(1). *JHEP*, 09:023, 2016. 32, 175, 177, 178, 178, 179

[49] G. Drexlin, V. Hannen, S. Mertens, and C. Weinheimer. Current direct neutrino mass experiments. *Adv. High Energy Phys.*, 2013:293986, 2013. 32

[50] Stefano Dell'Oro, Simone Marcocci, Matteo Viel, and Francesco Vissani. Neutrinoless double beta decay: 2015 review. *Adv. High Energy Phys.*, 2016:2162659, 2016. 32

[51] C. Patrignani et al. Review of Particle Physics. *Chin. Phys.*, C40(10):100001, 2016. 32, 35, 50, 57

[52] C. H. Llewellyn Smith. Neutrino Reactions at Accelerator Energies. *Phys. Rept.*, 3:261–379, 1972. 34

[53] P. A. Cerenkov. Visible radiation produced by electrons moving in a medium with velocities exceeding that of light. *Phys. Rev.*, 52:378–379, 1937. 35

[54] John David Jackson. *Classical electrodynamics*. Wiley, New York, NY, 3rd ed. edition, 1999. 35

[55] I. Tamm. Radiation Emitted by Uniformly Moving Electrons. *J. Phys. USSR*, 1:439–454, 1937. 35

[56] H. Zhang et al. Supernova Relic Neutrino Search with Neutron Tagging at Super-Kamiokande-IV. *Astropart. Phys.*, 60:41–46, 2015. 36

[57] D. A. Brown et al. ENDF/B-VIII.0: The 8th Major Release of the Nuclear Reaction Data Library with CIELO-project Cross Sections, New Standards and Thermal Scattering Data. *Nucl. Data Sheets*, 148:1–142, 2018. 36

[58] H. Watanabe et al. First Study of Neutron Tagging with a Water Cherenkov Detector. *Astropart. Phys.*, 31:320–328, 2009. 36

[59] Andrew Renshaw. Research and Development for a Gadolinium Doped Water Cherenkov Detector. *Phys. Procedia*, 37:1249–1256, 2012. 38

[60] I. Anghel et al. Letter of Intent: The Accelerator Neutrino Neutron Interaction Experiment (ANNIE). 2015. 38, 62, 87

[61] John F. Beacom and Mark R. Vagins. GADZOOKS! Anti-neutrino spectroscopy with large water Cherenkov detectors. *Phys. Rev. Lett.*, 93:171101, 2004. 38

[62] Chenyuan Xu. Current status of SK-Gd project and EGADS. *J. Phys. Conf. Ser.*, 718(6):062070, 2016. 38

[63] K. Abe et al. Letter of Intent: The Hyper-Kamiokande Experiment — Detector Design and Physics Potential —. 2011. 40

[64] K. Abe et al. Physics potential of a long-baseline neutrino oscillation experiment using a J-PARC neutrino beam and Hyper-Kamiokande. *PTEP*, 2015:053C02, 2015. 40, 212

[65] K. Abe et al. The T2K Experiment. *Nucl. Instrum. Meth.*, A659:106–135, 2011. 40, 41, 44, 45

[66] T. Koseki. J-PARC Accelerator: achievement and future upgrade, 2015. Talk presented at the Workshop for Neutrino Programs with Facilities in Japan, August 4, 2015 Tokai, Japan. 41

[67] T. Kobayashi. Potential J-PARC beam power improvement and beam delivery before 2026, 2015. Talk presented at the Workshop for Neutrino Programs with Facilities in Japan, August 4, 2015, Tokai, Japan. 41

[68] K. Abe et al. Evidence of Electron Neutrino Appearance in a Muon Neutrino Beam. *Phys.Rev.*, D88:032002, 2013. 42

[69] K. Abe et al. Physics Potentials with the Second Hyper-Kamiokande Detector in Korea. 2016. 44, 119, 128, 162, 165, 167

[70] A Blondel, M Yokoyama, and M Zito. The T2K-ND280 upgrade proposal. Technical Report CERN-SPSC-2018-001. SPSC-P-357, CERN, Geneva, Jan 2018. This proposal is the follow-up of the Expression of Interest EOI-15 submitted to SPSC in January 2017. 45

[71] C. Andreopoulos et al. TITUS: the Tokai Intermediate Tank for the Unoscillated Spectrum. 2016. 46, 47, 48, 48, 83, 84

[72] S. Bhadra et al. Letter of Intent to Construct a nuPRISM Detector in the J-PARC Neutrino Beamline. 2014. 46, 49

[73] P. Bagley et al. KM3NeT: Technical Design Report for a Deep-Sea Research Infrastructure in the Mediterranean Sea Incorporating a Very Large Volume Neutrino Telescope. 2009. 46

[74] Jan 2018. NuFit v3.2, http://www.nu-fit.org. 50

[75] Jiro Arafune, Masafumi Koike, and Joe Sato. CP violation and matter effect in long baseline neutrino oscillation experiments. *Phys. Rev.*, D56:3093–3099, 1997. [Erratum: Phys. Rev.D60,119905(1999)]. 51

[76] Andre de Gouvea, James Jenkins, and Boris Kayser. Neutrino mass hierarchy, vacuum oscillations, and vanishing |U(e3)|. *Phys. Rev.*, D71:113009, 2005. 52

[77] Hiroshi Nunokawa, Stephen J. Parke, and Renata Zukanovich Funchal. Another possible way to determine the neutrino mass hierarchy. *Phys. Rev.*, D72:013009, 2005. 52

[78] K. S. Babu et al. Working Group Report: Baryon Number Violation. In *Proceedings, 2013 Community Summer Study on the Future of U.S. Particle Physics: Snowmass on the Mississippi (CSS2013): Minneapolis, MN, USA, July 29-August 6, 2013*, 2013. 57

[79] K. Abe et al. Search for proton decay via $p \to \nu K^+$ using 260 kiloton·year data of Super-Kamiokande. *Phys. Rev.*, D90(7):072005, 2014. 59

[80] K. Abe et al. Search for proton decay via $p \to e^+\pi^0$ and $p \to \mu^+\pi^0$ in 0.31 megaton·years exposure of the Super-Kamiokande water Cherenkov detector. *Phys. Rev.*, D95(1):012004, 2017. 59

[81] K. Abe et al. Search for nucleon decay into charged antilepton plus meson in 0.316 megaton·years exposure of the Super-Kamiokande water Cherenkov detector. *Phys. Rev.*, D96(1):012003, 2017. 59

[82] K. Abe et al. T2K neutrino flux prediction. *Phys. Rev.*, D87(1):012001, 2013. [Addendum: Phys. Rev.D87,no.1,019902(2013)]. 62

[83] C. Andreopoulos et al. The GENIE Neutrino Monte Carlo Generator. *Nucl. Instrum. Meth.*, A614:87–104, 2010. 62

[84] Yoshinari Hayato. A neutrino interaction simulation program library NEUT. *Acta Phys. Polon.*, B40:2477–2489, 2009. 62, 91

[85] Omar Benhar and Adelchi Fabrocini. Two nucleon spectral function in infinite nuclear matter. *Phys. Rev.*, C62:034304, 2000. 62

[86] D. Rein and L. M. Sehgal. PCAC and the Deficit of Forward Muons in pi+ Production by Neutrinos. *Phys. Lett.*, B657:207–209, 2007. 62

[87] Dieter Rein and Lalit M. Sehgal. Coherent pi0 Production in Neutrino Reactions. *Nucl. Phys.*, B223:29, 1983. 62

[88] Dieter Rein and Lalit M. Sehgal. Neutrino Excitation of Baryon Resonances and Single Pion Production. *Annals Phys.*, 133:79–153, 1981. 62

[89] Krzysztof M. Graczyk and Jan T. Sobczyk. Form Factors in the Quark Resonance Model. *Phys. Rev.*, D77:053001, 2008. [Erratum: Phys. Rev.D79,079903(2009)]. 63

[90] M. Gluck, E. Reya, and A. Vogt. Dynamical parton distributions revisited. *Eur. Phys. J.*, C5:461–470, 1998. 63

[91] A. Bodek and U. K. Yang. Modeling neutrino and electron scattering inelastic cross- sections in the few GeV region with effective LO PDFs TV Leading Order. In *2nd International Workshop on Neutrino-Nucleus Interactions in the Few GeV Region (NuInt 02) Irvine, California, December 12-15, 2002*, 2003. 63

[92] S. Agostinelli et al. GEANT4: A Simulation toolkit. *Nucl. Instrum. Meth.*, A506:250–303, 2003. 63, 91

[93] Wing Ma. Low Energy Reconstruction. In *UK General Hyper-Kamiokande Meeting*, 2015. 63

[94] A. A. Aguilar-Arevalo et al. The MiniBooNE Detector. *Nucl. Instrum. Meth.*, A599:28–46, 2009. 63

[95] Stephen J. Brice. *Monte Carlo and Analysis Techniques for the Sudbury Neutrino Observatory*. PhD thesis, Oxford U., 1996. 63

[96] M. Shiozawa. Reconstruction algorithms in the Super-Kamiokande large water Cherenkov detector. *Nucl. Instrum. Meth.*, A433:240–246, 1999. 65, 67

[97] E.B. Saff and A.B.J. Kuijlaars. Distributing many points on a sphere. *The Mathematical Intelligencer*, 19(1):5–11, 1997. 65

[98] F. James and M. Roos. Minuit: A System for Function Minimization and Analysis of the Parameter Errors and Correlations. *Comput. Phys. Commun.*, 10:343–367, 1975. 68

[99] Greig Cowan, Evangelia Drakopoulou, Matthew Needham, and Mahdi Taani. Machine Learning-based Energy Reconstruction for Water-Cherenkov detectors. In *Proceedings, Prospects in Neutrino Physics (NuPhys2016): London, UK, December 12-14, 2016*, 2017. 68

[100] Richard J. Bonventre. *Neutron multiplicity in atmospheric neutrino events at the Sudbury Neutrino Observatory*. PhD thesis, Pennsylvania U., 2014. 68

[101] R. B. Patterson, E. M. Laird, Y. Liu, P. D. Meyers, I. Stancu, and H. A. Tanaka. The Extended-track reconstruction for MiniBooNE. *Nucl. Instrum. Meth.*, A608:206–224, 2009. 68, 97

[102] WCSim. https://github.com/WCSim/WCSim. 91

[103] nuPRISM fork of WCSim. https://github.com/nuPRISM/WCSim. 92

[104] Additional gadolinium support for GLG4sim. http://neutrino.phys.ksu.edu/~GLG4sim/Gd.html. 92

[105] Kaito Hagiwara et al. Comparison of γ production from thermal neutron capture of gadolinium with the MonteCarlo simulation. *PoS*, KMI2017:035, 2017. 92

[106] Iwa Ou, Takatomi Yano, Yoshiyuki Yamada, Takaaki Mori, Tsubasa Kayano, Makoto Sakuda, Atsushi Kimura, and Hideo Harada. Measurement of the Energy, Multiplicity and Angular Correlation of γ-rays from the Thermal Neutron Capture Reaction Gd(n, γ). *JPS Conf. Proc.*, 1:013053, 2014. 92

[107] Shirley Weishi Li and John F. Beacom. First calculation of cosmic-ray muon spallation backgrounds for MeV astrophysical neutrino signals in Super-Kamiokande. *Phys. Rev.*, C89:045801, 2014. 95

[108] Yosuke Takubo. *A Study of Muon Neutrino Oscillation with Low Energy Spectrum in a Long Baseline Experiment*. PhD thesis, Osaka U., 2006. 95

[109] C. Hagmann, D. Lange, and D. Wright. Cosmic-ray shower generator (cry) for monte carlo transport codes. In *2007 IEEE Nuclear Science Symposium Conference Record*, volume 2, pages 1143–1146, Oct 2007. 96

[110] Shimpei Tobayama. *An analysis of the oscillation of atmospheric neutrinos*. PhD thesis, University of British Columbia, 2016. 97

[111] M.Smy. Low Energy Event Reconstruction and Selection in Super-Kamiokande-III. In *Proceedings of 30th International Cosmic Ray Conference*, pages 1279–1282, Mexico, Mexico, 2007. 97

[112] G. D'Agostini. A Multidimensional unfolding method based on Bayes' theorem. *Nucl. Instrum. Meth.*, A362:487–498, 1995. 108

[113] Tim Adye. Unfolding algorithms and tests using RooUnfold. In *Proceedings, PHYSTAT 2011 Workshop on Statistical Issues Related to Discovery Claims in Search Experiments and Unfolding, CERN,Geneva, Switzerland 17-20 January 2011*, pages 313–318, Geneva, 2011. CERN, CERN. 108

[114] J.K. Ahn et al. Observation of Reactor Electron Antineutrino Disappearance in the RENO Experiment. *Phys.Rev.Lett.*, 108:191802, 2012. 118

[115] F.P. An et al. Improved Measurement of Electron Antineutrino Disappearance at Daya Bay. *Chin.Phys.*, C37:011001, 2013. 118

[116] A. A. Aguilar-Arevalo et al. Unexplained Excess of Electron-Like Events From a 1-GeV Neutrino Beam. *Phys. Rev. Lett.*, 102:101802, 2009. 118

[117] A. A. Aguilar-Arevalo et al. Improved Search for $\bar{\nu}_\mu \to \bar{\nu}_e$ Oscillations in the MiniBooNE Experiment. *Phys. Rev. Lett.*, 110:161801, 2013. 118

[118] A. Aguilar-Arevalo et al. Evidence for neutrino oscillations from the observation of anti-neutrino(electron) appearance in a anti-neutrino(muon) beam. *Phys. Rev.*, D64:112007, 2001. 118

[119] Ernest Ma. Soft $A_4 \to Z_3$ symmetry breaking and cobimaximal neutrino mixing. *Phys. Lett.*, B755:348–350, 2016. 118

[120] Jun-Nan Lu and Gui-Jun Ding. Alternative Schemes of Predicting Lepton Mixing Parameters from Discrete Flavor and CP Symmetry. 2016. 118

[121] Jeffrey M. Berryman and Daniel Hernández. Standard model flavor from an $SU(2)$ symmetry. 2016. 118

[122] M. Antonello et al. A Proposal for a Three Detector Short-Baseline Neutrino Oscillation Program in the Fermilab Booster Neutrino Beam. 2015. 118

[123] Fengpeng An et al. Neutrino Physics with JUNO. *J. Phys.*, G43(3):030401, 2016. 118

[124] Zelimir Djurcic et al. JUNO Conceptual Design Report. 2015. 118, 187

[125] Soo-Bong Kim. New results from RENO and prospects with RENO-50. *Nucl. Part. Phys. Proc.*, 265-266:93–98, 2015. 118, 187, 187

[126] P. Adamson et al. First measurement of electron neutrino appearance in NOvA. *Phys. Rev. Lett.*, 116(15):151806, 2016. 118

[127] P. Adamson et al. First measurement of muon-neutrino disappearance in NOvA. *Phys. Rev.*, D93(5):051104, 2016. 118

[128] K. Abe et al. Measurements of neutrino oscillation in appearance and disappearance channels by the T2K experiment with 6.6×10^{20} protons on target. *Phys. Rev.*, D91(7):072010, 2015. 118

[129] K. Abe et al. A Long Baseline Neutrino Oscillation Experiment Using J-PARC Neutrino Beam and Hyper-Kamiokande. 2014. 118, 119

[130] C. Adams et al. Scientific Opportunities with the Long-Baseline Neutrino Experiment. 2013. 118, 119

[131] C. Soumya, K. N. Deepthi, and R. Mohanta. A comprehensive study of the discovery potential of NOvA, T2K and T2HK experiments. *Adv. High Energy Phys.*, 2016:9139402, 2016. 119

[132] Pilar Coloma, Patrick Huber, Joachim Kopp, and Walter Winter. Systematic uncertainties in long-baseline neutrino oscillations for large θ_{13}. *Phys.Rev.*, D87(3):033004, 2013. 119

[133] Monojit Ghosh, Srubabati Goswami, and Sushant K. Raut. Maximizing the DUNE early physics output with current experiments. *Eur. Phys. J.*, C76(3):114, 2016. 119

[134] Valentina De Romeri, Enrique Fernandez-Martinez, and Michel Sorel. Neutrino oscillations at DUNE with improved energy reconstruction. 2016. 119

[135] Newton Nath, Monojit Ghosh, and Srubabati Goswami. The physics of antineutrinos in DUNE and determination of octant and δ_{CP}. *Nucl. Phys.*, B913:381–404, 2016. 119

[136] Vernon Barger, Atri Bhattacharya, Animesh Chatterjee, Raj Gandhi, Danny Marfatia, and Mehedi Masud. Optimal configurations of the Deep Underground Neutrino Experiment. *Int. J. Mod. Phys.*, A31(07):1650020, 2016. 119

[137] Vernon Barger, Atri Bhattacharya, Animesh Chatterjee, Raj Gandhi, Danny Marfatia, and Mehedi Masud. Configuring the Long-Baseline Neutrino Experiment. *Phys. Rev.*, D89(1):011302, 2014. 119

[138] Kalpana Bora, Debajyoti Dutta, and Pomita Ghoshal. Determining the octant of θ_{23} at LBNE in conjunction with reactor experiments. *Mod. Phys. Lett.*, A30(14):1550066, 2015. 119

[139] M. Bishai, M. V. Diwan, S. Kettell, J. Stewart, B. Viren, E. Worchester, and Lisa Whitehead. Neutrino Oscillations in the Precision Era. 2012. 119, 121

[140] S.K. Agarwalla et al. The mass-hierarchy and CP-violation discovery reach of the LBNO long-baseline neutrino experiment. 2013. 119

[141] Monojit Ghosh, Pomita Ghoshal, Srubabati Goswami, and Sushant K. Raut. Synergies between neutrino oscillation experiments: an 'adequate' configuration for LBNO. *JHEP*, 03:094, 2014. 119

[142] J. B. Lagrange, J. Pasternak, A. Bross, and A. Liu. Neutrinos from PIon Beam Line, nuPIL. In *17th International Workshop on Neutrino Factories and Future Neutrino Facilities Search (NuFact15) Rio de Janeiro, Brazil, August 10-15, 2015*, 2015. 119, 125

[143] Ao Liu, Alan Bross, and Jean-Baptiste Lagrange. A FODO Beam Line Design for nuPIL. In *Proceedings, 7th International Particle Accelerator Conference (IPAC 2016)*, page THPMB055, 2016. 119, 125

[144] Jean-Baptiste Lagrange, Jaroslaw Pasternak, Alan Bross, Ao Liu, Robert Appleby, and Sam Tygier. FFAG Beam Line for nuPIL - Neutrinos from PIon Beam Line. In *Proceedings, 7th International Particle Accelerator Conference (IPAC 2016)*, page THPMB054, 2016. 119, 125

[145] S. Choubey et al. International Design Study for the Neutrino Factory, Interim Design Report. 2011. 119

[146] Shinya Fukasawa, Monojit Ghosh, and Osamu Yasuda. Complementarity Between Hyperkamiokande and DUNE in Determining Neutrino Oscillation Parameters. 2016. 119, 133, 140, 144

[147] Katsuhiro Asano and Hisakazu Minakata. Large-Theta(13) Perturbation Theory of Neutrino Oscillation for Long-Baseline Experiments. *JHEP*, 1106:022, 2011. 120

[148] Sanjib Kumar Agarwalla, Yee Kao, and Tatsu Takeuchi. Analytical Approximation of the Neutrino Oscillation Probabilities at large θ_{13}. 2013. 120

[149] Mikkel B. Johnson, Ernest M. Henley, and Leonard S. Kisslinger. Analytical Theory of Neutrino Oscillations in Matter with CP violation. *Phys. Rev.*, D91(7):076005, 2015. 120

[150] Hisakazu Minakata and Stephen J Parke. Simple and Compact Expressions for Neutrino Oscillation Probabilities in Matter. *JHEP*, 01:180, 2016. 120

[151] Peter B. Denton, Hisakazu Minakata, and Stephen J. Parke. Compact Perturbative Expressions For Neutrino Oscillations in Matter. *JHEP*, 06:051, 2016. 120

[152] Sanjib Kumar Agarwalla. Physics Potential of Long-Baseline Experiments. *Adv. High Energy Phys.*, 2014:457803, 2014. 121, 122

[153] Patrick Huber and Joachim Kopp. Two experiments for the price of one? – The role of the second oscillation maximum in long baseline neutrino experiments. *JHEP*, 03:013, 2011. [Erratum: JHEP05,024(2011)]. 121, 122

[154] Steve Geer, Olga Mena, and Silvia Pascoli. A Low energy neutrino factory for large θ_{13}. *Phys. Rev.*, D75:093001, 2007. 121

[155] Pilar Coloma and Enrique Fernandez-Martinez. Optimization of neutrino oscillation facilities for large θ_{13}. *JHEP*, 04:089, 2012. 121

[156] S. K. Agarwalla et al. Optimised sensitivity to leptonic CP violation from spectral information: the LBNO case at 2300 km baseline. 2014. 122

[157] Hisakazu Minakata and Stephen J. Parke. Correlated, precision measurements of θ_{23} and δ using only the electron neutrino appearance experiments. *Phys. Rev.*, D87(11):113005, 2013. 122

[158] Pilar Coloma, Hisakazu Minakata, and Stephen J. Parke. Interplay between appearance and disappearance channels for precision measurements of θ_{23} and δ. *Phys. Rev.*, D90:093003, 2014. 122

[159] S. Antusch, P. Huber, S. F. King, and T. Schwetz. Neutrino mixing sum rules and oscillation experiments. *JHEP*, 04:060, 2007. 122

[160] Peter Ballett, Stephen F. King, Christoph Luhn, Silvia Pascoli, and Michael A. Schmidt. Testing atmospheric mixing sum rules at precision neutrino facilities. *Phys. Rev.*, D89(1):016016, 2014. 122

[161] I. Girardi, S. T. Petcov, and A. V. Titov. Determining the Dirac CP Violation Phase in the Neutrino Mixing Matrix from Sum Rules. *Nucl. Phys.*, B894:733–768, 2015. 122

[162] Peter Ballett, Stephen F. King, Christoph Luhn, Silvia Pascoli, and Michael A. Schmidt. Testing solar lepton mixing sum rules in neutrino oscillation experiments. *JHEP*, 12:122, 2014. 122

[163] I. Girardi, S. T. Petcov, and A. V. Titov. Predictions for the Leptonic Dirac CP Violation Phase: a Systematic Phenomenological Analysis. *Eur. Phys. J.*, C75:345, 2015. 122

[164] Pilar Coloma, Andrea Donini, Enrique Fernandez-Martinez, and Pilar Hernandez. Precision on leptonic mixing parameters at future neutrino oscillation experiments. *JHEP*, 06:073, 2012. 122, 123, 123, 123, 124, 124

[165] Patrick Huber, M. Lindner, and W. Winter. Simulation of long-baseline neutrino oscillation experiments with GLoBES (General Long Baseline Experiment Simulator). *Comput. Phys. Commun.*, 167:195, 2005. 125, 132, 186, 189

[166] Patrick Huber, Joachim Kopp, Manfred Lindner, Mark Rolinec, and Walter Winter. New features in the simulation of neutrino oscillation experiments with GLoBES 3.0: General Long Baseline Experiment Simulator. *Comput. Phys. Commun.*, 177:432–438, 2007. 125, 132, 186, 189

[167] Vaia Papadimitriou et al. Design of the LBNF Beamline. In *Proceedings, 7th International Particle Accelerator Conference (IPAC 2016)*, page TUPMR025, 2016. 125

[168] M. Sorel. private communication. 127

[169] Patrick Huber, Manfred Lindner, and Walter Winter. Superbeams versus neutrino factories. *Nucl. Phys.*, B645:3–48, 2002. 128

[170] C. Andreopoulos et al. The GENIE Neutrino Monte Carlo Generator. *Nucl. Instrum. Meth.*, A614:87–104, 2010. 128

[171] M. C. Gonzalez-Garcia, Michele Maltoni, and Thomas Schwetz. Updated fit to three neutrino mixing: status of leptonic CP violation. *JHEP*, 11:052, 2014. 133, 134, 135, 139

[172] D. V. Forero, M. Tortola, and J. W. F. Valle. Neutrino oscillations refitted. *Phys. Rev.*, D90(9):093006, 2014. 134, 141

[173] F. Capozzi, E. Lisi, A. Marrone, D. Montanino, and A. Palazzo. Neutrino masses and mixings: Status of known and unknown 3ν parameters. *Nucl. Phys.*, B908:218–234, 2016. 134, 141

[174] X. Qian, A. Tan, W. Wang, J. J. Ling, R. D. McKeown, and C. Zhang. Statistical Evaluation of Experimental Determinations of Neutrino Mass Hierarchy. *Phys. Rev.*, D86:113011, 2012. 135

[175] Emilio Ciuffoli, Jarah Evslin, and Xinmin Zhang. Confidence in a neutrino mass hierarchy determination. *JHEP*, 01:095, 2014. 135

[176] Mattias Blennow, Pilar Coloma, Patrick Huber, and Thomas Schwetz. Quantifying the sensitivity of oscillation experiments to the neutrino mass ordering. *JHEP*, 03:028, 2014. 135

[177] Jessica Elevant and Thomas Schwetz. On the determination of the leptonic CP phase. *JHEP*, 09:016, 2015. 140

[178] Mattias Blennow, Pilar Coloma, and Enrique Fernandez-Martinez. Reassessing the sensitivity to leptonic CP violation. *JHEP*, 03:005, 2015. 140

[179] Tommy Ohlsson. Special issue on "neutrino oscillations: Celebrating the nobel prize in physics 2015" in nuclear physics b. *Nuclear Physics B*, 908:1, 2016. Neutrino Oscillations: Celebrating the Nobel Prize in Physics 2015. 174, 175

[180] S. F. King. Neutrino mass models. *Rept. Prog. Phys.*, 67:107–158, 2004. 174

[181] Hajime Ishimori, Tatsuo Kobayashi, Hiroshi Ohki, Yusuke Shimizu, Hiroshi Okada, and Morimitsu Tanimoto. Non-Abelian Discrete Symmetries in Particle Physics. *Prog. Theor. Phys. Suppl.*, 183:1–163, 2010. 174

[182] Stephen F. King, Alexander Merle, Stefano Morisi, Yusuke Shimizu, and Morimitsu Tanimoto. Neutrino Mass and Mixing: from Theory to Experiment. *New J. Phys.*, 16:045018, 2014. 174

[183] Peter Minkowski. $\mu \to e\gamma$ at a Rate of One Out of 10^9 Muon Decays? *Phys. Lett.*, 67B:421–428, 1977. 174

[184] Murray Gell-Mann, Pierre Ramond, and Richard Slansky. Complex Spinors and Unified Theories. *Conf. Proc.*, C790927:315–321, 1979. 174

[185] Tsutomu Yanagida. HORIZONTAL SYMMETRY AND MASSES OF NEUTRINOS. *Conf. Proc.*, C7902131:95–99, 1979. 174

[186] S. L. Glashow. The Future of Elementary Particle Physics. *NATO Sci. Ser. B*, 61:687, 1980. 174

[187] Rabindra N. Mohapatra and Goran Senjanovic. Neutrino Mass and Spontaneous Parity Violation. *Phys. Rev. Lett.*, 44:912, 1980. 174

[188] J. Schechter and J. W. F. Valle. Neutrino Masses in SU(2) x U(1) Theories. *Phys. Rev.*, D22:2227, 1980. 174

[189] Stephen F. King. Neutrino Mass and Mixing in the Seesaw Playground. *Nucl. Phys.*, B908:456–466, 2016. 174

[190] S. F. King. Large mixing angle MSW and atmospheric neutrinos from single right-handed neutrino dominance and U(1) family symmetry. *Nucl. Phys.*, B576:85–105, 2000. 174

[191] S. F. King. Constructing the large mixing angle MNS matrix in seesaw models with right-handed neutrino dominance. *JHEP*, 09:011, 2002. 174, 175, 175

[192] P. H. Frampton, S. L. Glashow, and T. Yanagida. Cosmological sign of neutrino CP violation. *Phys. Lett.*, B548:119–121, 2002. 174

[193] Keisuke Harigaya, Masahiro Ibe, and Tsutomu T. Yanagida. Seesaw Mechanism with Occam's Razor. *Phys. Rev.*, D86:013002, 2012. 174

[194] Stephen F. King. Minimal predictive see-saw model with normal neutrino mass hierarchy. *JHEP*, 07:137, 2013. 174, 175, 176

[195] Fredrik Björkeroth, Francisco J. de Anda, Ivo de Medeiros Varzielas, and Stephen F. King. Towards a complete $A_4\times$ SU(5) SUSY GUT. *JHEP*, 06:141, 2015. 174

[196] Fredrik Björkeroth, Francisco J. de Anda, Ivo de Medeiros Varzielas, and Stephen F. King. Towards a complete $\Delta(27) \times SO(10)$ SUSY GUT. *Phys. Rev.*, D94(1):016006, 2016. 174

[197] Fredrik Björkeroth, Francisco J. de Anda, Ivo de Medeiros Varzielas, and Stephen F. King. Leptogenesis in minimal predictive seesaw models. *JHEP*, 10:104, 2015. 174

[198] S. F. King. Atmospheric and solar neutrinos with a heavy singlet. *Phys. Lett.*, B439:350–356, 1998. 175, 175, 176

[199] S. F. King. Atmospheric and solar neutrinos from single right-handed neutrino dominance and U(1) family symmetry. *Nucl. Phys.*, B562:57–77, 1999. 175, 175, 176

[200] S. F. King. Predicting neutrino parameters from SO(3) family symmetry and quark-lepton unification. *JHEP*, 08:105, 2005. 175, 176

[201] Stefan Antusch, Stephen F. King, Christoph Luhn, and Martin Spinrath. Trimaximal mixing with predicted θ_{13} from a new type of constrained sequential dominance. *Nucl. Phys.*, B856:328–341, 2012. 175

[202] S. F. King. Minimal see-saw model predicting best fit lepton mixing angles. *Phys. Lett.*, B724:92–98, 2013. 175

[203] Stephen F. King. A model of quark and lepton mixing. *JHEP*, 01:119, 2014. 175

[204] Stephen F. King. A to Z of Flavour with Pati-Salam. *JHEP*, 08:130, 2014. 175

[205] Fredrik Björkeroth and Stephen F. King. Testing constrained sequential dominance models of neutrinos. *J. Phys.*, G42(12):125002, 2015. 175, 175, 177, 177, 179

[206] Stephen F. King and Christoph Luhn. On the origin of neutrino flavour symmetry. *JHEP*, 10:093, 2009. 175

[207] Zhi-zhong Xing and Shun Zhou. Tri-bimaximal Neutrino Mixing and Flavor-dependent Resonant Leptogenesis. *Phys. Lett.*, B653:278–287, 2007. 175

[208] Carl H. Albright and Werner Rodejohann. Comparing Trimaximal Mixing and Its Variants with Deviations from Tri-bimaximal Mixing. *Eur. Phys. J.*, C62:599–608, 2009. 175

[209] Carl H. Albright, Alexander Dueck, and Werner Rodejohann. Possible Alternatives to Tri-bimaximal Mixing. *Eur. Phys. J.*, C70:1099–1110, 2010. 175

[210] Xiao-Gang He and A. Zee. Minimal Modification to Tri-bimaximal Mixing. *Phys. Rev.*, D84:053004, 2011. 175

[211] Werner Rodejohann and He Zhang. Simple two Parameter Description of Lepton Mixing. *Phys. Rev.*, D86:093008, 2012. 175

[212] Ivo de Medeiros Varzielas and Luís Lavoura. Flavour models for TM_1 lepton mixing. *J. Phys.*, G40:085002, 2013. 175

[213] Walter Grimus. Discrete symmetries, roots of unity, and lepton mixing. *J. Phys.*, G40:075008, 2013. 175

[214] Christoph Luhn. Trimaximal TM_1 neutrino mixing in S_4 with spontaneous CP violation. *Nucl. Phys.*, B875:80–100, 2013. 175

[215] Gui-Jun Ding, Stephen F. King, Christoph Luhn, and Alexander J. Stuart. Spontaneous CP violation from vacuum alignment in S_4 models of leptons. *JHEP*, 05:084, 2013. 175, 177

[216] Stefan Antusch, Stephen F. King, Christoph Luhn, and Martin Spinrath. Right Unitarity Triangles and Tri-Bimaximal Mixing from Discrete Symmetries and Unification. *Nucl. Phys.*, B850:477–504, 2011. 175

[217] S. S. Wilks. The Large-Sample Distribution of the Likelihood Ratio for Testing Composite Hypotheses. *Annals Math. Statist.*, 9(1):60–62, 1938. 183

[218] Xinheng Guo et al. A Precision measurement of the neutrino mixing angle θ_{13} using reactor antineutrinos at Daya-Bay. 2007. 187

[219] Jun Cao and Kam-Biu Luk. An overview of the Daya Bay Reactor Neutrino Experiment. *Nucl. Phys.*, B908:62–73, 2016. 187

[220] F. Ardellier et al. Letter of intent for Double-CHOOZ: A Search for the mixing angle theta(13). 2004. 187

[221] J. K. Ahn et al. RENO: An Experiment for Neutrino Oscillation Parameter θ_{13} Using Reactor Neutrinos at Yonggwang. 2010. 187